TOWARDS REAL-TIME STRUCTURAL HEALTH MONITORING USING LOW-COST DUAL FREQUENCY GNSS RECEIVERS

A GEODETIC PERSPECTIVE

Alexandru Mihai Lăpădat

Committee:

Prof. dr. ir. P. J. G. Teunissen

Dr. ir. C. C. J. M. Tiberius

Prof. dr. M. Veljkovic

TU Delft

Picture by Matías Santana on Unsplash

TOWARDS REAL-TIME STRUCTURAL HEALTH MONITORING OF TALL, SLENDER STRUCTURES USING LOW-COST DUAL FREQUENCY GNSS RECEIVERS

BY

Alexandru Mihai LĂPĂDAT

Geoscience and Remote Sensing,
Delft University of Technology, Delft, The Netherlands,
born in Sibiu, Romania.

Master Thesis

in partial fulfilment of the requirements for the degree of

Master of Applied Earth Sciences
in Geoscience and Remote Sensing

at the Delft University of Technology,
to be defended on the 20th of October ,2020

This thesis has been approved by the:
supervisor: Prof. dr. ir. P. J. G. Teunissen
co-supervisor: Dr. ir. C. C. J. M. Tiberius

Master Thesis Committee composition:

Prof. dr. ir. P. J. G. Teunissen,	chairman Geoscience & Remote Sensing department
Dr. ir. C. C. J. M. Tiberius,	daily supervisor Geoscience & Remote Sensing department
Prof. dr. M. Veljkovic,	2nd research group supervisor Engineering Structures department

Guest members:

E. Lourens,	guest supervisor Engineering Structures department
A. Krietemeyer,	additional guest supervisor Water Management department

Printed by: Grafico Delft

Cover Credit: Front: @Matías Santana (https://unsplash.com/photos/2ykXqiKHNfk)
Back: (https://pixabay.com/photos/skyscrapers-sky-cityscape-tall-up-1081737/)

ISBN 000-00-0000-000-0

An electronic version of this dissertation is available at
http://repository.tudelft.nl/.

CONTENTS

LIST OF FIGURES

LIST OF TABLES

List of Abbreviations

AID Artificially Induced Displacement

APs Application Programs

AR1 Auto-Regressive Noise Process of Order 1

ARP Antenna Reference Point

BDS BeiDou

CORS Continuous Operating Reference Station

CP Carrier Phase

CRS Coordinate Reference System

DC Direct Current

DD Double Difference

DIA Detection, Identification, Adaptation

ECEF Earth-Centered Earth-Fixed

EKF Extended Kalman Filter

ESA European Space Agency

ETRS89 European Terrestrial Reference System 1989

FFT Fast Fourier Transform

FIR Finite Impulse Response

GAL Galileo

GLONASS GLObal'naya NAvigatsionnaya Sputnikovaya Sistema

GLO GLONASS

GLR Generalized Likelihood Ratio

GNSS Global Navigation Satellite System

GPS Global Positioning System

GTRF Galileo Terrestrial Reference Frame

IAE Integer Ambiguity Estimation

IA Integer Aperture

IB Integer Bootstrapping

IIR Infinite Impulse Response

ILS Integer Least Squares

IMU Inertial Measurement Unit

IR Integer Rounding

ITRS International Terrestrial Reference System

LTI Linear Time-Invariant

MDB Minimum Detectable Bias

MEMS Micro Electro-Mechanical System

MEO Medium Earth Orbit

MP Multipath

NaN Not A Number

NRCAN National Resources Canada

NRTK Network Real Time Kinematic

NTRIP Network Transportation of RTCM Internet Protocol

OMT Overall Model Test

OTF On-The-Flight

PCO Phase Center Offset

PCV Phase Center Variations

PC Phase Center

PDF Probability Density Function

PLL Phase-Locked Loop

PPK Post Processing Kinematic

PPP Precise Point Positioning

PRN PseudoRandom Noise

PZ-90 Parametry Zemli 1990

RINEX Receiver Independent Exchange format

RTCM Radio Technical Commission for Maritime Services

RTK Real-Time Kinematic

RTS Robotized Total Statio

SD Single Difference

SHM Structural Health Monitoring

SISRE Signal-In-Space Range Error

UEE User Equipment Error

UERE Total User Equivalent Range Error

UTC Coordinated Universal Time

VRS ViRtual Station

WD Wind Direction

WGS-84 World Geodetic System 1984

WID Wind-Induced Displacement

WS Wind Speed

ZTD Zenith Troposheric Delay

PREFACE

This seven month long project has been driven by the desire to clear up all previously unanswered research questions from an additional experimental project carried out from October 2019 until February 2020 on one of the most iconic structures of Delft, the 90 meter tall EWI tower, for confirming the possibility of using reliable global navigation satellite systems (GNSS) sensors to capture the structure's response to strong winds blowing from the North Sea. By far these two projects represent the most important and fulfilling pieces of work I've been involved in during my academic years, learning a tremendous amount throughout this motivating, but at the same time challenging journey. This brings me to one of my personal favorite quotes, which can best reveal how steep and captivating the escalated learning curve was:

"Life's a mountain and you got
to bike it to enjoy the surrounding landscape from the top."

This best portrays the large amount of individual effort that has been put in this project to be able to reach the peak and self-reflect on the undergone pleasing learning process. However, some might argue that it is easier to hike a mountain than to ride it up, but the joy comes from our encounters with new experiences. Hence, I accepted to bike it and cope with topics, such as digital signal processing, that eventually were not the most enjoyable during my master programme. On the top, all what matters is to be grateful for the glamour of the taken journey, before you'll pack everything together and be ready to ride a steeper and higher mountain from the range you've just discovered!

Having a solid theoretical background in geodesy and surveying, at the beginning of my master programme I was eagerly looking for the opportunity of getting involved into a practical project that would give me the possibility to use the possessed "ingredients" to write a delightful "story", from which (hopefully) many others can benefit. Thus, the personal motivation for conducting research in the field of structural health monitoring (SHM) is related to the desire of contributing at the development of (hopefully) new theoretical and practical knowledge related to the high-precision GNSS positioning domain with application in civil engineering, from which social categories such as developing countries research institutes , civil engineering constructors, maintenance companies and end-users can benefit in the design, construction, maintenance and process of use of safe and useful structures.

However, this project could not be run without the guidance and help of a group of marvelous people, which I would like to express my gratitude to. From this list of people, first of all I would like to express my sincere gratitude to Dr. Ir. Christian Tiberius, in the role of my daily supervisor, for responding with the finest support and guidance throughout the entire project, and with by far the best practical manner of explaining complicated subjects, turning them into easy and enjoyable discussions. Secondly, I would like to thank Andreas Krietemeyer, for being more than a guest member of my graduation committee, and supporting me with all the needed GNSS instrumentation, practical instructions and suggestions for establishing an optimal experimental setup. Furthermore, I want to thank Prof. Dr. Ir. Peter Teunissen, in the role of the chairman of the graduation committee, for his suggestions on new ideas for implementation, from which some of them were concertized in the body of the present document. Thanks also to Prof. Dr. Milan Veljkovic and to Eliz-Mari Lourens, in the roles of additional supervisors part of the Engineering Structures department, for offering advice on the structural engineering side of the project and being actively interested in the development and integration of a smartphone accelerometer based validation procedure within the proposed experiment.

At the same level, my research could not have been possible without the help of Dr. Ir. Hans van der Marel and his large collection of Matlab scripts, which were adapted based on the requirements of this research project. Furthermore, I am grateful for his advice on establishing a compatible and stable data flow cabling network and for his many good email interventions, solving some of my urgent questions. Similarly, I want to thank Dr. Ir. Sandra Verhagen for her support and interventions on the complex topic on carrier-phase (CP) integer ambiguity estimation. A special thanks goes out to Han Dun and Dr. Marc Schleiss for providing me the needed auxiliary instrumentation in the form of a laser distometer and weather station sensors together with some insights on how to manipulate them in the best way. Furthermore, I want to thank Ostar Joostensz for his interest in my project, offering me cooperation with Rijkswaterstaat for the deployment of a GNSS based real structural health monitoring experiment on road signs, which in the end was hold off by the COVID-19 pandemic.

Last but not least, I would like to thank to my beloved parents for their unconditional support and encouragement during this project, despite being faraway from me but always spiritually close and wholehearted.

Alexandru Mihai Lăpădat
Delft, October 2020

ABSTRACT

Under urban sprawl the trend of new established complex structures has rapidly increased. In this context little importance has been given to maintenance, even if this represents an important step in combating and avoiding disasters and developing improved future structural designs. Over the last years low-cost Global Navigation Satellite System (GNSS) equipment has faced rapid and important development opening a new door to reliable and high accuracy positioning applications such as structural health monitoring (SHM).
This study focuses on assessing, from a geodetic perspective, the capabilities of a pair of low-cost dual frequency GNSS receivers for capturing the kinematic response of structures to wind. An experiment has been carried out with a stainless steel cantilever beam, aiming to highlight the advantages of employing a differential GNSS system for monitoring low frequency changes in the structure's body. Hence, in this context the nominal precision of the GNSS system in East, North and Up direction of 4, 5 and 10 millimeter (1σ), was further improved to 3, 4 and 8 miilimeters in the presence of a Global Positioning System (GPS) based multipath (MP) correction. However, it is safer to consider that the true displacement retention potential of the low-cost GNSS receivers corresponds to 3 times (3σ) the aforementioned standard deviation values, resulting in slightly larger than 1 centimeter detectable horizontal displacements, and up to 2.4 centimeters vertical displacements. To support this, wind-induced beam displacements of up to 1.9 centimeters were identified and attested based on a cross correlation analysis with meteorological information.
Next, the architecture of a GNSS based SHM system is proposed that can detect structural displacements in real time and rise safety alarms. Therefore, with real time kinematic (RTK) positioning and a position outlier and slip statistical testing procedure, a clear strategy for the estimation and identification of uni- or tri-dimensional displacement quantities in real time is proposed, to rise alarms about the magnitude and the direction of identified displacements.
Hence, there is no doubt that newly released low-cost dual frequency GNSS receivers represent an alternative to high-end geodetic equipment for SHM, by offering an optimal balance between precision and cost efficiency.

1

INTRODUCTION

This first chapter introduces GNSS based structural health monitoring (SHM) as the general topic of the master thesis project along with the universal motivation of performing SHM campaigns. For the deployment of such a study, a set of displacement sensing instruments are needed. Hence the working principle of the traditional accelerometer, laser distometer and of the newly adopted GNSS sensor is presented. Moreover, a brief enumeration of the existing GNSS satellite constellations along with their traditional coordinate reference systems and frames is given.
Prior to the deployment of the master thesis project, a thorough literature review was performed. The subjects of this literature review are listed in this chapter, focusing on: the use of high-end and low-cost GNSS systems for SHM, frequently encountered errors affecting the GNSS observations and some methods of mitigation, the use of accelerometers for SHM studies and its error budget, the integration of GNSS sensors with accelerometers, the growing interest in using smartphone accelerometers for SHM and the importance of statistically testing the significance of the estimated displacement quantities prior to their validation.
Lastly, the thesis goal of attesting the capability of low-cost dual frequency GNSS modules for sensing wind-induced structural displacements followed by the development of an integration procedure for the structural displacement identification in real time, is phrased. To achieve this, five research questions are formulated. In the end, a brief summary of the master thesis structure is presented to inform the reader about the treated topics of each chapter.

1

1.1. INTRODUCTION INTO STRUCTURAL HEALTH MONITORING

THE process of structural health monitoring (SHM) complies with the selection and implementation of different types of sensors able to measure in a nondestructive manner the key parameters that describe the health/ integrity of the structure under consideration over its entire life time. In this process, sensors are operating for the identification of any structural damage that can affect the current or expected performance of a structure. Hence, in very general terms the SHM process can be described as a process in which measurements are acquired by an array of sensors installed on the case study structure, which are then statistically assessed in order to extract structural features that can inform about any material of geometrical change in the structural system and describe the status of the considered structure.
The universal motivation for performing a SHM study lies in the fact that different parties such as end-users, civil engineering constructors and maintenance companies can obtain life-safety and economic benefits out of it. For instance workmen in a high-rise tower can benefit from safely using their workplace, which is continuously being monitored to avoid any catastrophic failure, civil engineers can economically benefit from the response of the already used materials in a structure to develop better and more sustainable future designs while maintenance companies can economically benefit from the acquired damage information to plan periodic maintenance along with precise detection surveys at specific locations where possible intervention is needed.
Historically speaking, "the civil engineering community has studied vibration-based damage assessment of bridge structures and buildings since the early 1980s"(Farrar and Worden [1]). In this context damage can be studied by searching for abnormal variations in the modal characteristics of the structure, such as the natural frequency, damping ratio and mode shape.
Dams were mentioned in (Brownjohn [2]) as the first structures to be mandated in 1975 by the British legislation to be continuously inspected. This all started after 254 human lives were lost near Sheffield, UK in 1864 due to a failure of an embankment dam. In the same paper, the purpose of building monitoring is mentioned to be closely related to the need of understanding of the building response performance during earthquakes and storms, and was initially conducted based on vibration tests in order to capture the building dynamic behavior. Another relevant example that can answer best the question on nowadays need of continuously monitoring of major structures, is related to the 2018 failure of a 243 meter section from the multi-span, cable stayed Morandi bridge in Genoa, Italy, which resulted in the death of 43 people. It is believed that this all happened due to evidence of corrosion of the supportive concrete-covered cable stays and faulty maintenance. In (Calvi *et al.* [3]) monitoring activity at the Morandi bridge was reported to have been sporadically conducted only in the early 1990s when the level of deterioration of the bridge was widespread and maintenance was crucial.
The most common sensor used for tracking the dynamic behavior of tall buildings is the accelerometer. But nowadays with the rapid advancement of sensors development, fibre optic sensors and GNSS receivers gained in popularity. The former type is known for collecting strain measurements with high spatial and temporal resolution while the latter sensor for measuring relative deformations describing very slow movements. Therefore, from a geodetic point of view a GNSS measuring system is ideal for studying the low frequent induced structural damage based on the identification of critical static and quasi-static displacements of the structure produced by natural factors such as wind storms, earthquakes or landslides.
From the beginning it is important to note that this study focuses on the geodetic approach, on behalf of a kinematic experimental study run on a stainless steel cantilever beam, aiming to present the advantages of considering a low-cost dual frequency GNSS system for monitoring low frequent changes in the structures body and fill the gap of conventional accelerometers for measuring static structural responses. Additionally, the use of a smartphone accelerometer is considered for inspecting and validating the capability of the GNSS system of capturing dynamic displacements and information about the natural frequency of the cantilever beam.

1.2. TRADITIONAL SHM SENSORS, THE ACCELEROMETER & LASER BASED ELECTRO-OPTICAL INSTRUMENTS

IN general, accelerometers are sensors that are traditionally used in the civil engineering sector for capturing fast, dynamic responses of major structures under the influence of loads exerted by natural factors. It is also known that they work very well over high frequency ranges but perform poor at sensing low frequent, static and quasi-static movements.

The basic working principle of an accelerometer is such as of a dumped mass on a spring that is suspended to a frame. When the frame faces movement, the responding mass inertia would make the spring stretch or compress creating acceleration. Every basic accelerometer system is composed out of a "proof mass, a spring/ suspension and a response transmitting pickoff", that measures the rate of change of velocity of the proof mass with respect to time or more explicit "the inertial force produced by the accelerating proof mass"(Lawrence [4]).

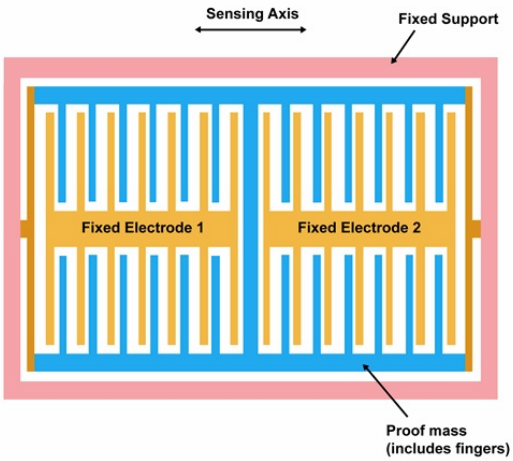

Figure 1.1: Sketch of an uni-axial MEMS accelerometer. Stationary (orange) and moveable (blue) fingers form the so called combed finger arrangement of a capacitor. Courtesy to: https://www.siliconsensing.com/media/1450/gemini-gif.gif?width=500&height=464.02660217654176

In case of a moving smartphone, a 3-axial micro electro-mechanical system (MEMS) measures the XYZ-displacement of some moveable silicon fingers (painted in blue in figure 1.1), attached to the proof mass relative to a second pair of stationary silicon fingers that are attached to the frame of the accelerometer system (painted in orange in figure 1.1). The XYZ-displacement values are quantified by the MEMS as a change in capacitance that can be used for inferring the XYZ-acceleration of the smartphone.

Prior to the use of GNSS sensors, geodesists were deploying periodic SHM campaigns for detecting the permanent response of a structure using classic theodolites and electro-optical total stations. A fairly affordable alternative to these instruments is the laser distometer, which works on the time of flight tracking principle of a pulse based laser signal for mearuing the two-way travel time. By dividing the recorded travel time by two and by multiplying the result with the propagation speed through the medium, the distance between the sensor and the targeted structure is derivable. Knowing the reference/ baseline distance between the laser distometer and the structure, displacement quantities can be derived based on subtraction of the baseline. Despite its full dependency of having an unobstructed line of sight during the measurement of distances, the laser distometer represents a cost effective alternative for the identification of critical static and quasi-static displacements of a structure, representing a fairly precise validation sensor for the GNSS based displacement quantities.

In the context of this study, the use of low-cost versions of a smartphone accelerometer and a laser distometer is studied for validation and sensor fusion purposes, along with the exploited GNSS sensors. Ideally, the implementation of such sensors in the form of an integrated SHM system should precisely capture the entire range of structural displacements, representing an affordable strategy for structural damage detection.

1.3. GNSS POSITIONING. IMPLICATION IN DISPLACEMENT SENSING

THE main sensor of this project is the GNSS receiver + antenna system, which is based on the acquisition of satellite born electromagnetic waves in the radio spectrum with wavelengths between 19-25 centimeters, for determining the waves travel time, followed by estimation of its position on Earth based on mathematical trilateration. The transmitted carrier radio waves are modulated with a characteristic pseudorandom noise (PRN) code that repeats itself clearly to make the measurement of the signal transmission time possible, and with broadcast navigation data that contains information about the orbital satellite position and the offset of the satellite clock from the GNSS system time. These signals can be used for determining the satellite-

receiver travel time, from which the satellite-receiver range can be derived[1]. This is done by a tracking loop procedure where the GNSS receiver is trying to determine the code delay and carrier phase difference, between the received code and carrier signal and a generated replica signal, equal with the signal travel time. These processes are known as pseudorange/ code and carrier phase (CP) ranging. While the former one is only decimeter precise, it is of much use for complementing the millimeter precise CP positioning principle to solve for its ambiguity[2] caused by the homogeneous (sinusoidal) behaviour of the carrier cycles.
Having the satellite-receiver distance precisely determined for at least four distinct satellites, the target position can be determined on behalf of the trilateration principle. Considering that the position of an object on Earth is commonly described by 3D Cartesian XYZ-coordinates, the need of a GNSS receiver of having at least 4 satellites in reach seems to be counter intuitive. This need is related to the fact that additional to the 3 unknown Cartesian coordinates of the GNSS receiver at ground, the GNSS receiver clock offset[3] represents a fourth unknown in the linearized system of (pseudorange) observation equations, part of the trilateration principle. Thus by solving such a linear system of observation equations, the GNSS receiver is capable to determine its 3D position and time.

This is all possible thanks to the launch and operation of a multitude of global navigation satellite systems such as the American Global Positioning System (GPS), the Russian GLObal'naya NAvigatsionnaya Sputnikovaya Sistema (GLONASS), the Chinese BeiDou, the European Galileo satellite systems and many more.
It is important to known that each of the aforementioned GNSS systems yield 3D Cartesian coordinates in different reference frames/ datums of different coordinate reference systems (CRS), such as the World Geodetic System 1984 (WGS-84) of the World Geodetic System for GPS, the Parametry Zemli 1990 (PZ-90) of the SK-42 reference system for GLONASS or the Galileo Terrestrial Reference Frame (GTRF) of the ITRS for Galileo.
Nevertheless, for most SHM applications a positioning technique known under the name of GNSS differential relative positioning is commonly used for determining relative positions/ baselines[4] between a stable GNSS reference station and a rover station installed on the case study structure, to estimate structural displacements. This technique is defined in section 2.4. In such a case, the relative positions are defined in the coordinate reference system of the GNSS reference station.
Generally, for any mapping and surveying applications[5] run on the European continent the recommended reference system is the European Terrestrial Reference System 1989 (ETRS89). "This coordinate reference system was defined to coincide with the International Terrestrial Reference System (ITRS) at epoch 1980.0 and was fixed to the Eurasian Plate making it a regional earth-centered, earth-fixed (ECEF) geodetic Cartesian reference frame"(Lapadat [5]). For any GNSS based SHM activity it is a good practice to have a rough idea about the used CRS and datum for ensuring a flawless integration of different sensors and data processing applications to work within the same CRS. Therefore, for the knowledge of the reader in this study GPS observations are primarily used for the deployment of SHM analyses. However, an attempt on using Galileo information is addressed in subsection 3.2.2, knowing that some of the frequency bands of the GPS and Galileo satellite constellations are interoperating. Furthermore, the use of Galileo is facilitated by the fact that both GNSSs yield positions in CRSs that are closely aligned. Hence, over short distances the desired baseline solutions would not be influenced by the "minor" differences between the two CRSs.
Despite the general advise of using ETRS89 for any geodetic application run on the European continent, all GNSS based results[6] within this study are corresponding or resulting from XYZ-Cartesian coordinates in ITRF14(2020.1) referred to the GRS80 ellipsoid. A brief explanation for the choice of this datum is given in in appendix H.

As previously mentioned, over the past decade geodetic engineers (Lienhart *et al.* [6]) have been performing triangulation and trilateration techniques based on networks of electro-optical total stations to precisely determine structural deformations at specific points of interests on the case study structure. But despite their extremely precise 3D positioning capabilities, total stations come with two major drawbacks. The first one is related to their dependency to clear line of sight between the control points and the targeted points equipped with prism reflectors, such that the electro-magnetic signal can travel uninterruptedly to determine the desired angular direction and range measurements. The second drawback of using total stations for SHM is

[1] via multiplication with the speed of light(c).
[2] more details on the integer CP ambiguity estimation can be found in section 5.4.
[3] this can be best explained by the fact that satellites are equipped with atomic clocks while GNSS receivers are using quartz clocks to keep their cost low. Hence, the GNSS receiver clocks will always perform less better than the satellite atomic clocks at tracking time.
[4] represents the distance between reference/ base station and rover receiver.
[5] including GNSS based SHM.
[6] unless it is not specifically mentioned.

caused by the influence of the atmospheric refraction on the sent electro-magnetic signal over long distances for effective data acquisition. Nowadays laser scanners are used as an alternative to total stations. These instruments work on the same principle as total stations but have a larger coverage, outputting very precise 3D structural models with high spatial resolution. However, the continuous processing of the large number of acquired point cloud measurements is very difficult to be conducted in real time. Additionally, photogrammetry based solutions using digital cameras for structural damage detection have grown in popularity (Xu [7]). However, due to the large number of frames captured by the digital cameras and the practical limitations related to the line of sight dependency to the installed targets on the case study structure, again such a solution is not optimal for real time SHM.
In this context, the rapid advancement in the development of GNSS modules, able to continuously acquire pseudorange and CP observations on multiple frequency bands from multiple satellite constellations, makes them be a great solution for the monitoring of important structures and solve the characteristic problems of total stations and of the other aforementioned sensors.

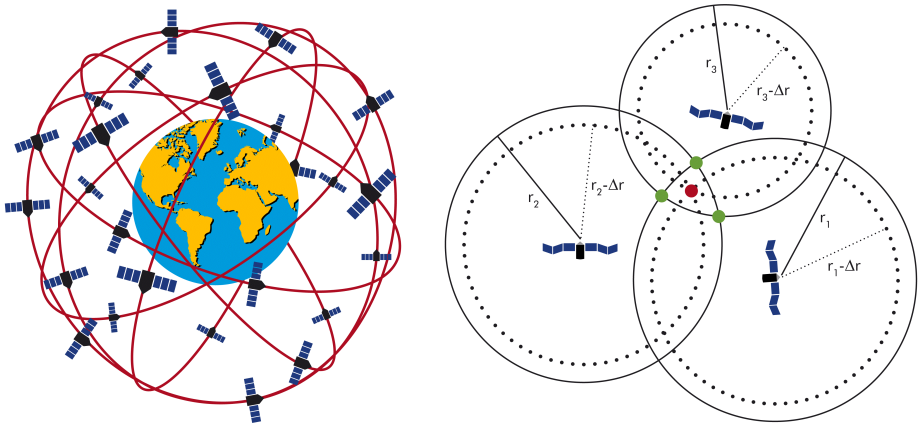

Figure 1.2: GPS constellation orbiting the Earth (left) and the trilateration principle for the determination of the 3D position of a GNSS receiver(right). In the trilateration principle the 4th satellite is needed for the estimation of the receiver clock offset for precisely determining the position of the red dot. Courtesy to: https://seos-project.eu/GPS/GPS-c01-p03.html and https://seos-project.eu/GPS/GPS-c01-p02.html

1.4. PREVIOUS RELATED WORK/ LITERATURE REVIEW

IN this section a summary is given of previously reported results from SHM studies of complex structures, primarily based on GNSS technology accompanied by low-cost accelerometers (e.g smartphone accelerometers).
From the presented information the displacement retention potential of low-cost dual frequency GNSS receivers can be estimated as a first step in understanding the capability of such sensors to sense (wind-induced) displacements of large-scale structures. In addition, frequently encountered problems and errors are listed to raise awareness to avoid them while implementing a real time monitoring system with minimal cost. Moreover, relevant research speaking about the importance of not only estimating displacement quantities but also testing their significance, is addressed within this section. The listed information represents a starting point for this SHM research, which should be further used in defining an optimal experimental setup and a cost-effective procedure for deploying a SHM campaign based on low-cost dual frequency GNSS equipment, additionally accompanied by smartphone accelerometers.

1.4.1. HIGH-END AND LOW-COST GNSS EQUIPMENT FOR SHM

HIGH-END GNSS EQUIPMENT

UNTIL now most of the relevant literature depended on the use of performant but expensive geodetic GNSS equipment for deriving wind, thermal or even earthquake induced structural displacements in real time from millimeter accurate 3D relative Real-Time Kinematic (RTK) position solutions. Additionally, one should note that in these research papers the GNSS equipment is characterized as a displacement detection system with outstanding retrieval capability of static and quasi-static displacements of flexible structures with low natural frequency values.

1

From (Im *et al.* [8]) and (Yi *et al.* [9]) summaries on GNSS technology for SHM, where several RTK positioning experiments run on dams and high-rise towers are briefly reviewed, it can be deduced that geodetic GNSS equipment with sampling rates of up to 20 Hz can be used for effectively retrieving larger than 5-10 millimeter static and quasi-static structural responses with natural frequencies in the range of likely up to 1-2 Hz. Additionally, this type of equipment can be used for retrieving sensitive dynamic responses of more rigid large-scale structures with natural frequencies of up to 4 Hz as well ((Psimoulis *et al.* [10]), (Lepadatu and Tiberius [11])).
More recent studies point on the improved capabilities of dual frequency GNSS equipment with a sampling rates of up to 100 Hz and the possibility of increasing the bandwidth of their phase-locked loop (PLL[7]), to measure dynamic responses of large-scale structures with frequencies larger than 5 Hz for facilitating the SHM process by deriving the dynamic characteristics of rigid structures more accurately (Moschas and Stiros [12]).

To support the aforementioned numbers, which are characterizing the displacement retention potential of high-end GNSS equipment, three important research papers are discussed in the next lines.
In the first addressed paper, (Tamura *et al.* [13]) run a experiment on testing the feasibility of a centimeter precise RTK-GPS module with a sampling rate of 10 Hz, in measuring displacements induced by an electronic exciter. Their results were validated on a 108 meter tall steel tower in Tokyo, equipped with the proposed GPS module and an accelerometer, showing that the GNSS equipment was able to measure wind-induced responses with amplitudes larger than 2 centimeters and natural frequencies lower than 2 Hz.
Within this study the authors proposed two promising visualization methods for correlation identification between the measured wind pattern and the estimated displacement responses of the considered tower during a typhoon. Specifically, in the first method they compared the variability in the standard deviation values of the 10 minutes mean GNSS based displacement- and accelerometer data with the 10 minutes mean wind speed pattern (compare plot ***c*** and ***d*** with ***b***) from figure 1.3). To further attest a strong correlation between meteorological and displacement information, a second plot of the 10 minutes mean along-wind direction displacement time series against the 10 minutes mean wind speed values was proposed (review plot ***a*** from figure 1.3).

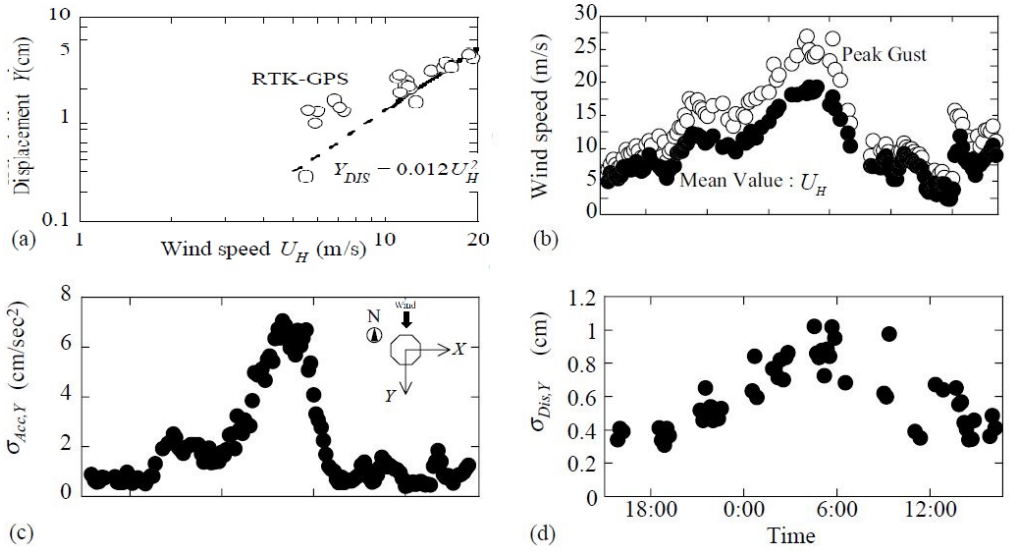

Figure 1.3: "Temporal variations of 10 min. mean values of wind speed and responses of the tower": a) 10 min. mean GNSS based Y displacement vs. 10 min. mean wind speed; b) wind speed and 10 min. mean wind speed vs. time; c) std. of Y acceleration vs. time; d) std. of GNSS based Y displacement vs. time. Courtesy to: (Tamura *et al.* [13])

Both plot types indicate a remarkable good match, hence strong correlation between the considered wind and displacement quantities. Thus, these two plotting methods can be considered as powerful validation tools of GNSS based displacements in further SHM studies.
Though, it is believed that the choice of a 10-minutes mean window is not feasible in case of short-period light breezes conditions, with significantly smaller maximum mean wind speed values than the considered $19\frac{m}{s}$. This is because the considered 10 minutes mean displacement values will not be able to capture the

[7] a control system integrated in the receiver that compares the acquired carrier-phase (CP) satellite signal with the receiver generated CP signal in order to recover the original signal.

displacement signal produced by quick light breezes. Most probably these will get covered by the preponderant quantities describing a stand still state of the case study subject within the considered 10 minutes window of the mean process. Hence, in the end no variability will be identifiable. Thus, in case of mild wind speed conditions one should form no longer than 1-minute mean wind speed and displacement time series, to capture meaningful displacement information and further identify correlation between this and the causing wind pattern.

Using an identical GNSS instrument, (Celebi and Sanli [14]) performed dynamic displacements acquisition tests based on the aforementioned RTK principle.
This study is specifically included in the literature review, being one of the first documented research projects where a real time RTK SHM network was developed in the context of a national hazard reduction program. Such a study was driven by the need of identifying an alternative to the classic accelerometers, for getting a better understanding from the dynamic response of tall buildings to earthquake activities in real time.
Firstly, laboratory-based tests were deployed on thin metal bars, that were simulating 30- to 40-story flexible buildings with natural frequencies of 0.25-0.30 Hz. Results demonstrate the capability of 10 Hz GNSS equipment in accurately determining dynamic characteristics[8] of flexible tall structures. Although, the experimental format was designed such that the test results were fully predictable, a cantilever beam experiment is desirable for optimization purposes before deploying an important SHM campaign on major structures. But in contrast to the presented laboratory-based tests, it is advisable to let the bending beam freely respond to wind loads over a longer period.
Additionally, results from a real case scenario dynamic displacement campaign run on a 34-story tower from San Francisco, were documented. In this case, GNSS modules and accelerometers were used for real time detection of lateral and torsional responses of this building. In the absence of strong winds, small amplitude vibrations close to the declared GNSS measuring precision of 1-centimeter, were manually triggered to the GNSS antenna. In this case, a natural frequency of 0.24-0.25 Hz of the case study building could be identified from the GNSS and accelerometer data sets. Hence the results attest that a GNSS plus accelerometer integrated monitoring system can effectively retrieve the dynamic characteristics of flexible major structures under the influence of severe wind loads.
Even though, this study was one of the first real time GNSS related studies, the presented SHM system was fully dependent on commercial software for deriving centimeter level building displacements, where the authors did not consider any form of correction for systematic errors that are strongly influencing GNSS measurements during SHM, such as multipath (MP)[9]. Moreover, the authors wrongly account the low frequent noise, identified in the presented cross spectra of the displacement time series, to “micro seismic” activities instead of most likely MP, indicating that at that moment they were not fully aware of the effect of MP on GNSS measurements.

More recent, (Psimoulis *et al.* [10]) tested the capabilities of a 20 Hz GPS receiver for determining larger than 5 millimeter displacements with oscillation frequencies up to 4 Hz, and for identifying the dynamic characteristics of relatively rigid civil engineering structures. The main reason for conducting such a study was to determine whether high-end GNSS equipment can precisely measure dynamic displacements within a much broader range of oscillations than the expected 0.2-2 Hz frequency range and derive multiple modal frequencies to extract additional response information from complex, rigid structures.
Considering that in practice most GNSS based displacement time series are fragmented by data gap errors, the authors proposed two novel alternatives for the conventional FFT method accompanied by zero-padding, which introduces additional noise. These two alternatives that facilitate the frequency analysis of discontinuous and short signals are related to least-squares spectrum analysis or a Lomb normalized periodogram solution.
The presented results are trustful considering that a large number (more than 250) of successful artificially induced oscillation experiments, inferred by a uni-axial one-, two- or three-degrees of freedom servo-motor setup, were deployed. The most important reported limitation resulting from the artificial experiments reads that "higher frequencies and smaller oscillation amplitudes yield less precise estimates of modal frequencies". Moreover, in the same paper results from two real-life tests deployed on rigid bridges were documented, indicating that the tested high-end GNSS equipment was able to identify effortlessly the natural frequencies of the case study subjects, ranging between 0.4-2 Hz.

[8] s.a natural frequency and damping ratio.
[9] for more details on this topic review the MP related paragraph from subsection 1.4.2 and subsection 3.2.1.

1

LOW-COST GNSS EQUIPMENT

THE outstanding mm-precise results that can be output by high-end geodetic GNSS equipment come with the high price one needs to pay for such equipment. In this context, with the release of the very first low-cost GNSS receiver, the interests in the SHM community of geodesists gradually shifted towards low-cost solutions. Though, until now there is very limited amount of SHM related research on the use of such equipment and if there is, its main focus is on the performance of low-cost GNSS equipment for real time landslide monitoring applications.
In this context an important example is documented by (Bellone *et al.* [15]), where an artificial micrometric slide was used to progressively induce 1-centimeter horizontal and vertical displacements to a single frequency low-cost GNSS external patch antenna to simulate low frequent landslide processes. Within this paper, the capability of estimating and statistically detecting manually induced displacements by means of an updated Chow test was discussed. Measurements were conducted at a 1 Hz rate and processed by an open-source software (RTKLib), using the virtual station (VRS) approach together with network Real Time Kinematic (NRTK) positioning method presented by (Cina and Piras [16]) as a method for virtually defining a reference station as close as possible to the operating rover to mitigate most of the frequently encountered atmospheric errors that are influencing the GNSS measurements.
Results show that by optimizing the proposed statistical testing procedure, this was capable of accurately detecting larger than 1-centimeter displacements and output correct alarms 90% of the time. The remaining 10% were distributed to miss detection and false alarm cases, from which 6.9% were corresponding to the much more dangerous miss detection cases.
Based on the obtained results it is demonstrate that landslide detection can be effectively deployed with more affordable instruments than with traditional geodetic GNSS systems. Though, the proposed VRS+NRTK procedure makes one be fully dependent on a continuous operating GNSS reference station (CORS) network, which is normally offering VRS solutions on behalf of a subscription making the continuous real time monitoring process expensive.
This should be the case also for SHM processes, where the larger than 1 centimeter static and quasi-static responses of a structure should be easily detectable. The latter assumption still needs scientific proof, considering that up until now no relevant paper was reporting about this topic.

From the previously presented information related to the capabilities of high-end and low-cost GNSS equipment of estimating large-scale structure displacements, one can expect from high-end GNSS modules with high sampling rate capabilities (up to 100 Hz) to effectively measure sub-centimeter static and quasi-static but also dynamic displacements, thus being able to complement or replace conventional accelerometers from a dynamic displacement detection process of structures with natural frequencies of up to 4 Hz.
In case of newly released low-cost dual frequency GNSS systems with reasonable high sampling rate capabilities (up to 10 Hz), these should be able to resolve structural displacements in the centimeter order and derive natural frequencies of up to 1.5 to maximum 2 Hz.

1.4.2. FREQUENTLY ENCOUNTERED GNSS ERRORS AND PROBLEMS

IN the next lines the most important difficulties identified in the GNSS based SHM literature are discussed to raise awareness and avoid facing the same problems in future research.

RTK BASELINE ESTIMATION

ALL previously discussed studies mention that the GNSS positioning principle is prone to a group of errors: satellite orbit errors, satellite clock errors, atmospheric time delay errors and receiver independent errors such as MP. Thereby, RTK differential relative positioning between close-by rover and reference GNSS modules was preferred by most authors for estimating structural displacements in real time and mitigate the effect of these errors as much as possible ((Kijewski-Correa and Kochly [17]), (Li *et al.* [18]), (Li *et al.* [19]), (Park *et al.* [20]), (Celebi and Sanli [14])). Though, the error mitigation functionality of the RTK principle holds true only if both antennas are placed relatively close to each other, knowing that in such a case "the carrier wave signals from the same satellite will be received almost simultaneously"(Tamura *et al.* [13]) with the same amount of error. Thus, by forming difference observations between the rover and reference stations, the satellite and atmospheric errors cancel resulting in more precise relative positioning.
Moreover, the antenna placement plays an important role in fulfilling the primary constraints of the RTK principle of acquiring more than four satellites and having a good satellite distribution in the sky over the entire experimental period. Therefore, in most of the addressed SHM studies the reference station was preferred to be emplaced on the roof top of a near-by, short and rigid building ((Kijewski-Correa and Kochly [17]), (Li

et al. [18]), (Li *et al.* [19]), (Celebi and Sanli [14])). Since one would need to install two GNSS equipment of the desired baseline, this solution is considered to be time consuming. Nevertheless, it is cost effective by not depending on a CORS network such as a VRS+NRTK solution.

MULTIPATH

SINCE RTK relative positioning proves to be optimal in mitigating a multitude of GNSS errors, at first sight one can believe that by using this processing technique all previously enounced GNSS errors can be mitigated. However this does not hold true for receiver independent error sources such as MP.
Multipath is one of the most vicious erroneous influences acting on the GNSS carrier wave signals, making them to be acquired by the GNSS antenna via multiple paths due to reflections and diffractions induced by close-by obstacles and/ or wet surfaces. The resulting error effect is a low frequent and time varying distortion of (at maximum) a quarter of a wavelength of the received satellite signal[10] (van der Marel [21]), which is "leaking" in the relative positions and CP residuals estimates. The distributed energy of this error is covering a low frequency bandwidth of 0-0.2 Hz ((Psimoulis *et al.* [10]), (Li *et al.* [18])), coinciding with the energy of the static and quasi-static displacements of flexible structures. Therefore, a mitigation and separation procedure is highly needed for any SHM process.

In most of the SHM related research papers, digital filtering via high pass[11] and/ or bandpass[12] filters was proposed as a reliable MP mitigation solution ((Kijewski-Correa and Kochly [17]), (Chan *et al.* [22])). Though, it is believed that such a solution is hard-to-be implemented in real time, due to its manually based design and definition process.
While the design process is fully dependent on the manual choice of some filter design parameters (review appendix E), the definition process of the filter needs to be run on relative position time series describing a steady state of the case study structure, where any identified displacement can be related to background noise due to MP. Moreover, these filtering techniques perform well at retrieving dynamic responses but poorly at retrieving static or quasi-static displacements, since these co-exist with the MP effect within the same frequency bandwidth, making the separation between them very difficult. Therefore, in order to not filter out frequencies related to dynamic displacements, authors generally design (bandpass) filters to filter out unwanted low and high frequency components and restrict/ maintain a larger bandwidth around the natural frequency of the case study building.
As an example, (Moschas and Stiros [12]) introduced a very effective bandpass filtering method for suppressing low and high-frequent noise[13] present in the derived displacements time series, in order to extract sensitive dynamic displacements. To do so, they designed a filter to maintain a narrow range (± 1 Hz) of energy centred around the highest detectable frequency value within the displacement signal, related to the natural frequency of the case study structure. This filter design choice is relevant considering that only the natural frequency and its neighbouring dominant frequencies can produce significant dynamic displacements. When comparing the filtered dynamic displacements results with the reference dynamic displacements recorded by a mechanical oscillator, it was shown that this filtering procedure can remarkably well recover artificially induced dynamic displacements with amplitudes larger than 4.8 millimeter.
Due to its viability, this method can be successfully reassigned within any SHM project as a post processing mitigation method for the low-frequent components attributed to MP and other background noise errors. Moreover, this method can be used as well within a double-integration validation process of the GNSS based dynamic displacements with accelerometer derived dynamic displacements, known as the reverse transformation process (see the paragraph on *integrated SHM system* from subsection 1.4.3), where one would first need to filter out unwanted noise and extract the dynamic displacements before performing any integration.

Since GPS satellites repeat every sidereal day[14] one can expect from MP to repeat within daily position and measurement residuals time series, if the surrounding obstacles remain unchanged and the satellite geometry is identical over every sidereal day. In such a case, the identified MP pattern in the daily position or measurement residuals time series can be used for MP correction.
(Kijewski-Correa and Kochly [17]) used the property of sidereal day repeatability of the GPS constellation to define a distortion signature over a full (sidereal) day, based on GPS displacement estimates over 2 consec-

[10] e.g maximum 5 centimeters.
[11] mitigate the low frequent information related to MP.
[12] constrain the needed information within a predefined frequency band, removing both unwanted low and high frequent components.
[13] produced by the increase of the PLL bandwidth of the GNSS receiver.
[14] equal to 23 hours 56 minutes 4 seconds.

utive wind-still days. After making sure that the satellite configuration was identical, the static (wind-still) data was split into twenty four 3-hour blocks, through which a least-squares based polynomial was fit and glued back together to form the GPS distortion signature. Under the premise that the surrounding obstacle positions did not change the resulting polynomial was further used for correcting on multipath over the next sidereal days.
Nevertheless, since no model is optimal it is believed that the proposed GPS distortion signature resulting from a least-squares polynomial fit will not perform best in mitigating the erroneous effect of MP, without statistically attesting the goodness of the fit through the daily position estimates of the MP pattern. Therefore, because the authors did not take such measure into consideration, they should have firstly considered to perform a statistical test, such as the overall model test (OMT), before applying such a correction.
Furthermore, it is believed that in case of GNSS modules with high sampling rate capabilities the proposed 3-hour block period will result in large observations variance-covariance matrices (Q_{yy}). The size of the Q_{yy} matrices will get reflected in the run time of the statistical testing process, making the inversion of such large matrices be computational expensive, and ultimately hamper the adaptation of such a process in real time. Therefore, a shorter block period is desirable. This will be reflected in stricter least-squares based polynomial fits that will model MP more effectively.
A second solution for effectively modelling the periodic behaviour of MP is to apply a least-squares harmonic estimation process, just like the one presented in (Lepadatu and Tiberius [11]) where the dominant frequencies with the highest amplitudes of the periodic components within a GNSS position time series were iteratively identified and removed to clean the considered position estimates from MP.
For the MP distortion signature definition, the authors considered only the dominant frequencies related to MP. This can be achieved by analysing a plot of the frequencies and amplitudes of the estimated harmonics, over consecutive days. Based on such an analysis, one should use for the definition of the MP distortion signature only the dominant harmonics that repeat themselves over consecutive days.
Lastly, it is important to mention that a MP distortion signature definition procedure can be easily applied on CP residual time series as well. Thus, one can define GPS distortion signatures for each satellite individually, making it easier to identify and exclude low elevation satellites that amplify the MP effect (Im *et al.* [8]).

Even though there are many solutions to reduce MP, most of the time researchers do not consider any post-processing MP mitigation technique but rather equip the proposed high-end GNSS equipment with expensive choke-ring antennas ((Im *et al.* [8]), (Kijewski-Correa and Kochly [17])), specially manufactured to suppress MP. Although, this equipment-based MP correction can work in real time, it can only partially mitigate MP at a high price.

ANTENNA PHASE CENTRE ERROR(S)

SPEAKING about GNSS error sources inferred by equipment, receiver antennas are producing an important error source to the GNSS relative positioning process. This error is caused by the use of different GNSS antenna types at the rover and reference stations while performing RTK positioning, and is formed out of two components known as, phase center offset (PCO) and phase center variations (PCV). In the next lines a short description of these two quantities is given.
In a nutshell, CP signals are received at the antenna level in an imaginary point, also known as phase center (PC), "whose position is being measured when a GNSS baseline is determined" (Mader [23]). In between PC and the physical antenna reference point (ARP), defined at the intersection between the antenna attachment surface and the antenna rotation axis (Z-axis), there is a offset known as the PCO. This vector quantity can be expressed as an average value between all epoch wise phase centres, resulting from a RTK process.
In addition to the PCO value there is a secondary error quantity, PCV, produced by the not homogeneous electromagnetic field of the antenna. This quantity describes a variation of the phase centre with respect to the mean PCO, which is changing depending on the satellite elevation and azimuth direction[15] of the received CP signals.
The identification process of a mean PC value, by deriving the "mean PCO with respect to ARP and the elevation and azimuth dependent PCV quantities with respect to the PCO" (Hu *et al.* [24]), is known as receiver antenna calibration process and is very important for RTK GNSS positioning performed with different antenna types at both baseline[16] ends. This holds true considering that the mean PCO can reach centimeter level and the PCV errors can bias the estimated relative positions from a few millimeters up to several centimeters, especially in the vertical direction. Unfortunately, their influence was mostly not considered in the

[15] only in case of obstructed signals.
[16] vector between the reference and rover stations.

previously discussed GNSS based SHM studies.

For baselines up to a several thousands of kilometers a relative calibration process is favourable. (Mader [23]) described a technique for performing such calibration process, where two identical pillars placed at a known distance over a grassy field were used. Taking into account that when using identical GNSS antennas for the RTK procedure the PCO and PCV errors will cancel out, firstly identical GNSS antennas were installed on both pillars to define the reference frequency dependent mean PC values of the test pillar. The resulting L1 and L2 reference mean PC values could be then compared with the mean PC values of a different GNSS antenna installed on the same test pillar to define the frequency dependent mean PC locations for the considered test antenna. Having these values defined, the desired L1 and L2 PCVs as a function of satellite elevation can be modelled via a least-square polynomial fitting procedure run through single difference (SD) CP residuals observations.
Due to the fact that, the antennas were installed on a grassy field without being strongly influenced by MP, the proposed procedure of (Mader [23]) represents an example of an idealized PC calibration process, considering that no azimuthal dependency of the PCVs was considered. This idealization is overestimating real case SHM scenarios where GNSS antennas are normally surrounded by other buildings that are inevitably influencing the PCV values. Therefore, in practice it is recommendable to calibrate the GNSS antennas at their own site, considering all possible surrounding GNSS signal perturbators.

In their recent study on the investigation of the potential for estimating Zenith Tropospheric Delays (ZTD) with low-cost dual frequency GNSS equipment, (Krietemeyer *et al.* [25]) discuss two SD CP residuals based techniques for performing short-baseline absolute antenna calibration to improve the potential of inexpensive dual frequency patch antennas for high-precision positioning applications. Though, because only the effect of PCVs is important for the ZTD estimation, the authors exclusively discuss the definition and application of PCV corrections.
The addressed corrections were defined by averaging SD observations over elevation respectively elevation and azimuth dependent bin sizes and further combine with pre-defined reference station PCV corrections to produce absolute calibration corrections.
Based on a 2 days long baseline test, the defined PCV corrections of the considered low-cost dual frequency patch antenna with an attached ground plane were characterized by zero-mean values with standard deviations on the L1 and L2 band of 6 millimeters. The zero-mean statement is a result of the proposed modification brought to the RTKLib processing algorithm, making it to use the mean of the resulting DD CP residuals as a reference to form SD CP residuals observations for defining the desired PCV corrections. Thus, when using this calibration method one can generally expect from the PCV effects of unobstructed low-cost patch antennas with attached ground planes to fluctuate around their zero-mean in the millimeter range, being generally higher at lower elevation angles. It is important to mention that in the absence of a ground plane, the L1 and L2 standard deviations of the PCVs can get considerably higher, in this case reaching 7 respectively 9 millimeters.

One can conclude that although, GNSS systems come with the advantage of outputting displacements results in real time, there are many errors affecting them during this process. While most of them can be effectively mitigated by performing short baseline RTK processing, there are two of particular interest that can drastically reduce the performance of GNSS sensors on outputting valid displacements.
MP is the first systematic error, for which digital signal processing or least-squares based post-processing solutions were previously introduced. Though, it is noteworthy to mention that up until now, there is no study discussing a possible real time implementation of a pre-defined MP correction.
Additionally, the antenna PC errors can strongly affect displacement results in case of using different antenna types at both baseline ends. The easiest and most effective method for eliminating such error from the GNSS error budget is to use identical GNSS antennas in the RTK relative position estimation process.

1

1.4.3. INTEGRATION OF SMARTPHONE ACCELEROMETERS IN THE GNSS SENSOR NETWORK

THE ACCELEROMETER & ITS ERRORS

IT has been known that accelerometers are traditionally used as SHM systems for measuring dynamic responses of major structures, being able to identify high frequency components (Im *et al.* [8]).
But their major drawback is that they cannot effectively sense the low frequent static and quasi-static component of the structure's response (Psimoulis *et al.* [10]). In addition, the desired acceleration-to-displacement conversion process, known as the reverse transformation, is not trivial due to the complexity of the imposed double numerical integration. This requires a relevant selection of the appropriate filters and baseline/ integration constant corrections (Celebi and Sanli [14]), making the deployment of accelerometer based SHM campaigns in real time harder. Without considering such correction measures, the integration process would exponentially amplify any present error in the acceleration data, such as the instrumental drift errors (Im *et al.* [8]) produced by temperature variations and constant triggering acceleration errors caused by the lack of capability of accelerometers to measure low frequent accelerations.
Moreover, since accelerometers are not time-based measuring sensors, different studies pointed on possible time correlation problems between GNSS and the accelerometer derived displacements quantities ((Psimoulis *et al.* [10]), (Lepadatu and Tiberius [11])).

INTEGRATED SHM SYSTEM, GNSS AND ACCELEROMETER

THEREFORE, many SHM studies ((Li *et al.* [18]), (Celebi and Sanli [14]), (Tamura *et al.* [13])) integrate GNSS modules and accelerometers to measure a broader range of frequencies and capture static, quasi-static and dynamic movements of major structure.
Considering that displacements can be converted to accelerations by double numerical differentiation, a process known as the forward transformation, and accelerations can be converted to displacements by double numerical integration, a process known as the reverse transformation, both sensors can be used as an alternative for validating each others results. But one should note that the reverse transformation process is more complex, due to its aggressive amplification effect of any present errors in the accelerometer data.
To facilitate the sensor fusion process, (Li *et al.* [18]) developed a procedure to convert and combine both types of measurements by "transforming one form of measurements to the other", in such a way that wind-induced and earthquake effects on buildings can be precisely retrieved.
Their approach is useful also for recovering displacement quantities that are too slow for the accelerometers but can be detected by GNSS modules.
Although, both the forward and reverse transformation processes are proposed within this study, in the next lines the emphasis is placed on the latter, more complicated process. Hence an optimal way to perform reverse transformation based on FFT analysis, Finite Impulse Response (FIR) filtering techniques along with cross-correlation time lag corrections and velocity linear trend estimation, was developed and tested on a 108-meter steel tower from Japan influenced by an earthquake and typhoon.
In this process, firstly the low-frequent acceleration components, corresponding to unwanted accelerometer instrumental errors, needed to be filtered out to avoid any amplification due to the following double integration operation. The double integration operation was run by setting the velocity and displacement constants equal to 0, making the derivation of only dynamic displacements possible. After the first integration step, the authors proposed to remove the mean velocity trend to correct for any possible integration inferred error amplification. After the second integration step, the missing static and quasi-static displacement components were extracted from the GNSS based displacement data by taking the mean and by fitting a low order polynomial over the considered period. These were then added back to the derived dynamic displacement time series resulting in the total accelerometer-based displacement. Remarkable similarity between the measured and the derived displacement time series was identified. Lastly, to compensate for the small discrepancies, an average between the derived total displacement and the GNSS based measured displacement was preferred to define a final true displacement time series.
The proposed reverse transformation method gave remarkably good results in deriving an optimal displacement time series by integrating GNSS based displacements with accelerometer derived displacements.
However, this method was applied only on a data set spanning over 50 seconds. Therefore, it is arguable that this sensor fusion method will give good results for precisely retrieving structure displacements in real time over longer periods. This will be the case since the definition of the quasi-static component is done by fitting a low order polynomial through a GNSS position time series, that might present highly variable (non periodic) displacement-related behaviour over a longer period. Nevertheless, this paper introduced two effective methods for validating GNSS based displacements by means of GNSS and accelerometer data sets.

LOW-COST SMARTPHONE ACCELEROMETER

RECENTLY, inexpensive MEMS accelerometers were integrated in handheld smartphones to facilitate their good functioning. Hence their capabilities for measuring 3D movements of flexible structures raise interest among the structural engineering research community. This makes one believe that such instruments can represent a good and cost effective solution for validating displacement quantities derived from GNSS equipment, when integrated in SHM systems.
To do so, one would first need to investigate their dynamic displacement retention potential. Recent studies ((Feldbusch *et al.* [26]), (Feng *et al.* [27])) tested several smartphone MEMS-accelerometers with different instrumental characteristics on cantilever beams, masonry columns, flexible pedestrian bridges and more rigid high-rise towers for measuring structural vibrations and derive dynamic characteristics for facilitating the diagnosis of their structural integrity over longer periods. Results demonstrate their capability to effortlessly derive natural frequencies ranging between 3-18 Hz, for both flexible and rigid structures in any situation (ambient vibrations or induced loadings).
On the other hand, their performance at retrieving the dynamic behaviour of ambient vibrations of more rigid structures in time domain was accounted to be poor. This is demonstrated in both aforementioned papers where small wind-induced amplitudes of just 0.45 $\frac{cm}{s^2}$ respectively 0.005 $\frac{cm}{s^2}$ could not been sensed, being covered by the inherent noise of the considered smartphone accelerometers.
Moreover, while validating the collected smartphone accelerometer vibration data with the data set of a high-end accelerometer, (Feng *et al.* [27]) noticed a time lag synchronization error between both data sets. This was caused by the time difference in the smartphone- and the high-end accelerometer clock, and needed to be corrected by searching for the cross-correlation lag in order to synchronize one of the data sets with respect to the other.
All in all, considering the robustness, low energy consumption and low price of smartphone MEMS-accelerometers, (Feldbusch *et al.* [26]) accounted these sensors with a limited measuring precision (resolution[17]) of 0.0001 to 0.015 $\frac{cm}{s^2}$, and a measuring range[18] of $\pm$ 4 $\frac{cm}{s^2}$ (and more). Though, the reader should note that these declared precision ranges might differ depending on the instrumental characteristics of the considered smartphone accelerometer, which tend to change with nowadays rapid technological development.

Based on the aforementioned results it can be concluded that depending on their resolution characteristics, smartphone accelerometers are able to sense various building dynamic responses of different amplitudes and frequency characteristics under ambient conditions but also under extreme loads, facilitating the desired validation process of GNSS based displacements. These inexpensive sensors showed their limitations in deriving very small ambient dynamic displacements of more rigid structures. Additionally, the reader should consider their possible time misalignments/ asynchronization with GNSS data sets, which can represent a real problem in the development of an integrated real time SHM system.

1.4.4. REAL TIME SHM. STATISTICAL TESTING ALONG WITH THE ESTIMATION PROCESS

REAL TIME SHM OPERATING SYSTEM

SINCE most of the GNSS based SHM literature was focusing on the optimization of RTK processing results by means of digital filters, only a limited amount of research papers focused on developing an adaptation procedure of such equipment into a real time operating system ((Celebi and Sanli [14]), (Lepadatu and Tiberius [11]), (Bellone *et al.* [15])) suited for:

- computing position solutions.
- output screening via graphic user interfaces.
- rising of safety alarms in near-real time to warn on unexpected change of construction parameters that can cause structure collapse when no maintenance action is taken.

It is believed that this trend was driven by the complicated definition of a real time workflow process including data capture, analysis and visualization. This holds true, especially after acknowledging the large amount of debugging problems caused by the integration of self-developed algorithms with other open source software for concurrently analysing GNSS and accelerometer data in real time, over the past years (Celebi and Sanli [14]).

[17] indicates the smallest detectable acceleration value.
[18] amount of acceleration that can be measure and accurately represent as an output. Note that typically, the smaller the range, the more sensitive the readings will be from the accelerometer.

1

STATISTICAL HYPOTHESIS TESTING FOR REAL TIME SHM

ADDITIONALLY, most of the conducted research was not considering to statistically assess the significance of the estimated displacement quantities before validating any results. In the next lines, statistical testing procedures are summarized, to be considered for the definition of a risk integrity procedure within this graduation project.

As previously mentioned in the first subsection, (Bellone *et al.* [15]) proposed a updated form of the Chow test for statistically testing and correctly predicting landslide-induced displacements in real time. Their considered functional model was based on a constant velocity model, which assumes that under the circumstances that the velocity is equal to 0 or constant over a long period, no deformation should be accounted. Within this displacement detection process, an uni-dimensional sliding window procedure is proposed, where the sum of squared residuals of a predefined number of position estimates is compared with the sum of square residuals of the position estimates from the previously determined window.
As a general comment this statistical test represents a good displacement detection alternative but it is important to note that the proposed method is intended for modelling physical processes with seasonal variations, such as landslides. Thus in order to implement such a statistical testing scheme for SHM purposes, one would first need to reconsider a simplified constant position model, where the difference between the sum of squared residuals of two neighbouring windows should be tested against a predefined critical displacement threshold. Moreover, results indicated that the proposed statistical test is outputting remarkable results for sliding windows that are consisting of 10 samples. Unfortunately, such large windows cannot be considered for SHM applications where fast dynamic displacements are subject of identification. Therefore, one would need to optimize the considered statistical test by defining an enough short window able to produce a quick response detection time with the lowest possible missed detection and false alarm probability.

In their study on the assessment of the performance of GNSS equipment for continuously monitoring of a newly built cable-stayed bridge during several loading tests, (Lepadatu and Tiberius [11]) studied the capabilities of such a system to successfully measure and identify vertical bridge displacements in real time by means of statistical hypothesis testing. Based on the assumption that the estimated displacements were normally distributed, the proposed procedure tries to identify when measurement noise can corrupt the displacement quantities such that the test will falsely detect a critical displacement or will completely miss its detection. For this, four critical values for the actual vertical displacement of the bridge were considered (1.5, 3, 5, 8 cm) and based on the empirical precision of the position estimates, which were grouped in observation duration windows ranging from 1 to 15 minutes, it was shown that the test would avoid producing false alarms by 99.99% of the time (for example) "for a critical value of 3 centimeters, if one is using at least a 8-minute GPS observation window". On the other hand, the considered test would falsely detect a critical displacement of 3 centimeters once out of 1000 cases, if the measurement window is no longer than 10 minutes.
Additionally by considering a certain number of false alarms that can be accepted per year, the authors show that with increasing GNSS observation duration, not only the precision of the position estimates but also the probability of correctly detecting a bridge displacement will improve. Results show that the missed detection probability of a SHM system will be smaller, if one considers a larger critical displacement, a longer window duration and a higher number of acceptable false alarms per year. Relating this conclusion to the previously considered case of a critical bridge displacement of 3 centimeters, when tolerating only 1 false alarm per year this will result in a minimum needed GNSS observation window of approximately 10 minutes.
Based on the conclusion that the GNSS observations need to be processed over at least 10 minutes time windows to reflect correct displacements quantities, the analysis results cannot be directly used for the detection of fast, dynamic displacements, due to the fact that in such a case position solutions need to be computed every second or even quicker, hampering the proposed statistical hypothesis testing procedure. Nevertheless, the principle of processing GNSS positions in time windows can be used for detecting long period quasi-static and static permanent displacements exceeding a large critical displacement values.
Therefore, further development of such a study to consider fast dynamic processes monitored by low-cost dual frequency GNSS receivers, raise high interest for assessing the capabilities of inexpensive GNSS equipment for performing real time SHM.

To conclude, the adaptation of a statistical testing procedure along with the integrated displacement estimation process within a real time monitoring system is of high importance in order to statistically certify any divergence in the structure position and be able to quantify the expected missed detection and false alarm rate of structure displacements of the considered statistical test. Without considering such a procedure any present systematic error in the measurements, can influence the displacement detection in an uncontrolled manner resulting in situations that can cause moral and material damage or even economic loses.

1.5. THESIS OBJECTIVES & STRUCTURE

In a context where traditional geodetic GNSS receivers and robotized total stations (RTS) were considered by the geodetic community as the only high-accuracy sensors for the monitoring of static structural responses, the current development of low-cost and low energy consumption dual frequency GNSS receivers opened a door to a cost effective approach, for precisely monitoring of low frequent structural responses of civil infrastructure (Lapadat [5]). Therefore, this master thesis project is proposing to experimentally evaluate the capabilities of a pair of newly released low-cost dual frequency GNSS modules to accurately measure the kinematic response of a simple cantilever beam system to turbulent wind influences. In the context of the proposed experiment, the captured kinematic behavior of the cantilever beam system should resemble a real life scenario that should simulate the responses of a tall, slender structure to powerful winds. With this being elucidated this study is further aiming for the development of an integration strategy of an GNSS based SHM system that can detect structural displacement in real time and rise safety alarms to warn on unexpected structural responses caused by strong winds. Additionally, the proposed displacement identification procedure should consider other low-cost sensors, such as a smartphone accelerometer, for complementing the low-cost GNSS system in capturing the full range of static, quasi-static and dynamic structural displacements caused by strong winds.
Furthermore, a large part of this study is dedicated to the definition of a mitigation procedure for one of the most influential errors affecting GNSS observations in build-up areas, known as multipath.

In order to achieve the primary goal of this study a set of five guiding research questions are proposed. Hence, the questions to be answered in this study read:

"What is the accuracy capability of a low-cost dual frequency GNSS receiver and is it sufficient for monitoring wind-induced displacement of tall, slender structures?"

"What are the main steps for developing a low-cost real-time GNSS based monitoring system for sensing static, quasi-static and dynamic displacements of tall, slender structures exerted by natural factors?"

"What are the benefits of integrating a secondary measuring technique such as smartphone accelerometers in the low-cost SHM system?"

"What are the steps for implementing a real-time MP mitigation procedure within the low-cost structural health monitoring system?"

"What is the effectiveness of such a system for measuring structural displacements in real time and accurately identify critical displacements?"

The methodology for finding an answer to these research questions and achieving the goal of the research is strongly dependent on the workflow involved in the followed steps within this study, which is structured in five chapters excluding this introductory chapter. Hence, in chapter 2 a detailed description of the proposed practical experiment, *"the cantilever beam experiment"*, is given including information about the experimental setup, equipment description and the data acquisition procedure. Furthermore, key elements such as an hypothetical wind-induced displacement value, the differential GNSS relative positioning principle, the need of meteorological data sets and the definition of validation procedures based on auxiliary sensors are introduced.
Chapter 3 starts by introducing the most common error sources that influence the proper functioning of the three considered sensor types, the laser distometer, the smartphone accelerometer and the GNSS sensor. In this chapter focus is placed on the MP effect and the two possibilities for developing a MP correction based on either CP residuals or relative position estimates.
Chapter 4 summarizes all obtained results from the conducted cantilever beam experiment together with their validation based on displacement data sets derived from the laser distometer and the smartphone accelerometer. Additionally, at the end of the fourth chapter the precision capabilities and the whiteness of the low-cost GNSS system and the smartphone accelerometer measurements are questioned. Lastly, an overall assessment of the capabilities of the used low-cost GNSS sensor for retaining wind-induced displacement is presented.

Chapter 5 introduces some useful processing techniques for the implementation of a GNSS based SHM system in real time. Here, the principle of RTK GNSS positioning is introduced, followed by a real-time implementation procedure of the relative position based MP correction. Then the concept of integer ambiguity estimation is defined and the real-time evaluation of its correctness based on success rate analyses is discussed. Furthermore, in order to statistically assess and identify the appearance of any structural divergences from the structures initial steady state, a uni- and a tri-dimentional statistical hypothesis testing based displacement identification procedure is introduced. Lastly, a strategy for the implementation of a low-cost real-time displacement sensing system for effectively estimating and identifying wind-induced displacements of tall, slender structures is presented in the form of a scheme (see figure 5.8).
Chapter 6 summarizes straightforward, conclusive answers to each of the aforementioned five research questions. Each answer is accompanied by a citation to the exact section(s), consisting of supporting arguments for the drawn conclusion. The chapter ends with a list of theoretical and practical recommendations to be followed for ensuring future successful deployment of low-cost GNSS based SHM campaigns.

REFERENCES

[1] C. R. Farrar and K. Worden, *An Introduction to Structural Health Monitoring,* Philosophical Transactions of the Royal Society A: Mathematical, Physical and Engineering Sciences **365**, 303 (2007).

[2] J. M. Brownjohn, *Structural Health Monitoring of Civil Infrastructure,* Philosophical Transactions of the Royal Society A: Mathematical, Physical and Engineering Sciences **365**, 589 (2007).

[3] G. M. Calvi, M. Moratti, G. J. O'Reilly, N. Scattarreggia, R. Monteiro, D. Malomo, P. M. Calvi, and R. Pinho, *Once upon a time in Italy: The tale of the Morandi Bridge,* Structural Engineering International **29**, 198 (2019).

[4] A. Lawrence, *Modern Inertial Technology-navigation, Guidance, and Control,* STIA **93**, 39795 (1993).

[5] A. Lapadat, *Precise Monitoring of Horizontal Displacement of Large-Scale Structures using Low-Cost Dual Frequency GNSS Receivers,* (2020).

[6] W. Lienhart, M. Ehrhart, and M. Grick, *High Frequent Total Station Measurements for the Monitoring of Bridge Vibrations,* Journal of Applied Geodesy **11**, 1 (2017).

[7] Y. Xu, *Photogrammetry-Based Structural Damage Detection by Tracking a Visible Laser Line,* Structural Health Monitoring **19**, 322 (2020).

[8] S. B. Im, S. Hurlebaus, and Y. J. Kang, *Summary Review of GPS Technology for Structural Health Honitoring,* Journal of Structural Engineering **139**, 1653 (2013).

[9] T.-H. Yi, H.-N. Li, and M. Gu, *Recent Research and Applications of GPS-based Monitoring Technology for High-Rise Structures,* Structural Control and Health Monitoring **20**, 649 (2013).

[10] P. Psimoulis, S. Pytharouli, D. Karambalis, and S. Stiros, *Potential of Global Positioning System (GPS) to measure Frequencies of Oscillations of Engineering Structures,* Journal of Sound and Vibration **318**, 606 (2008).

[11] A. Lepadatu and C. Tiberius, *GPS for Structural Health Monitoring-Case Study on the Basarab Overpass Cable-Stayed Bridge,* Journal of Applied Geodesy **8**, 65 (2014).

[12] F. Moschas and S. Stiros, *PLL bandwidth and noise in 100 hz GPS measurements,* GPS Solutions **19**, 173 (2015).

[13] Y. Tamura, M. Matsui, L.-C. Pagnini, R. Ishibashi, and A. Yoshida, *Measurement of Wind-induced Response of Buildings using RTK-GPS,* Journal of Wind Engineering and Industrial Aerodynamics **90**, 1783 (2002).

[14] M. Celebi and A. Sanli, *GPS in Pioneering Dynamic Monitoring of Long-period Structures,* Earthquake Spectra **18**, 47 (2002).

[15] T. Bellone, P. Dabove, A. Manzino, and C. Taglioretti, *Real-time Monitoring for Fast Deformations using GNSS Low-cost Receivers,* Geomatics, Natural Hazards and Risk **7**, 458 (2016).

[16] A. Cina and M. Piras, *Performance of Low-cost GNSS Receiver for Landslides Monitoring: Test and Results,* Geomatics, Natural Hazards and Risk **6**, 497 (2015).

[17] T. Kijewski-Correa and M. Kochly, *Monitoring the Wind-induced Response of Tall Buildings: GPS Performance and the Issue of Multipath Effects,* Journal of Wind Engineering and Industrial Aerodynamics **95**, 1176 (2007).

[18] X. Li, C. Rizos, L. Ge, Y. Tamura, and A. Yoshida, *The Complementary Characteristics of GPS and Accelerometer in Monitoring Structural Deformation,* in *ION 2005 Meeting* (Citeseer, 2005).

[19] H.-N. Li, T.-H. Yi, X.-D. Yi, and G.-X. Wang, *Measurement and Analysis of Wind-induced Response of Tall Buildings based on GPS Technology,* Advances in Structural Engineering **10**, 83 (2007).

[20] H. S. Park, H. G. Shon, I. S. Kim, and J. H. Park, *Monitoring of Structural Behavior of High-rise Buildings using GPS,* Proc., CTBUH 2004 , 1064 (2004).

[21] H. van der Marel, *Double Back-flip Corner Reflector GNSS Antenna Test Result,* (2017).

[22] W.-S. Chan, Y.-L. Xu, X.-L. Ding, Y.-L. Xiong, and W.-J. Dai, *Assessment of Dynamic Measurement Accuracy of GPS in Three Directions,* Journal of Surveying Engineering **132**, 108 (2006).

[23] G. L. Mader, *GPS Antenna Calibration at the National Geodetic Survey,* GPS Solutions **3**, 50 (1999).

[24] Z. Hu, Q. Zhao, G. Chen, G. Wang, Z. Dai, and T. Li, *First Results of Field Absolute Calibration of the GPS Receiver Antenna at Wuhan University,* Sensors **15**, 28717 (2015).

[25] A. Krietemeyer, H. v. d. Marel, N. v. d. Giesen, and M.-C. t. Veldhuis, *High Quality Zenith Tropospheric Delay Estimation using a Low-Cost Dual-Frequency Receiver and Relative Antenna Calibration,* Remote Sensing **12**, 1393 (2020).

[26] A. Feldbusch, H. Sadegh-Azar, and P. Agne, *Vibration Analysis using Mobile Devices (Smartphones or Tablets),* Procedia Engineering **199**, 2790 (2017).

[27] M. Feng, Y. Fukuda, M. Mizuta, and E. Ozer, *Citizen Sensors for SHM: Use of Accelerometer Data from Smartphones,* Sensors **15**, 2980 (2015).

2

CANTILEVER BEAM EXPERIMENT

The second chapter of this graduation project introduces from a theoretical and practical point of view the proposed structural health monitoring experiment, known as "the cantilever beam experiment". Its application has the goal to assess the accuracy capability of the considered low-cost dual frequency GNSS receiver(s) for monitoring wind-induced displacements of tall structures. Moreover, the motivation on choosing a cantilever beam as the case study subject for measuring wind-induced displacement is addressed, followed by the description and scope of each of the three integrated sensors within the considered displacement detection sensor network.
Based on predefined mathematical models, a-priori values for the expected cantilever beam deflection and the natural frequency are derived and presented to the reader, followed by a discussion on the integration of meteorological information in the displacement detection process for confirming the wind influence as the primary cause of beam deflections.
From a theoretical point of view the double difference carrier phase relative positioning principle is further introduced, to briefly explain how millimeter precise relative positions can be derived from GNSS measurements as a measure for beam displacements.
In the end, multiple validation algorithms based on auxiliary SHM sensors are proposed. To prepare the reader for applying these validation algorithms, several digital signal processing techniques are briefly discussed. In the last part of this chapter the emphasis is set on the use of low-cost accelerometer sensors for validating and complementing GNSS derived displacement values.
The entire chapter has the intention to inform and show how static, quasi-static and dynamic displacements can be derived and validated by means of low-cost sensor integration.

2.1. OVERVIEW ON THE PROPOSED EXPERIMENT. CHOICE OF THE CASE STUDY SUBJECT

WITHIN this project an SHM experiment was designed to be deployed on an open field area near Breda, the Netherlands over four days, from the 16th until the 20th of March 2020, where a stainless steel 2 x 0.03 x 0.005 meter cantilever beam weighting 3125 grams was chosen as case study element. For this a SHM sensor network, consisting of two low-cost dual frequency GNSS modules, a smartphone accelerometer, a laser distometer, a weather station and two laptop processing units, was configured. The main goal of this experiment was to assess the accuracy capability of a low-cost dual frequency GNSS receiver and to attest its sufficiency for monitoring wind-induced displacements of tall, slender structures. To prove so, centimeter order displacements of the cantilever beam should be trackable by the GNSS module under any circumstances.

Although the cantilever beam is a much simpler and easy responsive structural system than a complex tall structure, it represents a very good case study element by simulating the possible wind-induced vibrational behavior of a tall structure. Generally, this holds true because tall structures present more pronounced deflection responses at their top than at their rigid lower part. This is the case also for the proposed cantilever beam, which was rigidly fixed at the ground with two drill press vices (see right side of figure 2.1), realizing a close to an ideal point of suspension for the beam and leaving only 1.609 meters out of it above ground to freely respond to natural perturbing factors (s.a wind loads). Moreover, the beam was vertically positioned in such a way that its widest side was pointing to the West, in order to easily respond to typical West wind loads under the form of East-West displacements along its weak (X) axis (see figures in appendix A).
Moreover, the proposed cantilever beam represents a good case study element by being a more easily controllable structural system for establishing a valuable deformation hypothesis based on beam deflection models. The definition of such a hypothetical deflection value is described in the upcoming section 2.3 and should output an expected deflection value to be sensed by the proposed SHM sensor network under a certain wind load scenario.

The cantilever beam experiment was divided in two stages in order to enclose the entire displacement range of tall structures, which can be found in nature. This consisted of slow static and quasi-static displacements with varying amplitude and fast dynamic displacements/ vibrations.
The very first stage, entitled as "the artificially induced displacement (AID) stage", was deployed over a period of only six minutes from 17:21:30 until 17:27:50 UTC on the 16th of March 2020, when man-made displacements were induced in East-West (X) direction by manually pulling on a rope tightened around the cantilever beam. Over this period slow but also fast displacements with varying amplitude were induced to mimic static, quasi-static and dynamic displacements. The induced perturbations were measured by one of the GNSS modules, the smartphone accelerometer and the laser distometer at the same time, the first two sensors being installed on top of the beam while the last one being installed at approximately 6.6 meters away from the case study element (see figure A.2 in appendix A). A more detailed description of the experimental setup can be found in the next subsection.
Over the remaining experimental period the cantilever beam was let to freely respond in to wind loads and sense naturally induced beam responses and resemble a scenario that should simulate the responses of a tall structure to powerful windstorms. This second stage started immediately after the end of the artificially induced displacement stage and lasted until the 20th of March 2020, 09:23:32 UTC, being known as "the wind-induced displacement (WID) stage" .

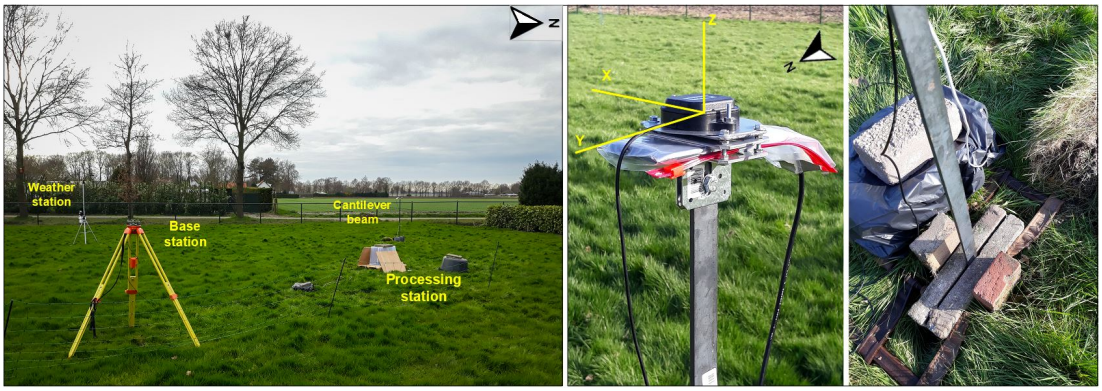

Figure 2.1: Experimental setup (left). Cantilever beam sensors alignment (GNSS antenna on top & smartphone below) & specific XYZ-coordinate system painted in yellow (middle). Drill press fixing method of cantilever beam (right)

2.2. EXPERIMENTAL SETUP, EQUIPMENT DESCRIPTION & DATA ACQUISITION

To be able to measure and validate the cantilever beam responses an integrated SHM sensor network composed out of three different sensors was proposed. The most important sensor from the sensor network was the low-cost dual frequency GNSS rover whose antenna was installed on top of the beam together with a metallic ground plane for MP mitigation. Over the entire experimental period the rover acquired pseudorange/ code and carrier phase observations from multiple constellations (GPS, GLONASS, Galileo and BeiDou) at a rate of 5 Hz.
Underneath it, a smartphone was installed to log acceleration measurements at 10 Hz rate. These can be converted in displacement values for validating the GNSS results and/ or compensate for the dynamic responses of the beam that were too rapid and small in amplitude for the GNSS equipment. Both sensors were in such a way oriented that their XYZ-coordinate axes aligned (see middle part of figure 2.1). Respectively their X-axes were pointing to the East, the Y-axes to the North and the Z-axes to the Zenith.
At approximately 15.6 meters to the South-East from the rover, an identical GNSS module, acting as a reference station, was installed on a tripod. Caution was taken during installation, to align its coordinate system with the coordinate systems of the sensors installed on the beam. This time the reference station was collecting code and carrier phase information at a rate of 1 Hz.
For further validation purposes a third integrated sensor under the form of a laser distometer was installed on a tripod somewhere in between the two GNSS modules, to independently measure the displacement quantities of the cantilever beam in the East-West (X) direction. This sensor was let to operate only over the AID stage. It is important to mention that due to the height limitation of the tripod the distometer was pointing to the beam at 1.515 meters above the ground, about 10 centimeters below the beam's top, resulting in slightly smaller deflection quantities (see figure A.2 in appendix A).
Last, but not least an auxiliary weather station with an anemometer was included in the SHM sensor network for logging wind speed (WS), wind direction (WD) and precipitation data every 3-seconds to be used for wind pattern and GNSS-meteorological data correlation identification. These were installed at about 8.5 meters and 16.4 meters away from the rover and base station on a metallic tripod with a pole extension, making sure that the anemometer was installed at at-least 30 centimeters above the weather station, with its vane pointing to the North.
A sketch of the previously described instrumental placement is presented in appendix A.

Table 2.1: Common instrumental characteristics of the SHM sensors: GNSS, Smartphone Accelerometer, Laser Distometer & Weather Station

Common Instrumental Characteristics				
↓Value|Sensor→	*GNSS*[1]	*Accelerometer*[2]	*Laser Distometer*[3]	*Weather Station*[4]
Model	u-blox ZED-F9P + ANN-MB	BOSCH BMI160 IMU	Leica disto pro	Davis Wireless Vantage Pro2 Plus
Sensor	Multi-band GNSS receiver + antenna	Digital triaxial Accelerometer & Gyroscope	Visible laser sensor	Weather Station + Aneometer
Size [mm]	17 x 22 x 2.4 + 60 x 82 x 22.5	2.5 x 3 x 0.8	223 x 78 x 51	536 x 246 x 406
Power consumption [V]	3.6 + 5.0 = 8.6	3.6	6 V	3*(1.2-2) + Solar Panel
Sampling Rate/ Period	1 - 8 Hz (GPS+GLO+GAL+BDS, RTK mode)	12.5 - 1600 Hz	0.5-4 sec	3 sec
Price [€]	176 + 53 = 229	4.49	at today's rate of 300	1285

In the next lines the most important instrumental characteristics of each sensor type are briefly introduced.
The proposed GNSS sensor is a low-cost dual frequency multi constellation GNSS module developed by u-blox, capable of centimeter-level accurate real-time kinematic (RTK) positioning. Its declared cost efficiency made one take it into consideration for using and testing its positioning potential for SHM purposes. Therefore, two identical u-blox ZED-F9P modules were used to establish a short distance rover-base station connection for determining baseline vector estimates and sense any baseline vector variations related to possible beam deflections.
In the context of the deployed cantilever beam experiment, the integration of a low-cost smartphone accelerometer was proposed for measuring possible wind-induced dynamic displacements of the cantilever beam and validate the derived displacement quantities from the rover GNSS module. Particularly, the SHM sensor network included a Xiaomi MI9 SE smartphone equipped with a Bosch BMI160 low noise 16-bit iner-

[1] https://www.u-blox.com/en/product/zed-f9p-module.
[2] https://ae-bst.resource.bosch.com/media/_tech/media/datasheets/BST-BMI160-DS000.pdf.
[3] https://www.kreitel-vermessungsgeraete.de/KREITEL%20DOWNLSERV%20BedAn%20Disto%20basicmemopro%20GER.pdf.
[4] https://www.davisinstruments.com/product_documents/weather/spec_sheets/6152_62_53_63_SS.pdf.

tial measurement unit (IMU) that can collect precise XYZ-acceleration and angular velocity measurements. Moreover a second validation sensor in the form of an outdated laser distometer was integrated. This was used only during the AID stage to measure East-West (X) beam deflections in order to compare them with the derived displacement quantities from the GNSS module. Particularly, this instrument was a 1998 Leica distometer model, known as Leica disto pro, which is capable for measuring and recording up to 1000 distance measurements.
Additionally, a meteorological sensor was proposed for measuring WS, WD and precipitation to be used for finding any correlation between them and possible beam deflections. In this case, a commercial weather station plus anemometer solution from Davis Instruments was chosen.
For getting a better view over the measuring capabilities of each sensor, the most important instrumental characteristics of the aforementioned sensors are summarized in table 2.1 and 2.2.

Table 2.2: Specific instrumental characteristics of the SHM sensors: GNSS, Smartphone Accelerometer, Laser Distometer & Weather Station

Specific Instrumental Characteristics							
↓Value|Sensors→	GNSS	Accelerometer		Laser Distometer		Weather Station	
GNSS	GPS; GLO; GAL; BDS; QZSS;	Range [g][5]	± 8	Emitted Wavelengths [nm]	620-690	WS precision $[\frac{m}{s}]$	±0.9
GNSS Bands	L1C/A, L2C; L1OF, L2OF; E1B/C, E5b; B1I, B2I; L1C/A, L2C;	Max. Range $[\frac{m}{s^2}]$	± 78.4532	Precision [mm]	±1.5-2	WD precision[°]	±3
Hor. & Ver. Precision [m+ppm]	0.01 + 1	Sensitivity $[\frac{LSB}{g}]$[6]	± 8g: 4096	Range [m]	0.3-100	Rain Collector precision [%]	±5 for 250 mm/h
		Noise Density $n_{A,nd}[\mu g/\sqrt{Hz}]$[7]	180				
		Resolution [bit][8]	16				
		Resolution $[\frac{m}{s^2}]$[9]	0.002393				

The data logging and screening functions were accomplished differently for each of the sensors. In case of the GNSS modules, a processing station under the form of a laptop was installed between them. Thanks to the STRSVR and RTKNAVI functionalities of RTKLib's software package[10], the processing station was able to concurrently perform three functions: logging, data processing and screening in near real-time. The connection between both receivers and the processing station was established via active USB cables. Figure 2.2 describes in more detail the data flow between the reference and rover station.
In case of the smartphone, this was permanently powered by a power bank battery. Though, due to power consumption reasons, the smartphone was set in airplane mode, being disconnected from any cellular network or GNSS service over the entire experimental period. The accelerometer data was logged via Matlab Mobile app and stored on the smartphone internal memory. In this case, the smartphone did not stream the information to an external screening device, therefore no screening function was deployed by the smartphone.
During the AID stage the laser distometer was linked to a second laptop used only for acquisition purposes. An in-house build GUI application was used for collecting distance measurements continuously.
In case of the weather station a wireless data transfer protocol was used for accomplishing the data logging function. This protocol was streaming the data every 3 seconds to a console, which was connected to the processing station. The screening function was performed by a third-party console software, Cumulus, while the logging function was performed by an in-house build Matlab script, which was scraping the meteorological information and storing it in a separate text file.

At last, a description of the encountered errors caused by the data acquisition process of each sensor is presented. Therefore, based on the first inspection on the acquired data it was found that GNSS data sets were the only one that were not affected by acquisition errors, being constantly collected at the desired sampling

[6] defines the range of measurable acceleration amplitude.
[7] defines at what rate the accelerometer converts mechanical energy into voltage. It is expressed in least significant bit per g (LSB/g). In case one wants to measure small vibrations, a higher sensitivity is desirable.
[8] shows the residual noise as a spectral noise parameter where one should multiply by the square root of the bandwidth to get the nominal root mean square acceleration noise level. The indicated value is related to nominal operating conditions: temperature of 25°C and nominal supply voltage of 3.0 V.
[9] counts the acceleration levels/bins the sensor can measure.
[10] $= \frac{2*8}{2^{16}*9.80665}$
[10] this software package is briefly introduced in the last part of section 1.4.

rate.

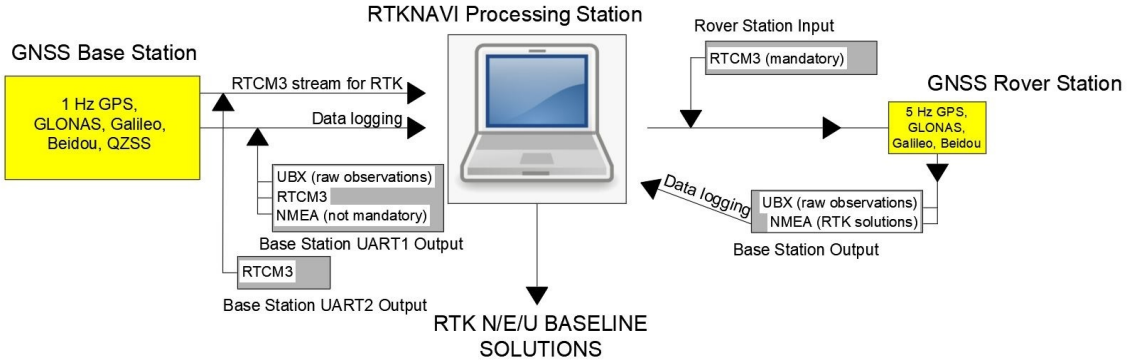

Figure 2.2: Data flow between GNSS base and rover station

The preliminary inspection on the smartphone accelerometer data showed that the smartphone accelerometer data was strongly fragmented and miss sampled by the used smartphone application, being 85% of the time recorded at a rate of 15.151 Hz instead of 10 Hz. Moreover, a non-linearly increasing time lag error between the smartphone accelerometer and the GNSS data sets was identified. It is believed that this happened because the smartphone was set to operate in airplane mode cutting connection with any cellular network or GNSS service. For a more detailed explanation of the cause of these errors please refer to appendix B.1.
Moreover, a discontinuous behavior in the sampling period of the laser distometer was identified as well. This can be visualized in the bottom subplot of figure B.3 in appendix B.2. The non-uniform sampling period of the laser distometer was caused by large and quick beam deviations. Hence, part of the displacement behavior of the cantilever beam could not be perfectly recovered by the distometer, which was inducing some time lag in the acquired displacement time series.
Last but not least, the raw meteorological information acquired by the weather station presented four large periods with missing observations. These were caused by an exceeding index error within the Matlab data scraping process. The identified meteorological data gaps are listed in appendix B.3, and can be visualized in the prepared WS and 10 minutes average WD plots from figure B.4.

2.3. WIND LOAD CALCULATIONS. DEFORMATION HYPOTHESIS

BASED on the acquired meteorological information from figure B.4, the definition of a hypothetical beam deflection value produced by 4 Beaufort moderate breezes was desirable. This value should model the deformation response of the cantilever beam to up to 6.7 $\frac{m}{s}$ winds and estimate an expected a-priori deflection value of the cantilever beam.
For this, the ***prEN 1991-1-4*** - *"Actions on structures - Part 1-4: General actions - Wind actions"* Eurocode[11] and a pre-defined cantilever beam uniform varying load model[12] were used for deriving the wind-induced force (F_w) and the maximum cantilever beam response (y_{max}) to a 6.7 $\frac{m}{s}$ moderate breeze, hitting perpendicularly on the 0.03 meter side of the cantilever beam.
Therefore (2.1) was first used for calculating the wind-induced force of a 6.7 $\frac{m}{s}$ moderate breeze, which was then uniformly distributed along the length of the cantilever beam in (2.2). The resulting uniformly distributed wind load value (w) was feed into the wind-induced deflection equation (2.3) that was particularized for computing the maximum deflection of the beam (y_{max}) at its free end by substituting x with 0. The expected beam deflection produced by a 6.7$\frac{m}{s}$ wind, which was perpendicularly hitting the 0.03 meter side of the cantilever beam, was equal to 2 centimeters.

$$F_w = c_s * c_d * c_f * q_p(z_e) * Aref = 1 * 1.84 * 28.4490 * 0.0483 = 2.53\,[N] \tag{2.1}$$

where:

F_w = wind-induced force [N]
$c_s * c_d$ = structural factor
c_f = force coefficient for this type of structure element
$q_p(z_e)$ = peak velocity pressure at reference height z_e $of 1.609 m$ $[\frac{N}{m^2}]$
Aref = reference area of the structural element $[m^2]$

[11] https://www.phd.eng.br/wp-content/uploads/2015/12/en.1991.1.4.2005.pdf
[12] for a thorough mathematical proof visit: table 8.1, formula 2a from (Budynas *et al.* [1])

$$w = \frac{F_w}{l} = \frac{2.53}{1.609} = 1.57\,[\frac{N}{m}] \tag{2.2}$$

where:

w = uniform varying wind load $[\frac{N}{m}]$
l = length of the cantilever beam [m]

$$y = \frac{1}{EI} * (-\frac{w * x^4}{24} + \frac{w * l^3 * x}{24} - \frac{w * l^4}{8}) \overset{x=0}{\rightarrow} y_{max} = -\frac{w * l^4}{8 * EI} = -\frac{1.57 * 1.609^4}{8 * 2.1 * 10^{11} * 3.125 * 10^{-10}} = 0.02\,[m] \tag{2.3}$$

where:

y = wind-induced beam deflection [m]
E = Young modulus[13] $[\frac{N}{m^2}]$
I = moment of inertia[14] [m^4]
x = distance to the point of interest along the beam [m]

To the resulting value from (2.3), one should consider also the additional deflection quantities produced by the wind action on the sides of the GNSS antenna and of the smartphone installed on the top of the cantilever beam. For this the wind load forces (F_w) that were acting on the 0.06 x 0.0225 meter and 0.1475 x 0.0075 meter sides of the antenna and smartphone were computed based on the same formula as before with slightly changed input parameters (see (2.4)). This time is was assumed that the structural element was not anymore a steel element with rectangular section and sharp edges but a signboard.

$$\begin{aligned} F_{w_{GNSS}} &= 1 * 1.8 * 28.4490 * 0.0013 = 0.0691\,[N] \\ F_{w_{Smartp}} &= 1 * 1.8 * 28.4490 * 0.0011 = 0.0563\,[N] \end{aligned} \tag{2.4}$$

The resulting wind load values (F_w) were then concentrated at the beam end by using a cantilever beam concentrated load at the free end model[15] described by formula (2.5), in which x was again substituted with 0. In such a case, the maximum beam deflection values induced by the wind action on the sides of the GNSS antenna and smartphone ($y_{GNSS/Smartp}$) were equal to 0.2 and 0.1 centimeters.

$$\begin{aligned} y_{GNSS/Smartp} &= \frac{1}{EI} * (-\frac{F_{w_{GNSS/Smartp}} * x^3}{6} + \frac{F_{w_{GNSS/Smartp}} * l^2 * x}{2} - \frac{F_{w_{GNSS/Smartp}} * l^3}{3}) \rightarrow y_{max} = \\ &= -\frac{F_{w_{GNSS/Smartp}} * l^3}{3 * EI} = -\frac{(0.0691|0.0563) * 1.609^3}{3 * 2.1 * 10^{11} * y * 10^{-10}} \\ y_{GNSS} &= 0.002\,[m] \quad \& \quad y_{Smartp} = 0.001\,[m] \end{aligned} \tag{2.5}$$

Therefore, when adding the resulting values from (2.3) and (2.5) together, it is expected from the cantilever beam to bend by approximately 2.3 centimeters under the perpendicular influence of a 6.7 $\frac{m}{s}$ wind breeze on its 0.03 meter side.
However, because the previously presented computations were not considering any specific information about the properties of the material of the cantilever beam, the drawn hypothesis should be treated as an indicative, likely over-estimated result, pointing on the order of magnitude of the expected wind-induced deformation.
For a more detailed explanation on the choice and calculation of each parameter from the previous equations, please refer to appendix C.

At this point, an a-priori value for the natural frequency of the first mode of vibration of the cantilever beam can be determined. This can be further used as a validation measure for the natural frequency value that can be derived from both the GNSS and accelerometer data sets via Fast Fourier transform (FFT).
For this, two different mathematical formulas were used for determining the natural frequency of the bending beam. The first one was modeling a cantilever beam influenced by a uniformly distributed (wind) load (w) including its self-weight while the second formula[16] was corresponding to a cantilever beam system influenced by a uniformly distributed (wind) load together with the weight of both measuring sensors from its top.

[14] for steel it can be considered equal to $2.1 * 10^1 1\,\frac{N}{m^2}$.
[15] can be computed based on the formula for the moment of inertia for a rectangular section, see http://www.clag.org.uk/beam.html
[15] for a thorough mathematical proof visit: table 8.1, formula 1a from (Budynas *et al.* [1])
[16] note that this formula is outputting an approximate value for the natural frequency.

Both formulas were taken from table 16.1 of (Budynas *et al.* [1]) and are presented below.

$$
\begin{aligned}
f_1 &= \frac{K_1}{2\pi}\sqrt{\frac{EI*g}{(w+W_{beam})*l^4}} = \frac{3.52}{2\pi}\sqrt{\frac{65.6250*9.81}{(1.5704+3.1250*9.81)*1.609^4}} = 0.97\,[Hz] \\
f_1 &\approx \frac{1.732}{2\pi}\sqrt{\frac{EI*g}{W_{GNSS+Smartp}l^3+0.236wl^4}} \\
&\approx \frac{1.732}{2\pi}\sqrt{\frac{65.6250*9.81}{((0.183+0.173)*9.81)*l^3+0.236*1.5704*1.609^4}} \approx 1.69\,[Hz]
\end{aligned}
\tag{2.6}
$$

where:

f_1	= natural frequency of the first mode for a cantilever beam [Hz]
K_1	= constant corresponding to the first mode of vibration
W_{beam}	= beam weight [N]
$W_{GNSS+Smartp}$	= concentrated weight of the GNSS antenna and Smartphone [N]

Based on the resulting natural frequency values, one is expecting to be able to derive a value in the order of 1 Hz from the energy within the wind-induced beam vibrations.

2.4. GNSS DOUBLE DIFFERENCE CARRIER PHASE RELATIVE POSITIONING PRINCIPLE[17]

As previously mentioned in section 1.3, GNSS receivers are capable of acquiring satellite signals that are individually composed out of a pseudorange code and a carrier wave signal. "The carrier wave for the GNSS signal is a sine wave with a wavelength of less than one metre"[18], which repeats on its way from the transmitting satellite to the GNSS antenna. Measuring the phase of the carrier wave in terms of distance can reach millimeter precision, but the measurement is ambiguous since the total number of cycles between satellite and receiver is unknown[19] but constant as long as the receiver can track the carrier wave signal uninterruptedly.
Based on this consideration, in this study the CP observations were preferred in the relative positioning process, also known as baseline estimation process, for determining a time series of East(X)/ North(Y)/ UP(Z) baseline vector estimates between the GNSS rover and reference station. This offers a good overview over possible position deviations within the time series of solutions, indicating structural deformations. But before introducing the relative positioning concept, it is of high importance to first understand the mathematical representation of CP observations (see (2.7)).

As one can see from the first part of (2.7), in order to accurately determine receiver positions, "one needs to model the right-hand side of the first observation equation to match as accurately as possible with the CP observations"(Teunissen and Montenbruck [3]).

$$
\begin{aligned}
\Phi^s_{r,j}(t) &= r^s_r(t) - \gamma_j I^s_{r,j}(t) + T^s_{r,j}(t) + c[\delta t_r(t) - \delta t^s(t)] + \lambda_j A^s_{r,j} + \varepsilon^s_{r,j}(t) \\
A^s_{r,j} &= \phi_{r,j}(t_0) - \phi^s_j(t_0) - f_j[\delta t_r(t_0) - \delta t^s(t_0)] + N^s_{r,j}
\end{aligned}
\tag{2.7}
$$

where:

[17] part of the presented equations and figures are extracted from the course "GPS For Civil Engineering and Geosciences", courtesy to (van der Marel *et al.* [2]).

[18] can vary between 19 and 24.4 centimeters; https://www.novatel.com/an-introduction-to-gnss/chapter-5-resolving-errors/gnss-measurements/

[19] this process is known as carrier phase ambiguity. Estimating the carrier phase ambiguity is the key to achieve accurate positioning. For more details on this process refer to section 5.4.

2

r, s, j, t = receiver no., satellite no., GNSS band frequency no., time epoch
$\Phi^s_{r,j}(t)$ = measured carrier phase [m]
$r^s_r(t)$ = satellite-receiver range [m]
$\gamma_j = \frac{f_1^2}{f_i^2}$ - ionosphere multiplication factor
$I^s_{r,j}(t)$ = ionosphere delay [m]
$T^s_{r,j}(t)$ = troposphere delay [m]
c, f = speed of light [$\frac{m}{s}$], frequency of the GNSS signal [Hz]
$\delta t_r(t)$, $\delta t^s(t)$ = receiver clock delay, satellite clock delay [s]
λ_j = carrier wavelength [m]
$A^s_{r,j}$ = carrier phase ambiguity [cycles]
$\varepsilon^s_{r,j}(t)$ = receiver noise + multipath [m]
$\phi_{r,j}(t_0)$, $\phi^s_j(t_0)$ = initial carrier phases [cycles]
$\delta t_r(t_0)$, $\delta t^s(t_0)$ = initial receiver and satellite clock delays [s]
$N^s_{r,j}$ = constant integer ambiguity [cycles]

Moreover, from the form of the CP observation equation it is clear that CP measurements are constantly influenced by instrumental, atmospheric and environmental errors. Therefore, the proposed double difference (DD) CP relative positioning technique can help at eliminating/ reducing part of these errors, such as the receiver and satellite clock delays, satellite orbit errors and the ionosphere and troposphere delays[20].
Hence, the DD CP relative positioning technique relies on a procedure where CP "observations on the same satellite at the same epoch are firstly differenced between receivers"(Teunissen and Montenbruck [3]) forming single difference (SD), Φ^k_{ur} (see (2.8)). Then the SD observations are subtracted between pairs of satellites forming DD observations, Φ^{kl}_{ur} $(see (2.9))$.

$$\begin{aligned} \Phi^k_{ur} &= \Phi^k_u - \Phi^k_r = r^k_{ur} - \gamma I^k_{ur} + T^k_{ur} + c[\delta t_{ur} - \cancel{\delta t^k}] + \lambda A^k_{ur} + \varepsilon^k_{ur} \\ A^k_{ur} &= A^k_u - A^k_r = \phi_{ur}(t_0) - \cancel{\phi^k(t_0)} - f[\delta t_{ur}(t_0) - \cancel{\delta t^k(t_0)}] + N^k_{ur} \end{aligned} \tag{2.8}$$

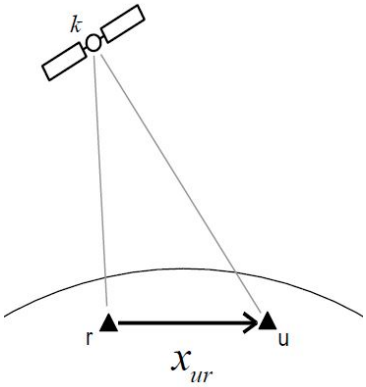

Figure 2.3: Single difference observation between receiver ***u*** and ***r*** on satellite ***k***

Since SD observations are formed with respect to the same satellite, the very first subtraction step eliminates the satellite clock error while the second subtraction step eliminates the receiver clock error.
On top, by performing a double difference procedure the carrier phase ambiguity term $A^s_{r,j}$ will reduces to a straightforward, estimable integer value $N^s_{r,j}$.

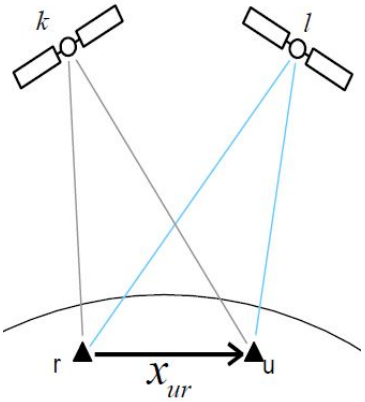

Figure 2.4: Double difference observation between SD observation on satellite ***k*** and SD observation on satellite ***l***

In addition, in case of a sufficiently short baseline already at SD level the composition of the atmosphere can be considered homogeneous, hence the ionosphere and troposphere delays can be neglected. Thus, it can be assumed that both atmospheric error terms have minor influence and can be neglected from the resulting DD equation, resulting in an simplified DD CP equation (see (2.10)).

$$\begin{aligned} \Phi^{kl}_{ur} &= \Phi^k_{ur} - \Phi^l_{ur} = r^{kl}_{ur} - \gamma I^{kl}_{ur} + T^{kl}_{ur} + \cancel{c\delta t_{ur}} + \lambda A^{kl}_{ur} + \varepsilon^{kl}_{ur} \\ A^{kl}_{ur} &= A^k_{ur} - A^l_{ur} = \cancel{\phi_{ur}(t_0)} - \cancel{f\delta t_{ur}(t_0)} + N^{kl}_{ur} \end{aligned} \tag{2.9}$$

$$\begin{aligned} \Phi^{kl}_{ur} &= r^{kl}_{ur} + \lambda A^{kl}_{ur} + \varepsilon^{kl}_{ur} \\ A^{kl}_{ur} &= N^{kl}_{ur} \end{aligned} \tag{2.10}$$

Though, in order to model the DD satellite-receiver range and the DD CP ambiguity terms from (2.10), one would first need to linearize the former term via Tylor series expansion[21].
After linearizing the satellite-receiver range term, one is able to set up a

[20] only if the rover-reference station baseline is short (up to 10-20 kilometers).
[21] for a in-depth demonstration of the Taylor series based satellite-receiver range term linearization process please refer to (Teunissen and Montenbruck [3]), sub chapter 21.2.1

functional model of linearized DD CP observation and use the least-squares principle for estimating the unknown baseline coordinates at every epoch and the unknown constant integer ambiguity terms. Considering four satellites[22] ,***k, j, l, m***, which were visible at the same time from two observation points, ***u*** and ***r***, the following functional model can be set:

$$y = A * x \Leftrightarrow \begin{bmatrix} \Phi_{ur}^{kj} \\ \Phi_{ur}^{lj} \\ \Phi_{ur}^{mj} \end{bmatrix} = \begin{bmatrix} (-\mathbf{1}_r^{kj})^T & \lambda & 0 & 0 \\ (-\mathbf{1}_r^{lj})^T & 0 & \lambda & 0 \\ (-\mathbf{1}_r^{mj})^T & 0 & 0 & \lambda \end{bmatrix} * \begin{bmatrix} \delta \boldsymbol{x}_{ur} \\ N_{ur}^{kj} \\ N_{ur}^{lj} \\ N_{ur}^{mj} \end{bmatrix} \tag{2.11}$$

Redundancy: (no. sat-1) - (no. of DD ambiguities) - (no. of unknown baseline vectors)=3-3-3=-3

where:

$(-\mathbf{1}_r^{kj})^T = -\frac{\boldsymbol{x}^{kj} - \boldsymbol{x}_{ur_0}}{\left\| \boldsymbol{x}^{kj} - \boldsymbol{x}_{ur_0} \right\|}$ - unit line-of-sight vector

$\delta \boldsymbol{x}_{ur} = [dx_{ur}, dy_{ur}, dz_{ur}]$ - unknown North, East, Up baseline vector values

When checking for the redundancy of the functional model from (2.11), it is clear that the linear system of DD observations cannot be solved for only four satellites received during one epoch. Though, when rewriting the functional model for more epochs of observations it can be proved that the minimum number of observed satellites should be at least equal with 7 and the number of epochs at least equal with 2 in order to be able to solve the system of DD CP observation equations via least-squares adjustment.

For implementing the aforementioned principle and process CP observations in real time and/ or after the data was collected, the open source RTKLib 2.4.3 software package was proposed[23]. Its rich offer of application programs (APs) and its user friendliness, packed under the form of a free software, makes it ideal for GNSS precise positioning applications, just like the one run within this graduation project.
Particularly, three APs were used for creating a data logging communication link between the rover and reference station during the data acquisition process and for performing post processing (PPK) and real time kinematic (RTK) relative positioning. These APs were STRSVR, RNX2RTKP and RTKNAVI. Out of all, the latter two APs are developed to perform DD CP relative positioning analyses that are based on the previously introduced mathematical models. Their method of functioning is slightly more complicated and incorporates an extended Kalman filter (EKF) plus a pseudorange- and CP DD relative positioning procedure for outputting precise baseline estimates. A thorough definition of RTKLib's relative positioning method can be found in appendix E7 from its user manual[24].

2.5. INTEGRATION OF METEOROLOGICAL INFORMATION IN THE DISPLACEMENT DETECTION PROCESSES

As previously mentioned in section 2.2, every 3-seconds WS, 10-minutes average WD and precipitation information was collected over the entire period of the cantilever beam experiment. This was performed in order to look for any correlation between them and possible beam deflections to prove that the beam responded under wind influences. But before being able of asking for similarity between these two data types, the meteorological information was collected and used for the identification of the wind still and windy periods during the cantilever beam experiment. This was needed in order to limit the correlation identification process to specific windy time intervals and ask for similarity between them and the GNSS derived displacements data set.
Moreover, the identification of wind still periods was important for defining a correction measure for the MP error of the GNSS measurements, which is thoroughly discussed in section 3.2 of the next chapter.

For deriving valuable information from the collected meteorological information, one first needed to correct for any encountered acquisition errors, such as the ones presented in appendix B.3. According to appendix B.3 all repetitive WS and WD values together with all the meteorological quantities related to WS values equal to 0 were eliminated from the meteorological time series of the cantilever beam experiment.
In the first step of the integration process of the meteorological data within the SHM process, the wind observations need to be treated as vector measurements with magnitude equal to their WS values and direction

[22] note that satellite ***j*** was considered reference satellite in the formation of DD CP observations.
[23] RTKLib 2.4.3 software package can be freely downloaded from http://www.rtklib.com/rtklib.htm
[24] http://www.rtklib.com/prog/manual_2.4.2.pdf

equal to the WD measurements. By this, one could separate these vectors into orthogonal wind components and better understand when the wind was powerfully blowing from one specific orthogonal direction. Based on the first illustration from appendix A, one was especially interested in wind blowing from the West since these were most likely to produce mechanical oscillation of the beam by not being obstructed by vegetation or any other obstructing objects.
To do so, the WD measurements needed to be converted from the wind barf convention[25] (WD_{wb}), to wind vector convention[26] (WD_{wv}). This can be done by subtracting all wind direction measurements from 270 degrees, changing the clockwise orientation of the barf system to a counterclockwise direction to further facilitate trigonometric operations.

$$WD_{wv} = 270° - WD_{wb} \tag{2.12}$$

A better explanation of the WD changes produced by this conversion can be seen in figure 2.5.

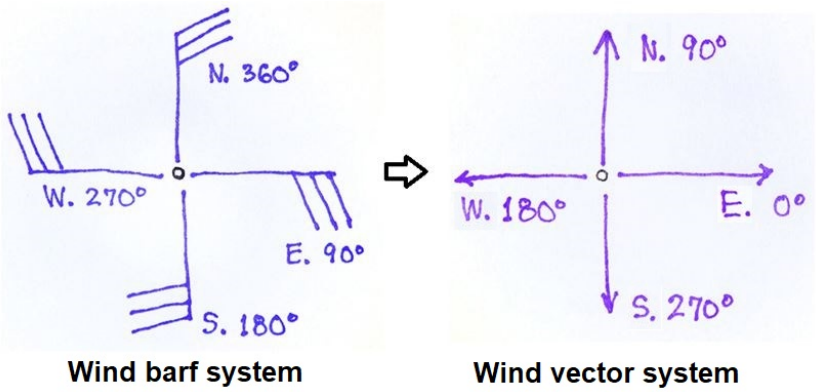

Figure 2.5: Conversion from wind barf (left) to wind vector system (right)

After converting the WD values, they should be coupled with the WS values to split each wind vector into U and V orthogonal wind component measurements[27]. For this, the following formulas can be applied:

$$\begin{aligned} U &= WS * \cos(WD_{wv}) \\ V &= WS * \sin(WD_{wv}) \end{aligned} \tag{2.13}$$

These two steps were applied on the every 3-seconds WS and WD measurements and on the 10-minutes WS and WD measurements of each windy day[28] of the cantilever beam experiment, resulting in two daily sets of U and V orthogonal wind components. The reader should take a note on the shorter day-of-year notation for the days of the experiment. Therefore, from this point the 17^{th}, 18^{th} and 19^{th} of March were labeled by their day of year notation as days *077, 078* and *079*. A short interpretation of the resulting plots of the 3-seconds and 10-minutes average U and V components time series of day 077 and 078 can be found in appendix D.

In order to get the reader familiar with all problems that can be encountered during the integration of the meteorological information in the displacement detection process, some additional mismatches that can be found between the meteorological and the GNSS derived data sets are briefly mentioned.
Before even searching for visual or statistical cross-correlation between specific windy intervals of the derived orthogonal wind component time series and of the GNSS based beam deflection time series, one should make sure that there is no time lag between both questioned data sets. Statistical cross-correlation[29] or visual matching are two options for solving this problem. Afterwards, one should check that both data sets are spanning exactly the same period and are sampled at the same rate. Otherwise, both data sets need to be cut to start and end at exact the same time and the data set that is sampled at a higher rate needs to be down sampled by interpolating its values at every time instant of the other data set.
These problems are further discussed in context of the cantilever beam experiment in section 4.2.

[25] this convention is indicating from where the wind is blowing: 0°-North, 90°-East, 180°-South, 270°-West, 360°-North.
[26] this convention is indicating towards which direction the wind is blowing: 0°-East, 90°-North, 180°-West, 270°-South, 360°-East.
[27] U component corresponds to East-West (X) direction while V component corresponds to North-South (Y) direction.
[28] from all three days of the experiment, the very first two were corresponding to windy days with winds blowing on average from the West (see figure B.4).
[29] this process gives good results only if both data sets are not fragmented.

2.6. MEANS OF VALIDATION IN THE DISPLACEMENT DETECTION PROCESS

IT is undoubtable that within a SHM process the GNSS sensor displacements should be not only accurately estimated but they should also resemble the real cantilever beam responses. Therefore, the integration of different types of validation sensors in the proposed displacement detection sensor network is indispensable. As previously presented in section 2.2, within the cantilever beam experiment a laser distometer and a smartphone accelerometer were considered for validation purposes of the GNSS derived cantilever beam displacements. In the next lines the main steps of manipulating their collected observation sets for beam displacements validation, are presented in the form of validation algorithms. The proposed validation algorithms were developed with a certain degree of generalization, therefore the reader can use them as ground truth validation procedures within SHM campaigns.

The laser distometer validation procedure represents a rudimentary but very effective solution for attesting displacements of structural elements such as the proposed cantilever beam. The primary steps one need to take into consideration when using such a displacement detection sensor are:

- ***Horizontally leveled installation of the distometer***.
  The distometer should be leveled in horizontal plane, installed as close as possible and directed towards the case study subject to limit any data sampling problems.
- ***Displacement determination at the same level/ height***.
  Preferably, the laser beam should point at the same level with the GNSS sensor to capture the same displacements.
- ***Determination of the beam displacements values***.
  This should be done by means of subtracting the acquired distance time series by a mean distance value[30] computed over a wind still period, when the beam should not present any mechanical excitation, or by a mean distance value with a standard deviation value lower than 2 times the precision of the instrument.
- ***Defining a concurrent, uniform sampling rate between the laser distometer and the GNSS sensor***.
  This step is mandatory in order to be able to ask for statistical correlation between the compared displacement data sets and can be established by down sampling the laser distometer displacements at the same rate of the GNSS sensor displacements, by interpolating them at every time instant of the GNSS data set.

On the other hand, the accelerometer validation procedure is more complex and depends on digital signal processing techniques for indirectly deriving displacement quantities from acceleration signals. Though, under controlled implementation it represents an effective validation solution for attesting dynamic displacements/ vibrations of structural elements.
It should be noted that this procedure can be run in two ways, by deriving vibration quantities from accelerometer values and vice versa, under the form of a forward and reverse transformation procedure. Moreover, the reverse transformation procedure offers a sensor fusion functionality that can be used to complement for the lacking capability of GNSS measuring units to measure small-scale vibrations, with acceleration based dynamic displacement values. Hence, by integrating an accelerometer sensor in the SHM process the reader will benefit from being able to effectively validate the GNSS based displacement estimation process, derive additional building response information and capture not only static and quasi-static but also sensitive dynamic displacements of (more rigid) structures.

2.6.1. DIGITAL SIGNAL PROCESSING. FILTER DESIGNING AND APPLICATION[31]

A short summary of the most important digital signal processing and digital filtering terms is desirable before introducing the two proposed accelerometer based validation algorithms, the forward and reverse transformation.
A digital filter can be conventionally understood as a system (H) that performs some mathematical operations on a digital signal (x_n), outputting a changed/ filtered version of the input signal (y_n).

[30] the defined mean distance value corresponds to the true (ground-truth) distance between the laser distometer and the case study element at rest.
[31] most of the theoretical aspects of this subsection were summarized from (Klees and Tiberius [4]) and (Brandt [5])

$$y_n = H(x_n) \tag{2.14}$$

In practice, the most common used class of filters is the linear time-invariant (LTI) filter class, which can be fully described by its difference equation (2.15), that can categorize a filter in two major classes: the finite impulse response (FIR) and the infinite impulse response (IIR) filter.

$$y_n = \sum_{k=0}^{p} a_k x_{n-k} - \sum_{l=1}^{q} b_l y_{n-l} = x_n + \sum_{k=1}^{p} a_k x_{n-k} + \sum_{l=1}^{q} b_l y_{n-l} \tag{2.15}$$

where:

a_k = the filter's forward coefficients
b_k = the filter's feed backward coefficients

A FIR digital filter is a filter type characterized by having all its feed backward coefficients equal to 0, being not depend on future inputs at all. Its filter order (o) is equal to:

$$o = p - 1 \tag{2.16}$$

where:

o = filter order
p = no. of filter taps, equal to the number of the filter's feed forward coefficients a_k

Note that this type of filter is commonly used in SHM applications for performing digital differentiation operations.

An IIR digital filter has, contrary to FIR filters, at least one feed backward coefficient different from zero and its order is equal to:

$$o = \frac{M}{2} - 1 \tag{2.17}$$

where:

M = length of the IIR filter equal to the number of filter's forward a_k and backward b_k coefficients +1 (=p+q+1)

Note that an IIR filter has normally a non-linear phase response and is designed for performing digital integration and/ or low-pass/ high-pass noise removal operations.

It is important to consider that by applying any of these two types of filters, the frequency components of the output signal will be delayed in time. Depending on the type of phase response of the used LTI filter[32], different time delay correction measures can be applied.
In case of linear phase response LTI filters, the output signal would face a time shift equal with half of the order of the applied filter. Hence the following time delay correction algorithm can be applied to correct for this problem:

- Compute the group delay response of the filter via Matlab's *grpdelay* function. If the group delay response is constant, store this constant as K.
- Pad the input signal with K zeros at its end.
- Apply the filter on the zero-padded input signal via Matlab's *filter* function.
- Shift the output signal by K samples. In other words, do not consider the first K samples of the output signal.

In case of a non-linear phase response LTI filter, Matlab's filtfilt can be used as an efficient correcting measure describing a zero-phase digital filtering process, which applies the filter forward and backward on the input signal (x_n), resulting in a zero phase distorted output signal (y_n).
IIR digital filters are generally preferred for analyzing acceleration data, whether one would like to filter out unwanted noise or integrate acceleration into velocity and displacement. Some of the most used IIR low and high-pass filters, designed for removing low and high frequent noise from the acceleration data, are the Butterworth and Elliptical filters.
In case of this experiment a 2^{nd} order Elliptical filter was proposed to be used in the noise removal process. This was done after identifying that this filter type is performing close to the desired low-pass/ high-pass frequency response by having a steep transition band and almost unnoticeable stop and passband ripples.
For an in-depth detailed description of the filter design, choice and application process within the cantilever beam experiment, please refer to appendix E.

[32] in practice Matlab's *grpdelay* function represents a handy tool for checking for the linearity of the phase response.

2.6.2. DIGITAL INTEGRATORS AND DIFFERENTIATORS

NUMERICAL integration and differentiation are indispensable operations that can be both applicable in time and frequency domain within the forward and reverse transformation algorithms, for deriving displacements from acceleration values and vice versa. Therefore, in the next lines a short description of their working principle and of the choice of the ideal integrator and differentiator type for the purpose of this project are be addressed.

Numerical integration of acceleration data is a process that implies division by frequency, causing amplification of any trace of low frequent noise and/ or constant direct current (DC) error in the input data.
An important point to be consider is that the acceleration signal is in general poor at measuring low frequent movements and "does not have a frequency response down to DC"(Brandt [5]). Therefore, one cannot expect to retrieve static but only dynamic displacements from a double integration process.
For further application within the reverse transformation process, the cumulative trapezoidal integration method was chosen. This method can be easily implemented in time domain in Matlab via *cumtrapz* function[33]. A second option would be the application in frequency domain of a cumulative trapezoidal IIR filters/ integrator with linear phase response via Matlab's *filter* function. Additionally, the last plot of figure F.1 in appendix F proves its efficiency by indicating that this type of integrator is falsely determining velocity and displacement values by a factor of only 5% relative error for acceleration signals that are containing a large amount of their energy above 2.5 Hz. Therefore, because most of the major structures have natural frequencies in the range of 1-2.5 Hz this integrator type can be considered a safe solution for SHM applications and therefore also for the cantilever beam, for which a natural frequency in the order of 1 Hz is expected.

On the other hand, numerical differentiation of displacement data is a process that is less prone to errors than integration, making it more attractive for validating GNSS based displacement values. Opposed to digital integration, digital differentiation implies multiplication by frequency in the frequency domain causing amplification of any trace of high frequent noise in the GNSS displacement data.
For this study, a maximum flat FIR differentiator with linear-phase response, known as *Parks-McClellan/Remez differentiator*, is proposed to be used in the forward transformation process. This type of differentiator is a linear-phase FIR filter that is ideally approximating an optimal differentiator and can be designed based on a recursive scheme that is thoroughly discussed in the last part of appendix F. Moreover, in the same appendix a comparison between the proposed differentiator and the most frequently used differentiators is made to prove that the Parks-McClellan/Remez differentiator "behaves better, close to the Nyquist frequency"(Brandt [5]).

It is noteworthy to remember that both the trapezoidal integrator and the Park-McClellan differentiator are IIR respectively FIR filters with linear phase responses, which are producing a constant time delay in the output signal equal with the group delay response of each filter. This should be corrected by following the previously presented time delay correction algorithm and not by the *filtfilt* function solution, which would make the digital integrator and differentiator lose their functionality.
All previously discussed theoretical aspects from subsection 2.6.1 and 2.6.2 form a knowledge basis that are exploited in the next subsection, when introducing the forward and reverse transformation processes.

2.6.3. ACCELEROMETER BASED DISPLACEMENT DATA VALIDATION AND SENSOR FUSION PROCEDURES

AFTER getting to know how to use the primary filtering tools in order to correct for noise that is frequently influencing the accelerometer measurements and perform integration and differentiation operations in frequency domain, the two desired accelerometer based dynamic displacements validation processes can be introduced.
The first process that is simpler and less prone to errors is the forward transformation process and is aiming on deriving acceleration values from GNSS dynamic displacements by means of numerical differentiation. The to-be-followed algorithm of this process is illustrated in figure 2.6 and consists of a double filtration and differentiation procedure.

In this case each of the two digital filtering operations are based on FFT amplitude spectra analyses for defining the optimal cutoff frequencies of the desired high- and low-pass filters. Having the desired filters designed and applied to constrain the energy corresponding to fast, dynamic movements of the cantilever beam, a differentiation operation can be performed twice for deriving the desired velocity and acceleration

[33] this integration method is breaking the area under the acceleration data curve into constant spaced trapezoids, computing their area and cumulatively summing each area result over time.

data sets. Then for validation purposes, the resulting acceleration data set should be compared with the accelerometer based data set.
Despite its ease of implementation, the forward transformation process is not offering any sensor fusion functionality for deriving additional relevant vibration information than what an accelerometer is outputting. This is caused by the fact that GNSS modules are in general performing poor at retrieving fast, dynamic displacements. Therefore, one should use this algorithm only for data validation purposes.

On the other hand, accelerometers can retrieve very well the dynamic displacements of a structure. Therefore, one can use the accelerometer based information to validate enough powerful vibrations that can be sensed by GNSS systems, and/ or to compensate for the lacking capability of the GNSS systems to measure vibrations with small amplitudes. In this context a second and more complex process, also known as the reverse transformation, is introduced below as a measure for deriving beam vibrations from acceleration measurements by means of integration.

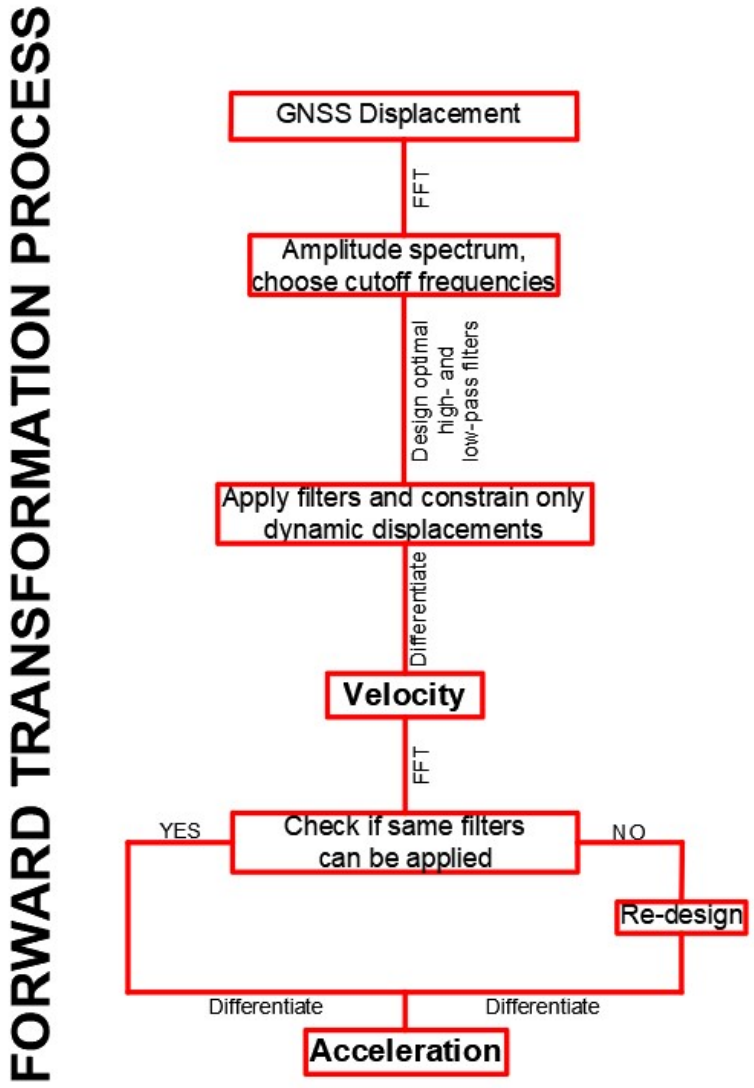

Figure 2.6: Proposed forward transformation process algorithm for deriving acceleration values from GNSS based displacement values

The complexity of this process is caused by the integration process, which amplifies any present low frequent noise in the accelerometer data. In addition, the problem of the unknown velocity and displacement integration constants makes the implementation of this process more complicated. The latter problem can be solved by defining such constants that can be further applied as correction factors on accelerometer based velocity and displacement time series. This can be achieved by taking the mean over a period when the GNSS based velocity and dynamic displacement time series presented no mechanical excitation of the bending beam, forcing the correction factors to reach 0.

The proposed algorithm is illustrated in figure 2.7 and consist of a double filtering and integration procedure. Also, in this case the filtering processes are based on cutoff frequency values derived from the analyses of FFT spectra of the accelerometer based data sets.
In comparison to the forward transformation algorithm, each integration step is followed by:

- a least-squares de-trending process, meant to correct for any amplified remains of low frequency noise, by fitting a trend line through the determined velocity and displacement values followed by a subtraction procedure.
- the implementation of the derived integration constant correction.

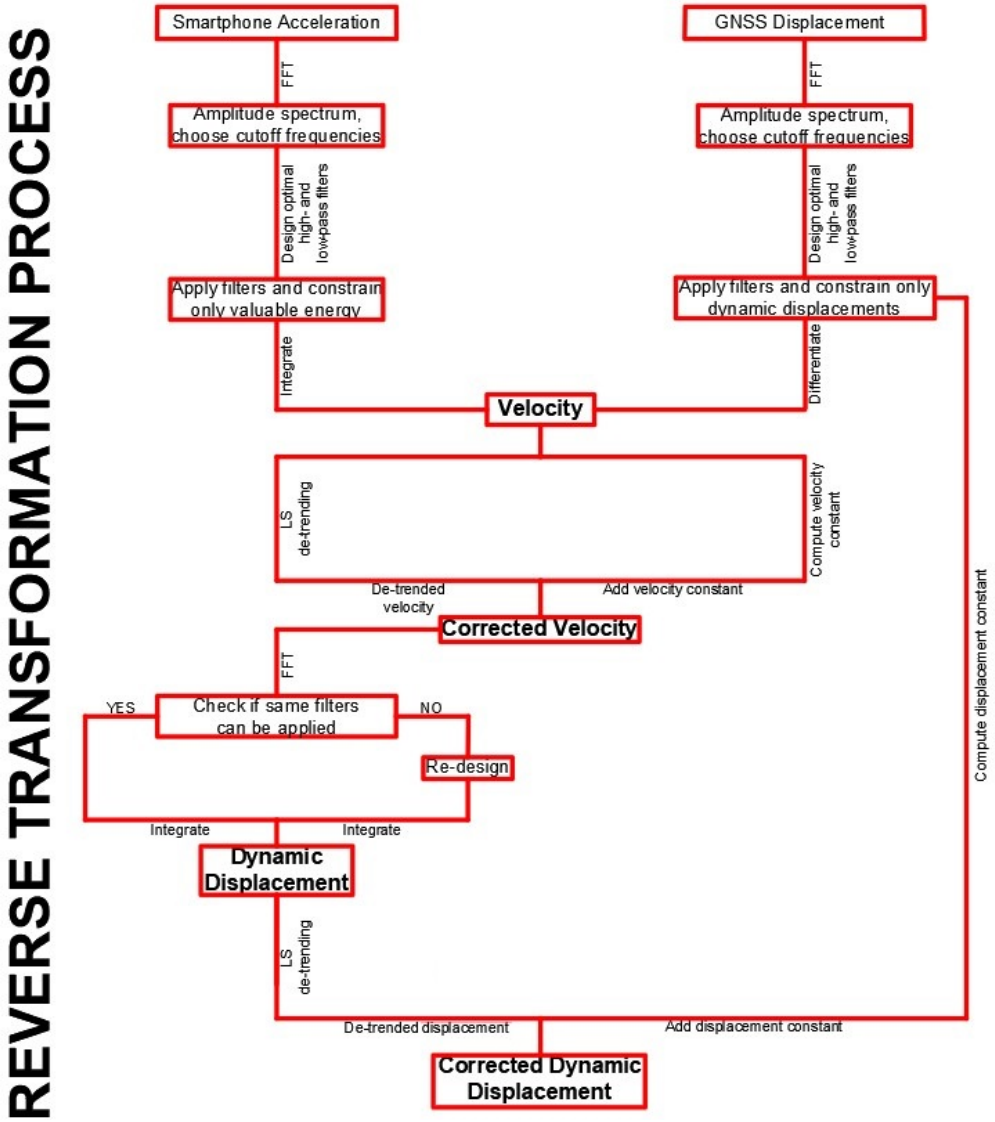

Figure 2.7: Proposed reverse transformation process algorithm for deriving displacement values from acceleration values

In case of enough powerful beam vibrations the resulting dynamic displacement data set derived from accelerometer measurements should be almost identical with the GNSS based dynamic displacement data set. Though, it might be possible to obtain slightly larger accelerometer derived vibration results considering the capability of the accelerometer to record high frequent movements.
On the other hand, when the amplitudes of the beam vibrations are small, the GNSS system will have difficulties in recording them, therefore a larger difference between the accelerometer derived and the GNSS measured vibrations is expected. In such a case, one can use the vibration information derived from the smartphone accelerometer to substitute the GNSS based vibrations. The latter process represents a good example of a sensor fusion process.

2

Chapter Highlights

- Within the proposed SHM experiment a metallic cantilever beam was chosen as case study subject. The wind-induced vibrational behaviour of this structural element resembles very well that of a tall structure.
- The main goal of the proposed cantilever beam experiment was to attest the accuracy capability of a low-cost dual frequency GNSS receiver for monitoring wind-induced displacements of tall, slender structures.
- The cantilever beam experiment was divided in two stages: the artificially induced displacement stage (should mimic static, quasi-static and dynamic displacements of the bending beam) and the wind-induced displacement stage (should resemble the free responses of the bending beam to wind loads in the form of dynamic displacements).
- Three types of sensors were integrated in the SHM sensor network: low-cost dual frequency GNSS modules (displacement detection scope), smartphone accelerometer (validation scope) and laser distometer (validation scope) plus an additional weather station unit and anemometer (validation scope).
- Under 4 Beaufort moderate breezes a beam deflection value of approximately 2.3 centimeters is expected. This value should be treated as an indicative hypothetical value.
  The natural frequency of the first mode of vibration of the cantilever beam should situate in the order of 1 Hz.
- The beam displacement values are derived from pseudorange and CP measurements based on the DD CP relative positioning principle.
- Meteorological data can be used for identifying wind still & windy periods during the SHM process. Moreover, this type of data can be used for identifying any signs of correlation between the wind and the displacement data to prove that winds were the cause of beam deflections.
- Within the cantilever beam experiment, the laser distometer & accelerometer were used for validating the GNSS derived beam displacement values.
  The laser distometer distance measurements can be easily converted in displacement quantities by subtracting them from a true distometer-beam distance value, defined during a stand still period of the beam.
  The accelerometer based validation process is more complex but offers a sensor fusion functionality, being able to measure small-scale beam vibrations. The proposed forward or reverse transformation algorithms can be run for deploying this validation process.

REFERENCES

[1] R. G. Budynas, W. C. Young, and A. Sadegh, *Roark's Formulas for Stress and Strain,* McGrwhill Publication (2002).

[2] H. van der Marel, S. Verhagen, and C. Tiberius, *GPS For Civil Engineering and Geosciences* (Geoscience and Remote Sensing Department, TU Delft, 2019).

[3] P. Teunissen and O. Montenbruck, *Springer Handbook of Global Navigation Satellite Systems* (Springer, 2017).

[4] R. Klees and C. Tiberius, *CIE4260-Measurement and Analysis of Vibrtions: "Digital Filters", Lecture 7* (Geoscience and Remote Sensing Department, TU Delft, 2019).

[5] A. Brandt, *Noise and Vibration Analysis: Signal Analysis and Experimental Procedures* (John Wiley & Sons, 2011).

3

Error Sources of GNSS Modules & Validation Sensors

Error sources are inherent to any measurement process as it is the case with displacement detection processes, such as the proposed cantilever beam experiment.
This chapter summarizes the most relevant errors influencing the laser distometer, smartphone accelerometer and low-cost dual frequency GNSS sensors within the bending beam experiment and defines correction procedures for deriving the most valuable wind response information from the case study subject.
Moreover, the emphasis is set on the multipath (MP) error, described as one of the major sources that influences the GNSS carrier phase measurements. The main scope is to thoroughly explain its defining causes and understand its behavior for deriving a universally valid real time MP mitigation procedure. In this context, two of the most important global navigation satellite systems, GPS and Galileo, are introduced, with the scope of identifying if one can rely on their ground track repeatability cycle for defining such a correction.
Last but not least, two specific MP correction methods are addressed. While the first one is applicable in the measurement domain, namely on carrier phase residuals, the second correction is deployed in position domain, on the estimated relative positions. Their definition and implementation are demonstrated by means of examples run on data acquired during the cantilever beam experiment. Moreover, their advantages and disadvantages are briefly discussed and illustrated in the context of the proposed experiment.

3.1. LIST OF ERRORS & CORRECTION PROCEDURES

EVERY sensor type that is been integrated in the SHM sensor network of the cantilever beam experiment has its own advantages and disadvantages. Within this section, the most likely instrumental and data interpretation errors of the laser distometer, smartphone accelerometer and dual frequency GNSS module are briefly addressed. Correction measures are presented to inform the reader on how to mitigate or eliminate these error types and derive valuable beam displacement quantities.

3.1.1. LASER DISTOMETER ERRORS[1].

AS previously presented in section 1.2, the laser distometer works on the "time of flight" principle, which is prone to dispersion and/ or output sampling period errors. These two error types are briefly introduced in this section together with good practice recommendations for mitigating them.

Minding that the transmitted laser signal of a laser distometer is frequency coherent, this allows the emitted pulse light to get concentrated into a narrow beam. Though, because the transmitted laser signal belongs to the visible domain, clear and uninterrupted line of sight is needed from the instrument to target in order to continuously record valuable range measurements. Therefore, the operator should avoid conducting measurement in dusty, smokey and/ or foggy environments, where the propagation of the laser signal can get easily perturbed.

Moreover, when trying to capture long distances[2] the atmospheric refraction influence should be taken into consideration. It is known that the Earth's atmosphere gets denser closer to the surface and with it also the refractive index (n) of the atmosphere gets larger[3]. Therefore, if a laser distometer pulse travels over a considerable long distance, its trajectory will slowly bend towards the Earth's surface resulting in a longer travel time (τ), hence a longer range measurement ρ. This entire erroneous effect can be accounted in (3.1) through v and τ, which are directly proportional to ρ.

$$\begin{aligned} \rho &= \frac{v\tau}{2} \\ v &= \frac{\lambda}{n} f \; ; \quad n = \frac{c}{v} \end{aligned} \tag{3.1}$$

where:

ρ = measured range [m]
v = propagation speed through the medium [$\frac{m}{s}$]
τ = two-way travel time [s]
$\frac{\lambda}{n}$ = apparent wavelength of the signal [m]
f = signal frequency [Hz]
n = refractive index
c = speed of light in vacuum [$\frac{m}{s^2}$]

Ideally, one should compute the laser range value (ρ) as a summation of range quantities, by inputting precise propagation speed values (v) in the laser ranging equation corresponding to each crossed horizontal atmospheric layer. Though, because this process can be hardly achieved in practice, manufacturers started to implement parameters[4] in modern ranging instruments to reflect the standard atmospheric conditions, giving the users free hand to change them and model the refractive index value.
Note that on average the error due to atmospheric refraction corresponds to a $3 * 10^{-4}$ effect (=300 ppm[5]).
As a good practice it is recommended to not let the laser distometer send pulses close to the ground, where large temperature variations happen that can strongly influence the range measurements. Therefore, "it is recommended to generally keep a ground clearance of at least half a meter for the line of sight"(Reudink and Tiberius [1]). Moreover, laser measurements over considerable large water accumulations (s.a lakes, streams) should be avoided "due to the fact that the refractive index may show strong gradients, leading to a strongly curved line of sight, and hence large ranging errors"(Reudink and Tiberius [1]).
In case of the cantilever beam experiment, the laser distometer was installed only 6.5856 meters away from the cantilever beam on a horizontally leveled tripod, at a height of 1.515 meters above the ground. The laser beam was travelling over a homogeneous land cover type (grass field) over the entire measuring period. Due to the fact that the distometer model was old, one could not introduce any atmospheric parameters. Hence,

[1] most of the theoretical aspects of this subsection were summarized from (Reudink and Tiberius [1]) and (Tiberius *et al.* [2])
[2] distances larger than 100 meters.
[3] if n gets larger, then v gets smaller than c. Therefore one should use v instead of c in the laser ranging equation (3.1).
[4] e.g. p=1013.25 mbar, T=10°C and a relative humidity of 60%.
[5] "hence for a 100 meters distance, the erroneous effect is 3 centimeters"(Reudink and Tiberius [1]

no specific atmospheric correction measure was applied, but all the aforementioned good practice recommendations were taken into consideration.

At this stage it is important to take into account that an ordinary laser distometer is not designed for continuously outputting displacement values but for reliably measure distances.
Thereby, within the laser distometer data set of the AID stage, a sampling period fluctuation error of the output displacements data sets was identified (see figure B.3). As briefly discussed in appendix B.2 the output data sampling interval appeared to fluctuate after the appearance of sudden, large beam displacements. This error is assumed to be caused by some digital filtering function implemented in the used laser distometer with the scope of checking the quality of the measurements by possibly analyzing neighbouring pulse based distance measurements in batches over smaller time windows. The main aim of this quality control function is to not output solutions, if sudden divergences between close-by distance measurements within the considered time window are identified. Through this process, it is believed that the manufacturer tried to eliminate suspicious measurements from being outputted by making the laser distometer wait a while until the distance measurements stabilize.
Unfortunately, no correction measure could be applied for this error type, which was acting like a data acquisition error of the measuring instrument.

3.1.2. ACCELEROMETER ERRORS

As previously addressed in section 2.6.3, the use of acceleration data for SHM is not trivial. Not only because of the elaborate data processing algorithms (see figure 2.6 and 2.7) one needs to follow in order to derive displacement quantities, but also because this type of data is naturally prone to instrumental and environmental and data interpretation errors. Therefore, in the next lines the most influential accelerometer errors are addressed.

- ***Instrumental errors:***
  - ***Instrumental drift*** → is caused by temperature variations, which are effectively causing thermal contraction and dilatation on the accelerometer capacitor, and by the accelerometer's internal components sensitivity.
    Appears as a slow evolving drift effect in the data and can be corrected by least-squares de-trending.
  - ***Constant triggering acceleration error (DC error)*** → it is caused by the wrong initialization of the accelerometer sensor and can be mostly identified as a constant offset from the zero-acceleration present in the acquired acceleration data set. This happens because most accelerometers do not possess a frequency response down to DC/zero-acceleration and start to record only after a specific level of acceleration was exceeded. Therefore, the location of the zero-acceleration is chosen arbitrarily by the accelerometer. When double integrating an acceleration data set with a "very small DC error, it would lead to a velocity error that increases linearly and a displacement error that increases quadratically with time"(Villaverde [3]).
    This type of error can be corrected by a baseline correction procedure, which can be implemented through least-squares de-trending or by "removing the mean from the accelerometer time series"(Brandt [4]). Both correction types do not have a specific physical meaning but can be related to physical assumptions on the monitored case study subject. Moreover, they are working very well in eliminating the aforementioned erroneous offset.
- ***Environmental and Data Interpretation errors:***
  - ***Gravitational component error*** → since smartphone accelerometers measure a quantity that is equal to the summation between the elastic and the gravitational force acting on the point mass, one wishes to eliminate the influence of the gravitational component and remain with a linear acceleration quantity.
    It's been known that the value of acceleration due to gravity on Earth is approximately equal to -9.81 $\frac{m}{s^2}$, hence one could subtract this value from the measured Z-acceleration under the assumption that the smartphone is not tilting and that gravity is acting only on the smartphone's Z plane. Since for most applications this is not holding true, a more suitable solution would be to use auxiliary measured quantities such as orientation angles and angular velocity values to determine the apparent tangential and radial acceleration components(Monteiro *et al.* [5]). Reminding us that during the cantilever beam experiment the accelerometer was placed on top of a vertical

bending beam, that was ideally presenting a constant Z-acceleration value of -9.81 $\frac{m}{s^2}$ in standstill condition, one was expecting reasonably small wind-induced tilt angles, hence also small changes in gravity over time.
Therefore, the most optimal correcting measure is the design and application of a high-pass filter for removing the low frequent influence of gravity from the acceleration measurements.

- ***Instrumental noise and close-by environmental/ background noise*** → most of the accelerometer noise and additional noise coming from close-by perturbators, such as traffic, construction activities or strong wind, can be identified in the high frequent bandwidth region of the accelerometer data.
  This type of noise can be as well filtered out by means of a low-pass filter.
- ***Integration and amplification of low frequent noise*** → when trying to derive velocity and displacement values from acceleration measurements, a double integration process is required. This process implies division by frequency that is amplifying the energy of the measured acceleration at very low frequencies. In such a case the summation of all error sources present in the low frequency bandwidth of the accelerometer data, such as the low frequent gravity effect and the low frequent background noise effect caused by far away processes, will get drastically amplified.
  The most optimal solution for this problem is given by the design and application of a high-pass filter.

Summarizing the aforementioned error sources that are affecting accelerometer measurements, an optimal correction process consisting of least-squares de-trending and digital filtering is desirable. Such correction measures were taken into consideration when designing the proposed reverse transformation algorithm (see figure 2.7).

3.1.3. GNSS ERRORS

THE total GNSS positioning error budget can be defined as a summation of different contributors such as: satellite clock and ephemeris errors, atmospheric errors, receiver noise and clock errors, and multipath(Teunissen and Montenbruck [6]). Therefore, the total error budget can be expressed by the total user equivalent range error (UERE) parameter that can be divided in two parts, the signal-in-space range error (SISRE) and the user equipment error (UEE). The former UERE component "comprises errors such as the broadcast satellite orbit and clock errors"(Teunissen and Montenbruck [6]) while the latter component comprises the user's receiver and environment errors.
Unfortunately, the UERE budget cannot be universally quantified due to the fact that "UEE contributors may differ among individual receivers and sites"(Teunissen and Montenbruck [6]). Though, an indicative value of 0.5 to 6 meters can be linked to it.

In the next lines some of the most influential UERE contributors and their corresponding correction measures are addressed. Priority is given to the error sources that were identified to influence the GNSS data sets acquired during the cantilever beam experiment.

- ***Multipath effect*** → Represents the most important error source that is addressed in this graduation project with the scope of defining a successful real time MP mitigation procedure. In a nutshell, MP can be understood as a phenomenon where satellite signals are acquired via multiple paths due to reflection and diffraction, causing errors in code and CP measurements. The MP effect is fully dependent on the surrounding around the GNSS antenna, the height of the antenna and the satellite elevation angle. Therefore, a universally valid MP correction measure does not exist since this effect has a distinct influence on each GNSS antenna. Though, two possible MP correction methods are proposed.
  The first one is related to the definition of a CP residuals based MP signature pattern spanning over a full sidereal day, which can be subtracted from raw CP residuals, while the second correction method is defined by a sidereal-long relative position estimates MP pattern(Kijewski-Correa and Kochly [7]), which can be subtracted from raw relative positions time series. Both procedures are dependent on constraining satellite geometry partially respectively entirely over each (sidereal) day of the experiment. Within this chapter these corrections will be further detailed in the context of the cantilever beam experiment.
  An alternative correction measure is represented by the identification of the dominant frequency range of MP via FFT analysis and the design and application of a high-pass filter scheme to separate structural displacement quantities from the low frequent behavior of MP ((Moschas and Stiros [8]), (Chan *et al.*

[9])). Due to the fact that this correction is dependent on digital filtering techniques its application in real time is hampered.

- ***Atmospheric delay errors. Troposphere zenith delay and Ionosphere delay*** → both errors drastically influence DD observation over long distances. This is because of the distinctive, constantly varying constituents of the troposhere- and ionosphere layers, causing signal refraction and delay of the GNSS signals on their way through the atmosphere to the reference and rover receivers.
  The zenith troposheric delay can be estimated as an extra hourly unknown parameter in the DD CP relative position estimation process or can be extracted from numerical troposheric delay models while the ionosphere delay can be eliminated by forming ionosphere-free linear combinations out of dual frequency GNSS observations or by using global ionosphere models (Teunissen and Montenbruck [6]).
  In case of the cantilever beam experiment, where short baseline estimation was performed, these errors had the same effect on the GNSS measurements collected by the reference and rover modules. Hence they were eliminated during the DD CP estimation process (see section 2.4 and equation (2.10)).

- ***GNSS antenna phase center (PC) error*** → is an important error source for GNSS differential positioning applications, caused by receiver antennas, especially in case of low-cost GNSS equipment. The PC is an imaginary point where CP signals are received by the GNSS antenna, which varies depending on elevation and azimuth direction of the received CP signal coming from a transmitting satellite. This error source is composed out of two quantities, an average phase center offset (PCO) with respect to the physical antenna reference point, and phase center variations (PCV) produced by the not homogeneous electromagnetic field of the antenna. Its influence is relevant for millimeter precise applications since only the phase variation errors can bias the CP measurements from a few millimeters up to several centimeters, especially in the vertical direction.
  The most common correction measure for this error source is described by a relative antenna calibration procedure (see 1.4.2). A thorough description on the relative antenna calibration procedure can be found in (Mader [10]). This procedure is run to define an antenna characteristic mean PCO, and an elevation and azimuth dependent PCV model, which should be taken into consideration in the relative positioning process.
  It is generally true that within the baseline estimation process the PC errors cancel out, if identical GNSS antennas at both ends of a short baseline are used (Mader [10]). Therefore, identical GNSS equipment was proposed for the cantilever beam experiment.

3.2. MULTIPATH EFFECT. IDENTIFICATION AND MITIGATION

IN this section the concept of multipath is in detail discussed with the aim of theoretically defining this concept and describe its cause of appearance and erroneous behaviour. Moreover, the concept of sidereal day is introduced for questioning on the possibility of defining a MP correction based on the orbit repeat period of the GPS and Galileo constellations. Last but not least, the two previously introduced MP correction measures are in detail discussed based on examples run on the beam experiment data sets.
All discussed concepts are useful aspects for the definition and implementation of a real time MP mitigation procedure in need for future SHM processes.

3.2.1. MULTIPATH EFFECT[6]

MULTIPATH is described as one of the major error sources that influences the GNSS CP measurements. It induces an erroneous effect which is 'leaking' in the relative position and residuals resulting from a DD CP baseline estimation processes. This discussion is meant to define MP and characterize its impact on the accuracy of the obtained CP relative position time series from the cantilever beam experiment, to see if this vicious effect can reach values that can cover the expected beam deflection value of 2.3 centimeters (review section 2.3) and make the identification of wind-induced displacements of the cantilever beam impossible.

Each GNSS antenna acquires satellite signals that travel along different paths through the atmosphere. Depending on the surrounding environment most of the signals get reflected and diffracted and are received latter than direct signals, resulting in inaccurate position estimates. Hence, MP can be understood as this erroneous effect that is affecting the relative position estimates.
In general, most of the GNSS error sources can be mitigated through differential relative positioning carried

[6] some of the presented concepts within this subsection have been discussed in (Lapadat [11]), where a thoroughly discussion on MP was done.

out between close-by GNSS rover- and base stations. But this is not the case of MP, which has a distinct influence for each GNSS antenna depending on the surrounding obstacles, the antenna height (h) and the satellite elevation angle (θ).
In practice, its influence can be modeled by applying some trigonometric formulas that were thoroughly presented in (Lapadat [11]). These formulas are adapted in the following lines for the cantilever beam experiment, corresponding to the general MP model of ground reflected signals, where one is not considering any reflections or diffractions caused by surrounding obstacles. This fits very well with the setup of the cantilever beam experiment (see A.1) where the beam and the rover antenna were placed on a grassy field, far away from any possible obstacles.
For this, firstly the relative delay (δ) of the signal was computed and plotted as a function of the satellite elevation angle (θ) by considering the antenna height (h) to be equal with the height of the cantilever beam above the ground of 1.609 meters.

$$\delta = 2 * h * sin(\theta) \tag{3.2}$$

where:

δ = MP relative delay with respect to the direct line of sight [m]
h = height of GNSS antenna [m]
θ = satellite elevation angle $\epsilon[1:180°]$

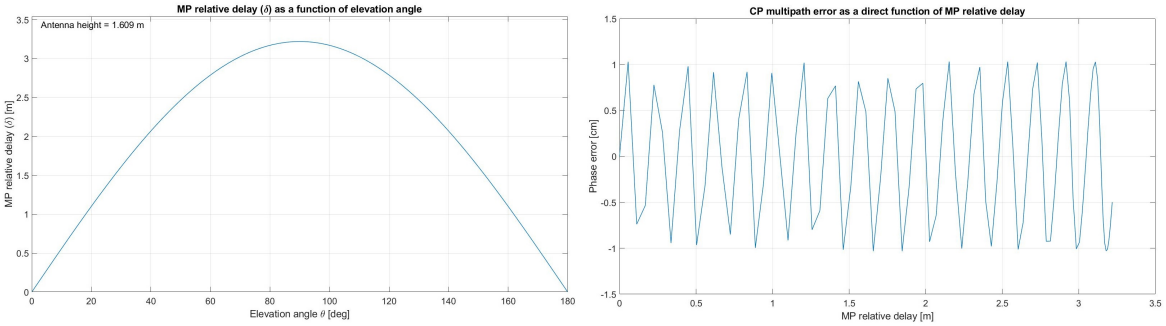

Figure 3.1: MP relative delay as a function of h and θ, for h=1.609 m (left). CP MP error as a function of MP relative delay δ (right). In the computation of the CP MP error ($a1$) was chosen to be equal with the reflection coefficient of 0.334 corresponding to grassy surfaces

The left side of figure 3.1 shows that the largest MP delay happened when the satellite was exactly overhead, while the right side of the same figure points on the repetitive sinusoidal behaviour of MP, which makes it act more like a deterministic time varying bias rather than a random bias.
Right after, the relative delay value was converted to MP relative phase (θ_m) by dividing it by the wavelength of L1 GPS signals[7] and multiplying it by 2π. The resulting angular quantity was used for computing the phase error (θ_c) of the composite received signal[8].

$$\theta_c = arctg(\frac{M_Q}{D + M_i}) = arctg(\frac{\alpha_1 * sin(\theta_m)}{1 + \alpha_1 * cos(\theta_m)}) \tag{3.3}$$

where:

θ_c = CP MP error [rad]
M_Q, M_i = orthogonal MP components (see figure 3.2)
D = satellite direct signal
α_1 = = $\frac{a1}{a0}$ - relative amplitude of the MP[9]
θ_m = MP relative phase [rad]

In the next step, after decomposing the MP vector into its orthogonal components (see figure 3.2) and omitting the influence of pseudorange MP, the resulting angular phase error θ_c was computed on behalf of (3.3). Last but not least θ_c was converted back to metric units. The resulting value, which is corresponding to the CP error induced by MP of a ground reflected L1 signal, was plotted as a function of δ in figure 3.1 at right, reaching its maximum of $\approx$ 1 centimeter. Hence, in case of the cantilever beam experimental setup this erroneous effect can influence the accuracy of the position estimates by 1 centimeter.

[7] λ_{L1}=0.1905 m.
[8] direct + reflected received satellite signal. To be mentioned that the direct signal has no influence on θ_c.
[9] is computed as a ratio between the amplitude ($a1$) of the MP (= reflection coefficient of 0.334 corresponding to grassy field) and the amplitude ($a0$) of the direct signal (= to 1).

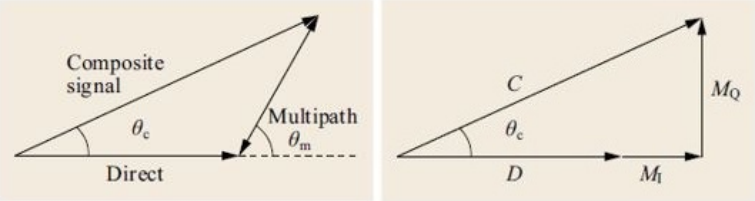

Figure 3.2: Figure of the phase (θ_c) of the composite received signal (left) and the decomposition of the MP vector into orthogonal components (right). Courtesy to (Teunissen and Montenbruck [6], p. 449)

To conclude, 'leakage' of MP effect in the relative position time series of the conducted experiment can cause errors of 1 centimetre. In such a case the MP noise would not completely cover the expected hypothetical deflection value of 2.3 centimetres discussed in section 2.3, but would make it more complicated for the low-cost dual frequency GNSS module installed on top of the bending beam to identify small dynamic displacements. Therefore, a mitigation strategy is strictly necessary to be defined and tested in the proposed experiment. In case of good results, this can be applied for high-accuracy positioning applications such as wind-induced deformation monitoring of tall structures.

3.2.2. USE OF GPS AND GALILEO SATELLITE CONSTELLATIONS FOR MULTIPATH MITIGATION[10]

SINCE nowadays multiple global navigation satellite systems are orbiting the Earth, not only the positioning estimation process can benefit from a combined use of multiple satellite constellation, but also the MP identification and mitigation process. Therefore, within this project the effectiveness of the GPS and Galileo constellations for defining a MP correction procedure is addressed. The choice of these two satellite constellations was made after knowing that the Galileo's E1 and E5 signals are occupying the same frequency with the GPS's L1 and L5 signals without interfering to each other, giving the possibility to a GNSS receiver to use them concurrently and increasing the positioning accuracy[11]. Before starting to discuss about their effectiveness in the MP mitigation process, in the next lines each satellite constellation will be shortly introduced to the reader.

The US Global Positioning System, also know as GPS, was designed by the United States Space Force as a medium Earth orbit (MEO) satellite constellation, known as the first fully operational GNSS. GPS was nominally formed out of 24 satellites, deployed in 6 near-circular and equally spaced orbital planes, ensuring to the users the tracking of at least four satellites from any point on the planet. Its declared scope is to "provide critical positioning capabilities to military, civil, and commercial users around the world"[12]. Currently, the constellation has been updated to 31 operational satellites (Teunissen and Montenbruck [6]) to ensure a better coverage around the world.

Table 3.1: Nominal constellation parameters of GPS & Galileo

↓ Parameters | GNSS →	***GPS***	***Galileo***
Constellation type	24 satellite MEO constellation, 6 equally spaced orbital planes	Walker 24/3/1 + 6 in-orbit spares
Semimajor axis (a) [m]	26560000	29600318
Orbital altitude [m]	20180000	23222182
Inclination [°]	55	56
Orbital Period [hh:mm:ss]	11:58:02	14:04:42
Ground track | Orbit repeat cycle [sidereal days/ revolutions]	1 | 1	10 | 17

On the other hand, the European GNSS, Galileo, was designed by the European Space Agency (ESA) as a Walker (24/3/1) constellation, formed out of 24 active satellites plus other 6 spare ones deployed in three near-circular orbital planes. Its declared scope is to offer precise positioning for a variety of commercial applications such as: geodetic applications, every-day use car and mobile phone positioning, emergency ser-

[10] most of the presented aspects within this subsection were adapted from (Lapadat [11]), where a thorough discussion on MP was done.

[11] in case of the proposed u-blox ZED F9P receiver the E1-B/C Galileo signal corresponds with the L1C/A GPS signal.

[12] https://www.navcen.uscg.gov/pdf/gps/geninfo/2020SPSPerformanceStandardFINAL.pdf

vices, road and railway safety[13]. The current status of Galileo indicates that 22 satellites are fully operational, two others are used for testing purposes and two more are marked as unavailable.
The main GPS and Galileo nominal constellation parameters are summarized in table (3.1).

Both of the to-be-introduced MP corrections depend on the ground track repeat cycle of the considered satellite constellation, which represents the amount of time it takes a satellite to observe the same point on Earth. Strongly related to the ground track repeatability is the fundamental principle behind the definition of desired MP corrections. This reads that if after one ground track repeat cycle the local environment of the receiving GNSS antenna is unchanged and the same satellite shows up at the same position in the sky, one would expect for the stationary receiving antenna to experience the same amount of MP bias affecting the CP and relative position time series. Hence, under the assumption that over the ground track repeat cycle the satellite configuration is kept identical and the GNSS receiver at the ground is stationary, one can define a MP correction from the resulting pattern of the CP residuals and/ or relative position time series.

Before discussing the possibility of deriving an external valid MP correction based on signals coming from the aforementioned satellite constellations, the concepts of mean sidereal and solar days are briefly introduced. Generally, one mean sidereal day[14] is the time it takes the Earth to complete one rotation about its axis with respect to a "fixed" star, while one mean solar day[15] "is the time interval between two consecutive passes of the Sun across the observer's meridian"(Teunissen and Montenbruck [6]). The latter one is approximately 4 minutes longer because of the extra needed rotation of the Earth caused by the orbital revolution about the Sun in order to get the Sun aligned with the observer's meridian. Therefore, one should note that when working in civilian Coordinated Universal Time (UTC) frame , the satellites will reach same position in the sky 4 minutes earlier each day.
Therefore, whether one decides to derive a CP residual or a relative position based MP correction along the UTC time frame, the concept of sidereal day repeatability should be accounted in order to constrain the same geometry of the GNSS satellites over each experimental day. This can be done by following some data processing steps labeled as *the created-sidereal day cut procedure*, which read:

- ***Origin day selection*** → Select an origin day that should be cut to span a full sidereal day: 00:00:00 - 23:56:04.0905. Most of the times this is chosen as the first full day from the data acquisition campaign.
- ***Sidereal day cut of upcoming days*** → For each next day one needs to take into account that it will start at the last time instant of its previous (sidereal) day and should span exactly 23 hours 56 minutes and 4 seconds from that moment on. To do so, one needed to subtract ***3.931825 minutes * number of elapsed days from the origin day*** from the start and end time instant of the origin day to define the timescale of each next (sidereal) day.

From table 3.1 one can identify that the GPS constellation is characterized by an orbital period of approximately 11 hours 58 minutes and 2 seconds, corresponding to one half of a sidereal day, meaning that its satellite ground tracks repeat every sidereal day. Hence under the assumption that the satellite configuration is kept identical, the MP effect of each GPS satellite will repeat every sidereal day at the same time. If so, the sidereal-day patterns described by the GPS based CP residual and/ or relative position time series should overlap (van der Marel [12]).
Moreover, because the ground track repeat cycle of the GPS constellation is at least three times shorter than the duration of the cantilever beam experiment, there is no doubt in using the acquired GPS based CP observations for deriving a MP correction for the acquired data during the cantilever beam experiment.
To support this statement, NORAD Two Line Elements from CelesTrack[16] containing the mean orbital parameters[17] for each operating satellite of any GNSS, were used for obtaining and plotting the on-Earth projected positions of GPS satellite PRN24 during day 077, 078 and 079. Figure 3.3 illustrates a very good alignment between the ground tracks of satellite PRN 24 over the three full days of the cantilever beam experiment.

On the other hand, since the orbital period of the Galileo constellation is larger than one half of a sidereal day, its repeat cycle is exceeding the duration of the beam experiment, being equal to ten sidereal days. Hence, there is no straightforward solution for defining a MP correction from Galileo based relative position time series. Though, in the next lines the ground track repeatability of the Galileo satellite system will be

[13] https://www.gsc-europa.eu/galileo/what-is-galileo
[14] one mean sidereal day corresponds to 23h 56m 04:0905s in solar time (UTC).
[15] one mean solar day corresponds to 24h 03m 56:5554s in sidereal time.
[16] https://celestrak.com/NORAD/elements/table.php?tleFile=gps-ops&title=GPS%20Operational%20Satellites&orbits=32&pointsPerRev=90&frame=1
[17] semi-major axis a, eccentricity e, inclination i, right ascension of ascending node Ω, argument of periapsis ω and true anomaly ν.

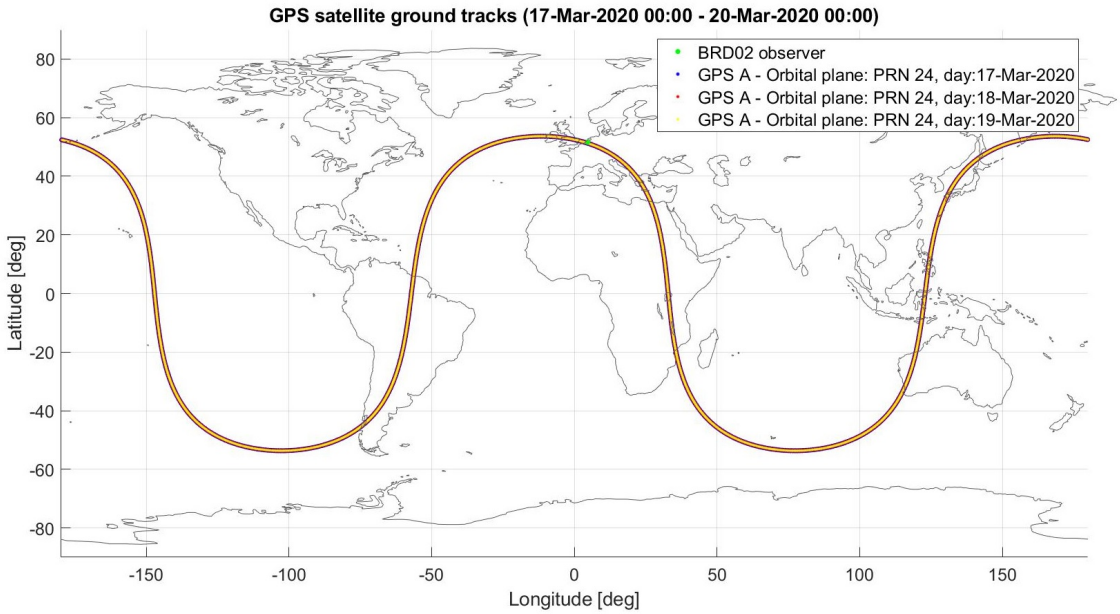

Figure 3.3: Ground track plot of GPS satellite PRN24. PRN24 describes the same ground track over day 077 (blue), 078 (red) and 079 (yellow) of the cantilever beam experiment. This is an indication that the sidereal day repeatability property of the GPS satellites can be used for defining a MP correction

thoroughly analyzed, for identifying any possibility of using it in developing a CP residuals MP correction procedure at satellite level. Such a correction can be distinctively applied on particular satellites at any time instant.

To do so, the identification of a possible ground track repetition between Galileo satellites placed in the same orbital plane is desirable. Therefore, in the next lines calculations based on satellite orbit determination principles are performed to see if any repetition between the ground track of a specific satellite and the ground tracks of its orbital neighbours was happening over the 3 full days of the experiment.

Based on the orbital repeat period value of the Galileo constellation of 14 hours, 4 minutes and 42 seconds[18] one can attest that this value will not correspond to satellite ground tracks that are repeating as quick as the GPS constellation ground tracks[19] do, but only after 10 sidereal days.

Knowing the angular distance between neighbouring satellites in one plane and the constellation repeat period (see appendix G), one can compute the amount of time (tf) it takes for a satellite to reach the position of its neighbouring satellite in the same plane. Concretely, satellite A1 was considered the "origin" satellite of orbital plane A and satellite A8 was the satellite for which tf needed to be determined. From figure G.1 one can clearly see that A8 is positioned with 45° behind A1 on the same orbit. Therefore it will take it:

$$360° \cdots 50682.2102\ sec$$

$$45° \cdots tf\ sec \tag{3.4}$$

$$tf = 6357.776\ sec = 1.76604897\ h = \textbf{1h 45min 57.7763sec}$$

to reach the position of A1 on orbital plane A.

Now "while the satellite is revolving around the Earth also the Earth is rotating beneath the satellite" (Teunissen and Montenbruck [6]) with an angular velocity of $\omega_E \approx 7.292 * 10^{-5} [\frac{rad}{sec}]$ corresponding to a rotation period T_E of:

$$T_E \approx \frac{2\pi}{\omega_E} = \frac{2\pi}{7.292 * 10^{-5}} = 81615.45951\ sec = \textbf{23.93484986 h = 23h 56min 5.4595sec} \tag{3.5}$$

approximately equal to one sidereal day. Therefore, the ground track of satellite A8 will not correspond with the ground track of A1 after 1 hour 45 minutes and 57.7763 seconds.

Remembering that the GPS system is having an ideal orbital repeat period of approximately 11 hours and 58 minutes, reflected in the repetition of its satellite ground track after just two revolutions, one is interested to find if any Galileo satellite from the same orbital plane (in this case plane A) would reach position of satellite A1 after approximately 23 hours 56 minutes and 4 seconds.

[18] a thorough mathematical derivation of Galileo's orbital repeat period can be found in appendix G.

[19] mind that the GPS system is considered a special case having an ideal orbital repeat period of 11 hours and 58 minutes, making possible the repetition of the ground track after just two revolutions.

$$?° \cdots 23.93444444 * 3600\ sec$$

$$45° \cdots 6357.776\ sec$$
$$= \frac{45 * 23.93444444 * 3600}{6357.776} = 609.86° \approx 610° \tag{3.6}$$

Based on the previous calculations, this can happen if one would move over orbit A, from the initial orbital position of A1 satellite, 610° back or forward in time.

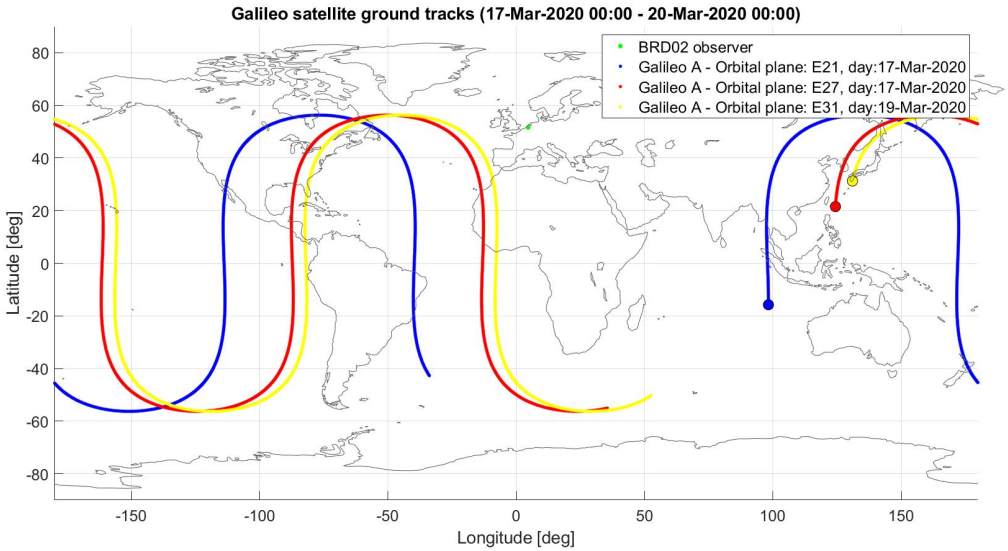

Figure 3.4: Ground track plot of satellites A3 E21 (blue), A4 E27 (red) during day 077 and A1 E31 (yellow). Starting points are marked by filled circles. This plot has the purpose of checking if the ground tracks from both satellites from day 077 get close to the ground track of satellite A1 to validate the previous computations

Minding that the angular distance between consecutive satellites on the same orbital plane is equal to 45°, one may ask if the resulting value of 610° is a multiple of 45° by means of division:

$$\frac{610}{45} = 13.56 \tag{3.7}$$

If that is the case, this will attest that neighbouring satellite from plane A would repeat the same ground track described by satellite A1, before or after 610° angular distance from a particular time instant. The result from (3.7) proves that the Galileo constellation is not designed to repeat the ground tracks between neighbouring satellites from the same orbital plane over time. Therefore, no CP residual based MP correction can be defined and tested based on Galileo measurements over the experimental period.
Though, when counting 13 and a half slots of 45° back from the initial position of A1 on orbital plane A, it was found that the ground track defined by the orbital revolution of satellite A3 or A4, two days before the revolution of satellite A1 should have got close to the A1 satellite ground track on the present day (review figure G.1).
To see if this holds true, NORAD Two Line Elements from CelesTrack were again used for deriving and plotting the on-Earth projected positions of Galileo satellites A3, A4 on day 077 and A1 on day 079. Figure 3.4 proves that the ground track of satellite A4 on day 077 is very close to the ground track of the "origin" satellite A1 on day 079, proving the correctness of the previous made projection.

3.2.3. CARRIER PHASE RESIDUALS BASED MULTIPATH CORRECTION

IN the context of the addressed MP error, the first considered correction within this project is defined based on CP residual values. The generic procedure for defining and applying such a MP correction is introduced in the next lines, followed by an example based on acquired CP data belonging to a specific GPS satellite during the cantilever beam experiment.

In order to introduce this MP correction, firstly a short form of the baseline estimation DD equation (2.10) is considered (see top part of figure 3.8). It is of great importance to observe from this equation how every

DD CP estimate is influenced by the double difference form of the $\varepsilon^{s}_{r,j}(t)$ term, which models the combined effect of the receiver noise and multipath error on CP observations.
Whilst the receiver noise error presents a random behaviour, this does not hold true for MP, which is behaving more like a time varying bias with its mean different from 0 inducing a slow sinusoidal erroneous behaviour in the DD baseline estimation parameters: the relative positions and CP residuals. Consequently a more laborious MP correction needs to be defined.

Considering that the DD CP observations[20] are directly influenced by MP, one can use their corresponding CP residuals, resulting from a GPS-only DD baseline estimation process[21] run in static mode, as a form of MP mitigation. In this context a static DD baseline estimation process was preferred instead of a kinematic process, considering that in such a case the MP effect has less room to 'leak' in the relative position estimates, their number being reduced from 3∗no. of epochs to only 3 unknown values. Thus most of the MP effect will be constrained to propagate within the CP residuals, making the definition of a CP residual based MP correction significant.
Therefore, in order to define and apply such a MP correction procedure, the next steps should be followed:

- ***CP RESIDUALS BASED MP CORRECTION, DEFINITION PROCEDURE:***
  - Choice of calibration day 1, as the first day with full day CP observations coverage.
  - First static DD baseline estimation process for defining the CP residuals time series of the calibration day ($\underline{\hat{e}}_1$) according to the following mathematical model:

$$\underline{y}_1 = Ax_1 + \underline{e}_1 \rightarrow \underline{\hat{x}}_1, \quad \underline{\hat{e}}_1 = \underline{y}_1 - (A\underline{\hat{x}}_1) \tag{3.8}$$

    where:

    $\_$, $\hat{}$ = random vector and estimate notation
    $\underline{y}_1$ = random CP observables of calibration day 1 [m]
    A = design matrix (see equation (2.10))
    x_1 = unknown East (X), North (Y), Up (Z) baseline vector values [m]
    $\underline{\hat{x}}_1$ = estimated East (X), North (Y), Up (Z) baseline vector estimators of calibration day 1 [m]
    $\underline{e}_1$ = random error vector
    $\underline{\hat{e}}_1$ = random CP residuals estimators of the calibration day 1 [m]

  - Application of the first step of the created-sidereal day procedure (see figure 3.8) to define the sidereal-cut (sc) CP residuals time series of the calibration day ($\hat{e}^{sc}_1$), corresponding to the desired MP correction pattern.
  - Definition of the ground-truth baseline distance (μ_1) equal with the only 3 relative position estimates resulting from the static DD baseline estimation process[22] :

$$\mu_1 = \hat{x}^{sc}_1 \tag{3.9}$$

    where:

    μ_1 = ground−truth East (X)/ North (Y)/ Up (Z) baseline distance value corresponding to the calibration day 1 [m]
    $\hat{x}^{sc}_1$ = resulting East (X)/ North (Y)/ Up (Z) relative position estimates of calibration day 1 from the static process

- ***CP RESIDUALS BASED MP CORRECTION, APPLICATION PROCEDURE:***
  - Application of the second step of the created-sidereal day procedure (see figure 3.8) to define the CP observations time series of the succeeding (windy) day(s) (y^{sc}_i).
  - MP correction of the CP observations of the succeeding (windy) day(s) ($y^{sc'}_i$):

$$y^{sc'}_i = y^{sc}_i - \hat{e}^{sc}_1 \tag{3.10}$$

    where:

    i = 2,3..n succeeding (windy) day no.
    $y^{sc'}_i$ = MP corrected CP observations of the succeeding (windy) day(s) [m]
    y^{sc}_i = CP observations of the succeeding (windy) day(s) [m]
    $\hat{e}^{sc}_1$ = sidereal-cut CP residuals time series of the calibration day 1 → CP residuals based MP correction [m]

[20] note that although RNX2RTKP AP returns CP residuals at satellite level, these are DD CP residuals quantities stored in SD format, where for each epoch the DD CP residual value of the reference satellite is accounted with a 0 value.
[21] following the same processing configurations as the one presented in table H.1.
[22] one should take into account that by using RTKLib for processing the GNSS data in static mode, the outputted .pos file will consist of EKF solutions sampled at the same rate with the acquisition rate. Thus, one should consider only the last (=m) East (X)/ North (Y)/ Up (Z) relative position estimates as ground truth baseline values.

– Second baseline estimation process[23] to estimate the desired MP corrected relative position time series of the succeeding (windy) day(s) ($\underline{\hat{x}}_i^{sc}$) :

$$\underline{y}_i^{sc'} = A x_i^{sc} + \underline{e}_i^{sc} \rightarrow \underline{\hat{x}}_i^{sc} \tag{3.11}$$

– Definition of the desired displacement time series of the succeeding (windy) day(s) ($\delta \hat{x}_i^{sc}$) :

$$\delta \hat{x}_i^{sc} = \hat{x}_i^{sc} - \mu_1 \tag{3.12}$$

where:

$\delta \hat{x}_i^{sc}$ = East (X)/ North (Y)/ Up (Z) displacement time series of the considered windy day(s)

The aforementioned procedure is schematically presented on the right hand-side of figure 3.8.

The major advantage of such a correction measure is represented by the fact that the CP residual based MP corrections ($\hat{e}_1^{sc}$) can be applied at satellite level, considering only the satellites that repeat their trajectory on daily basis throughout the examined experimental period. A second advantage for deriving such a correction is its possible direct applicability on raw DD CP measurements, by means of a simple subtraction operation (see (3.10)).
On the other hand, the downside of using such a MP correction is that its implementation in real time is slightly complicated. This is the case, since after defining a CP residuals MP correction pattern, the logged CP observations of the succeeding (windy) days need to be first decompressed from their raw form into RINEX [24] format, corrected for MP at DD level and then reprocessed in near-real time (see (3.11)) to instantaneously derive the desired wind-induced displacements time series.

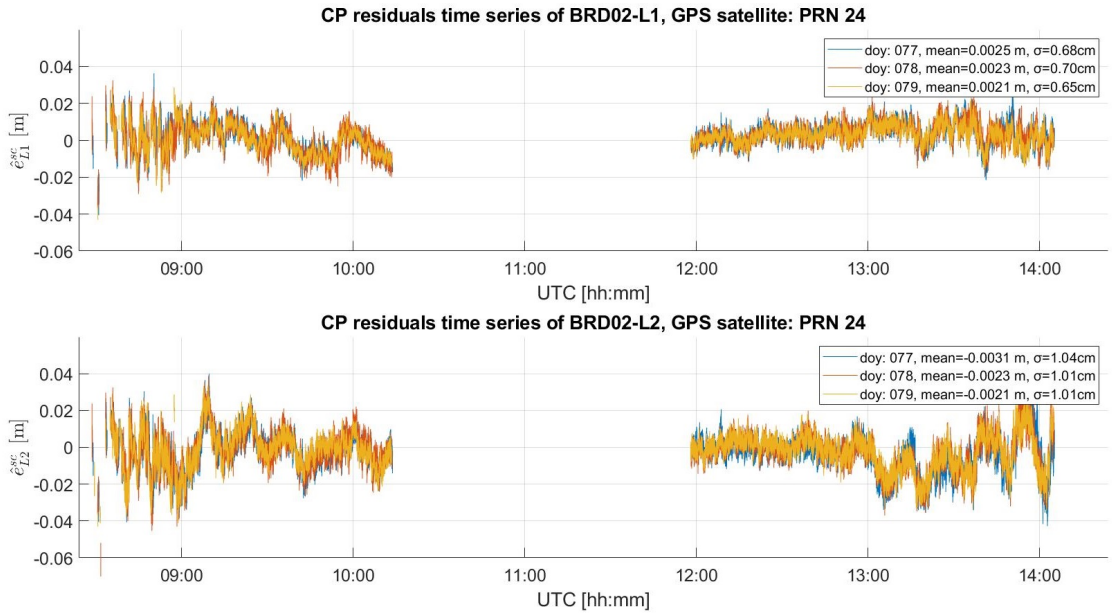

Figure 3.5: Plot of the created-sidereal CP residuals time series of GPS satellite PRN24 over day 077 (blue), 078 (red) and 079 (orange)

Due to the complexity of implementing such a MP correction in real time, only its definition is briefly discussed in the next lines. This is done by presenting an example of the encountered particularities in the definition process of the CP residual based MP correction pattern of satellite PRN24, the same GPS satellite that was used in the previous section to prove the sidereal day repeatability property of the GPS constellation. Hence after choosing day 077 as the calibration day, one would first need to check the sidereal long repeatability of satellite PRN24 over the entire experimental period. This can be achieved by applying the aforementioned created-sidereal cut procedure, to cut the CP residual time series of each day of the experiment with

[23] note that before feeding the MP corrected CP observations ($y_i^{sc'}$) in the second baseline estimation process, it is important to check if any satellite was missing or was deviating from its orbital trajectory throughout the considered experimental day. If so, its measurements should be discarded from the CP relative estimation process.

[24] the Receiver Independent Exchange (RINEX) format is a data interchange format that supports raw GNSS data of all major GNSS constellations (s.a GPS, GLONASS, Galileo, BeiDou, QZSS, IRNSS/NavIC and SBAS).

respect to the calibration day (review figure 3.8).
Note that theoretically within the created-sidereal cut process one should have subtracted 3.931825 minutes[25] but this number caused trouble on keeping the exact same length over the UTC timescale and CP residuals vectors of each day of interest.
Therefore, ***3.933333 minutes***[26] **** number of elapsed days from the origin day*** were subtracted from the start and end time instant of sidereal day 077 to define the timescale of each remaining experimental day. In such a case, generally one needs take into account that after every 10 days, a 1-second correction needs to be accounted to the first and final time stamp of the sidereal day cut.
By this the CP residual time series of day 078 and 079 were aligned against the timescale of the calibration day (see figure 3.5) to prove the sidereal repeatable trajectory of satellite PRN24 over the duration of the cantilever beam experiment.
From figure 3.5, one can see that satellite PRN24 was transmitting CP signals on two frequencies, L1 and L2, which were acquired on daily basis by the GNSS rover from the beam's top, from 8:31:34 until 14:06:57 UTC. The visible CP residuals data gap in the middle part of the previously mentioned time interval is caused by the fact that RNX2RTKP AP was taking advantage of satellite's PRN24 high elevation trajectory to use it as a reference satellite in the DD CP baseline estimation process. This can be concluded from figure 3.6. Moreover,

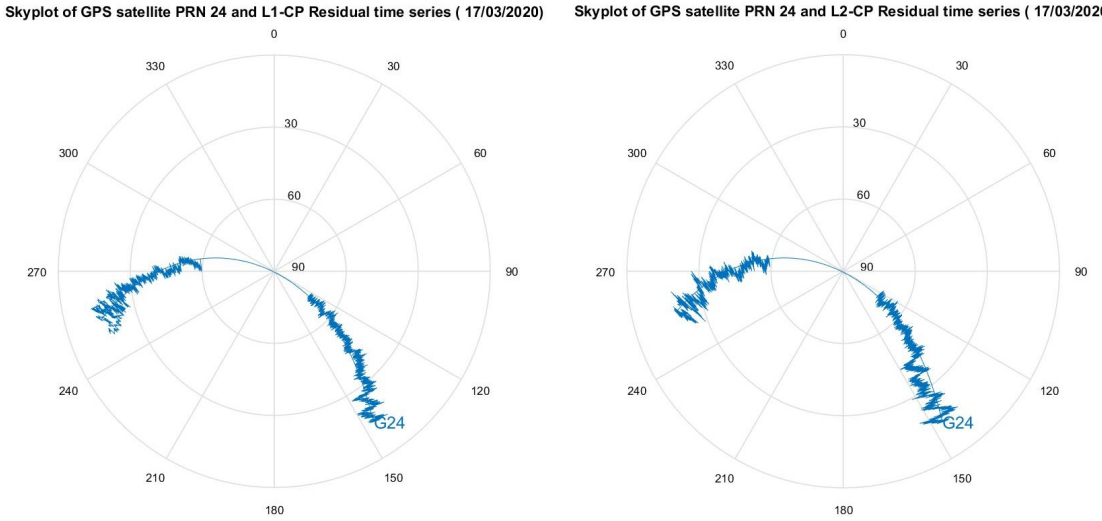

Figure 3.6: Skyplots of satellite PRN24 on day 077. The L1 (left) and L2 (right) CP residuals are plotted on top of the satellite trajectory. This figure shows that the CP residuals gap from figure 3.5 is produced since this satellite was picked as reference satellite in the baseline estimation process, being visible for a long time at a high elevation.

from figure 3.5 it can be concluded that after aligning the CP residual time series with respect to the timescale of day 077, all three CP residual time series were matching very well. To further quantify the similarity between the CP residuals time series of day 078 and 079 with respect to day 077 and test the effectiveness of such a MP correction, the difference between the former two time series and the one corresponding to day 077 were computed and plotted in figure 3.7. The close-to-zero mean values from the plot legends validate the similarity between the derived CP residuals time series, attesting that the satellite PRN24 followed a similar trajectory over the duration of the experiment.
Additionally, the empirical standard deviation values ($\hat{\sigma}_{\delta e_j^{sc}}$) from the plot legends of figure 3.7 indicate a reduction in variability instead of an expected increase by a factor of $\sqrt{2}$, to be found when deriving a-posterior formal standard deviation values ($\sigma_{\delta \hat{e}_j^{sc}}$) as part of the variance propagation law:

$$\sigma_{\delta \hat{e}^{sc}_{i-1,j}} = \sqrt{\hat{\sigma}^2_{\hat{e}^{sc}_{i,j}} + \hat{\sigma}^2_{\hat{e}^{sc}_{1,j}}}$$
$$\sigma_{\delta \hat{e}^{sc}_{078-077,L1}} = 0.98\,cm,\ \sigma_{\delta \hat{e}^{sc}_{078-077,L2}} = 1.45\,cm,\ \sigma_{\delta \hat{e}^{sc}_{079-077,L1}} = 0.88\,cm,\ \sigma_{\delta \hat{e}^{sc}_{079-077,L2}} = 1.45\,cm \tag{3.13}$$

where:

j = GNSS frequency band, L1 & L2
$\sigma_{\delta \hat{e}^{sc}_{i-1,j}}$ = formal standard deviation of the MP corrected CP residuals of the windy day(s) [m]

[25] corresponding to 3 minutes and 55.9095 seconds.
[26] corresponding to 3 minutes and 56 seconds.

Thus, a comparison between the obtained empirical and formal standard deviation values can be considered for attesting the effectiveness of the MP correction. This holds true since the variance propagation law treats the MP effect within the CP residuals quantities as a random error, resulting in overestimated formal standard deviation results ($\sigma_{\delta\hat{e}^{sc}_{i-1,j}}$). On the other hand, the empirical standard deviation values ($\hat{\sigma}_{\delta e^{sc}_{i-1,j}}$) are computed by feeding the MP corrected CP residuals of day 078 and 079 ($\delta\hat{e}^{sc}_{i-1,j}$) in the default expression of the empirical variance resulting in:

$$\hat{\sigma}_{\delta e^{sc}_{078-077,L1}} = 0.48\,cm,\ \hat{\sigma}_{\delta e^{sc}_{078-077,L2}} = 0.54\,cm,\ \hat{\sigma}_{\delta e^{sc}_{079-077,L1}} = 0.65\,cm,\ \hat{\sigma}_{\delta e^{sc}_{079-077,L2}} = 0.76\,cm \tag{3.14}$$

where:

$\hat{\sigma}_{\delta e^{sc}_{j}}$ = empirical standard deviation of the MP corrected CP residuals of the windy day(s) [m]

Since the values from (3.14) are considerably smaller than the expected standard deviation values from (3.13), one can attest that the MP correction was successful. Hence, it can conclude that the CP residual time series of day 077 can be successfully implemented as a correction measure for the MP error present in the L1 and L2 CP measurements of satellite PRN24, collected during the cantilever beam experiment.

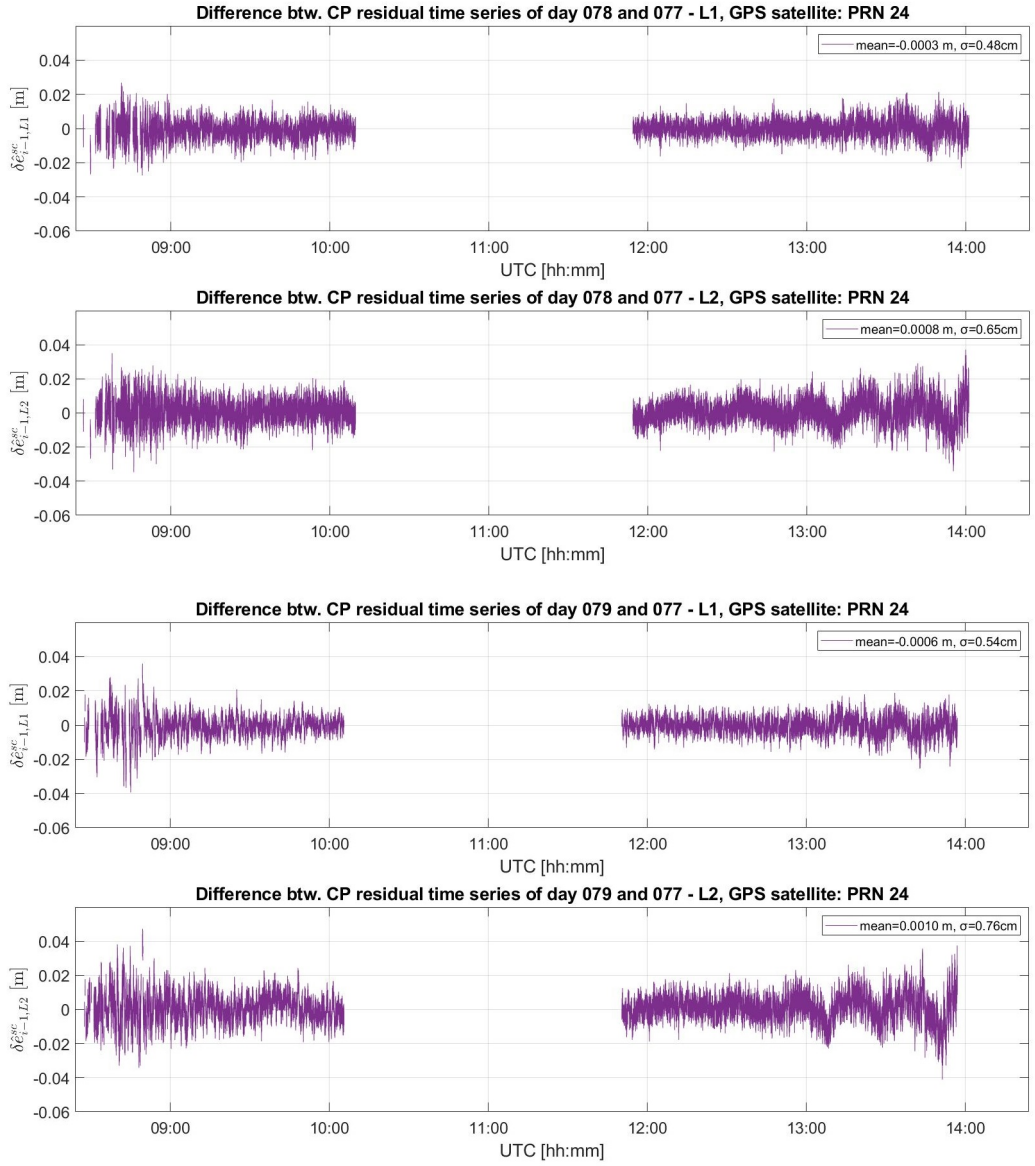

Figure 3.7: Plot of the difference between the created-sidereal CP residuals time series of day 078 (top) and 079 (below) with respect to day 077. This plot illustrates the minor encountered divergences between CP residual time series of the last two days of the experiment and the first one.

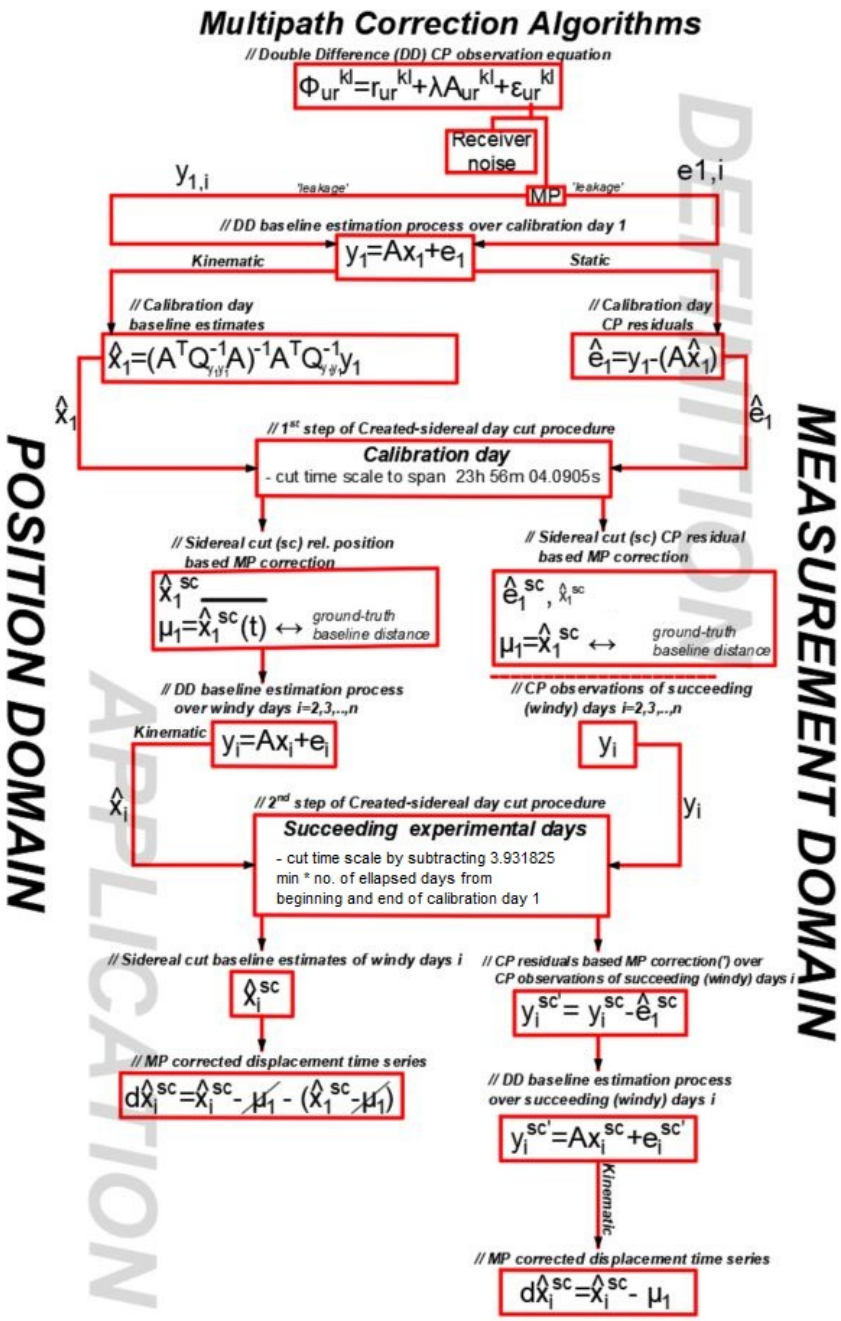

Figure 3.8: Computational flow diagram illustrating the definition and working principle of the two proposed MP correction methods based on relative positions (left wing) and CP residuals (right wing)

3.2.4. RELATIVE POSITION BASED MULTIPATH CORRECTION

LOOKING back at the DD equation from the computational flow diagram of figure 3.8, it is clear that the MP effect is not only 'leaking 'in the CP residuals but also in the relative position estimates, especially in the case of a kinematic baseline estimation process. Thereof, under the assumption that over a full sidereal day the rover antenna was not influenced by any mechanical excitation, a relative position based MP correction pattern/ signature can be derived from the resulting relative position estimates of a GPS-only baseline estimation process run in kinematic mode.

Hence, the second proposed MP correction ($\hat{x}_1^{sc}$) is defined in position domain, aiming to correct for the MP affecting the relative position estimates of a specific rover antenna over successive windy days ($\hat{x}_i^{sc}$) by means of subtraction (review the left-hand side illustration from figure 3.8). Through this subtraction operation, this type of correction can additionally separate and quantify the wind-induced displacements ($\delta\hat{x}_i^{sc}$) (see (3.18)) of the rover GNSS antenna.

Though, when applying such a correction it is mandatory to track the same group of satellites that were iden-

tified during the calibration day, at every time instant of the successive days. This holds true since the MP error is propagating in the relative position estimates as an error produced by a satellites signals assemble acquired at every time instant. Thus if the contribution of one satellite is missing at a specific time instant of the considered day, the MP effect at that moment will differ. In such a case the MP correction samples corresponding to that time instant should be discarded from the displacement detection process and the resulting displacement quantities should be treated with a lower degree of confidence.
In the next lines the general definition and application procedure of a relative position based MP correction ($\hat{x}_1^{sc}$) is stepwise presented. This step-by-step procedure is additionally illustrated on the left hand-side of figure 3.8.

- ***RELATIVE POSITION BASED MP CORRECTION, DEFINITION PROCEDURE:***
  - Choice of calibration day 1 as the first day ,during which the rover antenna was not influenced by any mechanical excitation. The choice should be made after confronting the patterns in the relative position time series of each candidate day with collected meteorological information. Note that the calibration day 1 should effectively model a steady state of the rover antenna.
  - First kinematic DD baseline estimation process for defining the relative position time series of the calibration day ($\hat{x}_1$) according to the following mathematical model:

$$\underline{y}_1 = Ax_1 + \underline{e}_1 \rightarrow \underline{\hat{x}}_1, \quad \underline{\hat{x}}_1 = (A^T Q_{y_1 y_1}^{-1} A)^{-1} A^T Q_{y_1 y_1}^{-1} \underline{y}_1 \tag{3.15}$$

    where:

    $\underline{y}_1$ = random CP observables of calibration day 1 [m]
    A = design matrix (see equation (2.10))
    x_1 = unknown East (X)/ North (Y)/ UP (Z) baseline vector values [m]
    $\underline{\hat{x}}_1$ = random East (X)/ North (Y)/ UP (Z) baseline vector estimators of calibration day 1 [m]
    $\underline{e}_1$ = random error vector
    $Q_{y_1 y_1}$ = variance-covariance matrix of the CP observations [m]

  - Application of the first step of the created-sidereal day procedure (see figure 3.8) to define the sidereal-cut relative position time series of the calibration day ($\hat{x}_1^{sc}$), corresponding to the desired MP correction pattern.
  - Definition of the ground-truth baseline distance value (μ_1)[27] by taking the mean over $\hat{x}_1^{sc}$:

$$\mu_1 = \overline{\hat{x}_1^{sc}(t)} \tag{3.16}$$

    where:

    μ_1 = ground−truth East/ North/ Up baseline distance value corresponding to the calibration day 1 [m]
    $\overline{\hat{x}_1^{sc}(t)}$ = time-wise average over East (X)/ North (Y)/ Up (Z) relative position estimates of the calibration day 1

- ***RELATIVE POSITION BASED MP CORRECTION, APPLICATION PROCEDURE:***
  - Second kinematic DD baseline estimation process for defining the relative position time series of the successive windy day(s) ($\underline{\hat{x}}_i$).

$$\underline{y}_i = Ax_i + \underline{e}_i \rightarrow \underline{\hat{x}}_i, \quad \underline{\hat{x}}_i = (A^T Q_{y_i y_i}^{-1} A)^{-1} A^T Q_{y_i y_i}^{-1} \underline{y}_i \tag{3.17}$$

    where:

    y_i = random CP observables of windy day $i = 2,3..n$ [m]
    x_i = unknown East (X)/ North (Y)/ Up (Z) baseline vector values [m]
    $\hat{x}_i$ = random East (X)/ North (Y)/ Up (Z) baseline vector estimators of windy day $i = 2,3..n$ [m]

  - Application of the second step of the created-sidereal day procedure (see figure 3.8) to define the sidereal-cut relative position time series of the windy day(s) ($\hat{x}_i^{sc}$).
  - MP correction of the relative position estimates of the considered windy day(s) ($\hat{x}_i^{sc}$). Definition of the desired displacement time series of the considered windy day(s) ($\delta\hat{x}_i^{sc}$) :

$$\delta\hat{x}_i^{sc} = \hat{x}_i^{sc} - \cancel{\mu_1} - (\hat{x}_1^{sc} - \cancel{\mu_1}) \tag{3.18}$$

    where:

    $\delta\hat{x}_i^{sc}$ = East (X)/ North (Y)/ Up (Z) displacement time series of the considered windy day(s)

[27] for plotting reasons from this point onward, any relative position time series corresponding to the considered windy day(s) i ($\hat{x}_i^{sc}$) should be centered around 0 by subtracting them by the ground-truth baseline distance (μ_1).

The major advantage of this type of correction in comparison to the previously introduced CP residuals based MP correction, is its more reliable and simple implementation for real time SHM applications. This holds true, since once determined one can instantaneously apply this correction to relative positions resulting from RTK processes, outputted by RTKNAVI.
On the other hand, the downside of such a correction is its full dependency on constraining the same satellite geometry over each day of interest. This can be firstly checked by searching if the same number of satellites was present over the SHM site at every instant over each successive day. In case of the cantilever beam data sets, this first check was satisfied and can be visualized in figure I.1.
A more significant test can be developed by checking on the epoch-wise repeatability of the pseudorandom noise (PRN) code numbers of each visible satellite over each experimental day. The latter testing procedure is in in-depth presented in subsection 5.3 of chapter 5, where the real time implementation of this specific MP correction is thoroughly discussed.

In the next lines two particular cases of the previously listed general MP correction procedure are discussed and compared to identify the best method for effectively mitigating MP from the derived relative position time series of the cantilever beam experiment. In the first proposed procedure the MP corrections of the calibration day are applied straightforward, epoch wise, while in case of the second correction a high order polynomials are first fit through the calibration day MP corrections, followed by their application on successive windy days time series.

- ***EMPIRICAL RELATIVE POSITION BASED MP CORRECTION*** ($\hat{x}_1^{sc}$)**, DEFINITION PROCEDURE:**

The first discussed approach is related to the definition of an empirical relative position based MP correction from raw baseline estimates ($\hat{x}_1$) resulting from a kinematic process, where the BRD02 rover antenna is assumed not to be influenced by any mechanical excitation. Such a model accounts any divergences in the relative position time series to MP.
Hence, based on the derived meteorological information, presented in figure B.4, one can make a first guess on the most appropriate day to be chosen as the calibration day 1. Considering that day 079 was largely presenting North winds with smaller amplitudes than the accounted West winds from day 077 and 078 (review figure B.4) and that the narrow side of the cantilever beam was oriented along the North-South (Y) direction, one was expecting from the bending beam to not effectively respond to wind forces on day 079. Therefore, day 079 can be initially proposed as the calibration day 1, but due to the fact that the meteorological information of the cantilever beam experiment was not describing any completely wind still periods, this choice cannot be not fully attested at this moment. Moreover, it should be accounted that such a choice represents an abnormal situation where a latter day of the experiment is considered as calibration day to be applied on previous days.

Thus an additional step was considered, where an overlapping plot of the zero-centered position time series of each experimental day ($\hat{x}_1^{sc} - \mu_1$ and $\hat{x}_i^{sc} - \mu_i$) was created to validate the made choice. This was done, after considering only the trustful, ambiguity fixed relative position estimates of each experimental day (077, 078, 079), by subtracting each daily relative position time series by their daily mean value (μ_1 and μ_i)[28] to convert them to position time series capable of modeling any position variations at the beam's top.
Note that for the estimation of the desired daily relative positions ($\hat{x}_1$ and $\hat{x}_i$), RNX2RTKP AP was used. A short description of the preferred PPK processing configurations and filtering steps used for selecting only trustful GNSS observations, can be found in appendix H.
In the next step, the previously discussed two-step created-sidereal cut procedure was applied to cut the position time series of each experimental day and align the resulting East (X)/ North (Y)/ UP (Z) position time series of day 078 and 079 with the time scale of day 077, the first day of the experiment offering full day baseline estimates coverage. The resulting plots of overlapping sidereal-cut position time series can be visualized in figure I.2 from appendix I.
By carefully inspecting the first plot from figure I.2, one can clearly identify a very good match between the East (X) position time series of day 077 and day 078. Though, these two time series present major deviations with respect to the East position time series of day 079. This can be related to beam deflections that were happening in the afternoon of day 077 and 078, in accordance with the previous comments on the derived meteorological information. Nevertheless, the remaining North (Y) and Up (Z) position time series (see the middle and bottom plot from figure I.2) show the same behavior over the three experimental days, with the

[28] this assumption is done only for plotting purposes and is reasonable, considering that at this moment of the MP definition process a final conclusion on the choice of the calibration day 1 is not taken.

exception of a short period at the end of day 079 when the Up (Z) position time series largely deviated from the expected pattern.
Based on this visual inspection and interpretation of the acquired WS and WD measurements and the derived sidereal-cut East (X)/ North (Y)/ UP (Z) position time series, one can attest day 079 as the calibration day 1. Thus, its East (X)/ North (Y)/ UP (Z) relative position time series define the desired empirical relative position based MP correction ($\hat{x}_1^{sc} \Rightarrow \hat{x}_{079}^{sc}$) for the GNSS module installed at BRD02.
To illustrate the resulting empirical relative position based MP correction ($\hat{x}_{079}^{sc}$) on each cardinal direction, they were firstly centered around 0 and plotted in yellow in the middle plots of figure I.3, I.4 and I.5. From this plot one should note a short time span at the end of the Up (Z) component time series describing some unexpected, large deviation that hampers its efficiency at correcting for MP on Up (Z) direction.
The demonstrated MP pattern definition process shows the need of making additional adjustments to the generalized MP correction procedure in order to define a physically meaningful MP correction and comply with the deployed cantilever beam experiment.

- ***LEAST-SQUARES POLYNOMIAL BASED MP CORRECTION ($\hat{x}_1^{p,sc}$), DEFINITION PROCESS:***

The second approach is related to the definition of a MP correction by modeling the MP's sinusoidal, low frequent and time varying behaviour through least-squares polynomial fitting. Such a MP correction method can be considered a particular case of the previously introduced empirical relative position based MP correction whose MP correction pattern is described by a best least-squares polynomial fit with the order equal to the number of baseline estimates ($n-1=m$). Thus, in the definition process of the second addressed MP correction, the previously introduced MP correction pattern will be assumed and further modeled by a smoother polynomial fit.
Concretely, a similar definition process with the one introduced in (Kochly [13]) is proposed, where the previously derived MP correction time series, equal with the East (X)/ North (Y)/ UP (Z) relative position estimates of day 079 ($\hat{x}_{079}^{sc}$) needed to be individually broken into 12 two-hour blocks. Then for each block a polynomial least squares fit was performed through an iterative process meant for identifying a reasonable high polynomial order by extending the order from 1 up to a value of 60 ($n-1=1:60$)[29], that will result in an appropriate least-squares fit reducing as much as possible the sum of squared residuals value ($\hat{e}^{pT}\hat{e}^{p}$). The proposed model of the followed iterative process is described below:

$$
\begin{aligned}
&\hat{x}_{079_{m,1}}^{sc} = \boldsymbol{A}_{m,n}^{p}\alpha_{n,1} \rightleftharpoons \hat{x}_{079}^{sc}(t) = \alpha_1 + \alpha_2 dT(t) + \cdots \alpha_n dT(t)^{n-1} \\
&\textbf{for (n-1)=1:60} \mid find\,(n-1) \Rightarrow min(\hat{e}_{m,1}^{p\,T}\hat{e}_{m,1}^{p}) \\
&\begin{cases}
\begin{bmatrix} \hat{x}_{079}^{sc}(1) \\ \cdots \\ \hat{x}_{079}^{sc}(m) \end{bmatrix} = \begin{bmatrix} 1 & \cdots & dT(1)^{n-1} \\ \vdots & \vdots & \vdots \\ 1 & \cdots & dT(m)^{n-1} \end{bmatrix} * \begin{bmatrix} \alpha_1 \\ \vdots \\ \alpha_n \end{bmatrix} \\
\hat{x}_{079_{m,1}}^{p,sc} = \boldsymbol{A}_{m,n}\hat{\alpha}_{n,1} \\
\hat{e}_{m,1}^{p} = \hat{x}_{079_{m,1}}^{sc} - \hat{x}_{079_{m,1}}^{p,sc} \rightleftharpoons \\
\hat{e}^{p}(t) = \hat{x}_{079}^{sc}(t) - (\hat{\alpha}_1 + \hat{\alpha}_2 dT(t) + \cdots + \hat{\alpha}_n dT(t)^{n-1})
\end{cases}
\end{aligned}
\tag{3.19}
$$

where:

m	= no. of E/ N/ U relative position estimates within a 2h block = $2h*3600sec*5Hz = 36000$
n	= no. of unknown polynomial coefficients α
t	= measurement epoch $[1:m]$
$\hat{x}_{079}^{sc}$	= vector of E/ N/ U relative position estimates of day 079 defining the empirical MP correction [m]
$\boldsymbol{A}_{m,n}$	= design matrix defining the least-squares polynomial model
$\alpha_{n,1}$	= vector of unknown polynomial coefficients
$\hat{\alpha}_{n,1}$	= vector of estimated polynomial coefficients
$dT(t)^{n-1}$	= elapsed time: $(T(t)-T(1))*24*3600$ [sec]; T - time measurement expressed in [days,]
$\hat{x}_{079_{m,1}}^{p,sc}$	= vector defining the least-squares polynomial based MP correction [m]
$\hat{e}_{m,1}^{p}$	= vector of estimated least-square residuals, resulting from the least-squares polynomial (p) fit procedure [m]

On behalf of this process, it was found that a 35th order polynomial was on average modeling the best the long-period distortion of MP of rover antenna BRD02 over day 079. After deriving the 12 least-squares polynomial fits for each cardinal direction, these were merged together to form the second proposed relative position based MP correction pattern ($\hat{x}_{079}^{p,sc}$), which is described by the purple curves plotted on top of the yellow empirical MP correction time series from the middle plots of figure I.3, I.4 and I.5.

[29] throughout this identification process, it was found that orders that were larger than 40 were generally producing numerical computation problems in the inversion of the design matrix $A_{m,n}$.

The resulting least-squares based MP correction has the advantage of being a smooth representation of the empirical MP correction, which should approximate its behavior and separate the effect of MP from the random instrumental noise.
Though, because this solution corresponds to a model of a physical quantity described by the relative position estimates of day 079 ($\hat{x}^{sc}_{079}$), one should first quantify by how well the least-squares fit is modeling the empirical MP correction. To do so, along with the least-squares estimation process, statistical testing is desirable. Thus the overall model test (OMT) can be used for verifying the goodness of the fit of the polynomial model with the observations related to the empirical relative position based MP correction. This is done, by computing the test statistics (T_q) of the considered MP observations[30] and comparing it with a the critical value (k_α), extracted from a specific statistical distribution table. Note that under the underlying assumption that the considered MP observations are normally distributed, T_q was considered to follow a χ^2 distribution due to the fact that this type of distribution is characterized by a skewed probability curve, which results in the largest possible displacement detection probability (γ)[31] for a given probability of false alarm (α) (Teunissen [14]). Hence, T_q can be computed by the following equation, which indicates its full dependency on the estimated least-squares residuals ($\hat{e}^p$) and the precision of the MP observations (Q_{yy}) described by the relative position time series of the calibration day 1 ($\hat{x}^{sc}_{079}$):

$$\begin{aligned} T_{(q=m-n)} &= \hat{e}^{p\,T} Q_{yy}^{-1} \hat{e}^p \\ H_0 &: T_{(q=m-n)} \sim \chi^2(m-n,0) \\ Reject\ H_0 &: T_{(q=m-n)} > k_\alpha \end{aligned} \tag{3.20}$$

where:

q	= degrees of freedom
$T_{(q=m-n)}$	= test statistics
k_α	= critical value corresponding to the probability of false alarm α
Q_{yy}	= mxm variance-covariance matrix of the relative position estimates of calibration day 1 ($\hat{x}^{sc}_{079}$) [m^2]
χ^2	= chi-squared distribution

'East MP'	'North MP'	'Up MP'
{'Accept, T_q: 9998.9574 < k_α: 36403.2555' }	{'Accept, T_q: 9791.2206 < k_α: 36405.2678' }	{'Accept, T_q: 8260.9023 < k_α: 36408.2862' }
{'Accept, T_q: 11475.2726 < k_α: 36403.2555'}	{'Accept, T_q: 16931.7271 < k_α: 36407.28' }	{'Accept, T_q: 17037.9645 < k_α: 36407.28' }
{'Accept, T_q: 13010.9657 < k_α: 36403.2555'}	{'Accept, T_q: 12550.9222 < k_α: 36410.2984'}	{'Accept, T_q: 21728.3489 < k_α: 36402.2494'}
{'Accept, T_q: 12475.1304 < k_α: 36405.2678'}	{'Accept, T_q: 28055.8493 < k_α: 36408.2862'}	{'Accept, T_q: 23686.2035 < k_α: 36402.2494'}
{'Accept, T_q: 19596.3688 < k_α: 36403.2555'}	{'Accept, T_q: 26601.3299 < k_α: 36403.2555'}	{'Accept, T_q: 20917.6723 < k_α: 36404.2616'}
{'Accept, T_q: 13922.2324 < k_α: 36403.2555'}	{'Accept, T_q: 16788.7432 < k_α: 36403.2555'}	{'Accept, T_q: 18604.9623 < k_α: 36407.28' }
{'Accept, T_q: 11000.6842 < k_α: 36402.2494'}	{'Accept, T_q: 20522.2364 < k_α: 36402.2494'}	{'Accept, T_q: 11135.5608 < k_α: 36404.2616'}
{'Accept, T_q: 17192.6402 < k_α: 36407.28' }	{'Reject, T_q: 38817.9952 > k_α: 36407.28' }.	{'Accept, T_q: 11067.9387 < k_α: 36407.28' }
{'Accept, T_q: 19779.8506 < k_α: 36406.2739'}	{'Accept, T_q: 22660.1658 < k_α: 36402.2494'}	{'Accept, T_q: 17206.7199 < k_α: 36407.28' }
{'Accept, T_q: 19443.1589 < k_α: 36412.3107'}	{'Accept, T_q: 17041.923 < k_α: 36402.2494' }	{'Accept, T_q: 32029.7654 < k_α: 36402.2494'}
{'Accept, T_q: 17788.9106 < k_α: 36407.28' }	{'Accept, T_q: 19788.8467 < k_α: 36407.28' }	{'Accept, T_q: 17181.1502 < k_α: 36407.28' }
{'Accept, T_q: 15342.9622 < k_α: 35218.9765'}	{'Accept, T_q: 15065.9749 < k_α: 35214.9515'}	{'Accept, T_q: 22642.6846 < k_α: 35214.9515'}

Figure 3.9: OMT results of the least-squares fitted East (X)/ North (Y) /Up (Z) MP correction time series on each block. One single block from the North MP correction got rejected

Note that since the GNSS observations were assumed to be uncorrelated, Q_{yy} was defined as a diagonal mxm matrix consisting of the variance values of the MP observations on the East (X)/ North (Y)/ Up (Z) direction ($\hat{x}^{sc}_{079}$).
These variance values were determined by squaring the approximate East/ North/ Up standard deviation values of ± 0.4, 0.5 and respectively 1 centimeter [32] from the legends of figure I.2 that quantify the instrumental noise level (for more details review subsection 4.4) of the proposed GNSS system straight out of box.
Hence, after performing the least-squares estimation on each block, T_q was computed and compared to k_α, which was extracted from the χ^2 distribution table for a α value of 0.05. The results of the OMT test from figure 3.9 indicate that the least-squares fit can be on average trusted. This holds true since the test failed for a single block, due to the fact that that particular North (Y) block was strongly fragmented by data gaps.

[30] corresponding to East (X)/ North (Y)/ UP (Z) relative position estimates of day 079 ($\hat{x}^{sc}_{079}$).
[31] in such a case the detection power γ is maximized, meaning that there is a large probability of correctly detecting displacements.
[32] the Up $\sigma_{\hat{x}^{sc}_{079}}$ was chosen to be equal to 1 instead of 1.2 centimeters as an approximation of the UP standard deviations of day 077 and 078, which do not describe the short-period deviation found in the time series of day 079.

- ***APPLICATION OF BOTH RELATIVE POSITION BASED MP CORRECTIONS. OUTCOMES COMPARISON***

After the definition of the previously introduced MP corrections ($\hat{x}^{sc}_{079}$ and $\hat{x}^{p,sc}_{079}$), these were individually subtracted from the sidereal-cut position time series of day 078 ($\hat{x}^{sc}_{078}$)[33] to correct for the erroneous effect of MP and separate the wind-induced displacements, forming day's 078 East (X)/ North (Y)/ Up (Z) wind-induced displacements time series ($\delta\hat{x}^{sc}_{078}$). The resulting wind-induced displacements time series[34] are plotted on top of each other and can be visualized in the last plots of figure I.3, I.4 and I.5 from appendix I.
Moreover, the outcomes of day 078, describing the complete definition and application procedure of the previously introduced empirical (red colored) and least-squares polynomial (purple colored) based MP correction processes, are specifically presented in figure I.3, I.4 and I.5 from appendix I.

At this stage, a decision needs to be taken on which correction mitigates the MP more effectively. To do so, three separate analyses were conducted.
Firstly, a visual analysis on the last plots of figure I.3, I.4 and I.5 was performed indicating that the purple wind-induced displacements time series of day 078 were still describing the characteristic time varying behavior of MP, even after correcting for MP. This can be best visualized in the last part of the purple East (X) displacement time series from the last plot of figure I.3, where a clear sinusoidal behaviour is noticeable. This observation can be considered as a first indication that the least-squares based MP correction is less effective at modeling and correcting MP in comparison to the empirical relative position based MP correction.
Secondly, for each correction measure the MP correction efficiency was assessed by comparing the empirical standard deviation values ($\hat{\sigma}_{\delta\hat{x}^{sc}_{078}}$) with the formal standard deviation values ($\sigma_{\delta\hat{x}^{sc}_{078}}$) derived from the variance propagation law. In addition, a percentage MP reduction factor (Kochly [13]) was defined for each relative position based MP correction method, by comparing the standard deviation values of the MP corrected displacement time series ($\hat{\sigma}_{\delta\hat{x}^{sc}_{078}}$) with the standard deviation values of the relative position time series affected by MP ($\hat{\sigma}_{\hat{x}^{sc}_{078}}$). These values were computed based on the following equations:

$$\begin{aligned} \sigma_{\delta\hat{x}^{sc}_{078}} &= \sqrt{\hat{\sigma}^2_{\hat{x}^{sc}_{078}} + \hat{\sigma}^2_{\hat{x}^{sc}_{079}}} \\ MP\ Reduction &= \left(1 - \frac{\hat{\sigma}_{\delta\hat{x}^{sc}_{078}}}{\hat{\sigma}_{\hat{x}^{sc}_{078}}}\right) * 100\ [\%] \end{aligned} \tag{3.21}$$

where:

$\hat{\sigma}_{\delta\hat{x}^{sc}_{078}}$ = empirical standard deviation of the wind-induced displacement time series [m]
$\sigma_{\delta\hat{x}^{sc}_{078}}$ = formal standard deviation of the wind-induced displacement time series [m]

The final results were centralized in table 3.2. From the listed results, one can observe that in case of both relative position based MP correction methods the empirical standard deviation values prove to be smaller than the formal standard deviation values, indicating that both applied MP corrections were effective. Here numbers show that the empirical standard deviation values of the empirical MP correction got reduced on average by 44% in comparison to the formal standard deviations, while in case of the least-squares based MP correction these got reduced by a factor of only 31%. Moreover, when making a comparison between the empirical standard deviations of the two MP corrections only, it is evident that the empirical MP correction produced better results. When looking over the MP reduction factor, the empirical MP correction was again performing better on each cardinal direction, reducing MP by a factor of 10.1, 29 respectively 21.4% in comparison to 8.5, 25.8 respectively 12.9%.
Moreover, assuming that the code and carrier-tracking loops within the used GNSS receiver do not use extremely narrow bandwidths, one was expecting from the tracked GNSS observations to not present significant time correlation patterns. To check if this holds true, one performed a quick noise analysis[35] on a residual time series, resulting from the subtraction of the first two-hour block polynomial fit based East (X) observations from the sequence of the empirical MP pattern based East (X) observations that is spanning over the same period ($\hat{x}^{sc}_{b,079} - \hat{x}^{p,sc}_{b,079}$where $b(\text{lock}) = 1 \in (1, 2..12)$).

[33] as a side note, from this point onward only the data sets from day 078 of each considered SHM sensor will be taken into account for further manipulation and interpretation. This is due to the identified large gap in the WS time series of day 077, which is hampering the use of the first experimental day (see B.4).

[34] the red colored wind-induced displacements time series result from the application of the empirical relative position based MP correction while the purple colored wind-induced displacements time series result from the application of the least-squares based MP correction.

[35] more details on how to perform a noise analysis are discussed in appendix M

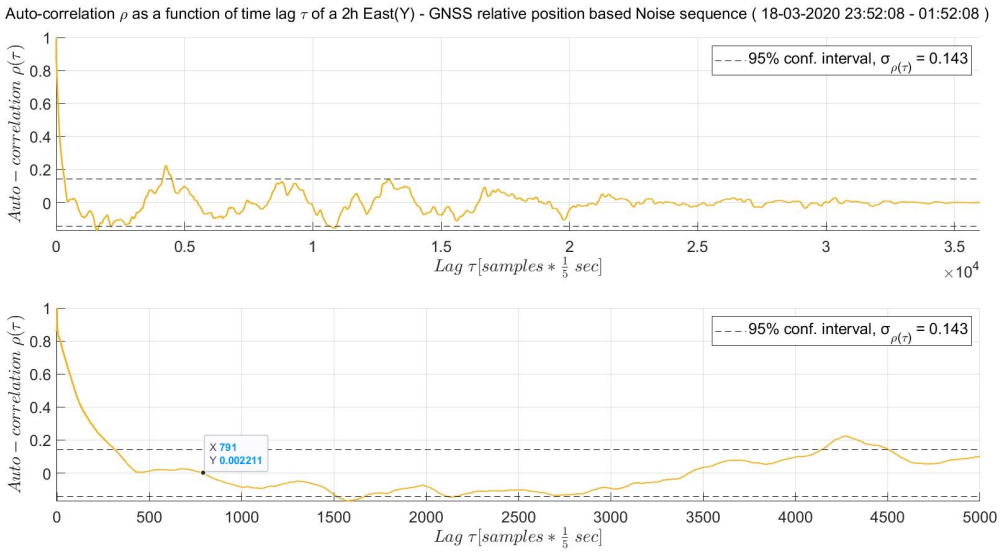

Figure 3.10: Correlogram of the random noise sequence derived from the first (b=1) East (X) MP correction block. Top panel contains the entire auto-correlation sequence. Panel from below contains a zoomed in preview over the first 5000 lags of the auto-correlation sequence. The latter plot indicates the point (sample no. 791) where the time correlation behavior of the GNSS data ends

The resulting auto-correlation sequence from figure 3.10 illustrates an exponential decaying behavior of approximately 3 minutes[36], which is a strong indication of exiting time correlation present in the considered aleatory noise sequence. Since the identified correlation period is unexpected long, one can conclude that the only source of time correlation within the resulting noise signal is residual MP, which was not modeled by the subtracted least-squares based MP correction.
Based on the previously discussed results, it was shown that an empirical relative position based MP correction resulting from raw baseline observations performs much better at reducing MP than a least-squares polynomial based MP correction. Thereby, the East (X)/ North (Y)/ Up (Z) wind-induced displacement time series of day 078 ($\delta\hat{x}^{sc}_{078}$) that were derived based on the relative position based MP correction, are considered for future analyses.

Table 3.2: MP correction efficiency results for the empirical MP correction and the least-squares polynomial based MP correction applied on the East (X)/ North (Y)/ Up (Z) position time series on day 078 at BRD02

Multipath Correction Efficiency, at BRD02, day 078 (18/03/2020)						
Correction type→	***Empirical MP correction***			***LS polynomial***		
↓ Measure	*East (X)*	*North (Y)*	*Up (Z)*	*East (X)*	*North (Y)*	*Up (Z)*
Empirical $\hat{\sigma}$ [cm]	0.35	0.39	0.81	0.36	0.40	0.90
Formal σ [cm]	0.54	0.77	1.56	0.46	0.66	1.37
MP Reduction [%]	10.1	29	21.4	8.5	25.8	12.9

[36] as a result of: (791 samples * 0.2 seconds)/60 seconds.

Chapter Highlights

- Within the cantilever beam experiment instrumental and/or data interpretation errors are inherent in the displacement estimation processes.
- The laser distometer sensor is prone to atmospheric refraction and output sampling period errors. To avoid problems it is advised to install the measuring instrument as close as possible to the case study subject and not let the laser pulses travel to close to the ground and/ or over considerable large water accumulations.
- Accelerometer errors are either related to the instrument itself or induced by the surrounding environment. Most of them can be corrected via least-squares de-trending and/ or digital filtering operations.
- The total GNSS positioning error budget is composed out of a summation of satellite clock & ephemeris errors, atmospheric errors, receiver noise and clock errors and multipath. It cannot be universally quantified since it differs for distinct receivers and sites, though it can produce an erroneous effect of up to 6 meters.
- MP effect is a phenomenon where satellite signals are acquired via multiple paths due to signal reflection and diffraction produced by surrounding obstacles around the rover antenna. For a stationary rover its behaviour is time varying and fully dependent on the satellite geometry.
- Within this experiment a value of $\approx$ 1 centimeter of MP error was estimated. This would not completely cover the expected beam deflection value of 2.3 centimeters but would hamper the displacement detection process.
- Due to GPS's sidereal ground track repeatability, its observations can be used to define a MP correction out of carrier phase and/ or relative position time series.
- On the other hand, in case of the beam experiment practically one cannot rely on Galileo constellation for defining a MP correction, since its ground track repeatability is of 10 sidereal days.
- A CP based MP correction has the advantage of being applicable at satellite level, directly on raw CP measurements, by means of subtraction.
  Due to its more demanding real-time implementation, this correction type is not preferred in this study, for the cantilever beam experiment.
- An empirical relative position based correction is preferred for correcting for MP and defining a real-time correction procedure. To do so, it is mandatory to keep the satellite geometry identical over every experimental day. In comparison to the least-squares based correction that was modelling MP through a polynomial curve fit, this correction was able to reduce MP from the East (X)/ North (Y)/ Up (Z) relative position time series more effectively, by up to 10.1, 29 respectively 21.4%.

REFERENCES

[1] R. Reudink and C. Tiberius, *CTB3310 - Surveying and Mapping:"Land Surveying: Leveling and Tachymetry"* (Geoscience and Remote Sensing Department, TU Delft, 2017).

[2] C. Tiberius, F. van Leijen, and A. Mousivand, *CTB3310/CTB3425-Physical Principles of Remote Sensing: an Introduction* (Geoscience and Remote Sensing Department, TU Delft, 2017).

[3] R. Villaverde, *Fundamental Concepts of Earthquake Engineering* (CRC press, 2009).

[4] A. Brandt, *Noise and Vibration Analysis: Signal Analysis and Experimental Procedures* (John Wiley & Sons, 2011).

[5] M. Monteiro, C. Cabeza, and A. C. Martí, *Acceleration Measurements using Smartphone Sensors: Dealing with the Equivalence Principle,* Revista Brasileira de Ensino de Física **37**, 1303 (2015).

[6] P. Teunissen and O. Montenbruck, *Springer Handbook of Global Navigation Satellite Systems* (Springer, 2017).

[7] T. Kijewski-Correa and M. Kochly, *Monitoring the Wind-induced Response of Tall Buildings: GPS Performance and the Issue of Multipath Effects,* Journal of Wind Engineering and Industrial Aerodynamics **95**, 1176 (2007).

[8] F. Moschas and S. Stiros, *PLL bandwidth and noise in 100 hz GPS measurements,* GPS Solutions **19**, 173 (2015).

[9] W.-S. Chan, Y.-L. Xu, X.-L. Ding, Y.-L. Xiong, and W.-J. Dai, *Assessment of Dynamic Measurement Accuracy of GPS in Three Directions,* Journal of Surveying Engineering **132**, 108 (2006).

[10] G. L. Mader, *GPS Antenna Calibration at the National Geodetic Survey,* GPS Solutions **3**, 50 (1999).

[11] A. Lapadat, *Precise Monitoring of Horizontal Displacement of Large-Scale Structures using Low-Cost Dual Frequency GNSS Receivers,* (2020).

[12] H. van der Marel, *Double Back-flip Corner Reflector GNSS Antenna Test Result,* (2017).

[13] M. C. Kochly, *Validation of Global Positioning Systems for Monitoring Civil Infrastructure Systems: Performance Assessment and Removal of Multipath Effects,* (2006).

[14] P. J. Teunissen, *Testing Theory* (VSSD, 2006).

4

CANTILEVER BEAM EXPERIMENT RESULTS

The purpose of the cantilever beam experiment is to test the capability of the studied low-cost dual frequency GNSS receiver for detecting wind-induced displacements of a flexible structural element in the form of a cantilever beam, that is simulating the response of a tall, slender structure to wind loads. This chapter presents the obtained displacement results from the two stages of the cantilever beam experiment, the artificially-induced and wind-induced displacement stages. With the artificially induced displacements the results of the laser distometer based validation process are enounced to demonstrate the potential of the studied low-cost GNSS module for measuring a wide range of displacements, including slow static and quasi-static but also fast dynamic displacements, in all three orthogonal directions. Then, the capability of the GNSS module to sense wind-induced displacements is questioned by feeding a short, representative sequence of GNSS and smartphone accelerometer observations in the previously introduced forward and reverse transformation algorithms to quest for statistical and visual correlation between the resulting high frequent, dynamic acceleration and displacement quantities of the cantilever beam.
Furthermore, the precision performance and the whiteness of the GNSS and accelerometer measurements is confronted with the declared precision measures of the two sensors. Lastly, all the obtained results are summarized and organized in tabular form and further used to provide an answer to two of the five addressed research questions, related to the accuracy potential of the low-cost dual frequency GNSS module and the usefulness of the smartphone accelerometer within the SHM system.

4.1. ARTIFICIALLY-INDUCED DISPLACEMENT STAGE RESULTS

As previously mentioned in section 2.1, in the first stage of the proposed beam experiment slow static, quasi-static- and fast dynamic displacements with different amplitudes were induced to the cantilever beam in the East-West direction[1] by manually pulling on a rope tightened around it. By this, one was intending to simulate the entire range of structural responses a structure can possibly face in real life.
The induced displacements were recorded on the 16th of March 2020 over a period of only six minutes[2] by the BRD02 GNSS module mounted at the beams top and by the auxiliary validation sensors, the laser distometer and the smartphone accelerometer. It is noteworthy to mention that during this stage, RTKNAVI was launched to acquire code and CP GNSS observations and compute baseline solutions in real time, but more on this topic is addressed in section 5.2 of chapter 5.

In the next lines focus is put on the estimation and presentation of the GNSS based displacements in all three cardinal directions during the AID stage. These should attest the capability of the low-cost dual frequency GNSS system of measuring a wide range of displacements in all three cardinal directions. For this, the acquired GNSS data sets of the rover and base station were first processed in PPK mode, based on the presented processing configurations from appendix H. For this experimental stage not only the GPS observations but also the acquired Galileo and GLONASS observations were fed in the estimation process to output more precise baseline estimates. For the preparation of the data interpretation and visualization, a selection of only trustful (ambiguity fixed) baseline estimates was conducted based on the filtering procedure presented at the end of appendix H. The resulting relative position estimates ($\hat{x}_{076}$) were transformed in displacement quantities ($\delta\hat{x}_{076}$) by subtracting the East (X)/ North (Y)/ Up (Z) ground-truth baseline value (μ_1) from them. Note that μ_1 was computed based on the sliding window procedure from below.

$$
\begin{aligned}
&st = 20 \\
&t = 1 \\
&\mu_1 = \frac{\sum_t^{st} \hat{x}_{076}(t)}{st},\ \sigma_{\mu_1} = \sqrt{\frac{1}{st}\sum_t^{st}(\hat{x}_{076}(t) - \mu_1)^2} \\
&\textbf{while} \quad \sigma_{\mu_1} < [1.5, 1.5, 2.5\ cm] \\
&\begin{cases} t = t + 1 \\ \mu_1 = \frac{\sum_t^{t+st-1} \hat{x}_{076}(t)}{st},\ \sigma_{\mu_1} = \sqrt{\frac{1}{st}\sum_t^{t+st-1}(\hat{x}_{076}(t) - \mu_1)^2} \end{cases}
\end{aligned}
\tag{4.1}
$$

where:

st = window step/ size
t = measurement epoch [1 : m]
μ_1 = East (X)/ North (Y)/ Up (Z) ground-truth baseline distance [m]
σ_{μ_1} = standard deviation of the ground-truth baseline distance [m]

The sliding window procedure from (4.1) was aiming to estimate East (X)/ North (Y)/ Up (Z) mean baseline values with their standard deviation values (σ_{μ_1}) lower than 1.5/1.5/2.5 centimeters[3]. Moreover this procedure is working by computing the average over every 20 baseline estimates[4] and comparing their standard deviation values with the previously addressed critical values, being considered a feasible solution for the identification of the ground-truth baseline length in real time. The resulting ground-truth baseline values are shown in the text labels in the lower part of figure 4.1, and correspond to the true baseline components from the reference antenna to the cantilever beam at rest[5].
Moreover, a last remark on the performed data analysis procedure is related to the need for mirroring the resulting GNSS based East (X) displacements time series for preparing the displacement data to be validated with the distometer based displacement quantities. This validation process is discussed in subsection 4.3.2. This was necessary, considering that the laser beam was oriented in such a way that the X axis of the distometer's coordinate system was pointing to the West, in opposite direction with the X axis of the rover GNSS module (see figure A.2 from appendix A). Hence, one should note that the final GNSS based East (X) displacements solutions of the AID stage correspond to negative values while the West quantities are positive (review right hand side labels from figure 4.1).

[1] corresponding to the weak (X) axis of the cantilever beam (see figure A.2).
[2] from 17:21:30 until 17:27:50 UTC.
[3] critical values assumed to be equal with 3 time the derived horizontal and vertical positioning precision of the GNSS module straight out of the box(see last part of subsection 3.2.4).
[4] corresponding to a period of only 4 seconds at a 5 Hz rate.
[5] under no wind influence.

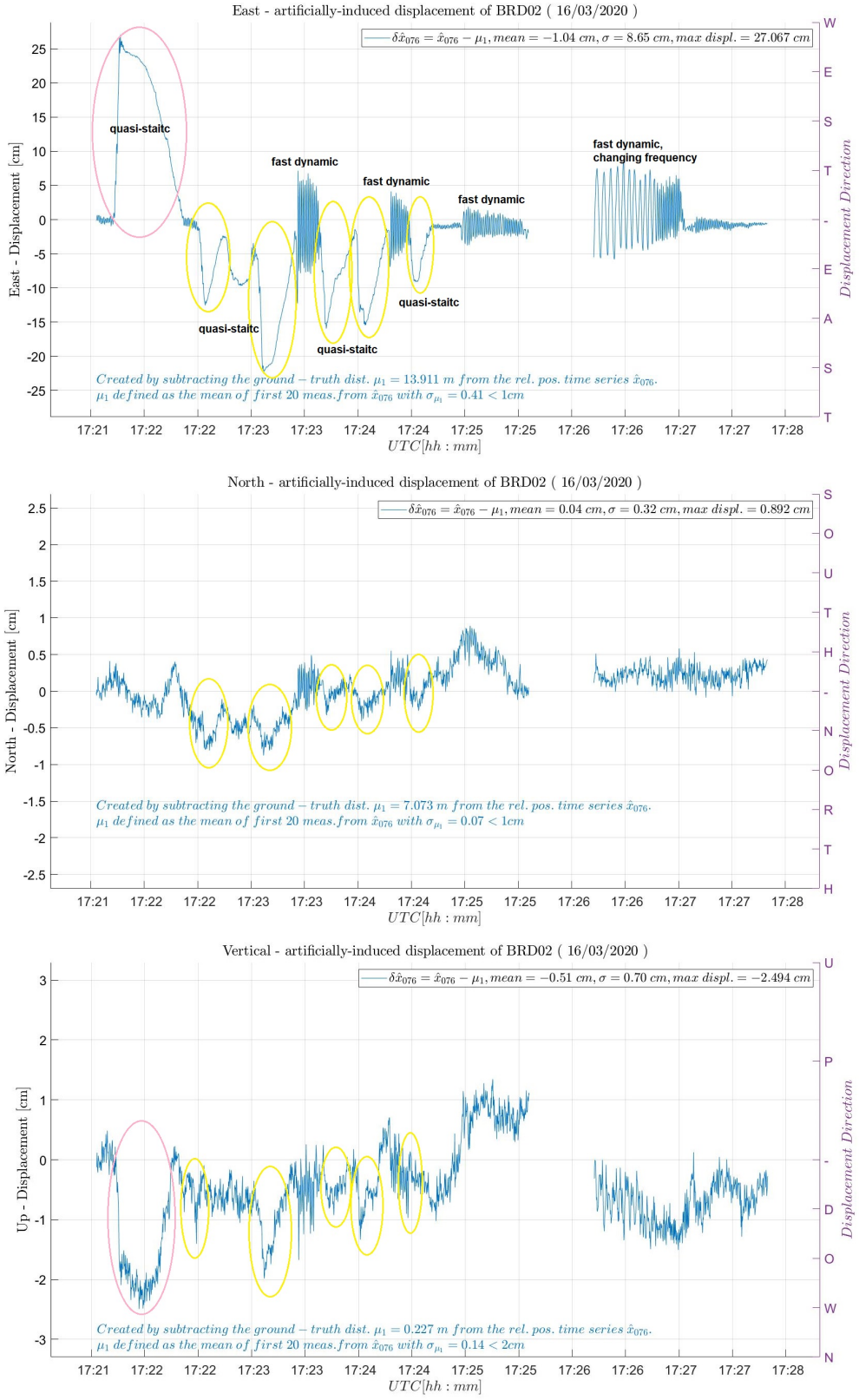

Figure 4.1: GNSS based displacements time series of the AID stage. Identified displacements are marked in pink (maximum displacement) and yellow. The displacement type is labeled in the top plot of the East (X) displacements time series. Plots indicate how the identified displacements happen at the same time in all three cardinal directions

The resulting displacements time series can be visualized in figure 4.1. The reader should take into account that for the determination of these displacements quantities, no relative position based MP correction was applied on the collected GNSS data sets. Hence the obtained displacements results indicate the displacement retention potential capabilities of the GNSS module straight out of the box.
From this figure one can identify a wide range of displacements with different amplitudes and frequencies recorded by the GNSS module during the AID stage. The maximum displacements that were recorded at the beam's top are equal to 27.067, -0.892 and -2.494 centimeters in the West (X), South (Y) and Down (Z) direction. Surprisingly, all identified large enough quasi-static displacements were found to happen at the same time within each displacement time series, being more visible in the East (X) and Up (Z) directions. The latter analogy was anticipated considering that under the man-induced East-West bending effect of the cantilever beam, the top of the beam should have predominately moved in the East (X) and Up (Z) direction.
Part of this behavior can be found also in the first part of the North (Y) displacement time series but this observation is highly subjective due to the fact that most of the displacements values lie in the ± 0.5 centimeter noise band. Thus, the deviations that exceed the limits of this band can be either considered possible North (Y) displacements, random noise effect or deviations caused by MP.
It is important to observe how that from 17:25 UTC onward the behavior of the North (Y) and Up (Z) displacements is completely random and is not visually describing the same displacements behavior as the East (X) displacement time series. It is believed that this was caused by the identified 1-second gaps in the East (X)/ North (Y)/ Up (Z) displacement solutions time series[6], which are related to filtered out float solutions caused by receiver cycle slips.
By considering only the aforementioned visual inspection of the determined displacements time series of the AID stage, one can assume that the low-cost dual frequency GNSS module is capable of sensing low but also high frequent displacements that exceed the declared ± 0.4, 0.5 and respectively 1 centimeter East (X)/ North (Y)/ Up (Z) noise level of the GNSS equipment (for more details review subsection 4.4). In order to attest this assumption a validation procedure is desirable. Thus, in section 4.3 the previously presented results are validated with the laser distometer based displacements data sets.

4.2. WIND-INDUCED DISPLACEMENT STAGE RESULTS

In the next experimental stage, one aimed to test the effectiveness of the low-cost dual frequency GNSS module for measuring beam displacements induced by wind, resembling a scenario that is simulating the response of a tall, slender structure to wind loads. To do so, statistical correlation between meteorological- and displacement information, in the form of orthogonal wind components (U(East)/ V(North)), and East (X) and North (Y) displacements ($\delta\hat{x}_i^{sc}$) derived from the GNSS based relative position estimates, is desirable. Recall that the WID stage covered three full days, where the first two presented favourable West wind patterns that could potentially produce beam displacements. But as enounced in appendix B.3 and D, over these two days wind information could be recorded uninterruptedly only over the second day (day 078). Therefore, due to the identified gap in day's 077 WS data (review figure B.4), a relevant correlation identification example between orthogonal wind components and displacement data sets of day 078 is further considered.

Taking into account that the derived orthogonal wind components and the GNSS based displacements of day 078 were sampled at different rates[7], before calling for statistical correlation between the candidate time series, one needed to follow the recommendation from the last paragraph of subsection 2.5 and make sure that the candidate time series:

- Span exactly the same period.
- Have the same sampling rate.

Therefore, one needed to cut the orthogonal wind components time series of day 078 to start and end at the same time with the GNSS based displacement time series. To do so, a new, every 3-seconds UTC time scale (***t'***), starting with the time instant of the first GNSS measurement and ending with the last one, was created. This was further used for interpolating new orthogonal wind component quantities[8] via nearest neighbour interpolation, resulting in the desired, time aligned orthogonal wind components time series.
Then in the next step, the GNSS based displacement time series needed to be down sampled to a sequences of every 3-seconds displacement quantities. The procedure for doing so, was to average the corresponding

[6] the gaps appear in between 17:25 and 17:26 UTC.
[7] GNSS data was sampled at 5 Hz = 0.25 seconds, while the meteorological data was sampled every 3 seconds.
[8] if the original orthogonal wind components time series contains data gaps, NaN values need to be introduced in the resulting U and V time series at the time instances of the original data gap records.

15 successive displacement quantities[9] from the original GNSS based displacement time series ($\delta\hat{x}^{sc}_{078}(t)$), to form a new GNSS based displacement time series ($\delta\tilde{\hat{x}}^{sc}_{078}(t')$) with the same sampling rate as the interpolated orthogonal wind components time series. Additionally, the empirical standard deviation values of each pair of 15 successive displacement quantities ($\hat{\sigma}_{\delta\tilde{\hat{x}}^{sc}_{078}(t')}$) were computed and stored for latter use of attesting possible wind-induced displacements. The empirical standard deviation quantities were computed considering their capability of describing any divergence (variability) of the cantilever beam from its steady state (mean state) to have happened within 3 seconds long time frames. Thus, one can consider the resulting $\hat{\sigma}_{\delta\tilde{\hat{x}}^{sc}_{078}(t')}$ time series as a valuable tool for validating any identified wind-induced displacements exceeding the noise level band.
All of these are mathematically expressed by (4.2). The resulting aligned and equally sampled orthogonal wind components ($U/V(t')$) – and displacement time series of day 078 ($\delta\tilde{\hat{x}}^{sc}_{078}(t')$) are plotted in figure J.1 and J.2 in appendix J.

$$
\begin{aligned}
&U/V(t') \rightarrow \boldsymbol{t'}\text{: } t'_0,\, t'_1, \cdots t'_{m'} \;\; where\; m' = 1,2\cdots 28722 \;\; and \;\; t'_0 = t_0,\, t'_{m'} = t_m \\
&\delta\hat{x}^{sc}_{078}(t) \rightarrow \boldsymbol{t}\text{: } t_0,\, t_1, \cdots t_m \;\; where\; m = 1,2\cdots 430820 \\
&\textbf{for} \quad st = 1 : m' \\
&\begin{cases}
\delta\tilde{\hat{x}}^{sc}_{078}(t'_i) = \sum_{i=15*(st-1)}^{15*st} \frac{\delta\hat{x}^{sc}_{078}(t_i)}{15} \\
\hat{\sigma}_{\delta\tilde{\hat{x}}^{sc}_{078}(t'_i)} = \sqrt{\frac{1}{15-1}\sum_{i=15*(st-1)}^{15*st}\left(\delta\hat{x}^{sc}_{078}(t_i) - \delta\tilde{\hat{x}}^{sc}_{078}(t')\right)^2}
\end{cases}
\end{aligned}
\tag{4.2}
$$

where:

m'	= no. of observations, sampled at a period of 3-seconds
$U/V(t')$	= every 3-seconds time aligned orthogonal wind components time series
$\boldsymbol{t'}$	= every 3-seconds UTC time scale
$\boldsymbol{t}$	= original UTC time scale of the GNSS observations
$\delta\hat{x}^{sc}_{078}(t)$	= original GNSS based displacement time series sampled at 5Hz
st	= 15 samples step/ counter of the for loop
$\delta\tilde{\hat{x}}^{sc}_{078}(t')$	= down sampled GNSS based displacement time series with a sampling period of 3 seconds
$\hat{\sigma}_{\delta\tilde{\hat{x}}^{sc}_{078}(t')}$	= empirical standard deviation of the down sampled GNSS based displacement time series

Considering the highest wind speed values of West wind recorded during this day and by visually comparing the resulting East (X) displacement - with the U wind components time series (review figure J.1) and respectively the North (Y) displacement - with the V wind components time series (review figure J.2), a strong statistical cross correlation between the first considered pair is expected.
After performing the statistical cross correlation analysis[10], the obtained results from figure 4.2 validate the previously addressed assumption on the identification of a good correlation between the resulting East (X) displacement - and the U wind components time series. Specifically, the first plot from this figure indicates a normalized cross correlation factor between the East (X) displacement - and the U wind components time series ($R_{\delta\tilde{\hat{x}}^{sc}_{078},U(East)}$) of 0.49, and a time lag error of the U wind components time series with respect to the East (X) displacement time series of -4 minutes and 48 seconds.
Despite that the candidate time series model different physical quantities, the obtained result is remarkable proving a moderate correlation between the considered candidate time series over a full (sidereal) day.

On the other hand, as one can see from the last plot of figure 4.2, no correlation could be identified between the North (Y) displacement- and the V wind components time series ($R_{\delta\tilde{\hat{x}}^{sc}_{078},V(North)}$), in concordance with the made assumption and the interpretation of the V components time series of day 078 from the last paragraph of appendix D.

In order to specifically test the wind-induced displacement retention potential of the GNSS module, the same cross correlation analysis can be deployed over a specific time period of day 078 when strong enough wind could have potentially influenced the steady state of the cantilever beam. In this context, the derived U and V wind components information was first used to identify the epochs with the largest recorded wind speed of the U respectively V wind components. The maximum wind speed value of the U components time series was identified around 10:35 UTC to be equal with 6.66 $\frac{m}{s}$, while in case of the V components time series this was identified around 9:10 UTC to be equal with 5.96 $\frac{m}{s}$. Centred around these moments, 40 minutes slices from the down sampled orthogonal wind components- and GNSS based displacement time series were selected as candidate time series for a second cross correlation analysis.

[9] 3 seconds * 5 samples per second.
[10] via Matlab's *xcorr* function.

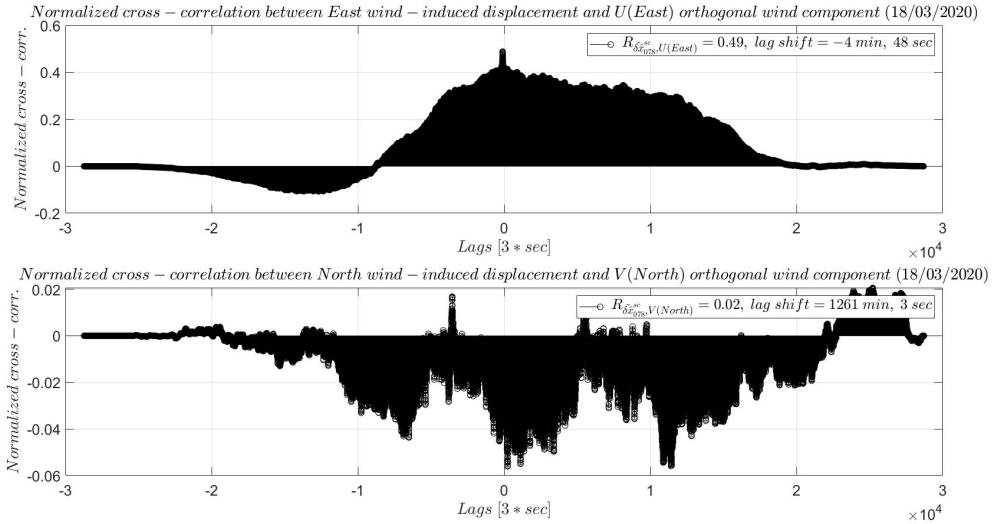

Figure 4.2: Normalized cross-correlation between the East (X) displacement- and U orthogonal wind components ($R_{\tilde{\delta x}^{sc}_{078},U(East)}, top$) and between the North (Y) displacement- and V orthogonal wind components ($R_{\tilde{\delta x}^{sc}_{078},V(North)}, below$). First plot indicates a moderate normalized cross correlation while the plot from below indicated no correlation at all.

Results of the second statistical cross correlation analysis between the selected U wind components- and the East (X) displacement time series, indicate a stronger normalized cross correlation coefficient than before of 0.73, and the same time lag error of -4 minutes and 48 seconds to be applied on the U wind components time series to align it with the East (X) displacement time series. In addition, after shifting the U wind components time series by 4 minutes and 48 seconds back in time, remarkable similarities between the patterns/ spikes described by the two candidate time series are identifiable (see figure 4.3). Therefore, the similar spikes are accounted as wind-induced displacements of the cantilever beam and are highlighted in black in figure 4.3.
Moreover, to better attest the identified divergence of the cantilever beam from its steady state, the previously computed every 3-seconds standard deviation values ($\hat{\sigma}_{\tilde{\delta x}^{sc}_{078}}(t')$) were plotted in faded grey on top of the East (X) displacement time series (review the second plot of figure 4.3). As one can see, their pattern is following very close the pattern of the East (X) displacement time series, giving more confidence that the identified divergences in the East displacement time series are indeed describing wind-induced displacements of the cantilever beam.
At first sight, one can assume that the behaviour of the North (Y) displacement time series pattern (see figure 4.4) is most likely corresponding to remaining MP rather than to beam displacements. Moreover, this interpretation is statistically validated by the resulting normalized cross correlation coefficient of only 0.03. This result is a confirmation that over the cantilever beam experiment the beam was generally not responding in the North (Y) direction.

But one needs to consider that by down sampling the GNSS based displacement time series from 5 Hz to 0.3 Hz[11], one is losing a lot of significant information about the building response to wind loads. Thus, for example the identified maximum East (X) displacement of 1.9 centimeters, resulting from the every 3-seconds averaging process from (4.2), could potentially correspond to a much larger displacement quantity. This is not acceptable for real time SHM applications, especially if one is interested in determining the exact amplitude of high frequent (dynamic) responses of the considered structure. Therefore, ideally one should use a weather station capable to sample at a faster rate than every 3 seconds, to limit as much as possible or even avoid to down sample the original GNSS based displacement time series.
Nevertheless, since this was not the case for the cantilever beam experiment, after validating the identified time lag correction (-4 min and 48 sec) with a large enough normalized cross correlation coefficient (=0.73) and a remarkable match between the every 3-seconds candidate time series on East (X) direction, one can potentially test its feasibility for deriving the true maximum beam displacement by applying it on the raw GNSS based displacement time series. Though, its feasibility can be only visually attested, by looking for any visual correlation between the original GNSS based East (X) displacement- and the U orthogonal wind components time series.

[11] $= \frac{1}{3\,seconds}$

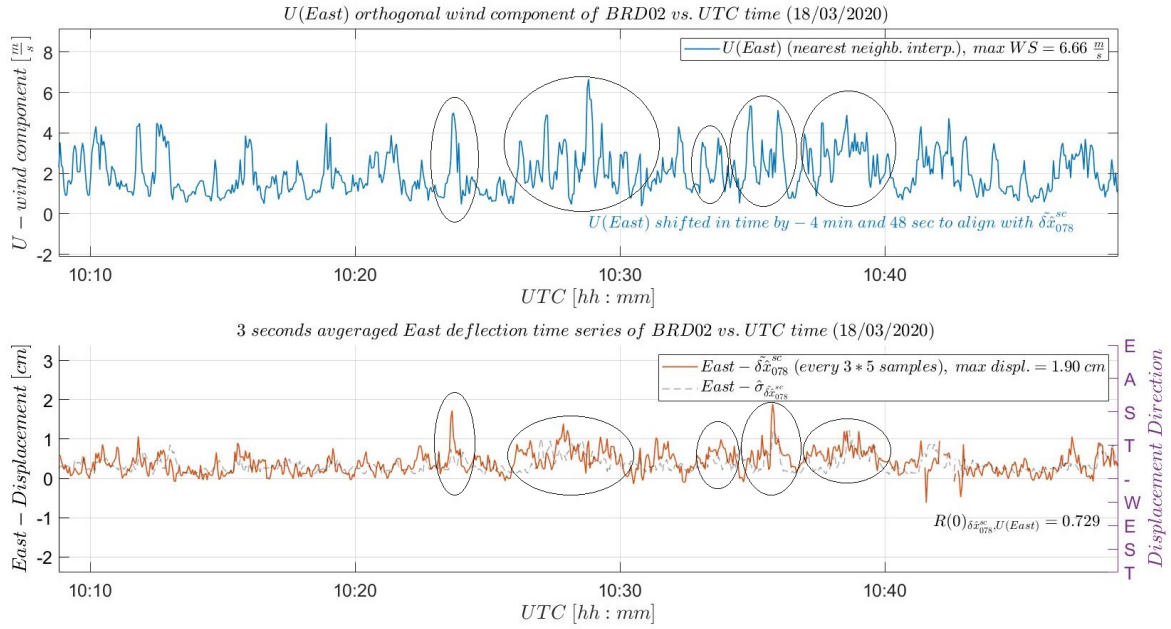

Figure 4.3: Figure of a 40-minutes period of the every 3-seconds U orthogonal wind components- (blue) and GNSS based East (X) displacement time series (red) of day 078, centred at the time stamp when the largest WS of 6.66 $\frac{m}{s}$ in U(East) direction was recorded. Strong visual and statistical correlation ($R(0)_{\tilde{\delta x}^{sc}_{078},U(East)}$ = 0.73) between both time series is found. Identified wind-induced displacements are highlighted in black.

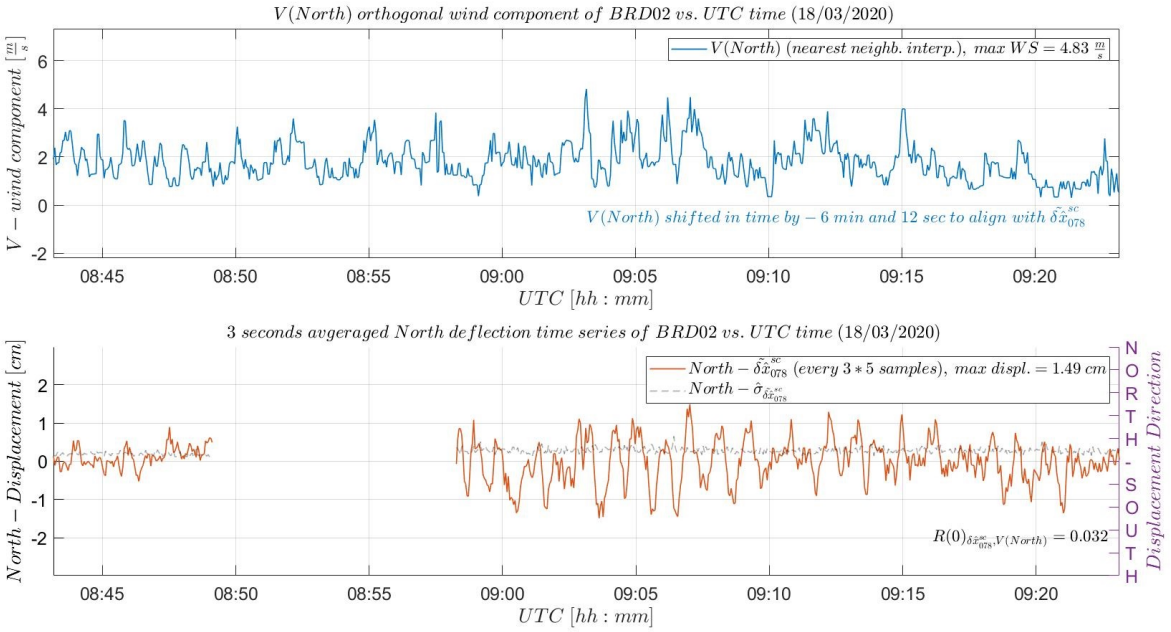

Figure 4.4: Figure of a 40 minutes period of the every 3-seconds V orthogonal wind components- (blue) and GNSS based North (Y) displacement time series (red) of day 078, centred at the time stamp when the largest WS of 5.96 $\frac{m}{s}$ in V(North) direction was recorded. No visual and statistical correlation ($R(0)_{\tilde{\delta x}^{sc}_{078},V(North)}$ = 0.03) between both time series is found. No wind-induced displacements are identifiable.

This visual analysis was performed only on the East (X) direction, being the only direction with identifiable wind-induced beam responses. Additionally, a plot of the displacement time series on Up (Z) direction was considered to check if the identified East (X) beam responses were large enough to make the beam bend towards the ground.
Figure 4.5 shows a remarkable match between the U orthogonal wind components- and the original East (X) displacement time series, after being aligned in time based on the previously derived time lag correction of -4

minutes and 48 seconds. All previously identified beam displacements spikes from figure J.1 could be identified in the middle plot of figure 4.5 again, attesting the wind-induced displacement retention potential of the GNSS module. This conclusion is supported by the good match between the original GNSS based East (X) displacement- and the faded yellow pattern of a standard deviation time series, as a result of a 15-tap moving average window process run on the original GNSS displacement time series.
The maximum identified wind-induced displacement of the cantilever beam is equal to 3.39 centimeters, proving that the expected displacement value of 2.3 centimeters from section 2.3 is under estimating the true response of the cantilever beam under the influence of a 6.7 $\frac{m}{s}$ wind breeze on its 0.03 meter side. However, the last plot from figure 4.5 attests that for such small displacement quantities, that barely reach 3 centimeters, the GNSS module was not able to capture any response of the cantilever beam in the Up (Z) direction.

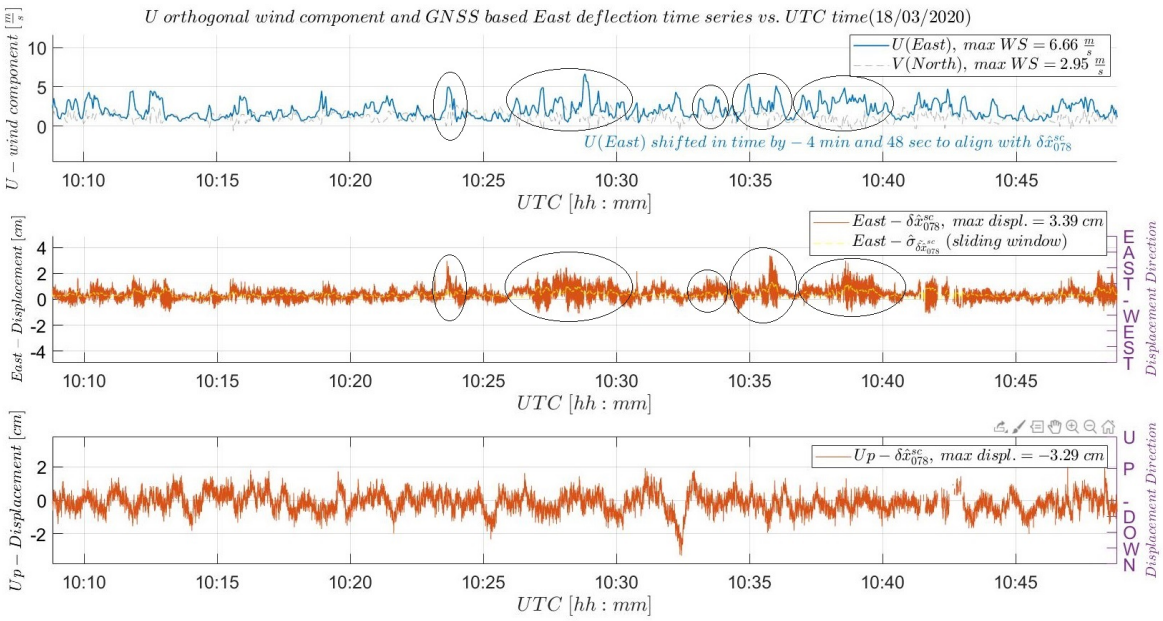

Figure 4.5: Figure of a 40 minutes period of the every 3-seconds U orthogonal wind components- (blue, top) and original GNSS based East (X) (middle) and Up (z) (below) displacement time series sampled at 5 Hz (red) of day 078, centred at the time stamp when the largest WS of 6.66 $\frac{m}{s}$ in U(East) direction was recorded. The U wind components time series was aligned with the East (X) displacement time series by applying a time lag correction of -4 min and 48 sec. Strong visual correlation between both time series is found. Identified wind-induced displacements are highlighted in black. Maximum wind-induced displacement is equal to 3.39 centimeters.

4.3. VALIDATION OF GNSS RESULTS

SINCE all the aforementioned results are derived from the collected data set of the GNSS system, validation is required for attesting the trustfulness of the derived displacement quantities. As being introduced in section 2.1, a laser distometer and a smartphone accelerometer were considered as part of the SHM sensor network of the cantilever beam experiment for facilitating the validation of the GNSS results. Therefore, in the following for each experimental stage one validation example is discussed. Specifically, for the AID stage a validation example on behalf of the laser distometer is presented, while in case of WID stage an example of the implementation of the forward and reverse transformation based on accelerometer data is considered.

4.3.1. VALIDATION OF THE AID STAGE BASED ON THE LASER DISTOMETER

STARTING with the validation of the AID stage results from section 4.1, recall that a laser distometer was installed on a tripod at about 6.586 meters from the cantilever beam to independently sense the displacement quantities of the cantilever beam in the East-West (X) direction. As being presented in section 2.6 the validation procedure follows a set of steps to determine beam displacement quantities from distance measurements.
Thus, after making sure that the laser distometer was horizontally levelled on the tripod and after having the distance measurements over the entire AID stage collected, one needed to derive displacement quantities by

subtracting the ground-truth distometer-to-cantilever beam distance (μ_1^d) of 6.586 meters from the distance measurements. The ground truth distance value was computed based on a sliding window procedure similar with the one from (4.1), with the difference that this time the critical value σ_{μ_1} was chosen to be equal to 0.3 centimeters[12].

After determining the distometer based displacement time series ($\delta\hat{x}_{076}^d$), the very first limitation to be resolved was related to the ***non-uniform sampling rate*** of the laser distometer distance measurements, produced by (likely) some quality control filtering function implemented within the laser distometer with the scope of avoiding to output close divergent distance measurements and stabilize the distance measurement process. Moreover, based on the interpretation from appendix B.2 it is believed that this data quality control function is producing a time lag error that is affecting the distometer based displacement time series. To correct for this time lag error, a cubic interpolation procedure[13] was first performed to bring the laser distometer displacement time series to the same rate (of 5 Hz) with the GNSS sensor displacement data sets over the entire period of the AID stage. Then a statistical correlation analysis was performed to align the up sampled distometer based displacement time series ($\delta\hat{x}_{076}^{d'}$) with respect to the GNSS based displacement time series($\delta\hat{x}_{076}$) based on a time lag correction of -0.4 seconds.

As one can observe from figure 4.6, which is showing a comparison between the GNSS (blue), original and up sampled distometer (brown, red) based East (X) displacement time series over the AID stage, the resulting red colored up sampled distometer based displacement time series is tightly following the brown pattern of the original distometer based displacement time series ($\delta\hat{x}_{076}^d$). In addition, in the lower right part of the same figure, one can observe in the zoom how the distometer based displacement time series was lagging behind, prior to the time lag correction, by 0.4 seconds with respect to the GNSS based displacement time series as a result of the implemented data quality control filtering function of the distometer.

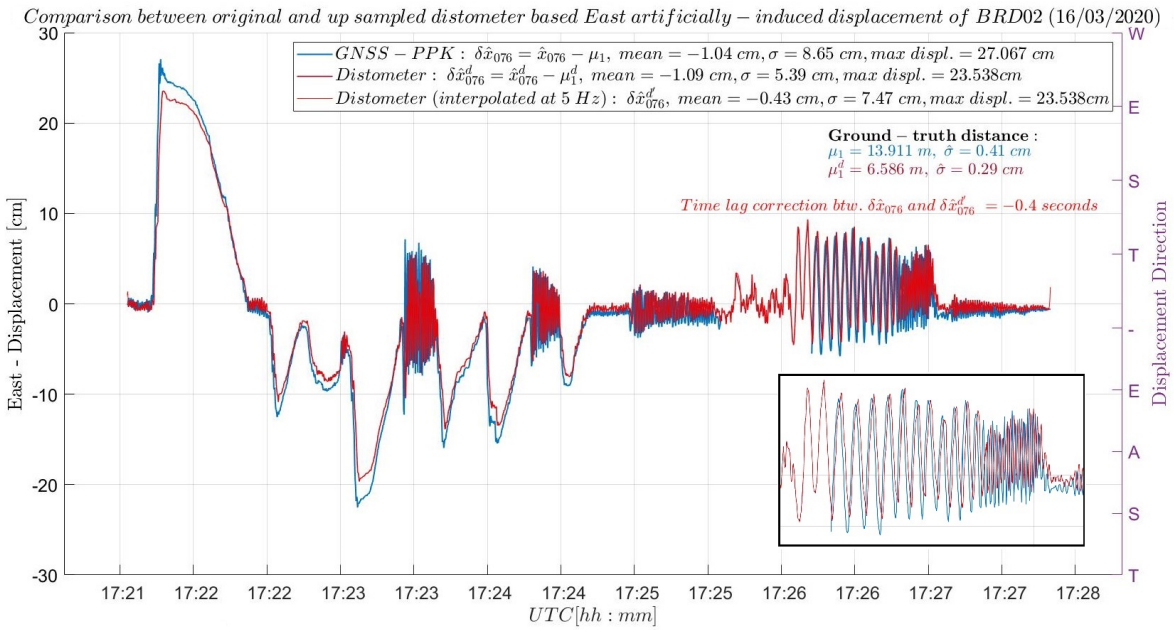

Figure 4.6: Comparison between the GNSS based ($\delta\hat{x}_{076}$, blue), original distometer based- ($\delta\hat{x}_{076}^d$, brown) and up sampled distometer based displacement time series ($\delta\hat{x}_{076}^{d'}$, red). Identified time lag correction between the GNSS based- (blue) and distometer displacement time series of -0.4 seconds

Already from this figure one can observe a very good match between the described behaviour of the GNSS based- and the up sampled distometer based displacement time series. Though, one can notice a difference in scale on the displacement (X) axis between the blue and red colored displacement time series. Recall that this was caused because the laser beam was pointing at 1.515 meters above the ground, about 10 centimeters below the beam's top. Therefore, in order to be able to fully validate the GNSS based displacement time series, a more intricate solution to this scaling error is desirable. Hence, an extrapolation of the laser distometer based displacement quantities, for bringing them as close as possible to the GNSS based displacements, is

[12] equal 2 times the declared precision of the laser distometer of 1.5 millimeters.
[13] via interp1 Matlab function.

considered. In this context, two extrapolation processes (see figure 4.7) were proposed and tested for identifying the most optimal solution. These two extrapolation processes are based on a:

- ***Linear trend model*** → assuming as an approximation that the beam is a rigid straight object, this model is considering that the deflection quantities ($\delta\hat{x}_{076}^{ltm}$) over the 10 centimeters offset can be modelled by a linear trend, from the geometrical point of the laser beam measurements (l) to the beam's top (L) (see figure 4.7). This can be expressed by the following formulas:

$$\begin{aligned} y &= mx+n \\ \delta\hat{x}_{076}^{ltm}(t) &= m(t)L+n(t) \end{aligned} \tag{4.3}$$

where:

$\delta\hat{x}_{076}^{ltm}(t)$ = cantilever beam displacements, extrapolated at the beam's top based on a linear trend model
m = $\frac{\delta\hat{x}_{076}^{d'}(t)}{l}$, linear slope computed based on the distometer based displacement quantities
$\delta\hat{x}_{076}^{d'}(t)$ = up sampled distometer based displacement time series [m]
L = 1.609 [m], cantilever beam height
l = 1.515 [m], height at which laser beam is pointing [m]
n(t) = 0(t), intercept

- ***Quadratic function model*** → this is considering that the deflection quantities ($\delta\hat{x}_{076}^{qfm}$) over the considered 10 centimeters offset can be modelled by a parabola, from the geometrical point of the laser beam measurements to the beam's top. This can be expressed by the following formulas:

$$\begin{aligned} y &= ax^2+bx+c \\ \delta\hat{x}_{076}^{qfm}(t) &= a(t)L^2+b(t)L+c(t) \\ a &= \frac{x_A*(y_C-y_B)+x_B*(y_A-y_C)+x_C*(y_B-y_A)}{(x_A-x_B)+(x_A-x_C)*(x_B-x_C)}\,,\; b=\frac{y_B-y_A}{x_B-x_A}-a*(x_A+x_B)\,, \\ c &= y_A-ax_A^2-bx_A \\ sh(t) &= \sqrt{l^2+\delta\hat{x}_{076}^{d'}(t)} \\ x_A(t) &= -sh(t),\; y_A(t)=\delta\hat{x}_{076}^{d'}(t);\; x_B(t)=0,\; y_B=0;\; x_C(t)=sh(t),\; y_C(t)=\delta\hat{x}_{076}^{d'}(t) \end{aligned} \tag{4.4}$$

where:

$\delta\hat{x}_{076}^{qfm}(t)$ = cantilever beam displacements, extrapolated at the beam's top based on a quadratic function model
$a(t), b(t), c(t)$ = parabola variables as a function of time
$x_{A,B,C}, y_{A,B,C}$ = Cartesian coordinates of the 3 points defining the parabola
L = 1.609 [m], cantilever beam height
l = 1.515 [m], height at which laser beam is pointing [m]
$sh(t)$ = slant height of the cantilever beam while bending at which the laser distometer is recording

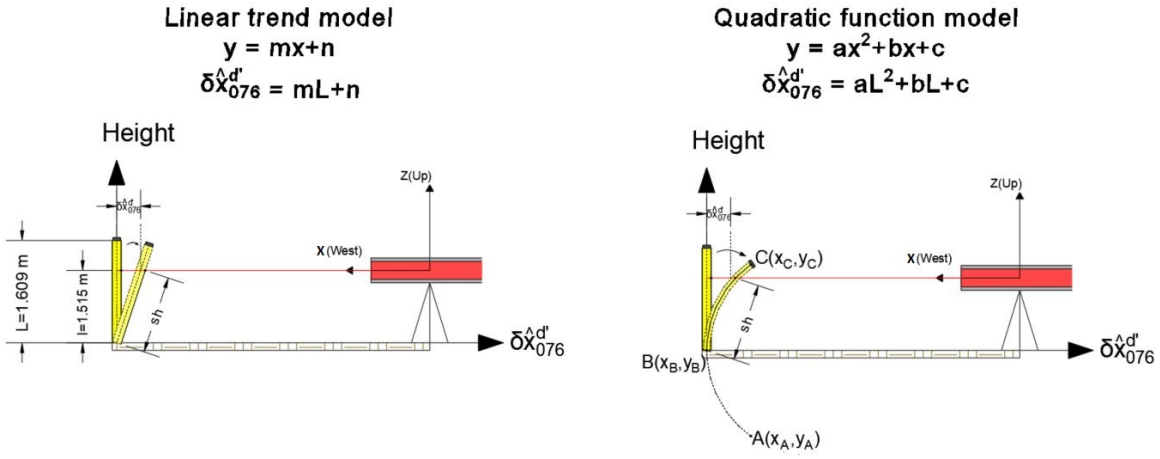

Figure 4.7: Figure of the linear trend- (left) and quadratic function models (right) used for extrapolating the laser distometer measurements to the beam's top

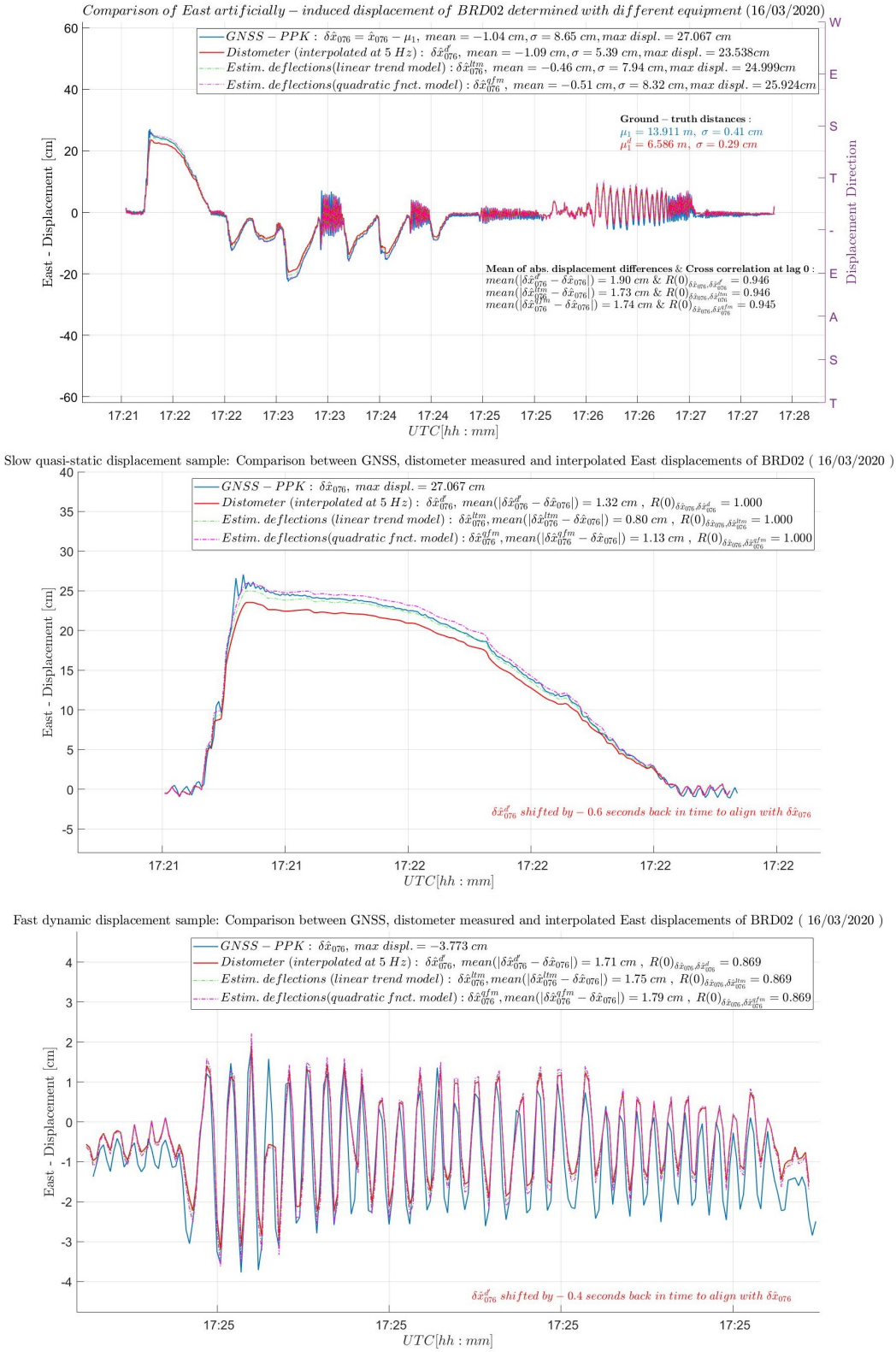

Figure 4.8: Distometer based validation results. Comparison between the GNSS (blue) - and the distometer based displacement time series (red, dashed green and dashed magenta) indicating very good similarity (top). Zoom in on a quasi-static displacement (middle) and a fast dynamic displacement (below) attesting the linear trend model as the best method for extrapolating the distometer displacements to the beam's top (compare legend values). The annotated time lag corrections of -0.6 and -0.4 seconds from the latter two plots correspond to the previewed time periods.

After extrapolating the laser distometer quantities based on the linear and quadratic models ($\delta\hat{x}_{076}^{ltm}$, $\delta\hat{x}_{076}^{qfm}$), the cross correlation coefficients at lag 0
($R(0)_{\delta\tilde{x}_{076},\delta\hat{x}_{076}^{ltm}}$, $R(0)_{\delta\tilde{x}_{076},\delta\hat{x}_{076}^{qfm}}$) were computed in order to decide which extrapolated displacement time series fits best the estimated GNSS based displacement quantities from the beam's top. From figure 4.8 one can generally conclude that the linear trend based displacement time series is following closer the displacement pattern of the GNSS based displacement time series. This is quantitatively attested by a slightly larger normalized cross correlation value of 0.946 compared to the cross correlation factor of the quadratic function model of 0.945. This holds true also when looking over particular displacements individually (review the last two plots of figure 4.8). Nevertheless, both models output remarkable good displacement time series, which are validating the GNSS based displacement results of the AID stage, attesting that the proposed low-cost dual frequency GNSS module is capable of measuring a wide range of displacements in all three orthogonal directions.

4

4.3.2. VALIDATION OF THE WID STAGE BASED ON THE SMARTPHONE ACCELEROMETER

THE WID stage, as presented in section 2.1, has the purpose of testing the capability of the proposed GNSS module to sense naturally induced (dynamic) responses of the cantilever beam produced by (West) wind, resembling a scenario of the response of a tall, slender structure to wind loads. Thus, in order to fully attest the results from section 4.2 a validation process needs to be performed. Therefore, a relevant example of the forward and reverse transformation procedures run on a one-hour sequence of GNSS based displacements and smartphone accelerometer data from day 078, centered again around 10:30 UTC, at the moment when the maximum wind speed value of 6.6 $\frac{m}{s}$ was recorded, is hereafter considered.

As already presented in section 2.6.3, the forward transformation validation process follows a simple set of steps (see figure 2.6) to derive accelerations from GNSS based (dynamic) displacement quantities. On the other hand, the reverse transformation validation process follows a more complex procedure (see figure 2.7) to determine (dynamic) displacements from the acquired smartphone accelerometer data set. In both cases, prior to any differentiation respectively integration procedure, an optimal low- and high-pass filtering scheme needs to be applied in order to constrain only the energy corresponding to fast, dynamic movements of the cantilever beam. In general, the energy related to dynamic displacements is characterized by the frequency bins surrounding the first natural frequency of the cantilever beam, which can be identified by the largest peak in the amplitude spectrum of an input signal.
In this case, based on the analysis in appendix E, a 2nd order Elliptical low- and high-pass filter was adopted for removing the unwanted low and high frequency noise components together with the energy related to the static and quasi-static displacements from the sequence of GNSS based displacements and measured smartphone accelerations.
Therefore, based on the results of a FFT analysis[14] run on the GNSS displacement- and smartphone acceleration time series, 2nd order Elliptical high- and low-pass filters with the following filter parameters were designed (see table 4.1).

Table 4.1: Filter design parameters of the 2nd order Elliptical high- and low-pass filters

↓ Filter Parameters | Type →	***2nd order Elliptical high-pass filter***	***2nd order Elliptical low-pass filter***
Stopband Frequency [Hz]	0.90	1.25
Passband Frequency [Hz]	0.95	1.30
Stopband Attenuation [dB]	-70	-70
Passband Ripple [dB]	0.01	0.01
Sampling Frequency [Hz]	5	5

Having the high- and low-pass filter scheme defined, one can focus on deploying the forward and reverse transformation processes. In the following subsections one should note that any graphs derived from the smartphone accelerometer data are plotted in blue while the graphs derived from the GNSS data sets are plotted in red.

[14] denoting a natural frequency value of about 1.1 Hz, in concordance with the expected value of 1 Hz from section 2.3.

VALIDATION OF THE WID STAGE. FORWARD TRANSFORMATION RESULTS

FOLLOWING the proposed algorithm of the forward transformation from figure 2.6, the defined 2nd order Elliptical filters were successively applied on the GNSS East (X) displacement input signal ($\delta\hat{x}^{sc}_{078}$) via Matlab's *filtfilt* function, resulting in a filtered displacement time series with zero-phase distortion. Having the displacement time series cleaned from unwanted noise, a 80th order Parks-McClellan/Remez differentiator (see appendix F) was designed and applied via Matlab's *filter* function. Moreover, the time delay correction algorithm from the last part of subsection 2.6.1 needed to be applied in order to correct for the time delay error resulting from the differentiation operation imposed by the Parks-McClellan/Remez differentiator. The result of the first stage of the forward transformation process corresponded to the East (X) velocity time series ($\delta\hat{v}^{sc}_{078}$, see middle panel of figure K.2 in appendix K).
Note that at this stage, a value for the GNSS based displacement and velocity constants[15] for the upcoming reverse transformation can be determined. These constants were determined based on a 20-minutes sequence of GNSS based displacements from day 077 ($\delta\hat{x}^{sc}_{077}$), that was centred around 00:10 UTC, corresponding to the lowest recorded wind speed value of the cantilever beam experiment. In this process, the extracted sequence of displacements was filtered for unwanted low and high frequency noise based on the aforementioned Elliptical high- and low-pass filtering scheme. The desired displacement constant ($ct_{\delta\hat{x}}$) was determined by taking the mean over the filtered displacement time series, resulting in -6.89*10^{-7} meters. In the next step of determining the velocity constant ($ct_{\delta\hat{v}}$), a McClellan/Remez differentiator was applied on the 20-minutes long filtered displacement time series. Then by taking the mean over the resulting velocity time series a value for the velocity constant of -1.75*10^{-6} $\frac{m}{s}$ was determined.
Before deploying the second digital differentiation operation, another FFT analysis on the derived velocity time series needed to be deployed to make sure that no unwanted frequency component of the output signal got amplified during the first digital differentiation process. In this case, the third amplitude spectrum from figure K.2 shows that there is no need to apply the Elliptical filtering scheme anymore. Hence, a second identical differentiation process was performed, taking into account to correct for the time delay of the resulting East (X) acceleration time series ($\delta\hat{a}^{sc}_{078}$).
The entire process of the forward transformation algorithm run on the selected one-hour sequence of GNSS based displacements is illustrated in figure K.2 of appendix K.

Before being able to compare the derived acceleration time series ($\delta\hat{a}^{sc}_{078}$) with the measured smartphone based acceleration time series ($\delta a^{S,sc}_{078}$), one should recall that the smartphone accelerometer data sequence is suffering from a non-linearly increasing time lag error with respect to the resulting GNSS based acceleration time series. According to section 2.2 and appendix B.1, this problem was most probably caused by the fact that the acceleration time series was recorded by the smartphone set on airplane mode, cutting the connection with any cellular network or GNSS service and hence disabling synchronization of the internal clock of the smartphone over the entire period of the cantilever beam experiment. Moreover, due to the strong fragmentation of the smartphone accelerometer data (see figure B.1), one could not properly align the two candidate time series on behalf of a statistical cross correlation analysis. Thus, a manual trial-and-error procedure was used for aligning the smartphone accelerometer time series with the GNSS based time series. Through this trial-and-error procedure a time lag correction of 16 minutes and 34 seconds was recognized to work the best (see figure K.2 from appendix K).
Secondly, for statistically attesting any similarity one needed to make sure that both candidate time series are sampled at the same rate. Therefore, the measured smartphone based acceleration time series needed to be down sampled from 15.151 Hz to the same rate (of 5 Hz, $\delta a^{S,sc'}_{078}$) of the GNSS derived acceleration time series via cubic interpolation. The final comparison between the down sampled smartphone acceleration time series and the resulting GNSS based acceleration time series is shown in figure 4.9.
As one can conclude from this figure, a good match between the two time series can be visually attested after 10:47 UTC. Though from a statistical point of view an almost inexistent correlation was found. This is because the two time series were remarkably well matching only in the middle of the studied period but not at the start and end, where the blue smartphone accelerometer time series was first running ahead and then slowing down at the end of the period, by running behind the GNSS derived acceleration time series (see figure 4.9). Thus, based on these results of the forward transformation process, the capability of the GNSS module of measuring (dynamic) displacements can be only visually attested.

[15] recall, that each of these constant can be used as a correction factor for the de-trended reverse transformation resulting velocity and displacement time series of each experimental day, to compensate for the velocity and displacement constants that are omitted during the integration process.

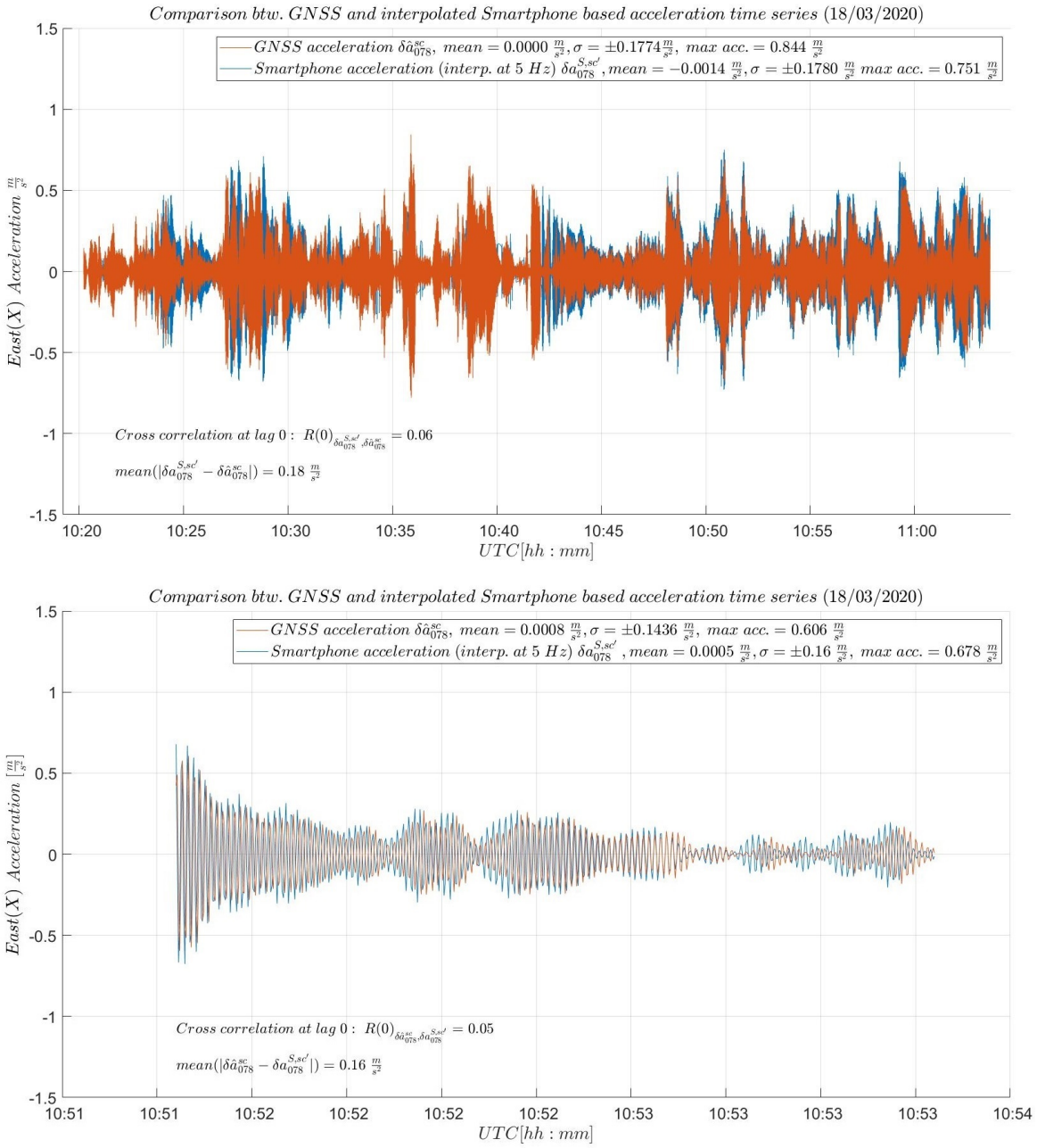

Figure 4.9: Comparison between the chosen one-hour long GNSS based acceleration- ($\delta\hat{a}^{sc}_{078}$, red) and the down sampled smartphone acceleration time series ($\delta a^{S,sc}_{078}$, blue). Alignment of the time series was performed manually by shifting $\delta a^{S,sc}_{078}$ forward in time by 16 min and 34 sec. Due to non-linearly increasing time lag error of the smartphone clock a good match can be observed only after 10:47 UTC. Below a zoom in of a 2 minutes long sequence centered at 10:52:30 UTC is presented to indicate initial good match between the two time series followed by an immediate out-of-phase behavior.

VALIDATION OF THE WID STAGE. REVERSE TRANSFORMATION RESULTS

In this subsection, the proposed, more laborious reverse transformation algorithm from figure 2.7 is deployed on the sequence of smartphone East (X) accelerations ($\delta a^{S,sc}_{078}$) in order to derive East (X) (dynamic) displacements ($\delta x^{S,sc}_{078}$) and validate the GNSS based (dynamic) displacement quantities($\delta\hat{x}^{sc}_{078}$).
The algorithm starts by removing the unwanted noise[16] from the one-hour sequence of measured smartphone acceleration values, by applying the previously introduced Elliptical high- and low-pass filtering scheme.

[16] s.a effects of the constant triggering acceleration error or the influence of the static and/ or quasi-static displacements on the recorded accelerations.

Having the smartphone acceleration time series cleaned from unwanted noise, the first step of the reverse transformation process was to integrate this time series into a velocity time series. In this case, the time domain trapezoidal integration rule (see subsection 2.6.2 and appendix F) was implemented via Matlab's *cumtrapz* function. At the same time an analysis in frequency domain was conducted, showing that the trapezoidal integration rule is not causing any time delay to the output velocity time series. Hence, in this case no time delay correction needs to be considered.
At first glance, the resulting smartphone derived velocity time series contained a constant offset, which was identified in the amplitude spectrum as a spike at DC. This constant offset appeared due to the fact that during the integration process no information about the initial velocity of the beam at rest was at hand, assuming that the velocity constant was equal to zero. Thus, by not taking into account on the velocity constant this will produce an error, which is strongly amplified by the integration process resulting in the constant error in the velocity time series.
Therefore, the usual correction process is to perform a least-squares de-trending operation on the signal of interest, in this case the velocity. In such a case the de-trending process yields the trend line intercept and slope parameters, which model the amplified velocity constant error. Thus, by subtracting the fitted trend line one is correcting for the integration error, centering the derived velocity time series around zero (see figure's L.2 "1st Integration Step" panel). This corresponds with the underlying boundary condition that over the entire observation time span the velocity/displacement of the cantilever beam is on average equal with zero[17].
After performing the proposed least-squares de-trending operation, one can consider the previously derived velocity constant value ($ct_{\delta\hat{v}}$= -1.75*10^{-6} $\frac{m}{s}$) from the forward transformation process, by simply adding it to the de-trended smartphone based velocity time series to derive the correct velocity time series ($\delta v_{078}^{S,sc}$).
Note that the previously enounced list of operations from this paragraph should be applied again during the second integration step of the reverse transformation algorithm to define the desired smartphone based (dynamic) displacement time series ($\delta x_{078}^{S,sc}$).
As already expressed, a second integration procedure needed to be deployed to obtain the desired sequence of smartphone derived displacements. Note, that one should feed the resulting de-trended velocity time series[18] in the second integration operation to avoid any integration amplification produced by the added velocity constant.
After integration, a displacement constant error was found in the amplitude spectrum of the derived displacement data set at DC. The error can be depicted as a constant offset in the smartphone derived displacement time series. Based on the underlying assumption that over the entire observation time span the velocity/displacement of the cantilever beam was on average equal to zero, the aforementioned least-squares de-trending technique was applied again in order to correct for this problem. Lastly, the derived displacement constant value ($ct_{\delta\hat{x}}$= -6.89*10^{-7} m) from the forward transformation process was added to the resulting de-trended displacement time series to produce the desired smartphone based East (X) displacement time series ($\delta x_{078}^{S,sc}$, see figure's L.2 "2nd Integration Step" panel).
Therefore, in the last stage of the reverse transformation validation process, the same time lag correction of 16 minutes and 34 seconds was applied on the derived smartphone based (dynamic) displacement time series ($\delta x_{078}^{S,sc}$) to align it with the filtered GNSS based (dynamic) displacement time series ($\delta \hat{x}_{078}^{sc}$) (see figure L.2 in appendix L). Moreover, the accelerometer derived displacement time series was down sampled at a rate of 5 Hz ($\delta x_{078}^{S,sc'}$) based on a similar procedure as the one presented in the last part of the previous subsection, to compute the cross correlation coefficients at lag 0 ($R(0)_{\delta \hat{x}_{078}^{sc}, \delta \hat{x}_{078}^{S,sc'}}$) for statistically attesting the similarity between the two displacement time series. The final comparison between the down sampled smartphone based displacement time series and the GNSS based displacement time series, resulting from the reverse transformation, is shown in figure 4.10.
Based on this figure and the results of the considered cross correlation coefficient, the same conclusion as with the forward transformation validation process can be drawn. Thus, due to the non-linearly increasing time lag error of the smartphone internal clock, one cannot statistically validate the GNSS based (dynamic) displacement results. Though, based on the remarkable visual similarity between the candidate displacement time series over day 078 (see figure 4.10), the usefulness of a smartphone accelerometer for validating GNSS based dynamic displacement quantities is attested. Nevertheless, considering the encountered time misalignment between the displacement data sets of the two sensors, it is believed that the implementation

[17] under normal meteorological conditions the beam is not moving and/ or changing its form.
[18] without considering the velocity constant $ct_{\delta\hat{v}}$.

of a smartphone accelerometer within a SHM sensor network for conducting real time monitoring applications, is very complicated.

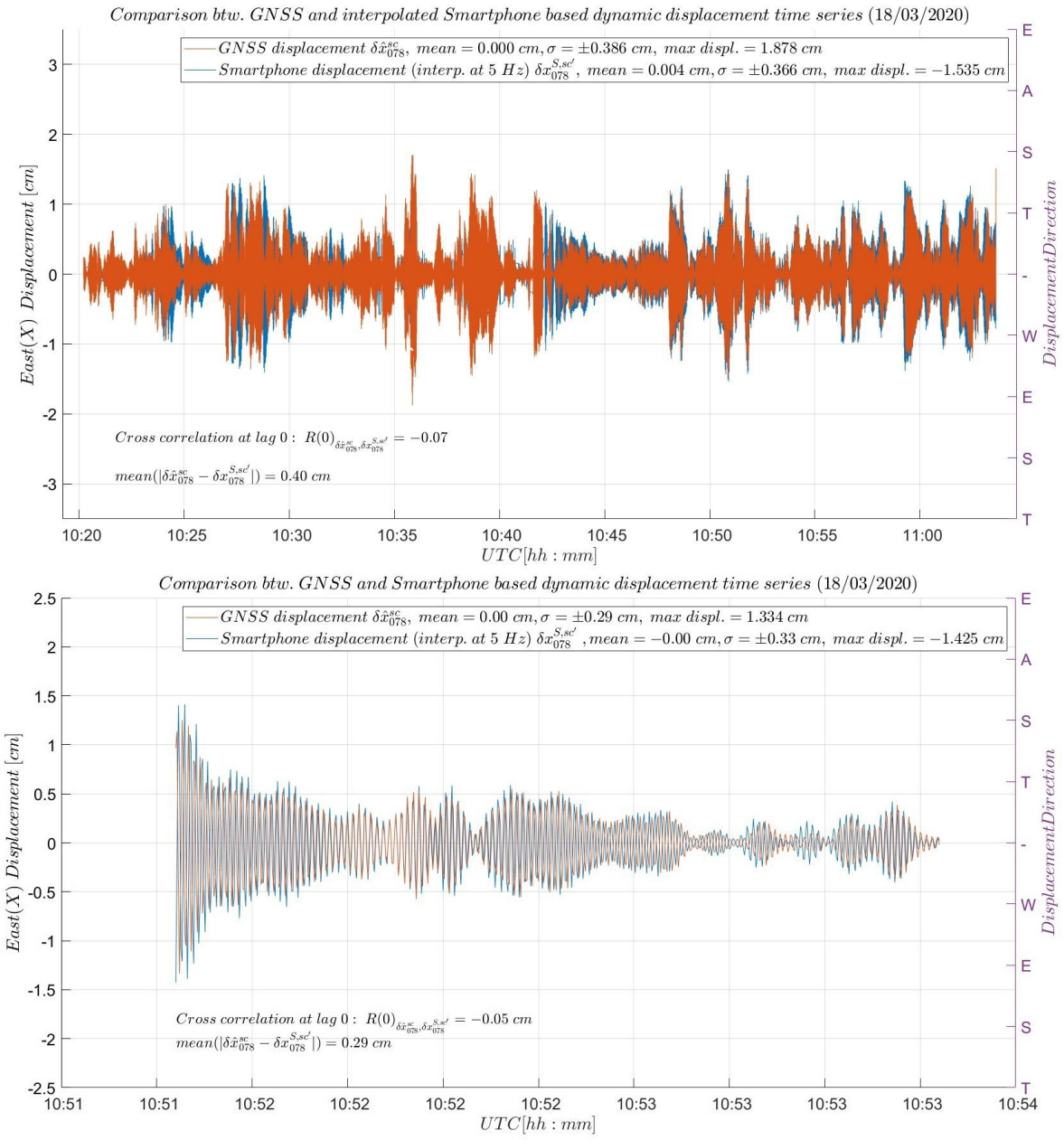

Figure 4.10: Comparison between the chosen one-hour long filtered GNSS based (dynamic) displacement ($\delta\hat{x}^{sc}_{078}$, red) and the derived, down sampled smartphone displacement time series ($\delta x^{S,sc'}_{078}$, blue). Alignment of the candidate time series was performed manually by shifting $\delta x^{S,sc'}_{078}$ forward in time by 16 min and 34 sec. Due to non-linearly increasing time lag error of the smartphone clock good match can be observed only after 10:40 UTC. Below a zoomed in preview over a 2 minutes long sequence centered at 10:52:30 UTC is presented to indicate the good match between the two time series followed by an immediate out-of-phase behavior.

4.4. GNSS & ACCELEROMETER PERFORMANCE. NOISE ANALYSIS

An important factor for selecting the most appropriate displacement detection sensor for specific SHM campaigns, is the offered precision prescribed by the imposed noise level of the output signal. Generally, if the level of noise exceeds the target output signal[19] broadband, then the desired (displacement/ acceleration) values cannot be recovered by the (GNSS/ accelerometer) sensor. Moreover, due to commercial reasons

[19] in this case portrayed by displacements and accelerations.

it is common practice for manufacturers to overestimate their product specifications by declaring too optimistic precision measures. Therefore, in the following the declared/ formal precision level of the proposed low-cost dual frequency GNSS system and of the smartphone accelerometer are confronted with their empirical noise level resulting from an analysis run on collected data sets, which are describing a steady state[20] of the two sensors during the cantilever beam experiment. Additionally, the whiteness of the acquired displacement and acceleration signals is analyzed, for identifying possible minded data replication, inferred by the manufacturer in order to improve the sampling rate and output more "precise" displacement and acceleration time series.

GNSS NOISE LEVEL ANALYSIS

ACCORDING to the already listed precision specifications in table 2.2 in section 2.2, the low-cost dual frequency GNSS system is labeled with a formal relative position coordinate precision of 0.01 meters + 1 ppm.
Based on the cantilever beam experiment results and in contradiction with the common practice of minded over estimation of the product precision performances, the declared formal value proves to under estimate the potential of the GNSS module for deriving displacement quantities. This holds true, considering that in case of the proposed short baseline cantilever beam experiment, the empirical instrumental noise level ($\delta\hat{e}^{sc}_{079}$) of the low-cost GNSS module was already accounted with East (X)/ North (Y)/ Up (Z) standard deviation values of ± 0.4, 0.5 and respectively 1 centimeter (see penultimate bullet point from subsection 3.2.4).
Recall that these values were derived by calling for the variability/ spread of the position estimates ($\hat{x}^{sc}_{079}$) from the daily mean estimates of the MP calibration day, 079. Nevertheless, the accounted empirical noise level is inevitably influenced by MP and by inevitable small responses of the flexible beam to light wind conditions over day 079. Therefore, it is believed that the empirical noise level of the low-cost dual frequency GNSS module can be even smaller, if a considerable amount of MP can be removed from the East (X)/ North (Y)/ Up (Z) position estimates time series of day 079. This can be achieved by subtracting the previously defined least-squares polynomial based MP correction ($\hat{x}^{p,sc}_{079}$) from the considered position estimates time series of day 079. This can be visually portrayed as a subtraction between the two overlapping MP correction time series from the middle panels of figure I.3, I.4 and I.5 from appendix I.
After removing part of the MP effect from the position estimates time series of day 079, a reduction of the empirical noise level to 0.3, 0.4 and respectively 0.8 centimeters can be attested (see figure's 4.11 legends).

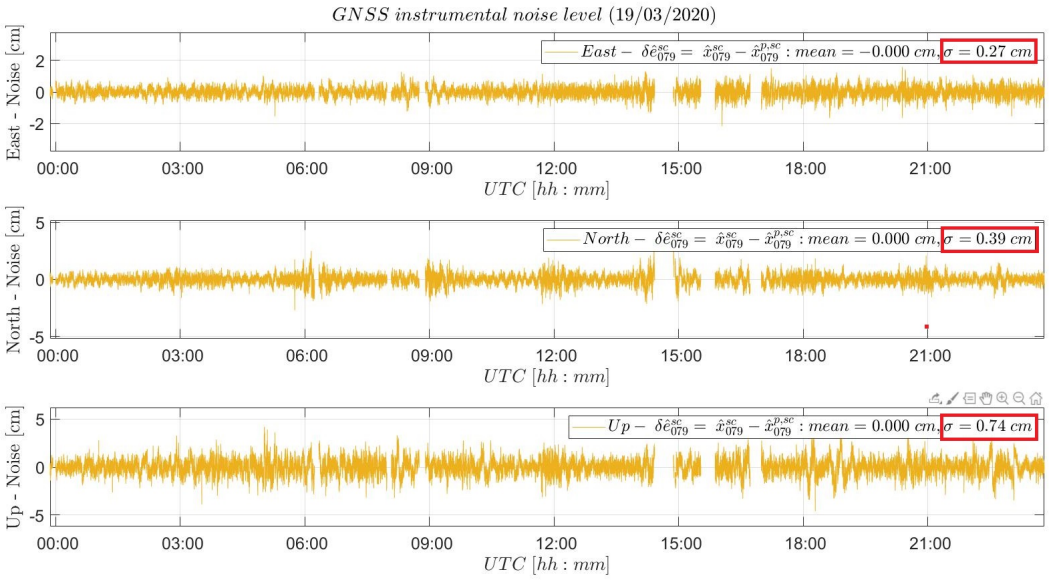

Figure 4.11: Empirical noise level of the low-cost dual frequency GNSS module on each orthogonal direction, resulting after the least-squares based MP correction of the daily position time series of day 079. A reduction in the empirical standard deviation values in comparison to the accounted values of ± 0.4, 0.5 and respectively 1 centimeter, is noticeable.

These results attest an exceptional precision potential of the proposed GNSS module. Hence, it is remarkable that for the low price of two identical low-cost GNSS systems, that goes way below 1000 €, one can perform

[20] with no mechanical induced excitations.

millimeter-precise RTK based SHM campaigns. To this, it is primordial to mention that for obtaining such precise SHM campaigns, the use of identical GNSS antennas plays an important role in mitigating antenna PC errors.

In the next stage, the whiteness of the least-squares based MP corrected displacement quantities ($\delta\hat{e}^{sc}_{079}$) is questioned. As previously mentioned in subsection 3.2.4, under the assumption that the code and carrier-tracking loops of the low-cost GNSS receiver do not use extremely narrow bandwidths in the relative position estimation process, one can expect from the GNSS observation to not strongly correlate over time. However, since the GNSS module was collecting data at a intermediate rate of 5 Hz the PLL mechanism will have some difficulties in tracking and estimating the phase difference between the incoming GNSS carrier wave signal and the receiver replicated carrier wave signal. Therefore, a certain degree of time correlation between the GNSS based displacement quantities is expected to be found.
On behalf of the presented knowledge from appendix M, the whiteness of the GNSS based displacement quantities can be assessed by computing the auto-correlation ($\rho(\tau)$) of a noise sequence in the form of the previously derived instrumental noise time series ($\delta\hat{e}^{sc}_{079}$) of the displacement data set. Then, if the resulting auto-correlation coefficients follow the behaviour of an AR(1) process, the whiteness of the derived displacements data can be neglected. Hence, a similar process with the one presented in the last part of subsection 3.2.4 was deployed, to additionally output the auto-correlation function of the first two-hour noise sequence from the previously derived North (Y) and Up (Z) instrumental noise time series. Furthermore, all three auto-correlation sequences were grouped and plotted in figure M.1 in appendix M. As one can see from this figure the two new computed auto-correlation sequences indicate similar results as the firstly derived auto-correlation sequence from figure 3.10, attesting that the East (X)/ North (Y)/ Up (Z) empirical noise sequences follow an exponentially decaying behavior of 2 to 3 minutes, which is a strong indication of existing time correlation present in the GNSS based displacement quantities.

These results attest the aforementioned expectations related to the possibility of identifying a certain degree of time correlation between the GNSS based displacement quantities. However, since the identified correlation period is unexpected long, one can consider residual MP[21] as an important source of time correlation within the empirical noise signal.

SMARTPHONE ACCELEROMETER NOISE LEVEL ANALYSIS

THE noise level performance of the smartphone accelerometer is quantified by a spectral noise parameter ($n_{A,nd}[\frac{\mu g}{\sqrt{Hz}}]$) of 180 (see table 2.2). Hence, to transform it to an universal precision measure, the spectral noise parameter can be multiplied by the square root of the accelerometer's bandwidth[22] in order to derive the expected nominal acceleration noise ($\delta e^{S,sc}$) of the accelerometer sensor. This can be mathematically expressed by the following formula[23]:

$$\begin{aligned} \delta e^{S,sc} &= \left(\sqrt{\frac{Output\ rate}{2}} * n_{A,nd}\right) * 10^{-6} * 0.01 \\ \delta e^{S,sc} &= \left(\sqrt{\frac{15.151}{2}} * 180\right) * 10^{-6} * 0.01 = 4.954 * 10^{-6} \end{aligned} \tag{4.5}$$

where:

$\delta e^{S,sc}$ = formal/ declared accelerometer noise level $[\frac{m}{s^2}]$
$n_{A,nd}$ = accelerometer spectral noise parameter

Therefore, in case of the cantilever beam experiment the expected nominal noise level of the smartphone accelerometer, that is sampling at a rate of 15.151 Hz, is equal to
$4.954 * 10^{-6}\ \frac{m}{s^2}$.
To see if the manufacturer specifications meet reality, the expected nominal noise level value of $4.954 * 10^{-6}\ \frac{m}{s^2}$ can be compared with the standard deviation value of a least-squares de-trended sequence of accelerations, collected during a wind-still period. To do so, the standard deviation value of a 20-minutes least-squares

[21] which was not efficiently removed by the subtracted least-squares based MP correction.
[22] the bandwidth of the accelerometer defines the frequency region that can be sensed by the accelerometer. This is computed as the half of the output data rate of the accelerometer in accordance to the Nyquist theorem, which states that a (analogue) signal needs to be sampled at more than twice the bandwidth of the signal in order to be reproduced. In case of the cantilever beam experiment, the bandwidth of the accelerometer needs to include the target vibration frequencies of the beam.
[23] note that this formula defines the nominal acceleration noise level corresponding to a system that is working at an ambient temperature of 25° Celsius.

de-trended East[24](X) acceleration sequence ($\delta a^{S,p,sc}$), centered at 00:20:00 UTC during the first day of the experiment (day 077), was computed (see figure 4.12).

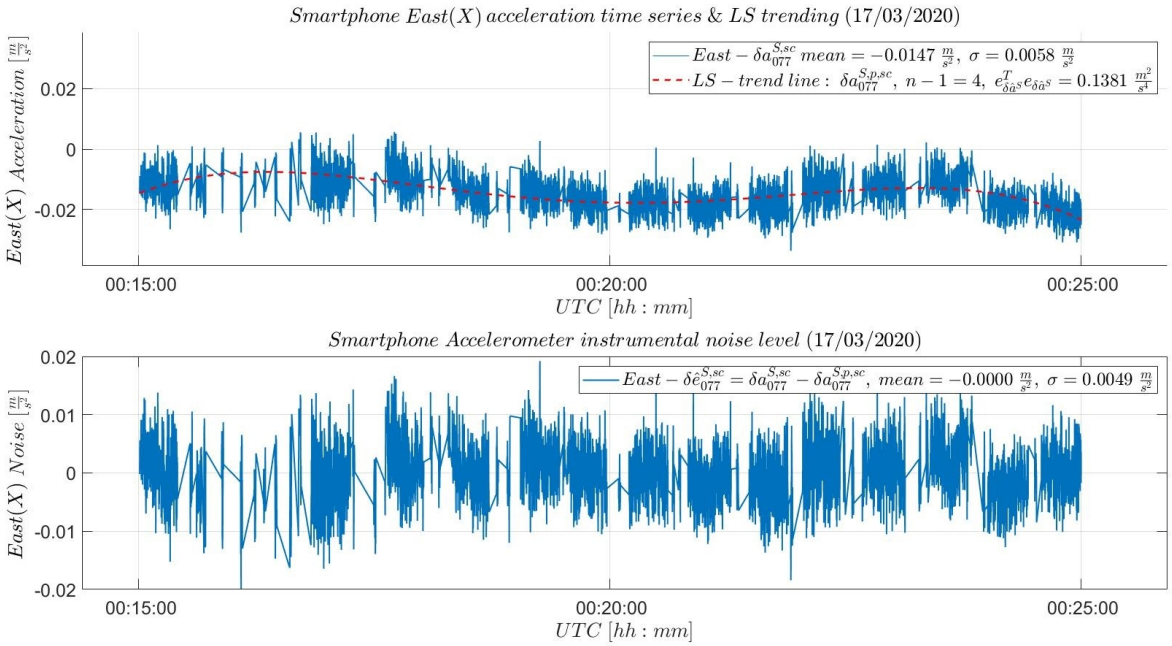

Figure 4.12: Least-squares de-trending process (top) run on the East(X) acceleration data sequence ($\delta a^{S,sc}$) to determine the desired empirical noise sequence ($\delta \hat{e}^{S,sc}$). Empirical noise sequence (below) of the smartphone accelerometer on East direction. The accounted noise level is equal to $\pm$ 0.005 $\frac{m}{s^2}$.

Note that the output of the proposed de-trending process is defining the empirical instrumental noise sequence ($\delta \hat{e}^{S,sc}$) of the smartphone accelerometer. Moreover, the performed least-squares de-trending process was based on an iterative process, similar with the one from (3.19), aiming to identify the ideal polynomial order to output the most appropriate least-squares fit. In this case a minimum sum of squared least-squares residuals ($e^T_{\delta a^S} e_{\delta a^S}$) of 0.1381 $\frac{m^2}{s^4}$ was achieved via a 4$^{\text{th}}$ (=n-1) order polynomial. As one can see, the resulting sum of squared residuals value is very close to zero, indicating a very good linear trend polynomial fit through the selected sequence of acceleration values (see top panel from figure 4.12). Thus, by subtracting the least-squares fitted polynomial from the original acceleration data set, one was correcting for any possible spurious effect and was remaining with a data sequence consisting of only instrumental random noise, corresponding to a perfect input quantity for a time correlation analysis.
The resulting empirical standard deviation value of the accelerometer noise level of 0.005 $\frac{m}{s^2}$ is exceeding the expected formal noise level value from (4.5), indicating that the presented precision specifications are too optimistic. Hence, one cannot fully rely on the product specifications for making a choice on the smartphone accelerometer, to make it comply with the required precision of the considered SHM campaign. However, one should take into account that the declared nominal noise level is corresponding (most likely) just to thermal noise in the sensor that's been quantified at an exact temperature of 25°Celsius in a calibration laboratory, as in case of the cantilever beam experiment the derived empirical noise level may be affected also by background processes, s.a traffic.

Lastly, any form of time correlation in the acquired smartphone accelerometer data sets is subject of interest in order to attest any degree of similarity between close-by acceleration samples. This can be an indication of deliberately data replication or manipulation inferred by a time correlation algorithm implemented within the smartphone to improve the sampling rate and the precision of the recorded acceleration sequence instead of just measuring and outputting raw acceleration information.
To do so, a time correlation analysis was performed by deriving the auto-correlation coefficients of the previously presented instrumental noise sequence of the the acquired East (X) acceleration data set from figure 4.12.

[24]compared to the noise analysis performed on the East (X)/ North (Y)/ Up (Z) GNSS data sets, this time an analysis only along the weak (X) axis of the cantilever beam was deployed.

The resulting correlogram of the de-trended East(X) acceleration time series is shown in figure 4.13. At first sight one would be tempted to say that the graph of the auto-correlation sequence follows the behaviour of an AR(1) process, with the auto-correlation sequence peaking at lag 0 and exponentially decaying reaching 0 after τ=6[25]. Though, taking into consideration that the de-correlation period was only 0.396 seconds and that the auto-correlation sequence got stabilized within the depicted 95% confidence interval after just 100 out of 5800 sampled, one can conclude that there is no evident sign for attesting deliberate acceleration data replication.

These results, indicate that the data sets output by the smartphone accelerometer during the cantilever beam experiment, likely correspond to raw acceleration information. This was attested by the auto-correlation sequence indicating a quick drop in auto-correlation in the proximity of lag 0 (see the second plot from figure 4.13). However in the first part of this subchapter it was shown how the declared acceleration retention performance of the proposed smartphone accelerometer tends to be largely overestimated by the manufacturer in the product specifications. Therefore, caution is required when choosing for a smartphone accelerometer that should meet the precision requirements of a sensitive SHM campaign.

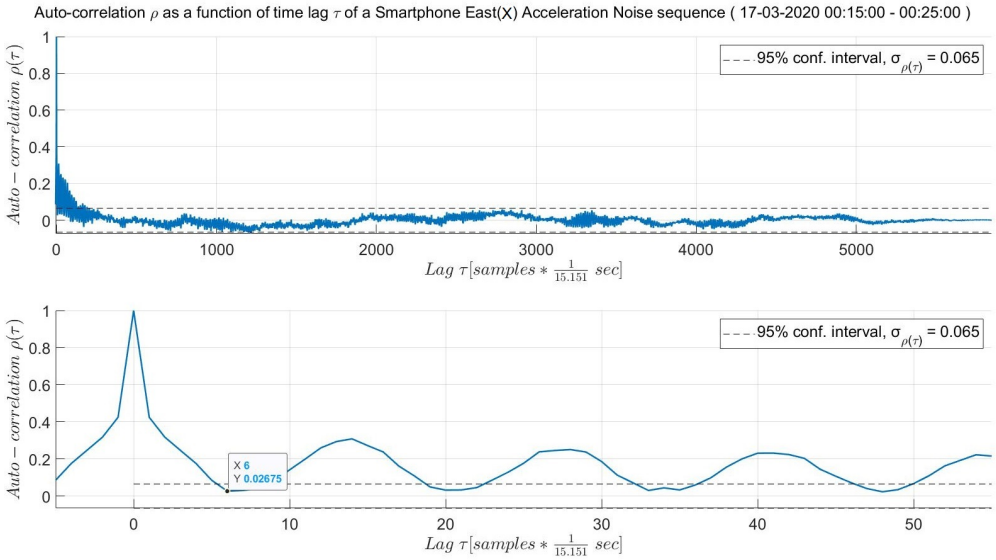

Figure 4.13: Correlogram of the random noise sequence derived from a 20-minutes East (X) acceleration sequence, recorded during a wind-still period. Top panel contains the entire auto-correlation sequence while the panel below contains a zoom in of the first 50 lags of the auto-correlation sequence. The latter plot indicates the point (sample no. 6) where the time correlation behavior of the smartphone accelerometer data ends. From the identified de-correlation period of $6 * \frac{1}{15.151} = 0.396$ seconds, it can be deduced that the accelerometer data virtually presents no sign of time correlation.

[25] corresponding to a de-correlation period of $6 * \frac{1}{15.151} = 0.396$ seconds.

4.5. OVERALL ASSESSMENT OF LOW-COST GNSS SENSORS

BEFORE drawing the final conclusion on the overall performance of the low-cost dual frequency GNSS module at deriving displacements of tall structures, all aforementioned results from this chapter are summarized in the following three tables.

Table 4.2: Summary of the displacement results obtained during the AID stage. Determined GNSS displacements (left) and the validation results based on the laser distometer (right)

AID stage, Day 076 (16/03/2020) 17:21:30 - 17:27:50 UTC							
GNSS based Displacements Results ($\delta\hat{x}_{076}$)				Validation Results			
				↓Value|Sensor→	Laser Distometer		
↓Value|Direction→	East (X)	North (Y)	Up (Z)	Method	Down sampled at 5 Hz ($\delta\hat{x}^{d'}_{076}$)	Linear trend model ($\delta\hat{x}^{ltm}_{076}$)	Quadratic function model ($\delta\hat{x}^{qfm}_{076}$)
Max displ. [cm]	27.07	0.9	-2.49	Max displ. [cm]	23.538	25	25.92
				σ [cm]	5.39	7.94	8.32
				$mean\,(\lvert\delta\hat{x}^{d'/ltm/qfm}_{076} - \delta\hat{x}_{076}\rvert)$ [cm]	1.9	1.73	1.74
σ [cm]	8.65	0.32	0.7	$R(0)_{\delta\hat{x}_{076},\delta\hat{x}^{d'/ltm/qfm}_{076}}$	0.946	0.946	0.945

Table 4.3: Summary of the displacement and acceleration results obtained during the WID stage. Determined GNSS displacements (left) and the validation results from the forward and reverse transformation algorithms based on the smartphone accelerometer sensor (right)

WID stage, Day 078 (18/03/2020) 10:20:13 - 11:03:36							
GNSS based Displacements Results ($\delta\hat{x}^{sc}_{078}$)		Validation Results of Dynamic Displacements					
		Forward Transformation			Reverse Transformation		
↓Value|Direction→	*East (X)*	↓Value|Sensor→	*Smartphone (S,sc')*[26]	*GNSS (sc)*	↓Value|Sensor→	*Smartphone (S,sc')*	*GNSS (sc)*
Max U WS [$\frac{m}{s}$]	6.66	Max acc. [$\frac{m}{s^2}$]	0.75	0.84	Max displ. [cm]	1.54	1.88
Max displ. [cm]	3.39						
Max $\tilde{\delta\hat{x}}^{sc}_{078}$ [cm][27]	1.9	σ [$\frac{m}{s^2}$]	0.178	0.177	σ [cm]	0.366	0.386
		$mean(\lvert\delta a^{S,sc'}_{078} - \hat{a}^{sc}_{078}\rvert)$ [$\frac{m}{s^2}$]	0.18		$mean(\lvert\delta x^{S,sc'}_{078} - \hat{x}^{sc}_{078}\rvert)$ [cm]	0.4	
$R(0)_{\tilde{\delta\hat{x}}^{sc}_{078},U}$	0.73	$R(0)_{\delta a^{S,sc'}_{078},\delta\hat{a}^{sc}_{078}}$	0.06		$R(0)_{\delta x^{S,sc'}_{078},\delta\hat{x}^{sc}_{078}}$	-0.07	

Table 4.4: Summary of the results of the noise level analysis performed on the GNSS sensor (left) and smartphone accelerometer sensor (right)

Precision Performance					
	GNSS Noise Band ($\delta\hat{e}^{sc}_{079}$)				*Smartphone Accelerometer Noise Band ($\delta\hat{a}^{S,sc}_{077}$)*
↓Value|Direction→	*East (X)*	*North (Y)*	*Up (Z)*	↓Value|Direction→	*East (Y)*
Formal/ Declared σ [cm + ppm]	1 + 1	1 + 1	1 + 1	Formal/ Declared σ[$\frac{m}{s^2}$]	4.954*10^-6
Empirical σ [cm] straight out of box	0.4	0.5	1		
Empirical σ [cm] MP correction considered	0.27	0.39	0.74	Empirical σ [$\frac{m}{s^2}$]	0.005
Whiteness	Correlated, time correlation of 2.6 mins.	Correlated, time correlation of 2.2 mins.	Correlated, time correlation of 2.4 mins.	Whiteness	White, time correlation of 0.4 sec.

Based on the previously summarized results from the above annexed tables, two out of the five addressed research questions can be already answered.

The first one called for the accuracy potential of the low-cost dual frequency GNSS system for monitoring wind-induced displacements of large-scale structures. The answer to this, can be framed around the accounted precision measures of the low-cost dual frequency GNSS module of ± 0.4, 0.5 and respectively 1 centimeters from table 4.4. These values define the noise band of the proposed GNSS sensor straight out of the box, and can be universally attested for RTK-GNSS based SHM campaigns that meet similar experimental setup conditions with the ones of the cantilever beam experiment (see subsection 2.2). Additionally, it was shown that if one is correcting for MP, the positioning precision can be improved to 0.3, 0.4 and respectively 0.8 centimeters. These values demonstrate the capability of the proposed GNSS sensor for (theoretically) sensing sub-centimeter wind-induced displacements of tall and slender structure, that describes a similar behaviour with the one of a cantilever beam with a natural frequency of 1.1 Hz, produced by large enough wind loads. However, according to the 3 σ criterion it is safer to say that the true displacement retention

[25] recall that the the smartphone based accelerations and derived displacement values were down sampled via cubic interpolation at the rate of 5 Hz, resulting in $\delta a^{S,sc'}_{078}$ and $\delta x^{S,sc'}_{078}$. They were used for asking on statistical cross correlation between them and the GNSS based displacements (δx^{sc}_{078}).

[26] recall that based on (4.2) the GNSS based displacements were down sampled at the rate of 0.33 Hz ($\tilde{\delta\hat{x}}^{sc}_{078}$) to ask for statistical cross correlation between them and the U orthogonal wind components.

potential of the low-cost GNSS receiver corresponds to 3 times these standard deviation values, resulting in slightly larger than 1 centimeter detectable displacements[28]. In such a case, one can be 99.87 % of the time sure that every GNSS derived displacement quantity that exceeds the 1-centimeter level, can be considered as a real structural displacement estimate. This final statement can be supported by the detected wind-induced displacement results from the 40-minutes period of the second day (day 078) of the cantilever beam experiment (see section 4.2), where (East (X)) displacements of up to 3.39 centimeters[29] were detectable. These displacement results are relevant after being statistically confronted with the derived orthogonal wind components (see first column of table 4.3) and visually validated with displacements derived from smartphone accelerometer data sets.
Moreover, since the cantilever beam responded to wind loads only in the East direction, along its weak (X) axis, the potential of the GNSS module of sensing wind-induced displacements in all three orthogonal directions was demonstrated by artificially inducing a wide range of displacements, consisting of slow static and quasi-static but also fast dynamic displacements, with amplitudes of up to 27 centimeters (see section 4.1). To validate this statement, the induced displacements were exceptionally well retrieved by a laser distometer at the same time (compare the GNSS based results with the laser distometer results from table 4.2).
All in all, the table results and conclusions attest that for the price to pay for two identical low-cost dual frequency GNSS receivers, that goes way below 1000 €, one should be able to detect wind-induced displacements of tall and slender structures in the order of 1 centimeter. Additionally, one should take into account that in case of considering a second GNSS constellation, besides the proposed GPS constellation, the displacement detection potential of the studied GNSS module will improve with the increase in number of code and CP observations and probably reach a steady sub-centimeter level. Note that in case of a longer-than-10-days SHM campaign, one can include Galileo constellation in the displacement detection process and additionally, derive also a MP correction based on these satellite observations (see subsection 3.2.2). Nevertheless, it is believed that the true displacement retention potential of the low-cost GNSS receiver of about 1 centimeter is sufficient for detecting unexpected structure responses produced by wind loads, and for rising safety alarms in near-real time to warn on change of construction parameters that can cause structure collapse when no maintenance action is taken. Only in case of more sensitive applications, where the precise simulation of the dynamic of a tall structure to wind loads is intended, the low-cost dual frequency GNSS module is not a feasible option, such as the traditional accelerometer.

In the context of identifying a cost effective replacement to the traditional accelerometers, the second question was interrogating on the benefits brought by the integration of a second affordable sensor, such as a smartphone accelerometer, to the low-cost SHM system.
Generally, since accelerometers can retrieve very well the dynamic displacements of a structure, one can use accelerometer based information to validate enough powerful dynamic displacements (vibrations) that can be sensed by GNSS systems, and/or to compensate for the lacking capability of the GNSS systems to measure vibrations with small amplitudes. Hence, the smartphone accelerometer data in combination with the reverse transformation process can be used to derive information about sensitive structural vibrations that can be hardly sensed by the GNSS modules.
In this context, the smartphone based displacement results ($\delta x_{078}^{S,sc'}$) from the WID stage of the cantilever beam experiment (see table 4.3) that were (visually) matching very well with the filtered GNSS based dynamic displacements (see figure 4.10), attest the capability of inexpensive, rudimentary smartphone integrated accelerometers to recover wind-induced vibrations from structural elements such as cantilever beams. Therefore, through the reverse transformation algorithm (East (X)) dynamic displacements with amplitudes of up to 1.9 centimetres could be derived in order to validate the filtered GNSS based dynamic displacement quantities over a specific windy period of day 078. At the same time, a correct value of the noise level of the smartphone accelerometer was of $\pm 0.005 \frac{m}{s^2}$ (standard deviation), defining the limiting bandwidth below which noise can corrupt the accelerometer samples. Moreover, the trustfulness of the derived dynamic displacements from the smartphone accelerometer was demonstrated by the attested whiteness of the outputted acceleration quantities. Therefore, by considering also the functionality of a smartphone accelerometer of not only validating the obtained GNSS based displacements quantities but also to fuse its measurements with different types of sensors in order to compensate for the lack of capability of GNSS systems of recovering small vibrations, it was shown that the integration of a smartphone accelerometer in the studied SHM system

[28] =East (X) : 0.9 cm, North (Y): 1.2 cm, Up (Z): 2.4 cm.

[29] note that this displacement value of 3.39 centimeters is proving that the expected displacement value of 2.3 centimeters from section 2.3 is under estimating the true response of the cantilever beam under the influence of a 6.7 $\frac{m}{s}$ wind breeze on its 0.03 meter side.

is benefic.
However, considering the identified time lag error of the smartphone internal clock, which was hampering the time lag correction procedure and inevitably making it impossible to statistically attest the identified similarity between the smartphone and GNSS displacement data sets, one should be more reluctant about attesting the usefulness of a smartphone accelerometer for real time monitoring applications. To further support this idea, one should consider that the forward and reverse transformation validation processes cannot be applied in real time, being dependent on in-deep analysis and decision-making on the filter design and application procedure.
Thus, so far it is believed that the use of a smartphone accelerometer is beneficial only for post processed validation processes, since its integration within a real time SHM system proves to be very difficult.

Chapter Highlights

- Results of the AID stage show that the GNSS module was able to sense a wide range of displacements with different amplitudes and frequencies. The maximum displacements that were recorded at the beam's top are equal to 27.067, -0.892 and -2.494 centimeters in the West (X), South (Y) and Down (Z) direction.
- In the WID stage, East (X) wind-induced displacements of the cantilever beam were identifiable. This was attested based on a strong normalized cross correlation coefficient of 0.73 and a time lag error of -4 minutes and 48 seconds, identified between a relevant sequence of orthogonal wind components (U(East)/ V(North)) and East (X) and North (Y) displacements ($\delta \hat{x}_i^{sc}$) during day 078. The maximum identified wind-induced displacement of the cantilever beam in East (X) direction is equal to 3.39 centimeters. No displacement could be identified in North (Y) and Up (Z) direction.
- Specifically, for the AID stage a validation example using a laser distometer was proposed. After applying a linear trend and a quadratic function model to extrapolate the derived displacement quantities of the laser distometer to the beam's top, a very good statistical and visual match between the GNSS based – and distometer based displacements was attested.
- For validation purposes of the WID stage results, a relevant example of the implementation of the forward and reverse transformation based on accelerometer data was considered. Due to the strong fragmentation of the smartphone accelerometer data and the encountered non-linearly increasing time lag error with respect to the GNSS based acceleration and displacement time series, the capability of the GNSS module of measuring wind-induced (dynamic) displacements could be only visually attested.
- The precision potential of the low-cost dual frequency GNSS module is underestimated by the manufacturer. The empirical precision of the GNSS module in East (X), North (Y) and Up (Z) direction was equal to ± 0.4, 0.5 and respectively 1 centimeter (standard deviation). If one is considering a MP correction, the precision can be further improved to a noise level of 0.3, 0.4 and respectively 0.8 centimeters.
  A certain degree of time correlation in the GNSS based displacement quantities was found. The East (X)/ North (Y)/ Up (Z) noise sequences follow an exponential decaying behaviour characterized by a de-correlation time of 2 to 3 minutes. A significant part of it can be likely accounted to residual MP that could not be efficiently removed.
- The smartphone accelerometer performance tends to be largely overestimated by the manufacturer (empirical noise level of the accelerometer $\rightarrow 0.005 \frac{m}{s^2} > 4.954 * 10^{-6} \frac{m}{s^2} \leftarrow$ specified formal noise level).
  Since the identified de-correlation period of the data sets output by the smartphone accelerometer during the cantilever beam experiment was of only 0.396 seconds, these data sets can be considered to correspond to uncorrelated, raw acceleration information.

5

Real-Time Displacement Identification

Having shown that the studied low-cost dual frequency GNSS system is capable of precisely sensing wind-induced displacements of slender structures, in the next step one would be interested to discuss the technicalities for implementing a GNSS based SHM system to operate in real time.
This chapter introduces and discusses some of the most important aspects, such as RTK positioning, MP correction integration, integer ambiguity estimation and statistical hypothesis testing for the identification of structural displacements, that need to be considered in the design and implementation process of a real-time SHM displacement identification system. Hence the deployment of RTK positioning via RTKNAVI AP, a PRN code based satellite geometry similarity check for the implementation of the MP correction, a integer ambiguity quality flag based filtering procedure and success rate analysis for considering only precise, ambiguity fixed baseline solutions and the computation of a continuously updated daily success rate quantifier, and a 1D and 3D displacement identification algorithm based on an outlier & slip test based statistical hypothesis testing procedure, are introduced as indispensable tools for real time structural displacement analyses.
This chapter offers answers to the remaining research questions. Hence an answer is formulated related to the necessary steps for the integration of a GNSS based real time SHM monitoring system, followed by answers describing the procedure of implementing of the discussed relative position based MP correction in real time, and to the effectiveness of the proposed displacement identification system for estimating and accurately identifying critical beam displacements.

5.1. REAL TIME STRUCTURAL HEALTH MONITORING. MOTIVATION & BENEFITS

A structural health monitoring system is a set of integrated sensors and statistical based data analysis algorithms that work together for (continuously) monitoring of a structure's current state in order to accurately detect any structural damage. During the life service of a structure, damage can be studied from a structural engineering point of view by searching for abnormal variations in the modal characteristics of the structure, such as the natural frequency, damping ratio and mode shape, but also from a geodetic point of view through the identification of critical static and quasi-static displacements of the structure, produced by natural factors such as wind storms, earthquakes or land slides. Thus, the usefulness of a real-time SHM operating system is evident, making it possible to monitor the structure well-being and deploy maintenance or evacuation decisions in near real time for ensuring conservation of important structures and public safety. This study focused more on the geodetic approach, aiming to present the advantages of a low-cost dual frequency GNSS system for monitoring low frequent changes in the structure's body and fill the gap of conventional structural engineering sensors. Furthermore, in this study some first steps towards fusing the results of the GNSS module with a smartphone accelerometer are made. Thus, based on the knowledge from chapter 3 and the knowledge to be presented in this chapter, a set of steps is proposed under the form of a scheme (see figure 5.8) that should ease and standardize the integration and implementation of a low-cost GNSS based SHM displacement sensing system in real time.

In operation mode the SHM monitoring system is collecting data at a high rate, analyzing them based on sophisticated statistical algorithms and monitoring any discrepancy in the nominal structure characteristic and current position. Throughout this, the set of collected data is fed through mathematical models in order to gain knowledge and describe the current state of the case study structure to investigate if sudden changes in its position appear. This process is also known as an estimation process, where observation data is ideally producing the best picture of the structures position. Nevertheless, caution needs to be taken because any observations is affected by measurement noise, which makes the estimation process offer a limited perspective over the real state of the structure. On top one should note that there is no mathematical model that can perfectly describe the physical reality as well. Therefore, an assessment process, also known as statistical validation process, is indispensable, to check if "the considered mathematical models are sufficiently consistent with the data observed"(Teunissen [1]). More on this topic can be found in section 5.5. Hence, the estimation and validation processes are key tools of the integrated displacement detection system for effectively deriving and identifying any deterioration in the structural integrity caused by natural factors.

The primary motivation for implementing a real-time low-cost GNSS based SHM monitoring system is driven by the current trend in civil engineering for building bigger and slender structures to satisfy the needs of nowadays society. Moreover, "the rapid advancement of the GNSS device and algorithms has enabled"(Im *et al.* [2]) its use for real-time SHM monitoring, while its low price makes it perfect for the installation of a large amount of GNSS modules in sensor arrays to cover the case study structure and have a detailed view over its structural integrity in real time. Moreover, developing countries that are frequently hit by hurricanes or earthquakes can benefit from their inexpensiveness for developing national GNSS based natural disaster monitoring systems to protect their population.

Throughout this, the civil engineering industry will benefit from being able to discriminate the static and quasi-static displacement component of a structure. On long term, by being able to monitor the permanent displacement of a structure over its service life a better understanding of the used materials can be derived and further used for developing better structure designs. Moreover, in case of a flexible structure the GNSS equipment is able to monitor the dynamic behaviour of the structure as well, offering a validation procedure for the results based on conventional monitoring sensors such as accelerometers and surveying equipment. Ideally conventional monitoring sensors should be coupled with a GNSS module to complement each other and facilitate SHM campaigns by capturing the static, quasi-static and dynamic movements of a major structure. Moreover, the inexpensiveness of a low-cost GNSS system and its compact form should bring economic benefits and make its installation procedure straightforward in any place with an open sky view. However, the most important benefit of using GNSS equipment is linked to the capability of running precise surveys in real time anywhere around the world via RTK positioning.

5.2. REAL TIME KINEMATIC POSITIONING. TESTS & RESULTS

THE first requirement for deploying real-time SHM campaigns is the need of estimating and screening structural displacements in near real time. To facilitate this, GNSS systems can produce precise relative positions based on the RTK positioning principle.

In this principle, CP, pseudorange and navigation data, are packed according to Radio Technical Commission for Maritime Services (RTCM) or Network Transportation of RTCM Internet Protocol (NTRIP) formats and transmitted in real time from a GNSS reference station to a rover station via radio link or internet connection. Throughout this, systems of DD observations (see section 2.4) are formed in real time to estimate sub centimeter precise baseline solutions, after the DD CP ambiguities[1] are resolved to integer values.

As previously mentioned in section 2.2, RTKLib software APs, STRSRV and RTKNAVI, were concurrently used during the cantilever beam experiment to log, process and screen position results in near real time. In this case the connection and data flow[2] between the BRD01 reference station and BRD02 rover station was established via active USB cables, where RTCM3 messages from the reference station together with UBX raw GNSS measurements from the rover station were processed by RTKNAVI via RTK positioning concurrently with the data acquisition. The exact RTK configurations that were fed in RTKNAVI can be found in table H.1 in appendix H. Note that in this case, three GNSS constellations were used to perform RTK positioning, mainly GPS, Galileo and BeiDou. This was set so, as to increase the number of the considered satellites, hence the number of CP and pseudorange observations, in order to speed up the integer ambiguity estimation process and derive baseline solutions with high precision.

Additionally, when configuring RTKNAVI to perform RTK positioning, it was found that this software is not able to frequently fix solutions[3] for a ratio-factor (c) larger than 2. Thus, for making RTKNAVI fix solutions as good as RNX2RTKP does through PPK relative positioning, the ratio-factor[4] was set equal to 1. This option is making the Ratio Test[5] loose its functionality of validating the resulting integer ambiguities. Consequently before attesting the correctness of the RTKNAVI based displacement quantities ($\delta\hat{x}_{076}^{RTK}$), these need to be compared with the PPK based displacements ($\delta\hat{x}_{076}$) resulting from the RNX2RTKP solutions, which were validated by a functional Ratio Test.

To do so, two RTK processing tests were conducted to assess the performance of RTKNAVI for deriving baseline solutions in near real time. The very first one was performed during the AID stage, when the East (X) and Up (Z) RTK based displacement time series were following a similar behavior with the PPK based displacement time series (see figure 5.1). To quantitatively attest this, the annotated cross-correlation parameter at lag 0 ($R(0)_{\delta\hat{x}_{076},\delta\hat{x}_{076}^{RTK}}$) on East(X) and Up(Z) direction from figure 5.1 was close to the desired value of 1. Moreover, in comparison to the PPK based observations, the RTK based observations were able to fix the ambiguities and derive displacement solutions between 17:25:30 and 17:26:00. Furthermore, in case of the RTK processing test, the returned daily ambiguity fixing rate was at maximum[6]. These results demonstrate the capability of the RTK positioning functionality of RTKLib software of deriving position solutions in real time and for conducting real-time SHM campaigns even in the presence of an non-existent ambiguity Ratio Test. However, one should consider that this first test was run over a short period of only 6 minutes.

Therefore, in order to test the potential of RTKNAVI to output baseline solutions over a longer period, a second RTK positioning test was performed during the WID stage, where RTKNAVI was let to compute relative position solutions in near real time from 16/03/2020 19:22:30 UTC over the three considered days of the experiment. However, it was found that the RTK baseline solutions were recorded only from 16/03/2020 19:22:30.2 until 16/03/2020 20:00:01.0 UTC. Hence, no comparison between the PPK and RTK based displacement solutions of the WID stage could be performed. It is believed that this was caused by the wrong setting of the RTK solution configurations under the pressure of the late equipment installation process. Therefore, a second test should be considered for effectively validating the capability of RTKNAVI to uninterruptedly output real-time position solutions over long periods.

[1] for a detailed discussion on integer CP ambiguity estimation please inspect section 5.4.
[2] for a more detailed picture of the data flow between the reference and rover station please refer again to figure 2.2.
[3] a fixed solutions corresponds to a relative position estimate for which the CP ambiguities were resolved.
[4] expressed by the "Min Ratio to Fix Ambiguity" parameter from the configuration panel of RTKNAVI.
[5] for more details about the Ratio Test please refer to (5.5) from section 5.4.
[6] $Q_1 = 100\%$.

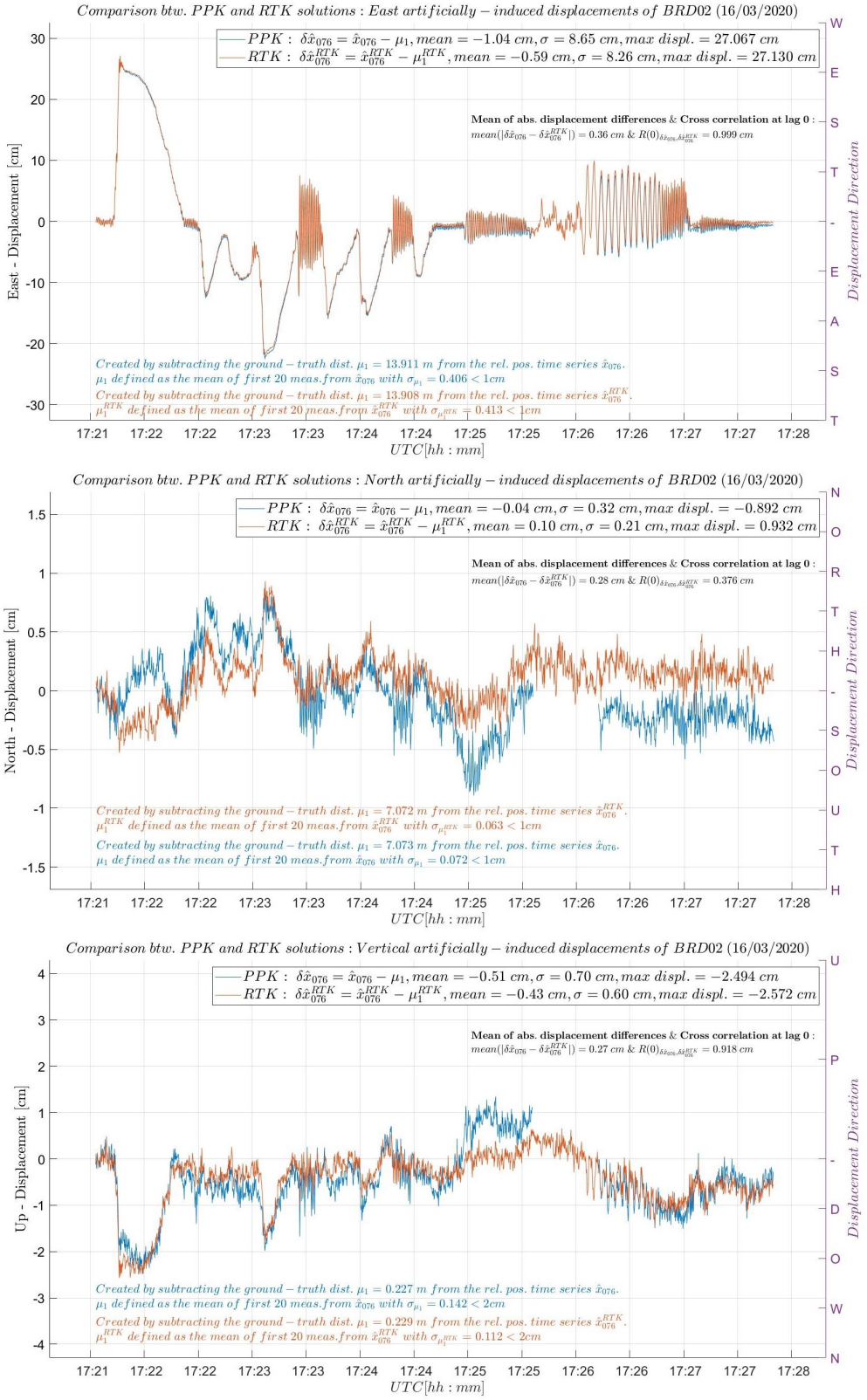

Figure 5.1: Comparison between East (top) / North (middle) / Up (bottom) PPK (blue) and RTK (red) based displacement solutions of the AID stage. Almost ideal match between the East (X) and Up (Z) candidate time series with a close-to-one cross-correlation parameter, can be observed. Note the different scaling of the vertical axis in these three plots.

5.3. REAL TIME IMPLEMENTATION OF MULTIPATH CORRECTION

As far as it is known, several studies ((Kijewski-Correa and Kochly [3]), (Chan *et al.* [4]), (Moschas and Stiros [5])) investigated the development process of MP corrections, but non of them have defined an implementation procedure of such corrections in a real time monitoring system. In the next lines a stable, real-time implementation procedure of the previously derived relative position based MP correction is introduced.
Recalling that the success of the proposed relative position based MP correction in effectively correcting for MP is fully dependent on keeping the satellite geometry unchanged over each considered (sideral) day, a checking procedure based on the satellites PRN code numbers information from the resulting RTKLib residual structures needs to be developed. This checking procedure aims to group all visible/ captured satellites into 5 Hz sampled cells, forming daily frequency dependent[7] cell arrays of grouped PRN codes.
Then in order to check if the same satellite geometry was kept over each successive day and to determine when to apply the proposed MP correction, the resulting array of grouped PRN codes of the MP calibration day can be cell wise compared with the cell array of each windy day. Hence, if a candidate cell holds identical PRN codes, the applicability of the MP correction at that specific time instant can be attested. This checking procedure can be developed to perform a cell wise comparison in real time, immediately after collecting and grouping the PRN codes. However, in this study its efficiency on already collected time series of PRN code numbers is studied, trusting that the real-time implementation can be easily worked out.

In the context of the cantilever beam, two frequency dependent cell arrays of PRN codes over (sidereal) day 078 and 079 were created to be compared for identifying the time stamps when the MP correction can be applied. Recall that day 079 was considered the calibration day of the relative position based MP correction while day 078 was chosen as a candidate day with favorable wind patterns and a very good data coverage.
Additionally, in the making of these time series a filtration step needed to be developed to consider only the satellites that are transmitting valid observations (vsat=1) and produced fixed position solutions (fix≥2).
Moreover, the resulting time series of grouped PRNs and their corresponding UTC time series needed to be filled with NaN values in order to follow the preset 5 Hz rate and compensate for any processing errors that were causing gaps in the outputted residual structures, just as presented at the end of appendix H. Furthermore, based on the presented two-step sidereal cut procedure in subsection 3.2.3, the resulting cell arrays needed to be cut to 430820[8] long cell arrays of grouped PRNs, spanning exactly over a sidereal long period of 23 hours 56 minutes and 4 seconds.
Below the entire set of steps for deriving the candidate frequency dependent cell arrays of grouped PRN codes is summarized. This set of steps, together with the approach developed in section 3.2.4, can be considered as a prompt answer to the research question asking for a real-time MP correction implementation procedure.

- For each candidate day select/ extract the PRN code number information corresponding:
  - to a specific GNSS frequency band (j=L1/L2).
  - to valid satellite information (flag: vsat[9]=1).
  - of satellites that are producing ambiguity fixed solutions (flag: fix[10]≥2).
- For every 0.2 seconds, group all selected PRN codes into cells and define frequency dependent cell arrays of grouped PRN codes for the considered experimental days.
- Fill the resulting cell arrays and their corresponding UTC time series with NaN cells at the time instants for which no CP residual solution is available.
- Based on the two-step created-sidereal cut algorithm, cut the resulting cell arrays to span a sidereal day.

Based on the obtained frequency dependent cell arrays of day 078 and 079, one can compare their grouped PRN information cell by cell, generating frequency dependent logical arrays.
Since the estimated GNSS based relative positions are a result of a dual frequency DD estimation process (see

[7] the recorded PRN codes correspond to GNSS satellites in view, which can transmit information either on the L1 or L2 frequency bands.

[8] $= ((23*60+56)*60+4)*5\,[seconds*samples]$.

[9] corresponds to the flag used by RTKLib for labeling valid satellite information. For more details please refere to RTKLib's manual: http://www.rtklib.com/prog/manual_2.4.2.pdf, pg 107.

[10] corresponds to the flag used by RTKLib for labeling CP residual estimates with their ambiguities fixed. For more details please refer to RTKLib's manual, pg 107.

section 2.4), for each day one can combine the resulting frequency dependent logical arrays via a point-wise multiplication process. The resulting logical array of day 078 and 079 can be finally compared to decide when the satellite geometry was matching, making the application of the MP correction possible. Thus, the MP correction ($\hat{x}^{sc}_{079}$) can be applied only in case of true(=1) values that correspond to time instants when the candidate groups of PRN codes matched. The application procedure can be performed based on (3.18). On the other hand, in case of different flags (0 or NaN) the MP correction should be discarded. Consequently, to complement for the lack of use of any correction, one can subtract the ground truth baseline ($\mu_1 = \overline{\hat{x}^{sc}_{079}}$) from the remaining, uncorrected relative positions of day 078 ($\hat{x}^{sc}_{078}$) to derive the desired displacement time series ($\delta\hat{x}^{sc}_{078}$). To better understand the workflow of the previously presented set of steps for the implementation of the proposed relative position based MP correction, a schematics of an example is appended in appendix N.

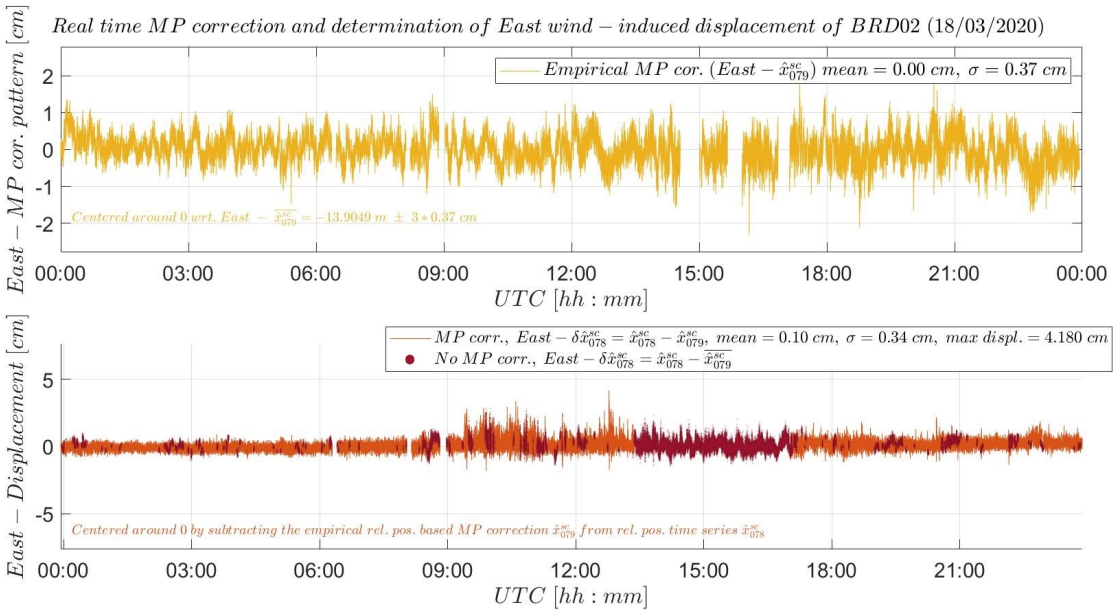

Figure 5.2: Figure of the implementation of MP correction in real time, containing the plot of the empirical, relative position based (yellow - $\hat{x}^{sc}_{079}$, top) MP correction and the plot of the resulting East (X) wind-induced displacements time series of day 078 ($\delta\hat{x}^{sc}_{078}$, below) consisting of MP corrected (red) and uncorrected (magenta) displacement samples

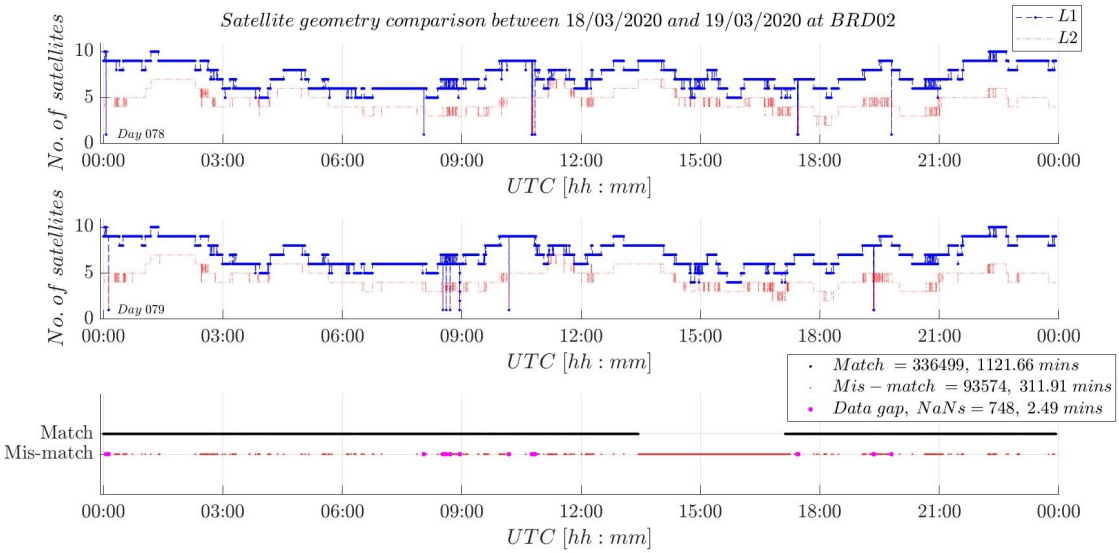

Figure 5.3: Comparison between the number of satellites in view at both the GNSS reference and rover receivers over day 078 (top) and 079 (middle). Both plots indicate the number of satellites in-view from which the GNSS reference and rover receivers recorded information on L1 (blue) and L2 (red) frequency. Below a plot of the logical array indicating when the MP correction can (flag=1, black) or cannot (flag=0 (red) or NaN (magenta)) be applied. In total the satellite geometries over the candidate days was mismatching over a period longer than 5 hours

The results of the aforementioned MP correction implementation process are displayed below in figure 5.2

only for the East (X) direction[11], where the resulting, uncorrected displacement quantities are marked with magenta dots. Additionally, a plot with the time stamps at which the MP correction could or could not be applied over day's 078 relative position time series, is presented in figure 5.3. This plot indicates a number of 93574 + 748 time stamps[12] at which the satellite geometry over the candidate sidereal days was mismatching.
On behalf of this result, it can be concluded that without performing such a check and by just approving the applicability of relative position based MP correction based on the visual interpretation of the repeatable behavior in the overlapping plot of the zero-centered position time series of the windy day and the MP correction (review figure I.2) one can obtain unrealistic displacement results, which can ultimately affect the displacement identification process. Therefore, it is important to identify and treat the uncorrected displacement quantities with caution and give them less importance in the displacement detection process.

5.4. REAL TIME AMBIGUITY SUCCESS RATE EVALUATION

So far, many references have been made within this document to ambiguity fixed position solutions, but no detailed explanation of this process has been given. Therefore, in this section four topics are introduced starting with the theoretical aspects underlying the process of integer ambiguity estimation (IAE), followed by a formal success rate analysis over the second day of the experiment based on the VISUAL software and the integer bootstraping (IB) principle, and an empirical success rate analysis based on RTKLib's integer least squares (ILS) principle. Lastly, a comparison between the results of the two considered success rate analyses is made to assess the daily success rate over the second day of the beam experiment, and the usefulness of the VISUAL software for performing preliminary formal success rate analyses for assessing the ambiguity success rate at a specific location, prior to the equipment installation.

INTEGER AMBIGUITY ESTIMATION PROCESS

To suggestively explain the process of integer ambiguity estimation (IAE), one can portray the transmitted GNSS carrier wave as a sinusoidal signal, which is received by the GNSS antenna at ground and passed to the receiver. In the process of CP based relative position estimation, the GNSS receiver is producing a carrier wave replica, which is then aligned with the received signal to estimate the fractional phase (difference) between the two sinusoidal waves. To facilitate the relative position estimation process and derive sub centimeter precise positions, loosely spoken, the receiver needs to additionally determine the integer number of cycles between the satellite and the GNSS receiver antenna. This process is known as integer ambiguity estimation and is not trivial due to the homogeneous behavior of the received sinusoidal signal.

In a nutshell an IAE process can be performed in three steps:

- Determination of the desired parameters of a DD estimation process based on a least-squares adjustment. This will result in the determination of a float baseline solution ($\hat{b}$), float carrier wave ambiguities ($\hat{a}$) and their corresponding variance-covariance matrices ($Q_{\hat{a}\hat{a}}$, $Q_{\hat{b}\hat{b}}$ and $Q_{\hat{a}\hat{b}}$).

$$\begin{aligned} y &= Aa + Bb + \epsilon \\ \hat{a}, \hat{b} &= \underset{\substack{a\epsilon\mathbb{R}^n \\ b\epsilon\mathbb{R}^p}}{min}(y - Aa - Bb)^T Q_{\hat{y}\hat{y}}^{-1}(y - Aa - Bb) \\ \begin{bmatrix} \hat{a} \\ \hat{b} \end{bmatrix} &; \begin{bmatrix} Q_{\hat{a}\hat{a}} & Q_{\hat{a}\hat{b}} \\ Q_{\hat{b}\hat{a}} & Q_{\hat{b}\hat{b}} \end{bmatrix} \end{aligned} \tag{5.1}$$

where:

a = unknown integer valued vector ($\epsilon\ \mathbb{Z}^n$) of DD ambiguities
b = unknown real valued vector ($\epsilon\ \mathbb{R}^p$) of DD baseline coordinates [m]
A, B = design matrices
y = observation vector
ϵ = random noise vector
$\hat{a}$ = float ambiguity estimate vector
$\hat{b}$ = float baseline estimate vector [m]
$Q_{\hat{a}\hat{a}}$ = variance-covariance matrix of the float ambiguities
$Q_{\hat{b}\hat{b}}$ = variance-covariance matrix of the float baseline solutions
$Q_{\hat{a}\hat{b}}$ = covariance matrix of the float ambiguities and baseline solutions

[11] corresponding to the weak axis of the cantilever beam which was influenced by West wind during day 078.
[12] equivalent to 314.4 minutes = 5.24 hours.

- Estimation of the integer ambiguities. For this three principles are mentioned in the literature (Teunissen [6]): integer rounding (IR), integer bootstrapping(IB) and integer least squares (ILS). The latter one is most optimal and is integrated in the famous LAMBDA method. The LAMBDA method consisting of two steps:

  – Z-transform decorrelation of the float ambiguities to improve their precision and reduce their correlation. This process is flattening the search space, facilitating the integer ambiguity search process. For more details please refer to (Teunissen [7]).

$$\begin{aligned} \hat{z} = Z^T \hat{a} \Rightarrow \check{a} = Z^{-T} \check{z} \\ Q_{\hat{z}\hat{z}} = Z^T Q_{\hat{a}\hat{a}} Z \ and \ Q_{\hat{b}\hat{z}} = Q_{\hat{b}\hat{a}} Z \end{aligned} \tag{5.2}$$

where:

$\hat{z}$	= transformed float ambiguity vector
$\check{a}$	= integer ambiguity estimate vector
$\check{z}$	= transformed integer ambiguity estimate vector
Z	= decorrelation matrix
z	= unknown true transformed ambiguity vector
$Q_{\hat{z}\hat{z}}$, $Q_{\hat{b}\hat{z}}$	= transformed variance-covariance matrices

  – Search for the correct integer ambiguities within the flattened pull in region, resulting in the desired integer ambiguity estimate vector $\check{a}$.

$$\check{a} = \underset{a \epsilon \mathbb{Z}^n}{min} (\hat{a} - a)^T Q_{\hat{a}\hat{a}}^{-1} (\hat{a} - a) \tag{5.3}$$

Minding that the IAE is not a perfect process, its application can result in incorrectly fixed integer ambiguities values. To take care of such a problem, one can additionally opt for an acceptance test, such as the Ratio Test, to check for the correctness of the fixed integer ambiguities values. The test statistics of the Ratio Test (see 5.4) is defined as "the ratio of the squared sum of the “second-best” ambiguity residual vector (a_2) and the squared sum of the “best” ambiguity residual vector (a)" (Verhagen and Teunissen [8]), which is then compared with a pre-set ratio factor/ critical value (c). In case this ratio is smaller than the user-defined critical value, than the computed integer ambiguity solution can be rejected in favor of the float solution. Such a test can facilitate three outcomes: "success if the integer ambiguity is estimated correctly, failure if the integer ambiguity is estimated incorrectly and undecided if the real-valued float solution is maintained"(Verhagen and Teunissen [8]).

$$Accept \ \check{a} \ if: \frac{(\hat{a} - a_2)^T Q_{\hat{a}\hat{a}}^{-1} (\hat{a} - a_2)}{(\hat{a} - a)^T Q_{\hat{a}\hat{a}}^{-1} (\hat{a} - a)} > c \tag{5.4}$$

where:

$(\hat{a} - a_2)^T Q_{\hat{a}\hat{a}}^{-1} (\hat{a} - a_2)$	= squared sum of the residuals with the second best integer vector
$(\hat{a} - a)^T Q_{\hat{a}\hat{a}}^{-1} (\hat{a} - a)$	= squared sum of the residuals with the best integer vector
c	= ratio-factor/ critical value

As previously mentioned this integer ambiguity validation procedure is optional and forms together with the IAE procedure the so called integer aperture (IA) estimation process.

- Application of a second least-squares adjustment with the determined integer ambiguities ($\check{a}$) as known values, resulting in high precision baseline estimates ($\check{b}$).

$$\begin{aligned} \check{b} = \hat{b} - Q_{\hat{b}\hat{a}} Q_{\hat{a}\hat{a}}^{-1} (\hat{a} - \check{a}) \\ Q_{\check{b}\check{b}} = Q_{\hat{b}\hat{b}} - Q_{\hat{b}\hat{a}} Q_{\hat{a}\hat{a}}^{-1} Q_{\hat{a}\hat{b}} \end{aligned} \tag{5.5}$$

where:

$Q_{\check{b}\check{b}}$ = variance-covariance matrix of the integer baseline solutions [m^2]

The main goal of the IAE process is to assist the DD relative position estimation process (see section 2.4) to improve the precision of the baseline estimates. This reads so since a float baseline solution is characterized by a meter precision level while a fixed baseline solution reaches the centimeter level precision, attesting that float baseline solutions are unacceptable for SHM purposes.
Particularly, within this research the IAE process was used to identify, which position estimates are precisely fixed and can be further considered for deriving significant displacement quantities. Hence the float baseline estimates could be filtered out based on the filtration process in appendix H, on behalf of IAE based ambiguity quality flags[13], resulting in data gaps within the derived cantilever beam displacement time series (see the last plots from figure I.3, I.4 and I.5 in appendix I). As one can see from the last plots from figure I.3, I.4 and I.5 in appendix I, the behaviour of the displacement time series in the proximity of the (float solutions based) data gaps is diverging from the steady state, close-to-zero behaviour. Thus, based on the consideration that the observed divergences are caused by the loss of fixed ambiguity, the IAE process is useful at identifying and highlighting the time periods when one should not confuse the (float solution based) divergences in the displacement time series with actual cantilever beam displacements.
Moreover, it is evident that in case of real time applications one is interested to filter out any float ambiguity estimates to derive only fixed displacement solutions of high precision and rise correct alarms. Hence, the importance of the IAE process for real time applications cannot be denied.

5

FORMAL INTEGER BOOTSTRAPING SUCCESS RATE ANALYSIS

HOWEVER, one should keep in mind that the IAE is not a perfect process due to the inevitable influence of measurement noise, resulting in a non-zero chance of incorrectly estimated integer ambiguities that can be translated in wrongly fixed baselines. Therefore, to quantify the correctness of the IAE process, one can perform an a-priori success rate analysis to verify if float ambiguities are sufficiently precise such that they will result in a high probability of correct fixing. This can be done by computing the probability of correctly estimating the integer ambiguities ($P_{s,B} \approx P_s$) via the IB success rate[14] (see 5.6), which can be exactly evaluated on behalf of only the variance-covariance matrix of the float ambiguity solutions ($Q_{\hat{a}\hat{a}}$).

$$
\begin{aligned}
P_{s,B} &= P(\check{z}_B = z) = \prod_{i=1}^{n} \left(2\Phi\left(\frac{1}{2\sigma_{\hat{z}_{i|I}}}\right) - 1 \right) \\
\Phi(x) &= \frac{1}{\sqrt{2\pi}} \int_{-\infty}^{x} exp\left\{ -\frac{1}{2} t^2 \right\} dt
\end{aligned}
\tag{5.6}
$$

where:

n = no. of considered ambiguities
$P_{s,B}$ = success rate of IB $\in [0:1]$
$\Phi(x)$ = cumulative normal distribution
$\sigma_{\hat{z}_{i|I}}$ = square root of the conditional variance of the i^{th} ambiguity (conditioned on previous I=1,$\cdots$,i-1 ambiguities)[15]

Since, the success rate can be computed without the need of actual GNSS observations, this means that P_s can be formally determined over a specific time interval by performing preliminary design calculations for a specific location, to discern when one should expect float baseline solutions that can be reflected in displacement quantities with poor precision.
To do so, the VISUAL software package (Verhagen [10]), was used to perform a formal success rate analysis on the second day (day 078) of the experiment. On behalf of predefined satellite ephemeris from downloadable almanac files, the VISUAL software is able to determine the required variance-covariance matrix of the float ambiguities and compute the IB success rate over a user-defined time interval, in this case of 1 minute, using only a single/ first snapshot of the satellite geometry, resulting in a every-minute time series of IB success rate values.
To do so a set of input parameters are needed to be input in the GUI of the software. The exact parameters that were used for performing day's 078 formal success rate analysis are listed below:

- ***GNSS system***: GPS
- ***Frequencies***: L1+L2
- ***Almanac file(s)***: GPS Yuma almanac for day 078 (18/03/2020)[16]
- ***Start date***: 17-Mar-2020 23:56:04
- ***Stop date***: 18-Mar-2020 23:52:08
- ***Number of epochs***: 1[17]

[13] Q_1 = correctly fixed ambiguity, Q_2 = float ambiguity or omitted/ rejected ambiguity.
[14] this is known to be a tight lower-bound for ILS method (Teunissen [9]).
[15] for more details review (Teunissen [6]).

- ***Time interval***: 60 seconds[18]
- ***Cutoff elevation***: 15°
- ***Scenario:*** Static[19]
- ***Ionosphere & Troposphere models:*** fixed[20]
- ***Phase standard deviations:*** 0.005 meters [21]
- ***Code standard deviations:*** 0.4 meters
- ***Location:*** *Lat:* 51.622146 °, *Lon:* 4.720445 °, *Ell H:* 47.0929 m (BRD02 ITRF14 geographic position referred to WGS-84 ellipsoid)[22]

For the computation of the every-minute success rate ($P_s(t')$) over (sidereal) day 078, equation (5.6) is assuming that the float ambiguity solutions are unbiased, hence that the proposed functional model is correctly defined. However, it is obvious that the VISUAL software is able to generate an approximated functional model, taking into account only atmospheric errors and not bias sources such as "the outlier in the code data, CP cycle slips or MP" (Verhagen [11]). The VISUAL software is computing the success rate every minute, on behalf of the variance-covariance matrices resulting from a single epoch approach, independent from the need of actual GNSS observations and without considering any connection with the previously determined success rate values. Thus, one should not overestimate the results of the formal success rate analysis and treat it as a preliminary/ design calculation process for getting an indication on the suitability of the GNSS system location, prior to the actual installation, for correctly deriving the integer ambiguity estimates reflected in the estimation of precise, fixed baseline solutions.

5

EMPIRICAL INTEGER LEAST SQUARES SUCCESS RATE ANALYSIS

To check how well the results match with reality, a validation procedure on behalf of an empirical success rate analysis based on GNSS observations and their corresponding ambiguity quality flags resulting from RTKLib processing software can be performed. In case of the cantilever beam experiment RTKLib's Continuous ambiguity fixing algorithm was preferred over the Fix and Hold and Instantaneous methods. This choice was made based on the results of a thorough analysis of the three ambiguity fixing methods during a SHM campaign run on a high-rise tower (Lapadat [12]), showing that the Continuous method works the best in case of low-cost equipment. Recall that the Continuous ambiguity fixing method works on the "principle of feeding each float ambiguity solution in a Kalman filter to continuously update the estimated CP biases on the basis of the current epoch's measurements and fix the ambiguities second by second" (Lapadat [12]). Moreover, note that the RTKLib's IAE process is based on solving an ILS problem via the LAMBDA method, where the resulting integer ambiguities are lastly validated by a Ratio Test, which is checking for a preset critical value[23] to be smaller "than the ratio of the squared sum of the residuals with the second best integer vector to with the best integer vector"[24] (see 5.4). Hence, the proposed empirical success rate time series ($\hat{P}_s(t')$) can be calculated as it follows:

$$\hat{P}_s(t') = \frac{\sum_{s=300*(t'-1)+1}^{300*t'} Q_1(s)}{\sum_{s=300*(t'-1)+1}^{300*t'} (Q_1(s) + \frac{Q_2(s)}{2})} \tag{5.7}$$

where:

$\hat{P}_s(t')$ = every-minute empirical success rate time series, $\in [0:1]$
t' = every-minute UTC time scale, t'=1$\cdots$1437 minutes[25]
s = every-minute stack of 300 ambiguity quality flags (sampled at 5 Hz), $\in [300*(t'-1)+1:300:300*t']$
Q_1, Q_2 = ambiguity quality flags: $Q_1 = 1$, fixed ambiguity; $Q_2 = 2$, float ambiguity

[16] downloaded from https://celestrak.com/GPS/almanac/Yuma/. For day 078 the following alamanc file was used: 0049.233472.

[17] in such a case the VISUAL software is considering the satellite configuration of the first epoch within the specified time interval for the computation of the every-minute IB success rate.

[18] corresponds to the time interval over which, the IB success rate is determined based on the considered snapshot(s) of the satellite geometry, related to the specified "number of epochs" parameter.

[19] a static model was assumed in concordance with the "number of epochs" parameter of 1, facilitating a single epoch IB success rate determination process. Furthermore, a static model was considered based on the underlying boundary condition of the cantilever beam experiment, which reads that over the entire observation time span the velocity/displacement of the cantilever beam was on average equal to zero.

[20] assumes that ionosphere and troposphere delays are completely eliminated/ absent for short baselines.

[21] the CP standard deviation parameter was set based on a mean value of the East (X)/ North (Y)/ Up (Z) noise level of the GNSS module, defined in section 4.4 (see legends from figure 4.11).

[22] BRD02's geographic coordinates referred to the WGS-84 ellipsoid, resulting from a Cartesian to degrees-decimal degrees transformation of the NRCAN based ITRF14(2020.1) XYZ-ECEF coordinates solutions from appendix H. Note that ITRF14(2020.1) XYZ-ECEF coordinates solutions were preferred instead of ETRS89 solutions, as a result of the handy NRCAN static PPP positioning service used for the determination of the absolute position at BRD01.

[23] typically chosen as 2 or 3. In this case this was chosen to be equal to 3.

[24] more details on RTKLib's IAE process can be found in appendix E7 within its user manual http://www.rtklib.com/prog/manual_2.4.2.pdf, pg. 166.

COMPARISON BETWEEN THE FORMAL AND EMPIRICAL SUCCESS RATE ANALYSES

IN the following the resulting minute wise empirical success rate time series ($\hat{P}_s(t')$), can be compared with the formal success rate time series ($P_s(t')$) from the VISUAL software for validation purposes.
Note that the empirical success rate time series results from a more laborious IA estimation process in combination with a recursive Kalman filter procedure, which is dependent on actual GNSS observations. Thus, due to the previously mentioned differences in the workflow of the VISUAL and RTKLib software, the proposed success rate comparison might not be completely fair but can be still considered as a rough validation of the formal success rate results.
Furthermore, before deploying this comparison, it is advisable to round both the formal and the empirical success rate values to two decimal units[26] and account for the final degree of equality between the candidate success rate time series, consisting of success rate samples[27] ≥ 0.99, over a full (sidereal) day through out a separate parameter cPs:

$$\textbf{IF } \left(P_s(t') == \hat{P}_s(t') \,\&\, P_s(t') \geq 0.99 \,\&\, \hat{P}_s(t') \geq 0.99\right) \Rightarrow \textbf{cPs(t')=1}$$
$$\textbf{ELSE } \left(P_s(t') \neq \hat{P}_s(t')\right) \Rightarrow \textbf{cPs(t')=0}$$

$$cP_s = \frac{\sum_{t'=1}^{1437} cP_s(t')}{1437} * 100$$

where:

$P_s(t'), \hat{P}_s(t')$ = every-minute formal & empirical success rate time series $\in [0,1]$
cPs = final degree of high success rate equality over a full sidereal day [%]

The aforementioned empirical success rate computation (5.7) can be easily implemented in real time on behalf of an external script that is scraping and using the on-the-flight (OTF) ambiguity quality flags of the real-time positioning AP RTKNAVI, to output minute wise empirical success rate values and update the daily cP_s factor.
Additionally, recall that one can use the raw ambiguity quality flags, Q_1 and Q_2, to develop a checking procedure, just like the one from the end of appendix H, for real-time exclusion of the float baseline solutions from the SHM process.

Based on the aforementioned information the final results of the proposed success rate comparison analysis of day 078 shows that only the minute-wise empirical success rate time series of success rate samples ≥ 0.99, was reaching a large probability of correct ambiguity fixing[28] of 99.2% over the entire day (see legend from figure 5.4). Furthermore, the overall empirical success rate ($\hat{P}_s^{sc}$) computed based on all RTKLib's raw ambiguity quality flags (see 5.8) reached a level of probability of 99.9%, attesting an almost optimal fixing rate over day 078.

$$\hat{P}_s^{sc} = \frac{\sum_{s=1}^{300*1437} Q_1(s)}{\sum_{s=1}^{300*1437} (Q_1(s) + \frac{Q_2(s)}{2})} * 100 \tag{5.8}$$

where:

$\hat{P}_s^{sc}$ = overall empirical success rate [%]

On the other hand, the formal success rate time series reached an average success rate that exceeds 0.99 of only 43.8%.
Considering the differences between the rudimentary way of VISUAL's software single epoch approach in comparison to the more laborious RTKLib's approach for determining the success rate, it is not surprising that the degree of equality (cP_s) between the two candidate success rate time series reached only 33.1%, discrediting the formal success rate analysis throughout the day. To better visualize the discrepancy between the compared success rate time series, in the last plot of figure (5.5) the difference between the empirical and formal success rate time series is shown in black. Large divergences during day 078 are identified around 4:00, 7:00 and 11:00 UTC. It is surprising that these divergences are not related to the divergences in the number of satellites in view from the first plot of figure (5.5), attesting that they are a result of the different way in which the two approaches compute the success rate.

[25] the 1437 minutes correspond to 23 hours and 57 minutes. This value represents the first integer number of minutes that entirely covers the duration of a sidereal day of 23 hours 56 minutes and 04 seconds, and mathematically speaking it results from the division of 431100 samples by the stack (s) length of 300 samples.
[26] this corresponds to rounding the decimal percentage values of the success rate probability values to whole numbers.
[27] a success rate value of at least 0.99 is deemed as a high enough success rate to lead to correctly fixed CP ambiguities.
[28] a success rate value of at least 0.99 is deemed as a high enough success rate to lead to correctly fixed CP ambiguities.

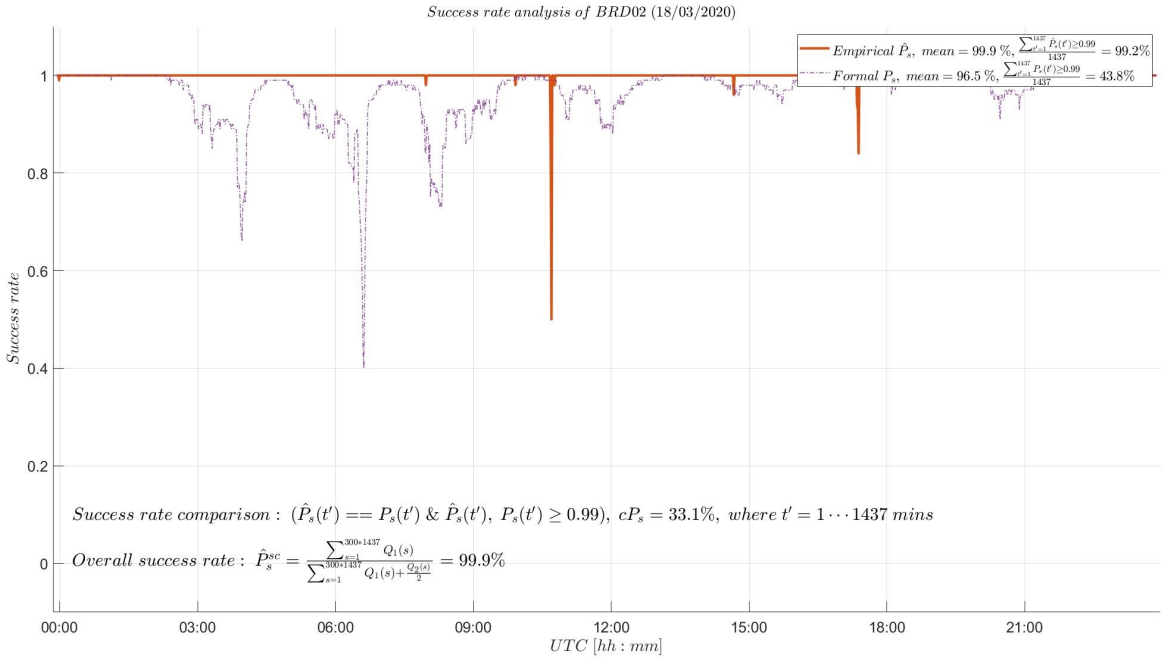

Figure 5.4: Comparison between the VISUAL based formal (P_s, purple) and RTKLib's based empirical success rate ($\hat{P}_s$, red) of day 078. Legend values indicate for $\hat{P}_s$ an almost perfect average success rate that exceeds 0.99 99.2% of the time, while in case of P_s this reached only 43.8%. Furthermore, the overall empirical success rate reached an almost optimal value of 99.9% over the entire (sidereal) day. The degree of success rate equality over the entire day (cP_s) is equal to 33.1%

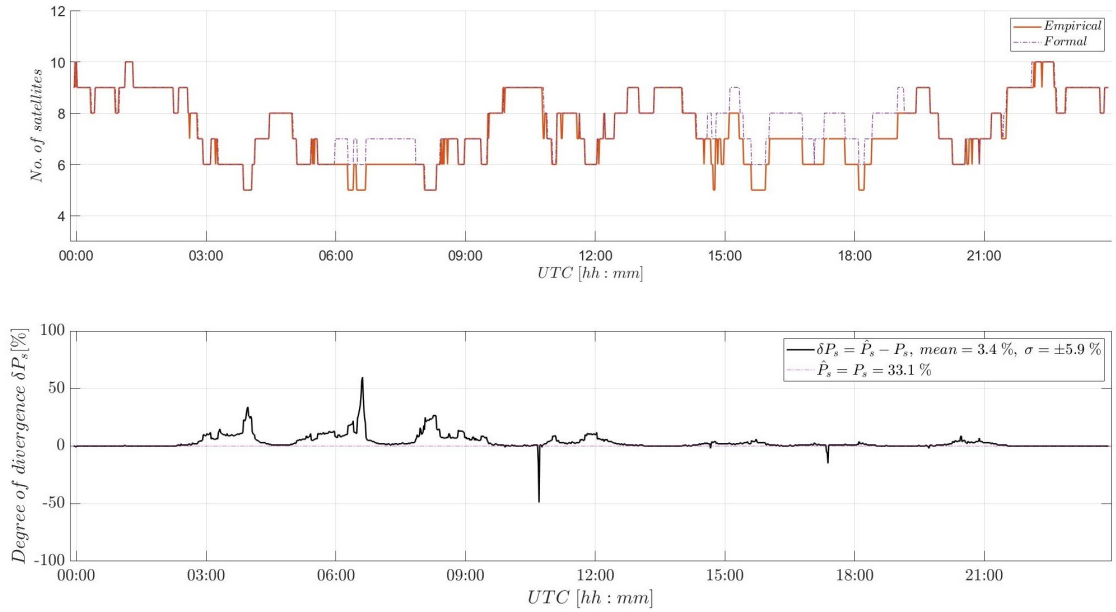

Figure 5.5: Top: Number of satellites vs UTC time plot, showing divergences between the formal and empirical number of visible satellites between 07:00-08:00 and 15:00-19:00 UTC. Below: Plot of the degree of divergence (δP_s) between the two success rate time series. The largest divergences between the candidate success rates can be observed around 04:00, 07:00 and 11:00 UTC

Hence, it is shown that the VISUAL software based success rate analysis could not reflect the actual probability of the BRD02 GNSS rover of effectively fixing the ambiguities, and this was primarily caused by its rudimentary single epoch approach for determining the success rate. Additionally, one should take into account that the proposed comparison is not very fair due to the more laborious way in which RTKLib outputs the ambiguity flags as a result of a IAE process in combination with a Kalman filter, which is improving the ambiguity

fixing rate resulting in a larger probability of correctly estimating the integer ambiguities. Thus, in the process of designing and setting up a SHM system, the use of VISUAL software is only recommendable for having a first view at the ambiguity success rate at a specific location. Moreover, in the future it would be interesting to perform a comparison between a VISUAL based formal success rate time series and an RTKLib ambiguity flags based empirical success rate time series on behalf of the more simple Instantaneous ambiguity fixing algorithm, to check if their results are getting close to each other. However, the overall empirical success rate attest that one can be 99.9% of the time assured that the IAE ran correctly over day 078, producing precise displacement quantities at BRD02 site.
Thus, through this analysis it has been demonstrated that the obtained VISUAL software based formal success rate results are underestimating the capability of the GNSS module to correctly fix the CP ambiguities at the experimental site. Furthermore, within this section a proposal of a real-time procedure for filtering out of unwanted float baseline solutions and deriving every-minute empirical success rate values that can be used for updating the daily success rate quantifier, was proposed. Lastly, it was shown that at this stage of development the VISUAL software is only useful for performing preliminary formal success rate analyses to make a first guess on the ambiguity success rate at a specific location.

5.5. Statistical Hypothesis Testing as an Integrated Part in the Displacement Identification Process

To close the circle of the displacement identification process, after deriving the cantilever beam displacement time series from estimated GNSS baseline solutions, it is decisive to develop an algorithm that can identify critical displacements of the case study structure with a certain level of confidence and rise correct alarms in near real time. This will result in a procedure that can be applied for correctly detecting and rising alarms in case of the appearance of any irregularity in the behavior of the cantilever beam, and answer the last research question related to the effectiveness of the proposed GNSS based displacement detection system for not only estimating but also accurately identifying structural displacements. From the beginning, it is important to stress that the resulting testing procedure does not work at pseudorange and CP measurements level but uses estimated coordinates/ displacement values as observations.
Therefore, in the next lines this section is divided into multiple subsections introducing the core principles of statistical hypothesis testing for displacement identification followed by the proposal of two testing hypotheses, forming a powerful uni-dimensional displacement identification procedure known as the 1D (position) outlier & slip test or simply said "the 1D outlier & slip test". Since, the proposed identification procedure is functioning based on a sliding window procedure, the choice for the most optimal window length on behalf of a 40-minutes long displacement time series of the WID stage is studied in a separate subsection, followed by a simulation analysis of a generated, synthetic displacement time series to assess the factual capability of the 1D displacement identification procedure for correctly detecting displacements. Furthermore, similar to the 1D test a tri-dimensional displacement identification strategy, known as "the 3D (position) outlier & slip test", is introduced. Its displacement identification performance is then compared to the one of its uni-dimensional predecessor. Last but not least, the internal reliability of the nominal uni- and tri-dimensional outlier testing procedures is studied from a theoretical point of view, for specifying the minimum displacements that these testing procedures can certainly identify.

Statistical Hypothesis Testing for Displacement Identification

To accurately identify structural displacements, one can appellate at basic concepts from the statistical hypothesis testing theory where the selection of an appropriate functional model, that should identify as reliably as possible the appearance of structural divergences from the structures initial steady state, is crucial. Hence, two models, formulated under two different hypothesis, should be confronted with the MP corrected GNSS based displacement quantities in order to identify which one is modelling best the displacement data. The first model is meant to test if all observations, under the form of cantilever beam displacement quantities ($\delta\hat{x}^{sc}_{078}$), describe the same neutral structural behavior/ position over a certain time period. Such a model is formulated under the null-hypothesis (H_0). If H_0 turns to be true, one can conclude that over the considered period the cantilever beam did not respond to any natural factors such as wind breezes. Otherwise, if H_0 turns to be false the alternative hypothesis (H_a) should be accepted. In such a case H_a tests if there is one or many displacement quantities describing a divergent/ extraordinary behavior from the nominal state of the considered structure within the period of interest.

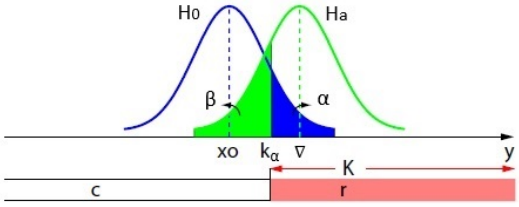

$$H_0 \ : \ \underline{y} \sim N(x_0, \sigma^2)$$
$$H_a \ : \ \underline{y} \sim N(\nabla, \sigma^2)$$

Figure 5.6: PDF of $\underline{y}$ under H_0 and H_a. The false alarm probability (α) is highlighted in blue, while the missed detection probability (β) is highlighted in green. The critical region (K) starts from the critical value (k_α) to the right. Courtesy to: (Teunissen [1])

To better visualize this testing procedure, picture the two hypothesis as two probability density function (PDF) curves (see figure 5.6) of the studied set of normally distributed (random) displacement observables, separated by the difference between their expectation values within each hypothesis. What the hypothesis testing procedure is doing, is to check if each displacement observation within the considered time period lies closer to the average displacement state (x_0) under the H_0 bell curve (=accept H_0) or closer to the average biased displacement state (∇) under the H_a bell curve (=reject H_0, accept H_a). This is done by comparing a single scalar quantity, also known as test statistic (T_q), "resulting from the "compression" of the observed displacement quantities" (Teunissen [1]) against a critical value (k_α), which is defining the limit(s) of the critical region (K) for which H_0 should be rejected.
Theoretically, the testing procedure has two possible outcomes:

- ***Accept*** H_0 = no displacement is present
- ***Reject*** H_0 ***and Accept*** H_a = displacement is present

But because any observation is subject to measurement noise, there is a possibility that the test outcome will not capture the real structural response of the structure, resulting in incorrect decisions. Thus, in practice there are two error types that can be encountered. The first one is known as a "false alarm" and expresses a state when for instance a structural displacement is detected although the structure never moved. This will have economic consequences, since for instance one should falsely evacuate the personnel from a business tower and stop the economic activity for no good reason. The probability of encountering such an error is mathematically expressed by parameter α and is known as the false alarm probability.
The second error type can have an impactful consequence for the safety of the personnel of the same business tower and is known as "missed detection". This is when "a structural change has taken places but it was not detected"(Teunissen [1]). In other words the test was not able to detect a critical displacement of the tower but in reality there was one which could make it collapse. The probability of such an event is denoted by parameter β. On behalf of this parameter one can define the "probability of correct detection" as $\gamma = 1 - \beta$, also known as the power of the test. This should be ideally maximum (=1) but in practice such value cannot be achieved. Thus, in the process of defining an optimal displacement detection test, the test(s) under proposal should be tuned to correspond to a high as possible γ value. In this process, it is important to understand that α and β are fully dependent on each other and when one is chosen to be larger, the other one will decrease and vice versa.

UNI-DIMENSIONAL DISPLACEMENT IDENTIFICATION TESTING PROCEDURES: THE 1D OUTLIER & SLIP TEST

THE scope of the proposed 1D testing procedure is to correctly identify "(potentially) real" wind-induced displacements[29] of the cantilever beam in one orthogonal direction, mainly along its weak (X) axis in the East direction. In the next lines a thorough explanation on the definition of a sliding window based uni-dimensional compound testing procedure and on the selection of the appropriate set of functional models for identifying the East (X) wind-induced cantilever beam displacements is given. This is presented in the context of the 40 minutes period of day 078 from figure 4.3, when the cantilever beam was responding to wind loads in the East (X) direction.

Prior to the deployment of any statistical test, the proposed 1D testing procedure should decide based on an auxiliary binary (m'=1) inspection, named as *"the* 3σ *check procedure"*, whether to look for of a nominal outlier in the m' long set of considered displacement observations, or to meticulously test for the identification of a possible position slip caused by a group of consecutive displacement observations from the m' long set, exceeding the noise level of the GNSS module. The 3σ check procedure can be expressed in the form of a

[29] by "(potentially) real" wind-induced displacements, it is meant all displacement estimates that have exceeded the 3σ boundaries of the GNSS noise band (=East (X): ± 0.9 cm, North (Y): ± 1.2 cm, Up (Z): ± 2.4 cm) over the studied 40 minutes period of day 078. Of course these values should be treated as possible beam displacements, modeling the true but unknown response of the beam to wind breezes.

statistical hypothesis testing procedure based on the following H_0 and Ha functional models:

3σ *Check Procedure - Null- and Alternative Hypothesis*

$$\begin{aligned} H_0 &: \underline{y}_{(m'=1,1)} = 0 + \underline{e}_{(1,1)}; \quad Qyy_{(1,1)} = \hat{\sigma}_E^2 \\ & E - \delta\hat{x}_{078}^{sc}(j) = 0; \quad Qyy_{(1,1)} = \hat{\sigma}^2_{E-\delta\hat{x}_{079}^{sc}(j)} = 0.003^2 \end{aligned} \tag{5.9}$$

$$\begin{aligned} H_a &: \underline{y}_{(m'=1,1)} = 0 + C_{y_{(1,q=1)}}\nabla_{(1,1)} + \underline{e}_{(1,1)}, \nabla(j) \neq 0; \quad Qyy_{(1,1)} = \hat{\sigma}_E^2 \\ & E - \delta\hat{x}_{078}^{sc}(j) = 0 + 1 * E - \hat{\nabla}(j); \quad Qyy_{(1,1)} = \hat{\sigma}^2_{E-\delta\hat{x}_{079}^{sc}(j)} = 0.003^2 \end{aligned}$$

m'	= number of considered displacement samples used to check the response of the beam to wind breezes
$E - \delta\hat{x}_{078}^{sc}$	= MP corrected East (X) displacement observation of day 078 $[m]$
$\hat{\sigma}^2_{E-\delta\hat{x}_{079}^{sc}(j)}$	= empirical standard deviation describing the GNSS noise level on East (X) direction $[m^2]$[30]
C_y	= matrix that links the observations to the unknown additional parameter ∇[31]
∇	= additional unknown parameters describing any bias in the considered stack of observations
q	= number of unknown additional parameters in ∇ vector within Ha, $\in [1, m'-n]$[32]
j	= sample number within the m' stack of considered displacement samples, $\in [1', \cdots, m']$

Generally speaking, the functional model under H_0 is testing for each observation (m'=1), if the East (X) displacement estimate is describing a still behavior of the cantilever beam, hence it cannot be considered as a "(potentially) real" displacement ($E - \delta\hat{x}_{078}^{sc} = 0$). On the other hand, the H_a is testing if the East (X) displacement estimate is corresponding to a bias, describing a divergent response of the beam from its neutral state ($E - \hat{\nabla} \neq 0$). Under the assumption that the direction of the (unknown) "true" beam displacement expressed by the East $\hat{\nabla}$ estimate is unknown[33], a test statistics value T_q for the 3σ check procedure can be derived on behalf of the particularization and simplification of the generalized formula (5.13) for the test statistics of a w-test:

3σ *Check Procedure - Binary Hypothesis Testing*

$$\begin{aligned} reject\ H_0\ if\ T_q(j) &= \hat{e}_0^T Q_{yy}^{-1} C_y Q_{\hat{\nabla}\hat{\nabla}} C_y^T Q_{yy}^{-1} \hat{e}_0 > k_\alpha \\ T_q(j) &= (y-0) * \frac{1}{\cancel{\hat{\sigma}_E^2}} * 1(1 * \frac{1}{\cancel{\hat{\sigma}_E^2}} * \cancel{\hat{\sigma}_E^2} * \frac{1}{\cancel{\hat{\sigma}_E^2}} * 1)^{-1} * 1 * \frac{1}{\hat{\sigma}_E^2} * (y-0) \\ &= \frac{y^2}{\hat{\sigma}_E^2} > k_\alpha \end{aligned} \tag{5.10}$$

$$|E - \delta\hat{x}_{078}^{sc}(j)| \geq 3\hat{\sigma}_E \Leftrightarrow T_q(j) = \frac{E - \delta\hat{x}_{078}^{sc}(j)^2}{\hat{\sigma}_E^2} > 9$$

Specifically, the preliminary 3σ check procedure is used as a conditional test, to check if more than half of the considered ($\geq \frac{m''}{2}$) displacement observations are consecutively exceeding the 3σ boundaries of the GNSS noise level. If this holds true, the displacement identification algorithm will follow the upper branch from the "Testing Workflow" box (see figure O.1) and run a 1D (position) outlier test followed by a (position) slip test[34] to identify all "(potentially) real" displacements, without letting them slip through the identification procedure. Otherwise, the algorithm will follow the lower branch from the "Testing Workflow" box and run only a nominal 1D outlier test. In the next lines, the functional models under H_0 and H_a of the nominal 1D outlier test and the slip test along with the "real" displacement identification and adaptation procedure are presented.

The proposed general functional model under H_0 is considering a set of m' East (X) displacement quantities for estimating the weighted average behavior/ position ($E - \delta\tilde{\hat{x}}_{078}^{sc}(t'')$) of the cantilever beam over the 40 minutes period of day 078 from figure 4.3:

[30] this quantity was derived in section 4.4 based on the displacement observations of day 079, in the presence of a MP correction. In the remaining of this section this will be denoted by $\hat{\sigma}_E$.

[31] in case of the proposed 1D testing procedure, C_y will become a vector of the form of a canonical unit vector (see 5.11).

[32] for the 1D testing procedure q=1, while for the upcoming 3D case q=3.

[33] the "true" beam displacement can be either >0 or <0. Therefore, the functional model under H_a from (5.9) can be considered to describe a composite hypothesis. Hence, the T_q value can be derived on behalf of the Generalized Likelihood Ratio (GLR) test, which is used for the definition of the general formula of T_q from (5.13) as well. For more details on the GLR test please refer to (Teunissen [1]).

[34] the reader should note that the slip test is considered a conditional testing procedure, which is performed only if the preliminary 3σ check procedure gets passed. Moreover, one should not get confused by the "slip" term and relate it to the common cycle slips problem. The primary aim of the proposed slip test is to search for any constant slip/ jump in the displacement observations over time.

1D (Position) Outlier & Slip Test - Null-Hypothesis

$$H_0 : \underline{y}_{(m',1)} = A_{(m',n=1)} x_{(1,1)} + \underline{e}_{(m',1)}, \quad Qyy_{(m',m')} = \begin{bmatrix} \sigma^2_{E-\delta\hat{x}^{sc}_{078}(1')} & 0 & 0 \\ 0 & \ddots & 0 \\ 0 & 0 & \sigma^2_{E-\delta\hat{x}^{sc}_{078}(m')} \end{bmatrix}$$
$$y_{(m',1)} = \begin{bmatrix} E-\delta\hat{x}^{sc}_{078}(1') \\ \vdots \\ E-\delta\hat{x}^{sc}_{078}(m') \end{bmatrix}; \; A_{(m',1)} = \begin{bmatrix} 1 \\ \vdots \\ 1 \end{bmatrix}; \; \hat{x}_{(1,1)} = E-\delta\tilde{\hat{x}}^{sc}_{078}(t'') \tag{5.11}$$

where:

$E-\delta\tilde{\hat{x}}^{sc}_{078}$ = weighted average position of the beam in East (X) direction
t'' = average time period over which the response of the beam to wind breezes is confronted $[sec]$[35]
$\sigma_{E-\delta\hat{x}^{sc}_{078}}$ = RTKLib based formal standard deviation of MP corrected East (X) displacement observation[36] $[m]$

Generally, for the identification of many errors/ biases within the stack of considered observations, geodesists prefer a detection, identification and adaptation (DIA) procedure. In the *detection* phase, the DIA procedure starts by testing if the observed data comply with the H_0 functional model via an overall model test (see (3.20) from subsection 3.2.4). Otherwise, the procedure tries to identify the source of error and to resolve it.
Frequently, for the *identification* part a nominal *outlier test* is considered, which is testing each observation from the stack of considered observations for being influenced by a bias/ error. This is done by forming m' alternative hypothesis, which will be tested one-by-one against the H_0 with the w-test. In case of the proposed 1D outlier testing procedure the m' H_a functional models will have the following form:

1D (Position) Outlier Test - Alternative Hypothesis

$$H_a : \underline{y}_{(m',1)} = A_{(m',n=1)} x_{(1,1)} + C_{y_{(m',q=1)}} \nabla_{(1,1)} + \underline{e}_{(m',1)}, \quad Qyy_{(m',m')} = \begin{bmatrix} \sigma^2_{E-\delta\hat{x}^{sc}_{078}(1')} & 0 & 0 \\ 0 & \ddots & 0 \\ 0 & 0 & \sigma^2_{E-\delta\hat{x}^{sc}_{078}(m')} \end{bmatrix}$$
$$C_{y_{(m',1)}}(1') = \begin{bmatrix} 1 \\ 0 \\ \vdots \\ 0 \end{bmatrix}, \; C_{y_{(m',1)}}(2') = \begin{bmatrix} 0 \\ 1 \\ \vdots \\ 0 \end{bmatrix}, \cdots, C_{y_{(m',1)}}(m') = \begin{bmatrix} 0 \\ 0 \\ \vdots \\ 1 \end{bmatrix}, \; \hat{\nabla}_{(q,1)} = E-\hat{\nabla}(j) \tag{5.12}$$

In this case, ∇ consists of a single additional unknown bias parameter corresponding to each tested displacement observation. Hence, for each of these m' alternative hypothesis, a Chi-square distributed T_q value is computed based on the following formula for the test statistics of a w-test:

$$H_0 : \underline{T}_q \sim \chi^2(q,0); \quad H_a : \underline{T}_q \sim \chi^2(q,\lambda)$$
$$\lambda(j) = \nabla^T Q^{-1}_{\hat{\nabla}\hat{\nabla}} \nabla$$
$$T_q(j) = \hat{e}_0^T Q^{-1}_{yy} C_y Q_{\hat{\nabla}\hat{\nabla}} C_y^T Q^{-1}_{yy} \hat{e}_0 = \hat{\nabla}^T Q_{\hat{\nabla}\hat{\nabla}} \hat{\nabla} \tag{5.13}$$
$$Q_{\hat{\nabla}\hat{\nabla}} = (C_y^T Q^{-1}_{yy} Q_{\hat{e}_0\hat{e}_0} Q^{-1}_{yy} C_y)^{-1}$$

where:

λ = non-centrality parameter
$\hat{e}_0$ = vector of the estimated least-squares residuals under H_0[37]
$Q_{\hat{e}_0\hat{e}_0}$ = variance-covariance matrix of the estimated least-squares residuals under H_0
$Q_{\hat{\nabla}\hat{\nabla}}$ = variance-covariance matrix of the bias estimate $\hat{\nabla}$

[35] in the following lines, an example for $m' = 5$ will be given. In such a case t'' will correspond to the average period of 1 second over which 5 displacement observations, collected at a rate of 5 Hz, were considered. Equivalently, t'' indicates also the number of steps over which the testing procedure runs (=number of run tests).

[36] in case of the cantilever beam experiment, the standard deviation values of the displacement samples, that were not corrected for MP, were multiplied by $\sqrt{2}$ in order to account these displacement observations with less weight in the statistical testing procedure. Through the inversion process of the Q_{yy} matrix the weights of these displacement observations will decrease by a factor of 50%.

[37] the subscript $_0$ is a label related to the null-hypothesis H_0.

Note that (5.13) represents a generalized formula[38] for T_q that is fully dependent only on the vector of estimated least-square residuals ($\hat{e}_0$) under H_0. The second formulation shows that T_q is direct proportional to the bias estimate $\hat{\nabla}$. Related to this, the error estimates can be as well computed in terms of $\hat{e}_0$:

$$\hat{\nabla}(j) = Q_{\hat{\nabla}\hat{\nabla}} C_y^T Q_{yy}^{-1} \hat{e}_0 \tag{5.14}$$

For a detailed description of the derivation of the previously listed formulas for the test statistics T_q and its distribution please refer to (Teunissen [1]).
Having a vector of m' T_q values, in a next step these are one-by-one compared with a user-defined k_α value, which is extracted from the Chi-squared distribution table for a specific α value[39], in order to identify which displacement observations do not comply with the model under H_0:

1D (Position) Outlier & Slip Test - Statistical Hypothesis Testing

$$reject\ H_0\ if\ \ T_q(j) > k_\alpha,\ k_{\alpha=0.05,q=1} = 3.8415$$

In the *adaptation* step, after identifying the potential sources of error, as m' outlier hypothesis are considered (see (5.12)), for each hypothesis one can eliminate the observation that corresponds to the largest T_q value exceeding the critical value. The process will be repeated up until all potentially erroneous observations are eliminated, until there is no more rejection and H_0[40] is accepted.
Note that in case of a (position) slip test the aforementioned generalized DIA procedure is very similar. In the next paragraph the slip test and the differences in the application of the DIA procedure related to this test type are introduced based on a concrete example.

In practice, a simple (position) outlier test can have difficulties at identifying all displacements within the considered m' long window, especially when more than half ($\geq \frac{m'}{2}$) of the displacement observations are consecutively exceeding the 3σ boundaries of the GNSS noise level. In such a case, the outlier test will not be able to identify all displacements, letting some, or even all, of them slip through the identification procedure. A suggestive example that explains a position slip is shown in figure O.2 in appendix O , where the 8$^{\text{th}}$ displacement observation is slipping through the 1-second long overlapping sliding window of a nominal 1D outlier test procedure. As one can see from this figure, at step $t'' + 5$ the sliding window is containing 3 consecutive "real" displacements[41] at index 8,9 and 10, which are the cause of the slipping problem. Thus, to avoid such problems and strengthen the proposed displacement identification testing procedure, an additional *slip test* is set to run after the outlier test to update the $T_q(3',4',5')$ values corresponding to the 3 consecutive "real" displacement observations. Hence, the only difference between the slip and the outlier test lies in the identification stage, in the formation of the functional models under H_a, where 3 new C_y vectors of the following form are formed:

1D (Position) Slip Test - Alternative Hypothesis

$$C_{y_{(3',1)}} = \begin{bmatrix} 0 \\ 0 \\ 1 \\ 1 \\ 1 \end{bmatrix},\ C_{y_{(4',1)}} = \begin{bmatrix} 0 \\ 0 \\ 0 \\ 1 \\ 1 \end{bmatrix},\ C_{y_{(5',1)}} = \begin{bmatrix} 0 \\ 0 \\ 0 \\ 0 \\ 1 \end{bmatrix} \tag{5.15}$$

These C_y vectors are formed under the guidance of the accepted preliminary 3σ check procedure, in order to group the consecutive displacement observations and assign them to the same displacement value, resulting in larger $T_q(3',4',5')$ values, hence a straightforward displacement identification of the "real" displacements at index 8, 9 and 10.

However, in case of the proposed 1D testing procedure focus is put only on the identification and adaptation steps (see "Identification & Adaptation" box in figure O.1). This has to do with the way in which the proposed functional model under H_0 from (5.11) is constructed to test if m' displacement observations describe the same nominal structural position over a certain time period.
The decision of counting only on the identification and adaptation steps is best explained by a counterexample of blindly following a DIA procedure. In such a case, considering that over a period of 1 second, each of the

[38] despite the existence of a simplified formula for the computation of T_q for testing for the identification of a single observation error at once ($q = 1$), (5.13) was chosen to be applied in case of the currently introduced 1D testing procedure and the following 3D testing procedure.

[39] in this research the α, was chosen to be equal to 0.05. This value corresponds with the acceptance of letting the testing procedure output 5 false alarms out of 100 decisions.

[40] note that the H_0 functional model is suffering a number of adaptations until it gets accepted.

[41] these were identified by the preliminary 3σ procedure, which guides the algorithm for the formation of new C_y vectors (see 5.15).

5 (=m') displacement observations (at 5 Hz) are describing a "(potentially) real" East (X) beam displacement, then in the detection phase the 5 samples will comply with the H_0 functional model, making the algorithm skip the identification and adaptation phases and result in 5 missed detections.
Therefore, in the absence of an OMT, the proposed 1D displacement testing procedure will feed every m' stack of displacement observations through a sliding window procedure and perform the compound (position) outlier & slip test or just the nominal outlier test, depending on the preliminary decision of the 3σ check procedure, to identify any abnormal movement of the cantilever beam in the East (X) direction. More on the decision of using a sliding window procedure can be found down below in the next subsection.

As an advance to each drawn decision of the 1D displacement identification procedure, at the end of the adaptation stage the previously introduced 3σ check procedure (see (5.10)) should lastly check if each identified[42] biased observation exceeds the 3σ boundaries of the GNSS noise level. Then only if this last test gets passed, the alleged displacement observation is accounted as a "(possible) real" beam displacement, otherwise it should be accounted as a false detection.
For a better understating of the workflow of the previously introduced outlier and slip tests along with the followed identification and adaptation phases, the entire 1D outlier & slip displacement identification procedure is illustrated in figure O.1 in appendix O, in the form of a 5(=m') sample sliding window procedure.

SLIDING WINDOW PROCEDURE. CHOICE OF THE OPTIMAL WINDOW LENGTH

ON behalf of the introduced 1D outlier & slip test, one might wonder on the choice of using an overlapping sliding window procedure for the identification of possible wind-induced structural displacements. However, the usefulness of a sliding window selection procedure is straightforward. This reads so since it maximizes the probability of the statistical test for correct identification of a "(potentially) real" displacement by testing each sample within the considered window m' times. Hence, by shifting the window m' times over the same displacement estimate, there is a lower chance for the displacement identification algorithm to miss its detection. This comes with the price of raising delayed alarms, where the maximum delay period for each alarm can reach a period of $m' * \frac{1}{5Hz}$ seconds, representing the time it takes for the sliding window to fully evaluate the suspected displacement estimate. Throughout this repeated evaluation of the same displacement estimate, the algorithm might attest the same displacement multiple times, which is undesirable. Therefore, in case the same displacement quantity is identified, the algorithm is making sure to warn the user about it only once, by considering only the displacement observations with the highest T_q and $\hat{\lambda}$ values, as a result of a more powerful statistical test. A clear example of the method of working of the overlapping sliding window procedure can be seen in figure O.2 in appendix O. This argumentation holds true also for the following 3D outlier & slip testing procedure.

After having a statistical hypothesis testing procedure set for effectively identifying beam displacements in one particular orthogonal direction, in the next step its displacement identification performance needed to be tuned with respect to the user-defined sliding window length, to identify the best window length/ size that can maximize the displacement identification process. This was done by running the testing procedure multiple times over the considered 40 minutes period of day 078 from figure 4.3. For a larger window length, it is expected that the testing procedure will be able to identify more "real" displacements at the price of rising alarms of longer delay periods. This tuning process was run for both the 1D outlier & slip- as well as for the nominal 1D outlier displacement identification procedure. From the listed results in table (5.1) one can see that in both cases the test based on a 7-seconds long (=35 samples) sliding window was able to identify most "(potentially) real" beam displacements in East (X) direction. However, such a long time for rising an alarm is unacceptable for SHM purposes, hence a 5-seconds long sliding window is chosen as the best option for identifying a considerably large number of "real" East (X) beam displacements and rise enough fast alarms.

[42] as a result of the identification stage of the 1D outlier & slip test.

Table 5.1: Results of the 1D East (X) displacement identification procedure run over a 40 minutes long windy period of day 078 for different window lengths. The table is split in two sections. The left side consists the number of identified displacements of an outlier + slip test while on the right side the results of a nominal outlier test are listed. In both cases the testing procedure was run for a window length of 3, 5, 15, 25, 35, 50 and 75 samples. The largest number of displacement was identified by the testing procedure complying a 7 seconds long window (35 samples, colored in light orange). In order to rise displacement alarms quickly enough, the 5 seconds long window was indicated as the best option (colored in light yellow)

1D East (X) Displacement Identification Procedure WID stage, day 078 (18/03/2020), 10:10:00 - 10:50:00						
Test type	**1D w-test (Outlier + Slip test), α= 0.05**			**1D w-test (Outlier test), α= 0.05**		
↓ Test No./ Parameters →	***Window length [samples]***	***Window period [sec]***	***No. of identified East (X) displ.***	***Window length [samples]***	***Window period [sec]***	***No. of identified East (X) displ.***
1	3	0.6	598	3	0.6	548
2	5	1	664	5	1	519
3	15	3	648	15	3	612
4	**25**	**5**	**669**	**25**	**5**	**662**
5	35	7	678	35	7	679
6	50	10	669	50	10	669
7	75	15	651	75	15	644

SYNTHETIC DISPLACEMENTS SIMULATION ANALYSIS FOR THE ASSESSMENT OF THE EFFECTIVENESS OF THE 1D DISPLACEMENT IDENTIFICATION STRATEGY

UNTIL now, the displacement identification potential of the discussed 1D (position) outlier & slip test was empirically assessed over a 40 minutes windy period of the WID stage, where the real structural response of the cantilever beam was unknown. Hence, the listed number of identified displacements from table O.1 cannot be fully assigned to real beam displacements but to possibly existing beam displacements, hampering the proof of the effectiveness of the proposed uni-dimensional testing procedure for identifying real structural displacements.

Therefore, a 40 minutes long normally distributed random noise sequence ($\underline{e}$) with mean equal to 0 and standard deviation equal to the noise level on East (X) direction ($\hat{\sigma}_E$) of 0.003 meters can be generated to substitute the estimated displacement time series of day 078 ($\delta\hat{x}^{sc}_{078}$), without consisting of any real displacement quantity[43]. This random noise sequence can be further fed in the 1D outlier & slip testing procedure to quantify its probability of rising false alarms (α), by checking for how many noise samples are accounted as beam displacements after exceeding the 3σ boundaries of the GNSS noise band:

$$\alpha = \frac{No.\,identified\,displacements}{No.\,of\,run\,tests^{44}} * 100\,[\%] \tag{5.16}$$

Such simulation analysis was run for assessing the false alarm probability of the 1D outlier & slip testing procedure, with or without the endmost 3σ check procedure. Results from figure O.3 in appendix O, attest the service of the 3σ check procedure within the uni-dimensional displacement identification algorithm, by facilitating a drastic reduction of the false alarm probability from 7.16% to only 0.28% after its incorporation. Furthermore, the simulation analysis can be extended for assessing the power (see (5.17)) of the developed 1D outlier & slip test and of a nominal 1D outlier test, by manually inferring three sets of 26, 3 and another 26 consecutive displacements in the generated random noise sequence and checking if both displacement identification procedures can detect them entirely.

$$\gamma = \frac{No.\,identified\,induced\,displacements^{45}}{No.\,identified\,displacements} * 100\,[\%] \tag{5.17}$$

Throughout this analysis the usefulness of a slip test can be assessed. According to the results from figure O.4 in appendix O, the usefulness of the slip test is attested by the capability of the developed 1D outlier & slip test to identify all 55 induced displacements, resulting in a maximum power level of 100%. On the other hand, the 1D outlier test missed to detect 5 from the 55 induced displacements, resulting in a power level of 91%.

Based on the obtained results one can conclude that the developed compound 1D (position) outlier & slip displacement identification algorithm accompanied by the 3σ check procedure represents a good methodology for effectively identifying 1D structural displacements with a considerably low level of significance α and a high power level γ.

[43] no noise sample is exceeding the 3σ boundaries of the GNSS noise band in East (X) direction. Since the noise samples are normally distributed, this will hold true for 99.7% of the generated samples, while the rest will exceed the imposed 3σ level.

[44] = no. of samples - window length +1. In the context of a window length of 25 samples (= 5 seconds) and the considered 40 minutes period the number of run tests is equal to = 40*60*5 - 25 + 1= 11976.

[45] in the context of the proposed simulation analysis, three sets of 26,3 and 26 displacements were induced.

TRI-DIMENSIONAL DISPLACEMENT IDENTIFICATION TESTING PROCEDURES: THE 3D OUTLIER & SLIP TEST

HOWEVER, because in real life the response of tall structures to the disruptive wind action is far more complicated than the structural response of a cantilever beam, one should additionally consider the development of a 3D(q=3) (position) outlier test based statistical hypothesis testing procedure that is able to identifying simultaneous structural displacements in East (X), North (Y) and Up (Z) direction. To do so, the nominal functional models under H_0 and H_a need to be updated to the following form:

3D (Position) Outlier & Slip Test - Null-Hypothesis

$$H_0 : \underline{y}_{(3m',1)} = A_{(3m',n=3)}\, x_{(3,1)} + \underline{e}_{(3m',1)}; \quad Qyy_{(3m',3m')} = \begin{bmatrix} Q_{\delta\hat{x}^{sc}_{078}(1')_{(3,3)}} & 0 & 0 \\ 0 & \ddots & 0 \\ 0 & 0 & Q_{\delta\hat{x}^{sc}_{078}(m')_{(3,3)}} \end{bmatrix}$$

$$Q_{\delta\hat{x}^{sc}_{078}(j)_{(3,3)}} = \begin{bmatrix} \sigma^2_{E-\delta\hat{x}^{sc}_{078}(j)} & \sigma_{E-\delta\hat{x}^{sc}_{078}(j)}\sigma_{N-\delta\hat{x}^{sc}_{078}(j)} & \sigma_{E-\delta\hat{x}^{sc}_{078}(j)}\sigma_{U-\delta\hat{x}^{sc}_{078}(j)} \\ \sigma_{N-\delta\hat{x}^{sc}_{078}(j)}\sigma_{E-\delta\hat{x}^{sc}_{078}(j)} & \sigma^2_{N-\delta\hat{x}^{sc}_{078}(j)} & \sigma_{N-\delta\hat{x}^{sc}_{078}(j)}\sigma_{U-\delta\hat{x}^{sc}_{078}(j)} \\ \sigma_{U-\delta\hat{x}^{sc}_{078}(j)}\sigma_{E-\delta\hat{x}^{sc}_{078}(j)} & \sigma_{U-\delta\hat{x}^{sc}_{078}(j)}\sigma_{N-\delta\hat{x}^{sc}_{078}(j)} & \sigma^2_{U-\delta\hat{x}^{sc}_{078}(j)} \end{bmatrix} \tag{5.18}$$

$$y_{(3m',1)} = \begin{bmatrix} E-\delta\hat{x}^{sc}_{078}(1') \\ N-\delta\hat{x}^{sc}_{078}(1') \\ U-\delta\hat{x}^{sc}_{078}(1') \\ \vdots \\ E-\delta\hat{x}^{sc}_{078}(m') \\ N-\delta\hat{x}^{sc}_{078}(m') \\ U-\delta\hat{x}^{sc}_{078}(m') \end{bmatrix}; \; A_{(3m',1)} = \begin{bmatrix} 1 & 0 & 0 \\ 0 & 1 & 0 \\ 0 & 0 & 1 \\ \vdots & \vdots & \vdots \\ 1 & 0 & 0 \\ 0 & 1 & 0 \\ 0 & 0 & 1 \end{bmatrix}; \; \hat{x}_{(3,1)} = \begin{bmatrix} E-\delta\tilde{\hat{x}}^{sc}_{078}(t'') \\ N-\delta\tilde{\hat{x}}^{sc}_{078}(t'') \\ U-\delta\tilde{\hat{x}}^{sc}_{078}(t'') \end{bmatrix}$$

3D (Position) Outlier - Alternative Hypothesis

$$H_a : \underline{y}_{(3m',1)} = A_{(3m',n=3)}\, x_{(3,1)} + C_{y_{(3m',q=3)}} \nabla_{(3,1)} + \underline{e}_{(3m',1)}; \quad Qyy_{(3m',3m')} = Qyy_{(3m',3m')|H_0}$$

$$C_{y_{(3m',3)}}(1') = \begin{bmatrix} 1 & 0 & 0 \\ 0 & 1 & 0 \\ 0 & 0 & 1 \\ 0 & 0 & 0 \\ 0 & 0 & 0 \\ 0 & 0 & 0 \\ \vdots & \vdots & \vdots \\ 0 & 0 & 0 \\ 0 & 0 & 0 \\ 0 & 0 & 0 \end{bmatrix}, \; C_{y_{(3m',3)}}(2') = \begin{bmatrix} 0 & 0 & 0 \\ 0 & 0 & 0 \\ 0 & 0 & 0 \\ 1 & 0 & 0 \\ 0 & 1 & 0 \\ 0 & 0 & 1 \\ \vdots & \vdots & \vdots \\ 0 & 0 & 0 \\ 0 & 0 & 0 \\ 0 & 0 & 0 \end{bmatrix}, \cdots, C_{y_{(3m',3)}}(m') = \begin{bmatrix} 0 & 0 & 0 \\ 0 & 0 & 0 \\ 0 & 0 & 0 \\ 0 & 0 & 0 \\ 0 & 0 & 0 \\ 0 & 0 & 0 \\ \vdots & \vdots & \vdots \\ 1 & 0 & 0 \\ 0 & 1 & 0 \\ 0 & 0 & 1 \end{bmatrix} \tag{5.19}$$

$$\hat{\nabla}_{(m',1)} = \begin{bmatrix} \hat{\nabla}_{(3,1)}(1') \\ \vdots \\ \hat{\nabla}_{(3,1)}(m') \end{bmatrix}; \; \hat{\nabla}_{(3,1)}(j) = \begin{bmatrix} E-\hat{\nabla}(j) \\ N-\hat{\nabla}(j) \\ U-\hat{\nabla}(j) \end{bmatrix}$$

Hence, the difference between these functional models and the 1D models under H_0 and H_a from (5.11) and (5.12), lies in the way in which the displacement observations are now treated as 3D observation blocks for testing whether they comply with the average East (X), North (Y) and Up (Z) position of the case study structure at moment t'' ($E-\delta\tilde{\hat{x}}^{sc}_{078}(t'')$, $N-\delta\tilde{\hat{x}}^{sc}_{078}(t'')$, $U-\delta\tilde{\hat{x}}^{sc}_{078}(t'')$), or otherwise if any of the m' observation blocks describe a divergent behaviour, simultaneously in East (X), North (Y) and Up (Z) direction[46], from the nominal state of the considered structure.

A major difference from the previous 1D displacement identification algorithm lies in the general method of functioning of the auxiliary 3σ check procedure, which in this case should not only attest if the identified "(potentially) biased" block of observation is exceeding the 3σ noise level of the GNSS module to account for a possible "real" 3D displacement block, but also detect in which orthogonal direction the case study structure

[46] modeled by $E-\hat{\nabla}(j), N-\hat{\nabla}(j), U-\hat{\nabla}(j)$).

has predominately moved. Hence, depending on the position of each observation within each biased block of observations, the checking procedure will examine if:

- The absolute value of the first observation ($E-\delta\hat{x}^{sc}_{078}$) within the j-th block AND the absolute value of the j-th $E-\hat{\nabla}$ are larger than $3\hat{\sigma}_E = 0.009$ m
- The absolute value of the second observation ($N-\delta\hat{x}^{sc}_{078}$) within the j-th block AND the absolute value of the j-th $N-\hat{\nabla}$ are larger than $3\hat{\sigma}_N = 0.012$ m
- The absolute value of the last/ third observation ($U-\delta\hat{x}^{sc}_{078}$) within the j-th block AND the absolute value of the j-th $U-\hat{\nabla}$ are larger than $3\hat{\sigma}_U = 0.024$ m

On behalf of (5.9) and (5.10) these checks can be expressed by the following three pairs of binary hypothesis tests:

Tri-dimensional 3σ ***Check Procedure - Binary Hypothesis Testing***

$$|E/N/U-\delta\hat{x}^{sc}_{078}(j)| \geq 3\hat{\sigma}_{E/N/U} \Leftrightarrow T_q(j) = \frac{E/N/U-\delta\hat{x}^{sc}_{078}(j)^2}{\hat{\sigma}^2_{E/N/U}} > 9$$

AND (5.20)

$$|E/N/U-\hat{\nabla}(j)| \geq 3\hat{\sigma}_{E/N/U} \Leftrightarrow T_q(j) = \frac{E/N/U-\hat{\nabla}(j)^2}{\hat{\sigma}^2_{E/N/U}} > 9$$

Prior to the "Testing Workflow" (see figure O.5) such checking procedure is preliminary used for guiding the algorithm towards deploying a 3D outlier & slip test procedure, in case if more than half ($\geq \frac{m'}{2}$) of the observations on one particular cardinal direction, within a considered 3D block are consecutively exceeding the 3σ boundaries of the GNSS noise level. The result of such checking procedure will be reflected in the formation of the slip test based C_y matrices under H_a. Otherwise, the tri-dimensional displacement identification algorithm will follow the lower branch from the "Testing Workflow" box in figure O.5 and only apply a nominal 3D outlier test at block level.

This time for the application of the 3D compound or just nominal displacement identification procedure, a vector of m' T_q values corresponding to each block of East (X), North (Y) and Up (Z) displacement observations needs to be constructed based on (5.13). In this process each obtained T_q value should be compared with the user-defined k_α value, extracted from the Chi-squared table for a predefined α value[47] and $q = 3$, in order to identify which block of displacement observations does not comply with the model under H_0.

3D (Position) Outlier & Slip Test - Statistical Hypothesis Testing

$$reject\ H_0\ if\ \ T_q(j) > k_\alpha,\ k_{\alpha=0.05,q=3} = 7.8147$$

The adaptation stage of the DIA procedure should be similarly applied as in case of the 1D testing procedure, but now at a block level and the entire identification procedure should be repeated up until all blocks of possibly erroneous observations are eliminated, until there is no more rejection and H_0 is accepted. Differently from the 1D testing procedure, at the end of the "Identification & Adaptation" stage (see figure O.5) the endmost 3σ check procedure should decide which from the identified biased observations of the considered block exceeds the 3σ boundaries of the GNSS noise level. Then only if any of the three pairs of binary hypothesis tests from (5.20) is accepted, the corresponding displacement observation from the considered block is accounted as a "(potentially) real" displacement to its corresponding orthogonal direction. Otherwise it is accounted as a false detection. Hence, the 3σ check procedure will help at marking the orthogonal direction in which the case study structure has predominately moved.
A similar sliding window approach as before is desirable, where the endmost 3σ check of the 3D displacement identification algorithm should store the attested erroneous observations only once. This is necessary to overcome the limitations of the sliding window procedure of identifying the same block of observations multiple times. Hence, prior to the application of the last auxiliary 3σ check procedure, the algorithm should choose for the block with the highest T_q value. Moreover, one should note that in case of using a sliding window approach the alarm delay period will be up to 3 times longer as in case of the 1D testing procedure, since it will take more time for the overlapping sliding window to evaluate each block of displacement observations.

[47] in this case α=0.05.

In case of considering the position slip test procedure, the C_y vectors from (5.15) will become matrices. To exemplify the form of such C_y matrices, one will consider each dot from figure O.2 to correspond to a block of East (X), North (Y) and Up (Z) displacement observations. This example is illustrated in figure O.6 in appendix O. Then by considering that the East (X) displacement observations within the 8^{th}, 9^{th} and 10^{th} blocks correspond to "(potentially) real" East (X) displacements of the cantilever beam, the needed C_y matrices for applying a slip test and updating their corresponding T_q values get the following form:

3D (Position) Slip Test - Alternative Hypothesis

$$C_{y_{(15,1)}}(3') = \begin{bmatrix} 0 & 0 & 0 \\ 0 & 0 & 0 \\ 0 & 0 & 0 \\ \vdots & \vdots & \vdots \\ 1 & 0 & 0 \\ 0 & 1 & 0 \\ 0 & 0 & 1 \\ 1 & 0 & 0 \\ 0 & 0 & 0 \\ 0 & 0 & 0 \\ 1 & 0 & 0 \\ 0 & 0 & 0 \\ 0 & 0 & 0 \end{bmatrix}, \; C_{y_{(15,1)}}(4') = \begin{bmatrix} 0 & 0 & 0 \\ 0 & 0 & 0 \\ 0 & 0 & 0 \\ \vdots & \vdots & \vdots \\ 0 & 0 & 0 \\ 0 & 0 & 0 \\ 0 & 0 & 0 \\ 1 & 0 & 0 \\ 0 & 0 & 0 \\ 0 & 0 & 0 \\ 1 & 0 & 0 \\ 0 & 0 & 0 \\ 0 & 0 & 0 \end{bmatrix}, \cdots, C_{y_{(15,1)}}(5') = \begin{bmatrix} 0 & 0 & 0 \\ 0 & 0 & 0 \\ 0 & 0 & 0 \\ \vdots & \vdots & \vdots \\ 0 & 0 & 0 \\ 0 & 0 & 0 \\ 0 & 0 & 0 \\ 0 & 0 & 0 \\ 0 & 0 & 0 \\ 0 & 0 & 0 \\ 1 & 0 & 0 \\ 0 & 0 & 0 \\ 0 & 0 & 0 \end{bmatrix} \tag{5.21}$$

For a better understanding of the aforementioned concepts related to the 3D testing procedure, the entire 3D (position) outlier & slip displacement identification procedure is illustrated in figure O.5 in appendix O. Note that this type of displacement identification algorithm is more useful than the 1D procedure for detecting more complex structural displacements, but on the other hand it is weaker at rising alarms if the case study structure did not simultaneously respond to wind loads in all three orthogonal directions. Furthermore, the functional model under H_a (see (5.19)) of the principal 3D outlier test allows to be rephrased, in order to search for wind-induced structural displacements in any horizontal intercardinal direction, such as the North-East direction.

Table 5.2: Results of the 3D displacement identification procedure run over a 40 minutes long windy period of day 078 for different window lengths. The table is split in two sections. The left side contains the number of identified possible East (X), North (Y) and Up (Z) displacements of an outlier + slip while on the right side the results of a nominal outlier test are listed. In both cases the testing procedure was run for a window length of 3, 5, 15, 25, 35, 50 and 75 samples. The largest number of displacement was identified by the testing procedure to correspond with a 5 seconds long window (25 samples, colored in light light yellow)

3D Displacement Identification Procedure WID stage, day 078 (18/03/2020), 10:10:00 - 10:50:00										
Test type	**3D w-test (Outlier + Slip test), α= 0.05**					**3D w-test (Outlier test), α= 0.05**				
Parameters →	***Window***	***Window***	***No. of identified displ.***			***Window***	***Window***	***No. of identified displ.***		
↓ Test No.	***length [samples]***	***period [sec]***	***East (X)***	***North (Y)***	***Up (Z)***	***length [samples]***	***period [sec]***	***East (X)***	***North (Y)***	***Up (Z)***
1	3	0.6	249	0	0	3	0.6	229	0	0
2	5	1	256	0	0	5	1	182	0	0
3	15	3	267	0	0	15	3	211	0	0
4	**25**	**5**	**287**	**0**	**0**	**25**	**5**	**241**	**0**	**0**
5	35	7	249	0	3	35	7	221	0	3
6	50	10	210	0	3	50	10	206	0	3
7	75	15	247	0	11	75	15	237	0	11

This functional model can be used to model not only constant jumps in the displacement observations over time just as in case of the 3D position slip test (see (5.21)), but also a linear increasing displacement motion in the form of a position ramp test.

This being said, the developed 3D displacement identification testing procedure was tuned over the same 40 minutes period of day 078, with respect to the user-defined sliding window length. The tuning process was run for both the 3D outlier & slip displacement identification procedure as well as for the nominal 3D outlier displacement identification procedure. From the listed results in table (5.2) one can see that for both test types a 5-seconds long (=25 samples) sliding window was able to identify the most beam displacements. In accordance with what is been expected the numbers show that the beam responded predominately to wind loads in the East (X) direction. For larger window lengths, both 3D testing procedures started to detect a small number of Up (Z) beam displacements at the price of a slightly smaller number of identified East (X) displacements and a delayed alarm response, which is unacceptable for SHM applications. Therefore, by opting for a 5-seconds long sliding window the 3D outlier & slip test based algorithm performed best by identifying a maximum number of 287 East (X) beam displacements, being able to rise alarms within 5 seconds.

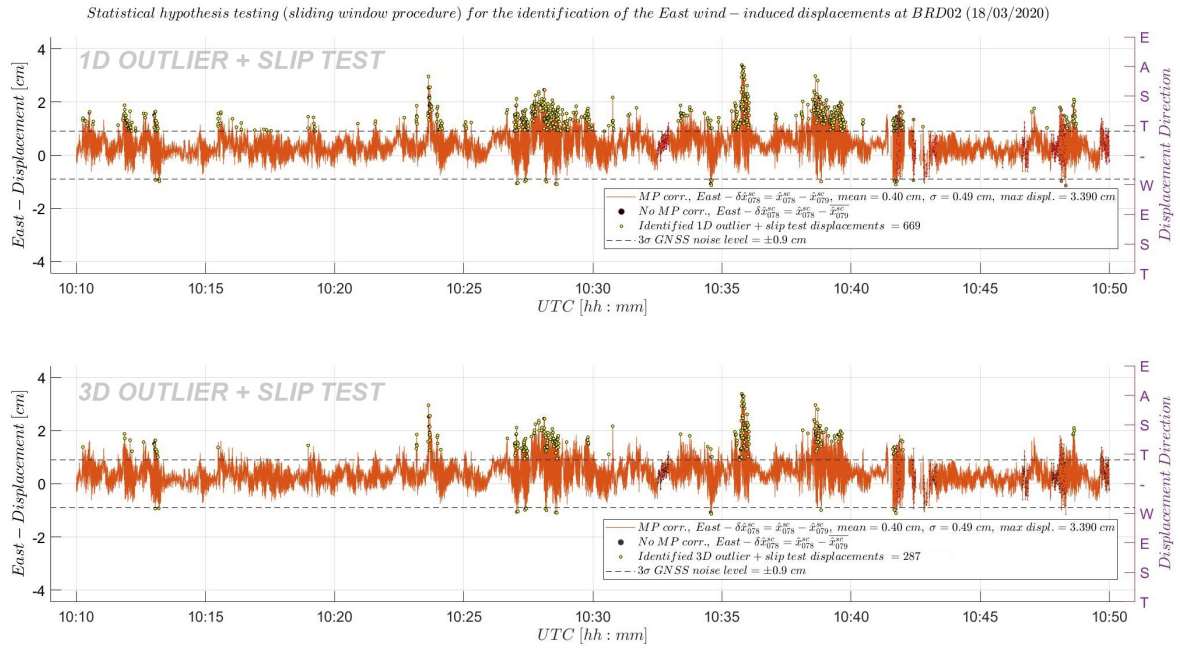

Figure 5.7: Comparison of the output of the 1D (above) and 3D (below) outlier & slip test based testing procedure in East (X) direction. Both testing procedures identify "real" displacements (yellow dots) that exceed the ± 0.9 GNSS noise band (black dashed lines). The 1D testing procedure was able to identify 669 East (X) displacements in comparison to the 287 East (X) displacements identified by the 3D testing procedure

When comparing the results of the 1D and 3D outlier & slip test identification procedures, highlighted in yellow in table 5.1 and 5.2, one can conclude that the 1D identification process had a better displacement identification performance. This is attested by the large number of 669 identified East (X) beam displacements in comparison to the 287 East (X) beam displacements of the 3D identification process. To additionally attest that the identified East (X) displacements correspond to trustworthy beam displacements, the identified samples from both testing procedures were marked with yellow dots in two (next to each other) plots of the considered 40 minutes displacement time series from day 078 (see figure 5.7). Both plots attest that all identified East (X) displacements exceed the ± 0.009 meter noise level of the GNSS module.
In conclusion, since the shape and the orientation of the case study beam was selected in such a way that the beam could respond to wind loads in the East direction, along its weak (X) axis, the use of the 1D outlier & slip displacement identification procedure is more beneficial for this application, being able to identify a large amount of divergences in the structural behavior of the beam caused by wind. Hence there is no need to perform a similar synthetic displacement simulation analysis for the assessment of the effectiveness of the 3D displacement identification algorithm.

THEORETICAL ANALYSIS OF THE INTERNAL RELIABILITY OF A NOMINAL 1D & 3D OUTLIER TEST

IN the last part of this section a theoretical analysis of the internal reliability of a nominal 1D (q=1) and 3D (q=3) outlier test is considered, in order to "describe the ability of the two functional models under H_a for tracing biases" (Teunissen [1]) related to structural displacements. Hence, based on this analysis, one can specify the expected minimum detectable bias (MDB) $|\nabla|$, directly in terms of displacement, that can be traced by an uni- or tri-dimensional outlier test with a predefined power, γ_0. Furthermore, it is important to mention why such a study is considering only the outlier test, without the slip test and 3σ check procedure. This is because at this moment there is no developed theoretical basis for the execution of a MDB analysis for assessing the internal reliability of a compound statistical testing procedure, like the discussed 1D and 3D outlier & slip testing procedures. In the present intensive research initiatives (Teunissen *et al.* [13]) are taken by the Mathematical Geodesy and Positioning department of Delft University of Technology for the development of theoretical concepts to facilitate such studies. Thus, in the following lines an internal reliability study of only a nominal outlier test is considered, this representing the compulsory prerequisite of statistical hypothesis based displacement monitoring studies.

In order to do so, the analysis is centred around the computation of the MDB in each orthogonal direction for a specific power and instrumental noise level:

$$|\nabla| = \sqrt{\frac{\lambda_0}{C_y^T Q_{yy}^{-1} Q_{e_0 e_0} Q_{yy}^{-1} C_y}} \tag{5.22}$$

where:

$|\nabla|$ = minimum detectable bias $[cm]$
λ_0 = non-centrality parameter corresponding to a predefined γ_0[48]

Note that (5.22) is defined only for the $q = 1$ case, hence C_y will correspond to a column vector of the form of $C_y(1')$ from (5.12)[49], which is describing a possible uni-dimensional structural displacement signature. Thus, in case of the 3D outlier test the $C_y(1')$ matrix from (5.19) needs to be split in three column vectors to be fed in (5.22) for the computation of the MDB in East (X), North (Y) and Up (Z) direction. Additionally, the analysis can be run with the scope of detecting the most optimal length of the sliding window for detecting a preset MDB threshold with a specific power.
Thus, for getting this analysis started the α parameter and a number of values for γ_0, $\sigma_{E/N/U}$ and the window length were selected:

- **Level of significance -** $\alpha = 0.05$
- **Test power -** $\gamma_0 = 0.85, 0.9, 0.95$[50]
- **GNSS noise level -** $1\sigma \mid 2\sigma \mid 3\sigma$[51]**:**
  - $\sigma_E = 0.3, 0.4 \mid 0.6, 0.8 \mid 0.9, 1.2$ [cm]
  - $\sigma_N = 0.4, 0.5 \mid 0.8, 1.0 \mid 1.2, 1.5$ [cm]
  - $\sigma_U = 0.8, 1.0 \mid 1.6, 2.0 \mid 2.4, 3.0$ [cm]
- **Window length/ size:** 3, 5, 15, 25, 35, 50, 75 [samples][52]

Therefore, in the first stage of the MDB analysis one is interested to identify the shortest window length for the 1D outlier testing procedure, in order to detect any structural displacement that exceeds a predefined MDB threshold[53] of 1 centimeter in the East (X), 1.4 centimeters in the North (Y) and 2.7 centimeters in the Up (Z) direction, with the highest possible power. Figure P.1 in appendix P shows that under the most optimistic scenario, when the noise level of the GNSS module can be kept within the MP corrected noise band[54], a 1D outlier test with a window length of 15 samples would represent the most optimal choice for detecting displacements that reach or exceed the considered MDB thresholds with a probability of 90% or even higher. On the other hand, a 3D outlier test with the same window length would not be able to detect such small structural displacements with the same power, but biases with slightly larger magnitudes of at least 1.4 centimeters in the East (X), 1.6 centimeters in the North (Y) and 3.2 centimeters in the Up (Z) direction (see figure P.2). Therefore, one can consider the 1D outlier testing procedure more appropriate for correctly tracing small structural displacements.
Thus, in the next lines a window size of 15 samples is used in the second stage of the MDB analysis where the behaviour of the MDB as a function of the instrumental noise is studied. By feeding the proposed noise level values in (5.22), one was able to compute the East (X), North (Y) and Up (Z) MDB as a function of the

[41] here the $_0$ index does correspond to H_a, since λ_0 is used for retrieving $|\nabla|$ on behalf of a predefined γ_0 and α value. This is done by creating an enough large artificial vector of λ_0 values, which should be fed in an iterative search process to identify the specific λ_0 value that corresponds to the γ value out of the computed power set: $\gamma = 1 - ncx2cdf(k_\alpha, 1, \lambda_0)$, equal with the desired γ_0. In this study λ_0 was chosen to span over $[1 : 0.0001 : 80]$

[49] there is no need to recompute the MDB for each m' canonical unit C_y vector, since each of them will result in the same MDB.

[50] these values correspond to a missed detection probability, β, of 0.15, 0.1 respectively 0.05, which can be translated in an acceptance that the test will fail to detect 15, 10 respectively 5 structural displacements out of 100 decisions. In the following plots related to the theoretical MDB analysis, each result corresponding to a γ_0 of: 0.85 is shown in blue, 0.90 is shown in red and 0.95 is shown in yellow.

[51] for each cardinal direction the very first pair of σ values corresponds to the defined noise level of the low-cost GNSS module accompanied by a MP correction and the noise level of the GNSS module straight out of the box (see section 4.5).

[52] in case of a sampling frequency of 6 Hz these values correspond to a window period of: 0.6, 1, 3, 5, 7, 10, 15 seconds.

[53] the choice of the MDB threshold values is purely empirical, such that the MDB threshold level is set as close as possible to the 3σ boundaries of the GNSS noise band.

[54] of ± 0.3 in the East (X), ± 0.4 in the North (Y) and ± 0.9 in the Up (Z) direction.

instrumental noise level for the three 1D (q=1) outlier tests and the other three 3D (q=3) outlier tests of different power. Figure P.3 in appendix L shows that for each preset γ_0 value, regardless the considered orthogonal direction the corresponding MDB value is linearly increasing with the instrumental noise level. By comparing the first row of plots, corresponding to the 1D case, with the last one of the 3D analysis, one can attest that a 1D outlier test is more powerful at identifying small structural displacements. This reads so, since for every γ_0 each MDB value from the 1D case is considerably smaller than its corresponding MDB value from the 3D analysis of the same noise level.
Table 5.3 presents the results of the 1D and 3D theoretical MDB analyses for a predefined window length of 15 samples. The dark blue highlighted row from the table attests that a 1D outlier test with a window length of 15 samples would represent a better choice than a 3D test for detecting displacements that are greater than or equal to the specified MDB thresholds, with a probability of 90% or even higher.

Table 5.3: MDB results of a 1D and 3 outlier test with a window length of 15 samples and an MP corrected instrumental noise level of 1σ

$\|\nabla\|$ 1D and 3D MDB for a window size of 15 samples										
Test power	**Window size [samples]**	**East σ = 0.30 cm**			**North σ = 0.40 cm**			**Up σ = 0.80 cm**		
		$\|\nabla\|$ MDB [cm]		**Difference**	**$\|\nabla\|$ MDB [cm]**		**Difference**	**$\|\nabla\|$ MDB [cm]**		**Difference**
		1D (q=1)	**3D (q=3)**	**[cm]**	**1D (q=1)**	**3D (q=3)**	**[cm]**	**1D (q=1)**	**3D (q=3)**	**[cm]**
0.85	15	0.931	1.089	-0.159	1.241	1.452	-0.212	2.481	2.904	-0.423
0.9		**1.007**	**1.169**	-0.162	**1.342**	**1.5587**	-0.217	**2.684**	**3.1173**	-0.433
0.95		1.12	1.29	-0.167	1.49	1.72	-0.223	2.99	3.43	-0.446

Knowing that the power of a test is monotonically increasing with the increase in the probability of false alarms (α) or with the increase in the non-centrality parameter (λ_0), and is decreasing with the increase in the number of additional parameters in H_a (q) (Teunissen [1]), the presented results and conclusions meet the theoretical expectations.

This brings one to the point of formulating an answer to the last addressed research question related to the effectiveness of the proposed GNSS based displacement detection system for not only estimating but also accurately identifying structural displacements of the cantilever beam during the conducted experiment. As being shown in the first part of this chapter, the need of a compound statistical hypothesis testing procedure is crucial for complementing the displacement estimation function and statistically assess and identify "true" beam displacements in near real time. For this, a 1D outlier & slip test based testing procedure, capable of raising alarms with a delay of at maximum 5 seconds, was able to identify a large amount of 669 East (X) beam displacements during a suggestive 40 minutes long windy period from the second day of the experiment. This test type performed better than a 3D outlier & slip test based testing procedure, which detected a number of 287 East (X) beam displacements on account of the slender shape and orientation of the cantilever beam, making it more likely for the beam to respond to wind loads in the East (X) direction. This statement is supported by the results from the synthetic displacements simulation analysis run on the 1D outlier & slip displacement identification algorithm. These results account the 1D outlier & slip test with a considerable low level of significance and high level of power, attesting the validity of the identified 669 East (X) beam displacements.
Furthermore, results of the conducted theoretical MDB analysis show that in case of a 1D nominal outlier test, the choice of a 5 seconds sliding window should result in a probability of correct displacement detection of more than 90% for East (X) beam displacements that are exceeding 1 centimeter, accounted to a measuring precision of only 0.3 centimeters. In case of a pessimist scenario with an instrumental noise level of 0.9 centimeters the displacement identification algorithm should be able to detect East (X) displacements of 3 centimeters with a probability of 90% or even larger. This still marks a good displacement identification performance for conducting a SHM study aiming on the identification of static or quasi-static structural displacements. Hence, the internal reliability of the proposed GNSS based displacement detection system is strongly related to the level of instrumental noise and the window size of the considered sliding window procedure, but because the level of noise of the low-cost GNSS module in the East (X) direction is expected to fluctuate between 0.3 and 0.9 centimeters, the ensamble of the GNSS system together with a nominal 1D outlier testing procedure can be considered very effective at identifying real quasi-static beam displacements of 1-3 centimeters.

5.6. PROPOSAL OF THE INTEGRATED LOW-COST GNSS BASED DISPLACEMENT SENSING SYSTEM

As a final summary of all the presented knowledge describing the workflow for the deployment of a precise GNSS based SHM monitoring campaign, a scheme with the most important steps to be considered for the implementation of a real-time low-cost displacement sensing system for effectively estimating and identifying wind-induced displacements of a slender structure is proposed in this section (see figure 5.8).
As one can see from figure 5.8, the workflow is divided in four primary stages:

- Instruments choice
- The MP & ground truth baseline definition stage
- The real-time displacement estimation stage
- The real-time statistical testing stage

Each stage speaks by its name about its purpose and the corresponding boxes from figure 5.8 summarize the necessary steps one needs to consider for implementing a low-cost SHM displacement sensing system in real time.
Hence, after choosing for the needed instruments and after defining a relative position based MP correction for the GNSS rover (see figure 3.8), pseudorange and CP observations need to be collected and processed in real time through RTKNAVI to output East (X), North (Y) and Up (Z) relative positions. Then via a scarping script, the resulting relative positions need to be selected in order to apply the filtering procedure from appendix H and consider only the ambiguity fixed relative positions solutions. In case if for each epoch the satellite geometry is identical with the satellite geometry recorded during the MP calibration day, then the MP correction can be applied resulting in MP corrected East (X), North (Y) and Up (Z) displacements quantities. Otherwise, for the epochs when this does not hold true, displacement quantities can be obtained by simply subtracting the ground truth baseline from the ambiguity fixed relative position times series. The aforementioned set of operations form the third stage of the algorithm are related to the real-time displacement estimation.
Having a precise set of displacement observations, these need to be tested throughout the sliding window procedure from section 5.5 for any abnormal behaviour related to real displacements of the considered structure. In case if the statistical testing procedure gets passed an alarm is raised to inform the user about the magnitude and direction of the identified displacement.
In parallel to the real-time displacement estimation and identification processes, a smartphone accelerometer can be linked to the GNSS based SHM system to perform a dynamic displacement analysis on behalf of the reverse transformation from subsection 2.6.3. The results of this analysis can be used for validation purposes. However, since the validation analysis is based on a double integration process that is fully dependent on digital filtering, its application in real time is limited. Additionally, after removing the low frequent noise from the GNSS based displacement quantities through a tuned high- and low-pass filter scheme, just as the one developed in subsection 4.3.2, an FFT analysis can be deployed to derive information about the natural frequency of the case study structure and update it in real time.
It is believed that the proposed set of operations describe an efficient procedure for integrating and implementing a low-cost GNSS based SHM displacement sensing system in real time.

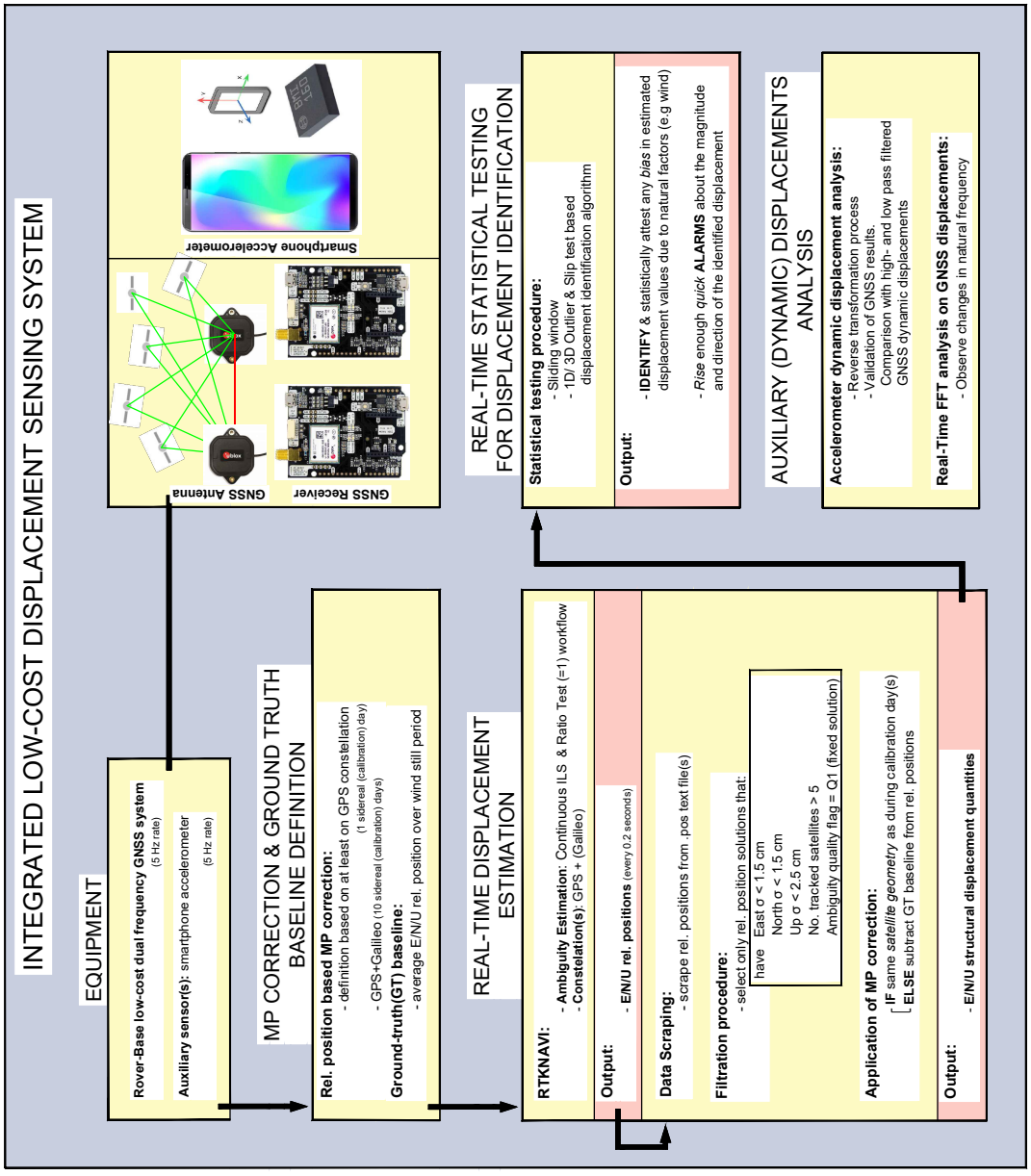

Figure 5.8: Scheme of the proposed integrated low-cost displacement sensing system and its workflow for estimating and identifying structural displacements

Chapter Highlights

- Throughout RTK positioning, systems of DD observations can be formed to estimate sub centimeter accurate baseline solutions in real time. In practice this can be achieved via RTKNAVI AP.
- The proposed relative position based MP correction can be implemented in real time thanks to a checking procedure which is probing the repeatability of the satellites PRN code numbers of the MP calibration day with the PRN code numbers of a windy day. Results from the second day of the cantilever beam experiment, show a mismatch in the satellite geometry over more than 5 hours in comparison to the calibration day, attesting the usefulness of such a MP implementation procedure for deriving precise displacement results.
- To quantify the correctness of the IAE, a success rate analysis is desirable. This can be performed prior to the equipment installation via the VISUAL software in the form of a formal success rate analysis and empirically, at the time of the data acquisition and estimation, based on RTKNAVI's on-the-flight integer ambiguity quality flags. The latter procedure delivered fixed displacement solutions at BRD02 site 99.9% of the time over day 078.
- The need of a statistical hypothesis testing procedure is crucial for complementing the displacement estimation function in order to statistically attest and identify structural displacements in near real time. Therefore, a 1D and a 3D outlier & slip test based testing procedure was developed to identify any abnormal movement of the cantilever beam in one, respectively three orthogonal directions. Results show that the 1D outlier & slip test based testing procedure performs better than the 3D version at detecting beam displacements, influenced by the orientation of the cantilever beam, which was making it to respond most prominently to wind loads in the East (X) direction. The effectiveness of the displacement identification function of the 1D outlier & slip test is supported by the results from a synthetic displacements simulation analysis, indicating a low level of significance and a high power for the considered testing procedure.
- From a theoretical point of view the reliability of the proposed GNSS based displacement detection algorithms is strongly related to the level of instrumental noise and the considered window size. Results of the internal reliability study show that a 1D outlier test with a window length of 15 samples represents a more reliable choice than a 3D test for detecting a larger number of beam displacements that reach or exceed a predefined MDB threshold of 1 cm in the East (X), 1.4 cm in the North (Y) and 2.7 cm in the Up (Z) direction, with a probability of 90% or even higher.

REFERENCES

[1] P. J. Teunissen, *Hand-out Data Quality Control, Excerpts from reader Probability and Observation Theory,* .

[2] S. B. Im, S. Hurlebaus, and Y. J. Kang, *Summary Review of GPS Technology for Structural Health Honitoring,* Journal of Structural Engineering **139**, 1653 (2013).

[3] T. Kijewski-Correa and M. Kochly, *Monitoring the Wind-induced Response of Tall Buildings: GPS Performance and the Issue of Multipath Effects,* Journal of Wind Engineering and Industrial Aerodynamics **95**, 1176 (2007).

[4] W.-S. Chan, Y.-L. Xu, X.-L. Ding, Y.-L. Xiong, and W.-J. Dai, *Assessment of Dynamic Measurement Accuracy of GPS in Three Directions,* Journal of Surveying Engineering **132**, 108 (2006).

[5] F. Moschas and S. Stiros, *PLL bandwidth and noise in 100 hz GPS measurements,* GPS Solutions **19**, 173 (2015).

[6] P. J. Teunissen, *Mixed Integer Estimation and Validation for Next Generation GNSS, Handbook of Geomathematics,* (2010).

[7] P. Teunissen, *Theory of Carrier Phase Ambiguity Resolution,* Wuhan University Journal of Natural Sciences **8**, 471 (2003).

[8] S. Verhagen and P. J. Teunissen, *New Global Navigation Satellite System Ambiguity Resolution Method Compared to Existing Approaches,* Journal of Guidance, Control, and Dynamics **29**, 981 (2006).

[9] P. J. Teunissen, *An Optimality Property of the Integer Least-squares Estimator,* Journal of Geodesy **73**, 587 (1999).

[10] S. Verhagen, *LAMBDA Software Package. Matlab Impementation, Version 3.0,* .

[11] S. Verhagen, *Manual for the Matlab user interface VISUAL,* Delft Institute of Earth Observation and Space systems (DEOS) (2006).

[12] A. Lapadat, *Precise Monitoring of Horizontal Displacement of Large-Scale Structures using Low-Cost Dual Frequency GNSS Receivers,* (2020).

[13] P. Teunissen, S. Zaminpardaz, and C. Tiberius, *On the Integrity of Deformation Monitoring,* Geomatics, Natural Hazards and Risk **11**, 399 (2020).

6

CONCLUSIONS & RECOMMENDATIONS

At last, in this chapter conclusive answers to the five research questions are formulated in order to achieve the final research goal of designing and conducting a low-cost GNSS structural deformation study for testing the factual accuracy capabilities of low-cost dual frequency GNSS modules in order to continuously capture static, quasi-static and dynamic wind-induced structural responses of a simple structural element in the form of a metallic cantilever beam, which is supposed to resemble the behaviour of a tall, slender structure under strong wind. To each answer a reference to the sections with arguments and relevant results is made to support the drawn conclusions.
Moreover, the benefits brought by the implementation of a MP corrections in real time are highlighted, this topic being considered as the most novel piece of knowledge from this study.
Lastly, based on the accumulated experience, a set of practical and theoretical recommendations are listed for good deployment of future GNSS based SHM studies.

6.1. SUMMARY OF FINDINGS

BASED on the previously discussed results from each chapter, in this section prompt answers to the five phrased research questions are formulated. The main goal of the research questions was to guide achieving the final research objective of designing and conducting a low-cost GNSS structural deformation study in order to test the factual accuracy capabilities of low-cost dual frequency GNSS modules to continuously capture the entire spectrum of (static, quasi-static and dynamic) wind-induced structural responses of a simple structural element in the form of a stainless steel cantilever beam, which is supposed to resemble the behaviour of a tall, slender structure under strong wind.
This was supposed to be achieved based on an set of low-cost sensors and statistical based data analysis algorithms integrated in the form of a real-time SHM displacement identification system (see figure 5.8), which is supposed to perform RTK positioning in order to accurately estimate relative position solutions between a (reference-rover) set of identical low-cost GNSS modules that need to be immediately corrected for the influence of multipath and further used in the determination of displacement quantities. Lastly, a statistical testing procedure is in charge of identifying and attesting any structural discrepancy as real displacement.
In the following lines, each research question is listed along with a straightforward, conclusive answer together with a citation/ guidance to the exact section(s) with supporting arguments for the drawn conclusion.

"What is the accuracy capability of a low-cost dual frequency GNSS receiver and is it sufficient for monitoring wind-induced displacement of tall, slender structures?"

6

Based on all DD CP relative positioning results presented in this study, it can be concluded that the used low-cost dual frequency GNSS module is capable of producing relative position estimates, and hence displacement observations with a ***horizontal precision*** *level which ranges from a* ***few millimeters to 1 centimeter****, while the* ***vertical precision*** *level can reach* ***up to 2.4 centimeters****. Results show that straight out of the box a precision level of ± 0.4 centimeters in the East (X), 0.5 centimeters in the North (Y) and 1 centimeter in Up (Z) direction can be reached, which can improve to ± 0.3, 0.4 and 0.8 centimeters in the presence of a MP correction procedure. However, according to the 3σ criterion it is safer to consider that the true displacement retention potential of the low-cost GNSS receiver corresponds to 3 times the aforementioned standard deviation values.*
It is believed that the true horizontal displacement retention potential of the low-cost GNSS receiver of about 1 centimeter is sufficient for detecting unexpected structure responses produced by wind. Only in case of more sensitive applications, where precise simulation of the dynamic response of a tall structure to wind loads is desirable, the use of low-cost dual frequency GNSS modules is not as appropriate as of the traditional accelerometers.

This conclusion is supported by the displacement and validation results from chapter 4, which are summarized and thoroughly discussed in section 4.5.

"What are the main steps for developing a low-cost real-time GNSS based monitoring system for sensing static, quasi-static and dynamic displacements of tall, slender structures exerted by natural factors?"

The most important steps for implementing a real-time low-cost GNSS based SHM displacement sensing system, that can efficiently sense the entire range of structural responses exerted by natural factors such as wind storms, are suggestively illustrated in ***figure 5.8*** *in section 5.6. The implementation procedure was divided in* ***four main stages*** *related to:*

- *instrumental choice*
- *the definition of a MP correction and of the ground truth relative distance between the considered (reference-rover) pair of the GNSS receivers*
- *the real-time displacement estimation process*
- *the real-time statistical hypothesis based identification process*

Each stage consists of a set of concrete steps, listed within their corresponding text boxes in figure's 5.8 scheme. More insights on the concrete steps of each stage can be found in subsection 3.2.4 and throughout chapter 5, mainly in section 5.6.

"What are the benefits of integrating a secondary measuring technique such as smartphone accelerometers in the low-cost SHM system?"

In this study, a cost effective replacement to the traditional accelerometers was considered to keep the costs of the integrated SHM system as low as possible. Hence, a smartphone accelerometer was proposed. Its use was beneficial for the ***validation*** *of large enough* ***GNSS based dynamic displacements*** *and for compensating for the lack of capability of GNSS systems of* ***recovering small vibrations****. However, because accelerometer based sensor fusion results are fully dependent on digital signal processing operations, its integration within a real-time SHM system is very difficult, making its use beneficial only for post processed validation processes.*

The entire workflow and conducted data analyses leading to this conclusions can be reviewed in subsection 4.3.2 and section 4.5.

"What are the steps for implementing a real-time MP mitigation procedure within the low-cost structural health monitoring system?"

The proposed procedure for the real-time implementation of the developed relative position based MP correction is dependent on a ***checking procedure*** *based on the satellites* ***PRN code numbers*** *information from the resulting RTKLib residual structures, which is checking if the* ***same satellite geometry*** *was kept over each successive day to determine when to apply the proposed MP correction. The MP correction can be applied only when the satellite geometry is identical with the satellite geometry recorded during the MP calibration day.*

The exact set of steps for the implementation of the relative position based MP correction in real time is listed and discussed in section 5.3.

"What is the effectiveness of such a system for measuring structural displacements in real time and accurately identify critical displacements?"

From a theoretical point of view the effectiveness of a real time SHM monitoring system for correctly detecting structural displacements can be explained based on the ***internal reliability*** *of the considered statistical hypothesis testing based displacement identification procedure, which is describing the ability of the statistical test under consideration to trace structural displacements at a predefined level of probability for correct identification γ. However, one should remark that the reliability of such a GNSS based displacement detection system is strongly dependent on the level of* ***instrumental noise*** *and the considered number of samples/* ***window size****. Therefore, this statement was demonstrated on behalf of a MDB analysis, which shows that even if the level of noise of the used low-cost GNSS module in the East (X) direction is expected to range between 0.3 and 0.9 centimeters, the proposed GNSS system can be considered successful at identifying real* ***low frequent beam displacements*** *of* ***1 to 3 centimeters*** *with a* ***probability of correct detection of 90%*** *or even higher.*

The answer to this question is elaborated and supported by the enounced number of identified displacements exceeding the 3σ noise level band, the synthetic displacements simulation analysis indicating a low level of significance and a high power for the considered testing procedure and the formal MDB results from section 5.5.

6.2. THE BENEFITS OF A REAL TIME MULTIPATH CORRECTION

A large part of this study was dedicated to the study of the MP effect, known for being one of the major error sources that influences the GNSS CP measurements, which cannot be mitigated based on DD CP relative positioning. Its influence is even more aggressive in built-up areas, where structures with different shape are affecting the satellite signals direct path. The magnitude of the CP MP error can cause errors in the order of centimeters (see subsection 3.2.1) especially when using low-cost receiver antennas, making it more complicated for an integrated low-cost GNSS based SHM system to identify small structural displacements. Hence, a real-time mitigation strategy is strictly necessary for high-accuracy positioning applications such as wind-induced deformation monitoring of tall structures.

As already addressed in section 5.3, many studies have investigated the development of MP corrections for improving the precision potential of GNSS systems but none of them have defined an implementation strategy of such corrections in real time. Therefore, this study is considered to be the first where a real time implementation strategy of a relative position based MP correction was introduced, representing the most novel piece of knowledge within this master thesis study.
As previously mentioned this procedure is using the satellites PRN code numbers information from the resulting RTKLib residual structures to perform a check and see if the same satellite geometry was kept over each successive day to pinpoint the epochs at which the MP correction can be applied. Results from the second day (078) of the cantilever beam experiment attest the usefulness of the PRN codes based checking procedure for marking exactly the moments when the MP correction can be applied. Figure 5.3 indicates a number of 94322 time stamps sampled at 5 Hz[1] when the satellite geometry over the candidate (sidereal) days was mismatching, demonstrating the importance of such a check for identifying and treating the uncorrected displacement quantities with caution by giving them less importance in the displacement identification process. The benefits brought by the MP implementation strategy are obvious, taking into account that in case if one is blindly applying the defined MP correction assuming without verifying that the satellite geometry over the candidate days is identical, one can obtain unrealistic displacement results, which can ultimately affect the decision making in the displacement identification process. Thus, in the presence of a relative position based MP correction and a real time implementation procedure, the GNSS based SHM process can benefit from determining more accurate displacement quantities, which ultimately will be reflected in (nearly only) correct raised alarms.
Nevertheless, it is important to remark the major drawback of a relative position based MP correction of being fully dependent on constraining the same satellite geometry over each day of interest. Hence, if the contribution of one satellite is missing at a specific time instant of the considered day, the MP effect on the position at that moment will differ and the MP correction sample at that time instant should be discarded. If this holds true for a large number of epochs over the examined period, its usefulness is arguable, representing a rather rigid MP correction procedure.
Hence it is believed that the implementation of a CP residual based MP correction within a real time GNSS based SHM system is more benefic and should be considered in future studies. Such a correction has the advantage of being applicable at satellite level, meaning that its rate of exclusion/ omission will get smaller. This reads so since there is a low chance that less than 5 captured satellites would not repeat their trajectory over the candidate days, resulting in a time slot when the MP correction is discarded. Additionally, such a MP correction can offer the possibility of incorporating more satellite constellations in the MP correction definition process simply by the fact that the CP residuals based MP correction can be independently defined at satellite level over the period of their ground track repeat cycles, regardless the considered constellation. Thus the importance of taking a CP residuals based MP correction into consideration is evident.

[1] equivalent to a time period longer than 5 hours.

6.3. DEPLOYMENT OF GNSS BASED STRUCTURAL HEALTH MONITORING CAMPAIGNS. RECOMMENDATIONS

ON behalf of the previous formulated answers to the research questions in section 6.1, a detailed strategy for implementing a real-time low-cost GNSS based SHM system capable of accurately capturing the entire range of wind-induced displacements of tall, slender structures, was introduced (see figure 5.8) for the benefit of building process constructors, municipalities and developing countries research institutes interested in the accurate tracking of the structural integrity of important structures from their geographic region. Therefore, based on all insights from this study, the recommendations for future successful GNSS based SHM campaigns include:

- ***THEORETICAL RECOMMENDATIONS***
  - ***Development and use of a CP residuals based MP correction***

    As previously mentioned in section 6.2, despite its more complicated implementation in real time, the development and use of a CP residuals based MP correction is very beneficial for achieving a better MP correction rate of the displacement time series, resulting in more accurate displacement quantities and (nearly only) correct raised alarms. Moreover, in the future it is strongly recommended to define such a correction, knowing that it can ease the integration of multiple GNSS constellation within the MP correction definition process, due to the fact that the CP residuals based MP correction can be independently defined at satellite level for every constellation over the period of their ground track repeat cycle.

  - ***Implementation of a CP MP correction based on statistical hypothesis testing and the external reliability***

    After having the CP MP correction defined at satellite level, a more complex but effective real-time application procedure of such correction can be developed. Hence, during the data acquisition a 1D outlier testing procedure can be performed on each CP observation, by forming i (= no. of CP observations within an epoch) alternative hypotheses just like the one from (5.12) and test them one-by-one against the H_0 functional models of the outlier test. If for one of the tests H_0 gets rejected, one can study the external reliability of that particular suspicious observation in order to assess the magnitude of the MP influence would have on the relative position estimates $\hat{x_0}$ under H_0, if undetected. The external reliability ($\nabla_{\hat{x}}$) can be quantified by the bias-to-noise ration parameter ($\sqrt{\lambda_{\hat{x}}}$). If this corresponds to a large value, one can decide to either assign less weight to the faulty observation in the DD CP baseline estimation process, or subtract the corresponding CP residuals based MP correction from it. Throughout this procedure, the decision of an outlier test along with the resulting impact of an undetected MP on the position estimates will surpass the proposed PRN code check to effectively decide on the necessity of applying a CP MP correction, (hopefully) resulting in better position estimates.
    More details on the concept of external reliability can be found in chapter 7 of (Teunissen [1]).

  - ***Choice of the w-test based testing procedure based on the shape, orientation and expected structural response of a structure to natural factors***

    The shape, orientation and expected wind load response of a structure should play an important role in the choice and development of the functional models of the testing procedure. In both cases of the 1D and 3D outlier & slip testing procedures, the functional models can be updated to model not only constant jumps in the displacement observations over time but also linear increasing or harmonic displacement motion in the form of a position ramp or harmonic test. Moreover, when the structural response of a structure is expected to be maximum in an intercardinal direction[2], such as North-West or South-East, the 3D outlier & slipt test based identification procedure from section 5.5 would be ideal. This reads so because one can reshape the functional model under H_a of this test to check for wind-induced structural displacements in any horizontal intercardinal direction.

[2] in particular when one does not know exactly this direction.

- ***PRACTICAL RECOMMENDATIONS***

  - ***Effective set-up of the RTKNAVI processing software for RTK positioning***

    For effectively making RTKNAVI software collect and process pseudorange and CP data in real time, it is highly advisable to use the listed configurations from table H.1 in appendix H. Based on multiple conducted tests, it was found that RTKNAVI is not able to effectively fix solutions when the ratio test critical value is set larger than 2. Therefore, it is of great importance to loose the validation functionality of its Ratio Test by setting the "Min Ratio to Fix Ambiguity" factor close to 1 and perform some validation tests by comparing the RTKNAVI based relative position solutions with the PPK based relative positions of the RNX2RTKP AP to attest the correctness in the RTK processing workflow of RTKNAVI.
    Moreover, it is advisable to not rush the configuring process of RTKNAVI AP while being in the field. This can result in unwanted data storage interruptions of the resulting RTK baseline solutions, just as in case of the WID stage test where the performance of RTKNAVI for outputting real-time baseline solutions over long periods was supposed to be investigated (see section 5.2).

  - ***Choice of identical antennas for the GNSS reference-rover pair***

    The choice of identical antennas at both ends of the short baseline is very important for the mitigation of the inherent antenna phase center error through RTK positioning. At the same time it represents the easiest and most effective method for eliminating such error from the GNSS error budget. Additionally, it is advisable to orient both antennas to point in the same cardinal direction such that both antenna phase centers and phase center variation patterns would match and get effectively mitigated throughout the RTK relative positioning estimation process.

  - ***Permanent connection of the smartphone (accelerometer) to a cellular network and/ or GNSS services***

    To avoid the encountered problem of the non-linearly increasing time lag error of the smartphone accelormeter data set with respect to the GNSS data sets (see 2.2 and appendix B.1), the smartphone should be connected to a cellular network and/ or GNSS service over the entire period of the experiment. In such a case the smartphone clock can sync with the time of the cellular network and get time corrections or, even better, get externally synchronized with the GNSS satellites atomic clock, resulting in an uniformly tracked UTC time series of the smartphone accelerometer data sets. This can facilitate the time alignment of smartphone accelerometer time series with GNSS based data sets on behalf of the determination and application of a uniform time lag correction that corresponds to the maximum identified statistical cross correlation between both data sets.

To the aforementioned recommendations, a list of auxiliary practical recommendations can be found in appendix R.

REFERENCES

[1] P. J. Teunissen, *Hand-out Data Quality Control, Excerpts from reader Probability and Observation Theory*, .

EPILOGUE: CRITICAL REFLECTION ON THE ACHIEVEMENT OF THE PROPOSED OBJECTIVES & FUTURE WORK

In the next lines a subjective reflection on the level of achievement of the proposed learning objectives of this master thesis project is given, followed by a succinct exposure of the future intended plans of the author after graduation .

Firstly, focus is placed on highlighting only the intended actions from the initial research plan (see appendix Q) that could not be achieved within the allocated time frame of this project.
The first difference from the initial form of the proposed cantilever beam experiment is related to the desired magnitude of the encountered wind load on site. Over the period of the three-days experiment, the maximum accounted wind speed was of 6.66 $\frac{m}{s}$, corresponding to a way lower Beaufort force of 4 instead of the desired 8 Beaufort value, which made it more complicated to discriminate if the GNSS based measured quantities correspond to real beam displacements. Nevertheless, even if the acting wind force was weak, the cantilever beam responded to it giving the possibility to the GNSS system to detect a maximum beam response in the East (X) direction of 3.39 centimeters. Furthermore, no study of the thermal influence on the cantilever beam response was conducted, this being way too sensitive compared to the considered wind load induced displacement scenario.
Based on the listed intentions from the project proposal, an extensive test on the structural response of road signs to wind breezes was set to be deployed in cooperation with Rijkswaterstaat, right after the completion of cantilever beam. However, due to the unexpected outbreak of the COVID-19 global pandemic, the imposed social distancing and lock-down measures made it impossible for this final experiment to be deployed anymore. From a personal point of view this represents the biggest underachievement of this master thesis project.
On behalf of the second research question related to the development of a strategy for the implementation of a low-cost GNSS based monitoring system in real time, time did not allow to develop a GNSS based SHM system prototype to demonstrate the capabilities of the proposed displacement detection system live during the thesis defense. However, this step was considered to be additional and was planned only in case of remaining spare time. On top, time was too short as well for the deployment of a thorough risk integrity study on the considered compound displacement identification statistical hypothesis tests. However, as a form of replacement a theoretical internal reliability study was conducted in order to quantify the potential of the displacement identification tests for identifying structural displacements that exceed a predefined bias level with a considerable large power.
Lastly, one should mention the need of making some changes in the allocated time for the intended actions, which was organized within a Gantt chart planning proposal[3] that can be reviewed in appendix Q. This was mostly facilitated by the imposed restrictions due to the COVID19 crisis and by an unexpected incident where the laptop and the backup hard drive of the author got stolen together with a big part of the created data processing scripts.
All in all, I confirm that the declared main goal of this research project was fully achieved thanks to the stated answers of all five addressed research questions from section 6.1. Furthermore, I can declare myself satisfied by achieving 90% of my proposed personal learning objectives listed in the initial project proposal (see appendix Q) and by having the chance to design and apply a low-cost GNSS based structural deformation study accompanied by a practical geodetic measuring campaign under the form of the cantilever beam experiment.

[3] the scope of a Gantt chart was to roughly summarize the initial intended actions along with the dedicated time period such that the final research objective can be achieved in time.

In the near future after my graduation I am intending to summarize the findings from this research project into a journal research paper. This will give me satisfaction that the achieved level of knowledge can be further used by researchers interested in low-cost GNSS based SHM monitoring applications. Right after, I am planning to personally acquire a set of the same GNSS sensors and run some individual experiments for studying the usefulness of developing CP residuals based MP corrections for Galileo satellites as well. This will give the possibility of using more satellites, hence more observations, to perform more robust GNSS based SHM campaigns.
Generally being driven by the dedication of finding answers to "WHY question(s)" and constantly asking for more knowledge, I am seriously considering to pursue a PhD in a topic that is closely related to GNSS based displacement monitoring of either structures or geophysical processes such as landslides, earthquakes or glacial ice melt. However, I am also taking into account to accept the challenge of working in a multinational company, focusing on developing geodetic based solutions for a better infrastructure development. Along these challenges I am indispensably considering not only to contribute and further develop my software engineering skills and theoretical knowledge on high-precision GNSS positioning but also conduct practical experiments and spend time outdoors in nature to collect data sets, this being the principal factor for choosing geodesy as my major study discipline.

A

Appendix A: Experimental setup, Illustration

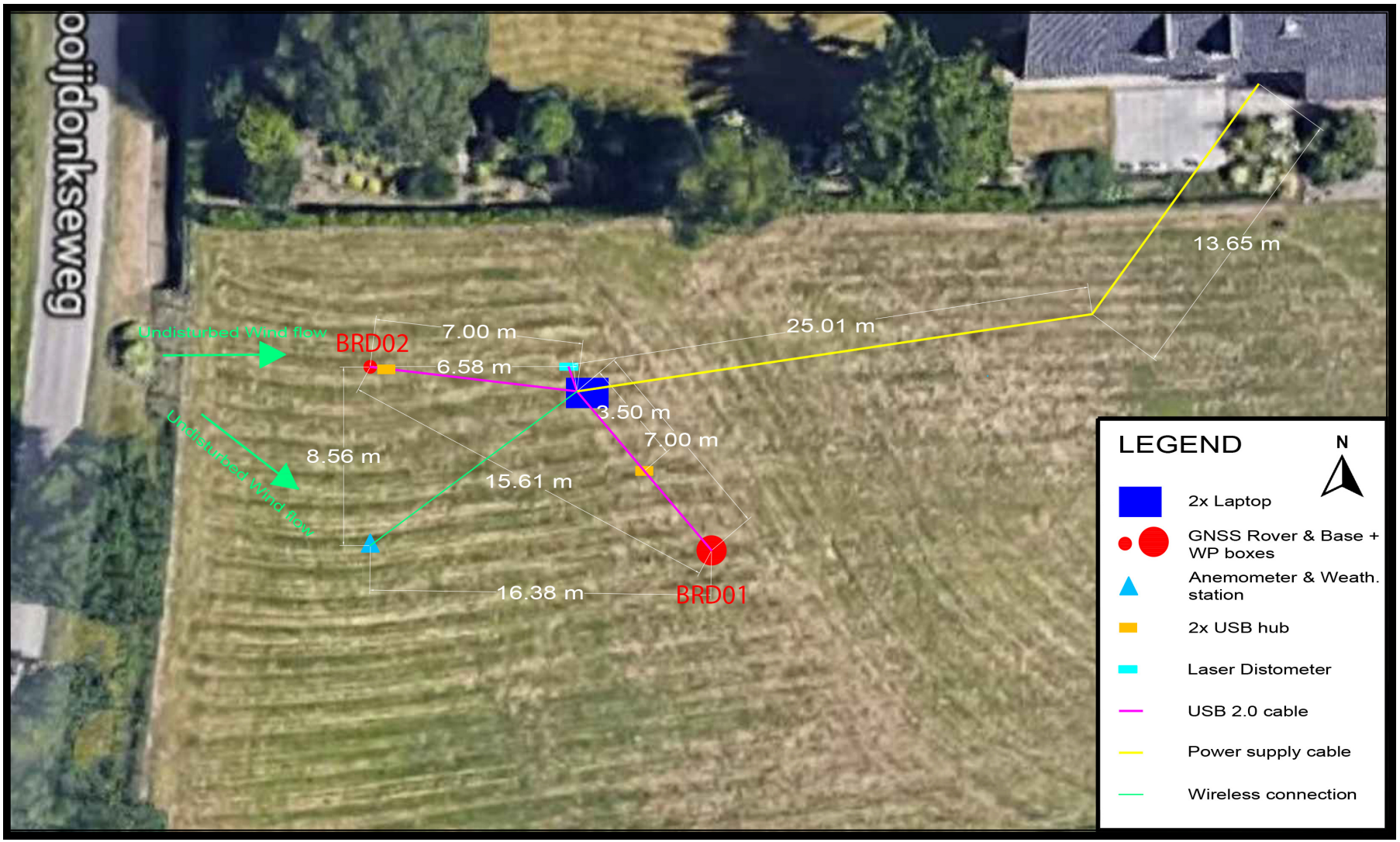

Figure A.1: Illustration of the experimental setup

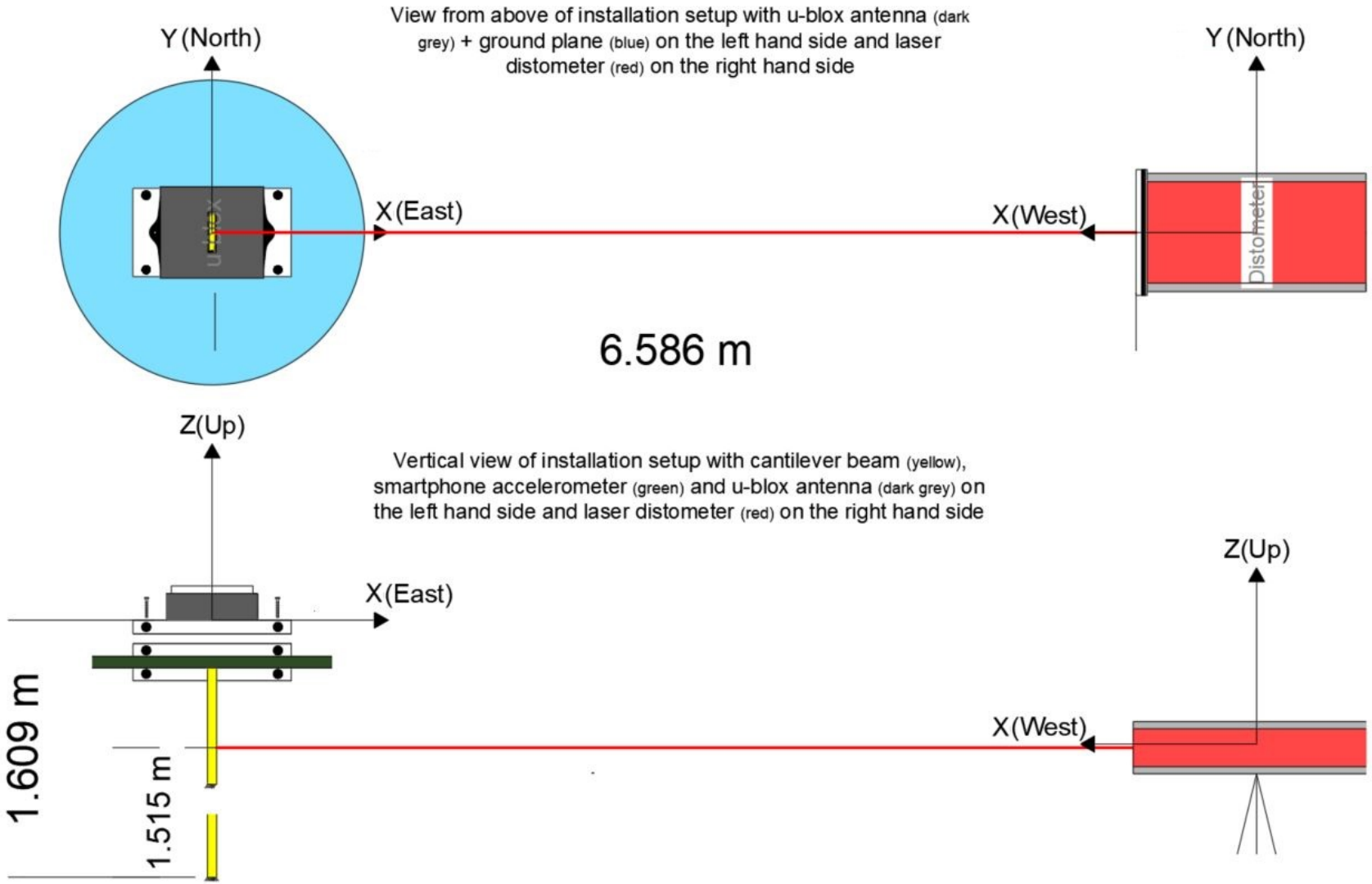

Figure A.2: Figure consisting of a horizontal and a vertical profile of the cantilever beam-distometer baseline. The exact emplacement of each sensor within the experiment and their corresponding XYZ Cartesian coordinates are presented. Note the mirrored orientation around the X(East) axis of the coordinate systems of the laser distometer with respect to the coordinate system of the GNSS module

B

Appendix B: Data Acquisition Errors

B

B.1. ACCELEROMETER DATA ACQUISITION ERRORS

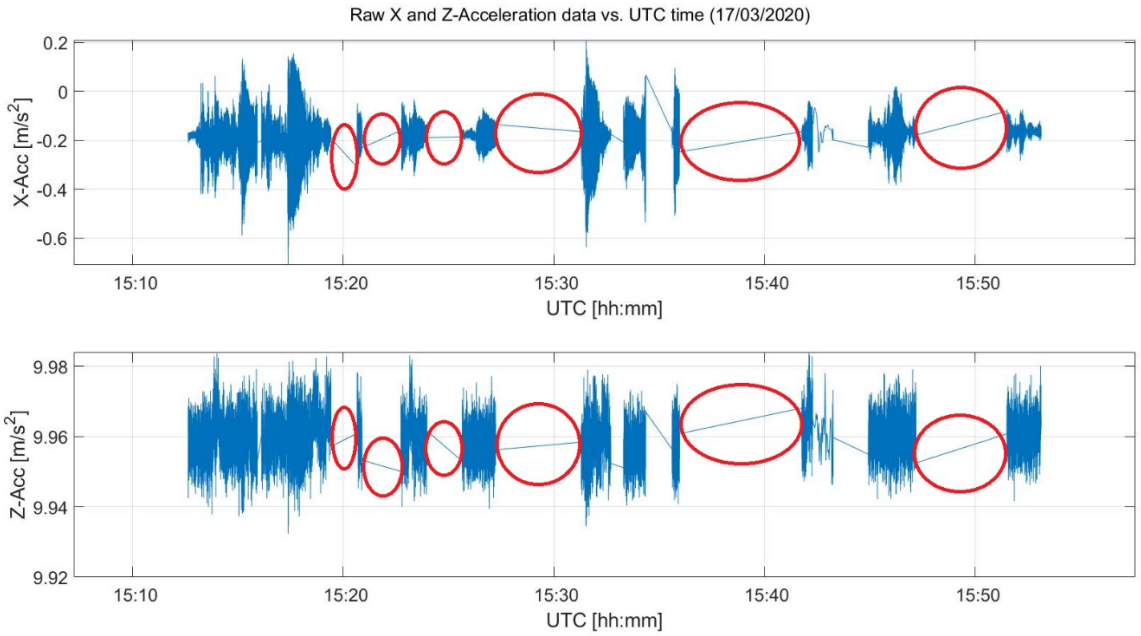

Figure B.1: Example of gaps in the Matlab Mobile X and Z acceleration data set recorded during the second day (077) of the WID stage of the experiment. Gaps are encircled in red

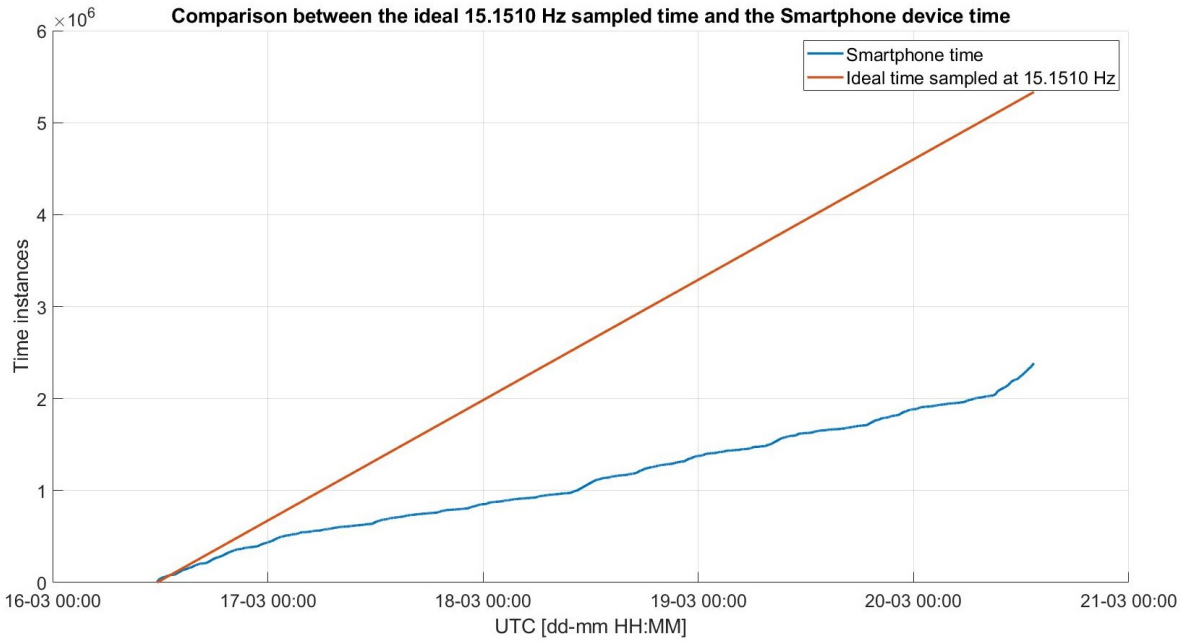

Figure B.2: Comparison between an ideal time vector sampled at 15.151 Hz (red) and the recorded time vector of the smartphone clock (blue).

When plotting the raw time instances recorded by the smartphone clock against a created time vector spanning over the entire experimental period, that was ideally sampled at a rate of 15.151 Hz, one can draw a conclusion that the accumulated time lag error is not following a linear behaviour. Ideally in figure B.2 the blue line should have followed the red line trajectory, if Matlab Mobile application would have recorded constantly at 15.151 Hz without producing any gaps in the recorded acceleration time series. Moreover, the final offset on the Y axis from figure B.2 proves that the accumulated acquisition errors made Matlab Mobile app miss more than half of the acceleration observations resulting in a strongly fragmented and miss-sampled acceleration time series.
Unfortunately, due to the fact that the smartphone acceleration data presented many gaps (see figure B.1), no automatized correction measure could be defined to be used for extrapolating by how much the acceleration time series was running behind or ahead the GNSS based time series. Therefore, within this study a manual trial-and-error procedure was used for shifting the acceleration time series forward or backward in time to align with the GNSS based time series at any time instant.

B.2. LASER DISTOMETER DATA AQUISITION ERRORS

As one can see from the second subplot of figure B.3, over the time period when artificial displacements were induced the distometer output sampling period fluctuated from 0.1-0.2 seconds to 0.6, 0.8 or even 1.9 seconds. Although most of these jumps are periodic, one can clearly identify an inverse parabolic behavior in the sampling interval discontinuities, which is strongly correlating with the appearance of sudden, large displacements. Therefore, it is susceptible that the laser distometer was lagging a bit behind while sensing sudden, large motions of the cantilever beam due to a data quality control function implemented at the distometer level with the scope of not displaying suspicious measurements. Hence, part of the displacement behavior of the cantilever beam could not be perfectly recovered by the distometer, which was inducing some time lag in the acquired displacement time series.

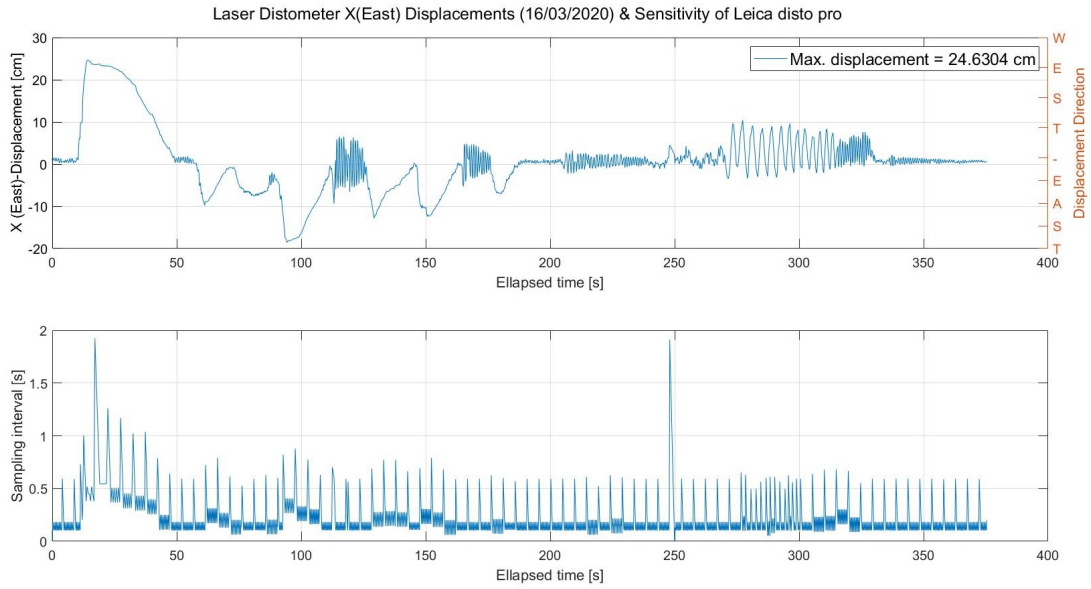

Figure B.3: Laser distometer displacement time series during AID stage (top) and its output sampling interval sensitivity (below)

B.3. WEATHER STATION DATA AQUISITION ERRORS

The weather station recorded raw information during the entire experiment at a 3 seconds rate and was even outputting 10 minutes average WS and WD values. Within the meteorological data set four large periods with missing meteorological observations were identified:

Day 077 8543 missing obs. - "17-Mar-2020 08:05:27.000" - "17-Mar-2020 15:12:38.000"

Day 079 4301 missing obs. - "19-Mar-2020 15:37:32.000" - "19-Mar-2020 19:12:39.000"
22 missing obs. - "19-Mar-2020 19:12:48.000" - "19-Mar-2020 19:13:57.000"
- "19-Mar-2020 19:14:03.000" - "20-Mar-2020 until the end"

These four data gap periods were defined as time intervals larger than 10 seconds between consecutive raw measurements with no meteorological information.
These data gap periods can be identified in figure B.4, in both the 3 seconds WS and 10 minutes average WD time series. They were caused by the Matlab scraping procedure along with some repetitive time instances and their corresponding measurement values. The Matlab scraping script was used to extract data from the console software, Cumulus, and log it in a separate text file.
These acquisition errors were corrected for each day of interest by first deleting the repetitive time instances and their corresponding measurement values and by filling the data gap intervals and their corresponding measurements with NaN values.
Note that Cumulus software, which is performing the data screening function, shows 0 wind direction/ bearing when the current wind speed is 0. Therefore, as a last correction measure, all meteorological observations with the recorded WS value of 0 were converted to NaN values as well. The same principle was considered for the 10 minutes average observations with average WS value equal to 0. This correction was particularly important to be applied to the WD observations, since one could falsely read the WD plots and interpret the 0-WS measurements as wind measurements coming from the North (= 0 °).

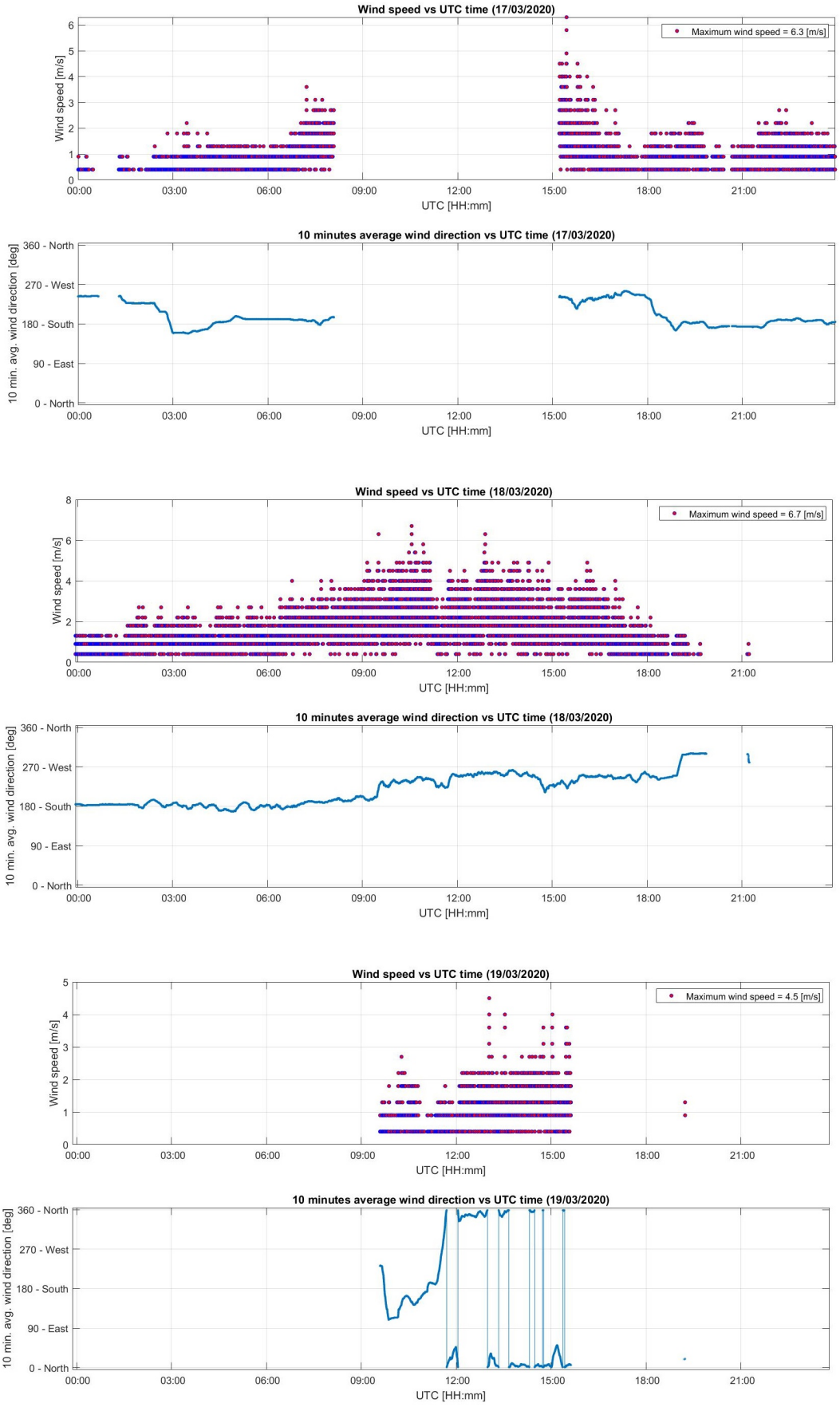

Figure B.4: Every 3-sec. WS (top) and 10-min. avg WD (below) vs UTC time over day 077 (17/03/2020), 078 (18/03/2020) and 079 (19/03/2020). Data gaps can be identified in each plot

C

Appendix C: Choice of Parameters. Wind Load Calculations

In this short appendix the choice of the ***parameters/ factors*** from 2.1, 2.2 and2.4 are explained. Each parameter was selected based on a thorough analysis of the listed information from the prEN 1991-1-4- "Actions on structures - Part 1-4: General actions - Windactions" Eurocode.

In the first treated case when the bending beam was considered to be a steel element with rectangular section and sharp edges, the choice of the $c_s * c_d$, c_f and $q_p(z_e)$ parameters was based on the following assumptions.

$c_s * c_d$ was considered equal to 1 since the height of the cantilever beam[1] of 1.609 meters was less than 15 meters.
For establishing a value for c_f formula[2] C.1 was used.

$$c_f = c_{f,0} * \psi_r * \psi_\lambda = 2 * 1 * 0.92 = 1.84 \tag{C.1}$$

where:

$c_{f,0}$ = force coefficient of rectangular sections with sharp corners and without free-end flow
ψ_r = reduction factor for square sections with rounded corners
ψ_λ = end-effect factor for elements with free-end flow

$c_{f,0}$ was chosen to be equal to 2 after visually interpolating a value from figure 7.23 of the prEN 1991 - Eurocode[3], taking into consideration that the wind was blowing perpendicular to the 0.03 meter wide (=b) side of the beam with a thickness (=d) of 0.005 meters. In this case the $\frac{d}{b}$ ratio was equal to 0.16.
ψ_r was not taken into account anymore since the cantilever beam had sharp edges.
ψ_λ was calculated based on the slenderness of the structure, λ, and the solidity ration, φ. The former one was chosen from table 7.16 of the prEN 1991 - Eurocode[4] by taking into account that the case study object was a rectangular and sharp-edged structure with its height/ length equal to 1.609 m (=l). Hence λ equals 70.
φ was calculated as a ratio between the sum of the projected areas of the members, A, and its overall envelope area, A_c, which in this case shared the same value. Therefore, φ equals 1.
Both λ and φ were used for extracting ψ_λ from figure 7.36 of the prEN 1991 - Eurocode[5] as 0.92.

$q_p(z_e)$ was computed based on the mean value of the wind pressure of a 4 Beaufort moderate wind breeze[6] expressed in $\frac{kg}{m^2}$ and converted to $\frac{N}{m^2}$. It was assumed that the wind pressure was kept constant over the entire height of the cantilever beam.

$$q_p(z_e) = \frac{3.9 + 1.9}{2} * 9.81 = 28.45\,[\frac{N}{m^2}] \tag{C.2}$$

In the second treated case when the GNSS antenna and smartphone sensors from the bending beam's top were considered to act as a signboard[7] with z_g[8]=1.609 meters, only the choice of the c_f factor differed from the previously presented parameter definition case when the beam was considered to be a steel element with rectangular section and sharp edges.
Since z_g=1.609 > $\frac{0.03}{4}$, c_f was chosen[9] to be equal to 1.8.

[1] prEN 1991-1-4 - Eurocode 1: Actions on structures - Part 1-4: General actions - Wind actions, p. 28
[2] prEN 1991-1-4 - Eurocode 1: Actions on structures - Part 1-4: General actions - Wind actions, p. 65
[3] prEN 1991-1-4 - Eurocode 1: Actions on structures - Part 1-4: General actions - Wind actions, p. 66
[4] prEN 1991-1-4 - Eurocode 1: Actions on structures - Part 1-4: General actions - Wind actions, p. 80
[5] prEN 1991-1-4 - Eurocode 1: Actions on structures - Part 1-4: General actions - Wind actions, p. 80
[6] http://home.kpn.nl/djansma1939/wissel_map/weten/windkracht.htm
[7] prEN 1991-1-4 - Eurocode 1: Actions on structures - Part 1-4: General actions - Wind actions, p. 64
[8] separation of the antenna and smartphone from the ground
[9] prEN 1991-1-4 - Eurocode 1: Actions on structures - Part 1-4: General actions - Wind actions, p. 63

D

Appendix D: Cantilever Beam Experiment - The Orthogonal Wind Components Time Series

Over each day of the cantilever beam experiment the 3-seconds WS and WD observations and the 10-minutes WS and WD measurements were split into two sets of U (East) and V (North) orthogonal wind components, by following the wind barf to wind vector system conversion process discussed in section 2.5. The 3-seconds and 10-minutes average U (East) and V (North) components were plotted on top of each other against UTC time for each day of interest and can be visualized below:

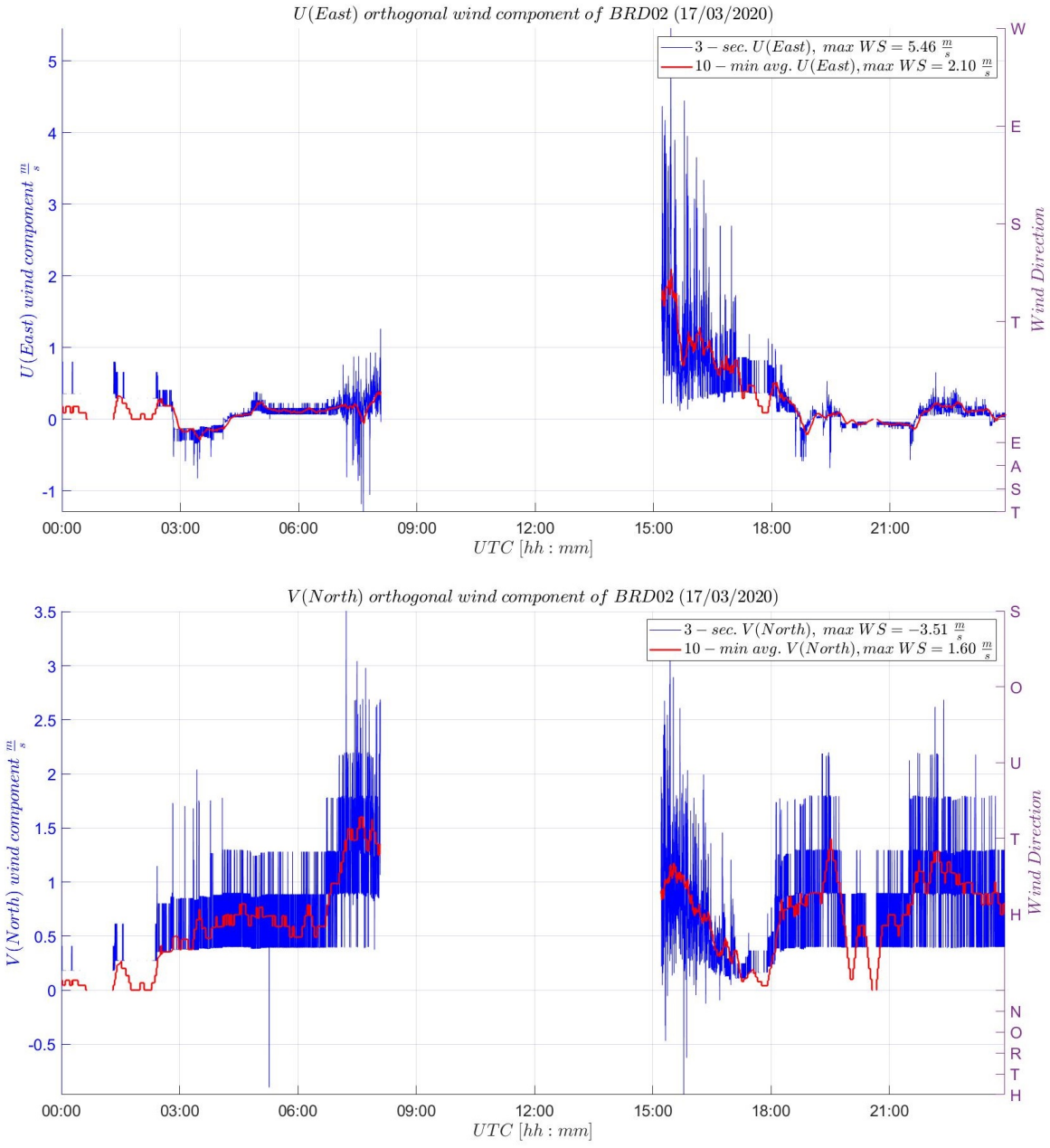

Figure D.1: 3-sec. (blue) and 10-min. avg. (red) U (East) and V (North) orthogonal wind components over day 077. Maximum values of 5.46 $\frac{m}{s}$ and 2.1 $\frac{m}{s}$ for the U (East) component and of 3.51 $\frac{m}{s}$ and 1.60 $\frac{m}{s}$ for the V (North) component

Because of the large gap in data present on the 17th of March, one cannot state how the wind was behaving in the morning and afternoon on that particular day. Although, one can make a guess based on the high peaks appearing before and after the data gap, that the wind was most probably blowing from South-West direction reaching the highest WS during this period.
From the recorded information the maximum recorded WS of the U (East) wind component was 5.46$\frac{m}{s}$ and 3.51 $\frac{m}{s}$ for the V (North) wind component. Therefore, one can conclude that the wind activity over day 077

was enough strong to put the cantilever beam under movement, especially during the time when the data could not be logged (8:00 – 15:00 UTC).

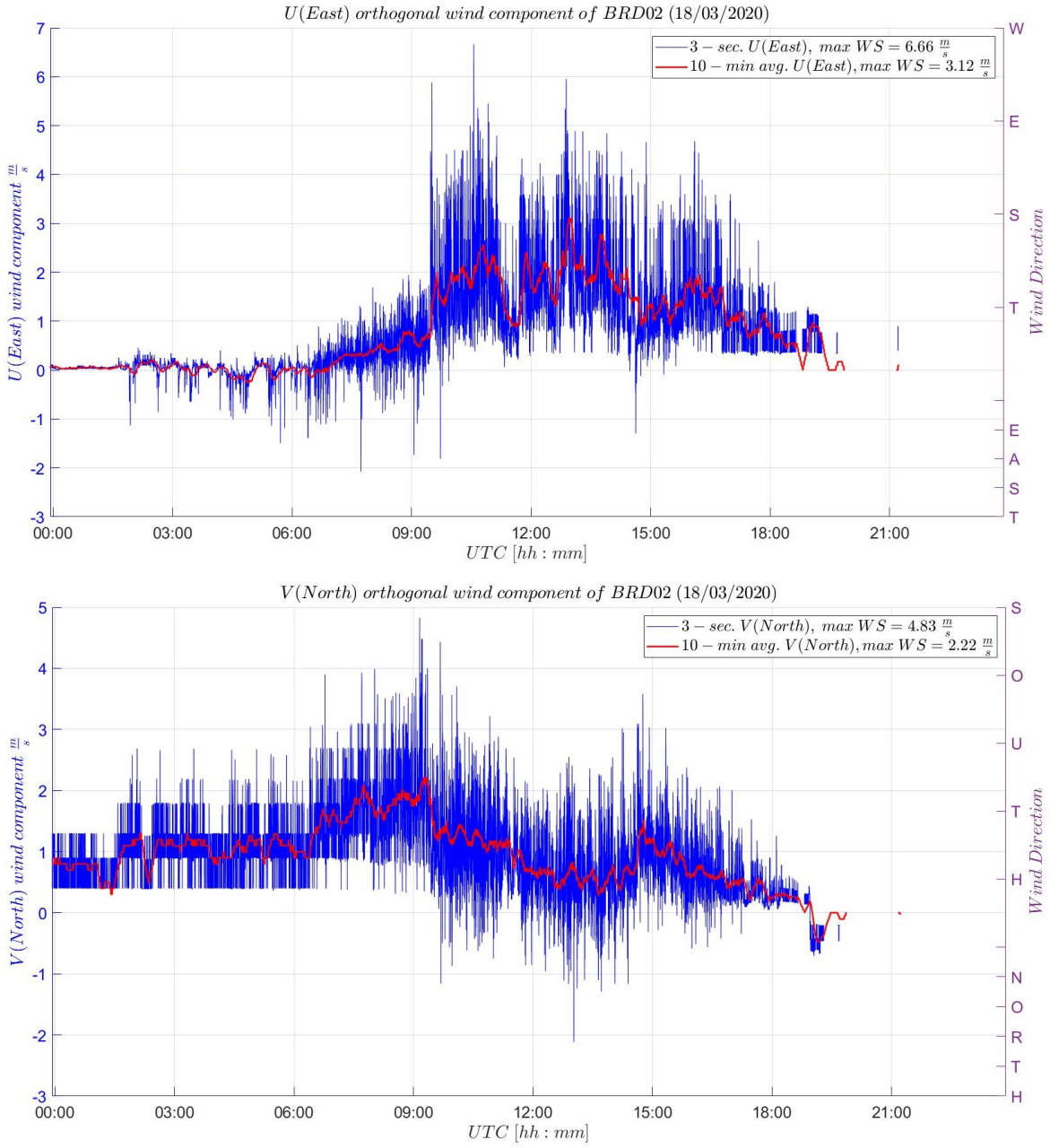

Figure D.2: 3-sec. (blue) and 10-min. avg. (red) U (East) and V (North) orthogonal wind components over day 078. Maximum values of 6.66 $\frac{m}{s}$ and 3.12 $\frac{m}{s}$ for the U (East) component and of 4.83 $\frac{m}{s}$ and 2.22 $\frac{m}{s}$ for the V (North) component were found

In case of day 078 the wind information presented no gaps. The blank period starting from 20:30 UTC corresponded to a wind still period where the recorded WS value was equal to 0 and therefore got removed. Slightly larger wind components of 6.66 $\frac{m}{s}$ were recorded during this day for West winds and 4.83 $\frac{m}{s}$ for South winds. From this time series one can expect East-West beam deflections to have happen between 9:00 – 18:00 UTC. If any North beam deflections were happening these should have happened between 6:00 – 9:00 UTC or around 15:00 UTC when the V (North) wind component time series peaked.

E

Appendix E: Cantilever Beam Experiment - Digital Filter Design, Choice and Application Process

The present appendix should be treated as a short ***motivation*** on the choice of the filter type for the noise removal process integrated in the cantilever beam experiment, describing the universal filter design and application phase more in detail.

In practice some of the most used IIR low- and high-pass filters, designed for removing low and high frequent noise from the acceleration data, are the Butterworth and Elliptical filters.
The former filter type presents no ripples in the pass- and stopband but has a broad transition band, letting unwanted frequencies pass through it. On the other hand, an Elliptical filter contains ripples in the pass- and stopband but has a steep and short transition band. Figure E.1 illustrated the behavior of the stopband, transition band and passband of some 2^{nd} order Butterworth and Elliptical high-pass filters. From this figure one can conclude that there is no ideal IIR filter to perfectly filter out the unwanted noise. Therefore, when designing a noise reduction IIR filter, there will be always a trade-off between letting some unwanted noise slowly pass through the transition band or let some fragmented noise components pass through the stop and passband ripples.
Hence, the filter design process is decisive in how well the acceleration noise removal can be achieved. Therefore, in order to achieve optimal results the choice of the following filter parameters is crucial:

- ***Cutoff frequency*** - is the frequency at which the magnitude response of the filter is $\frac{1}{\sqrt{2}}$ or $-3dB$ and can be understood as a filter boundary set for removing the unwanted energy from the input signal. It is mainly set based on the interpretation of the amplitude spectrum of the input signal, that can be derived from the FFT spectrum of the input signal. One should choose it in such a way that the unwanted frequency components of the noise will be eliminated/ cutoff.
- ***Filter order*** - defines the length of the impulse response of the filter. Generally, the higher the filter order the more the filter will approach an ideal state by shortening the transition band. In such a case the cut-off will be abrupt, but the number of the impulse response coefficients will be large.
- ***Passband and Stopband Frequency*** - in addition to the cutoff frequency, these two frequencies are helping to define the exact points of the transition band. They can be understood as frequency constraints for the transition band. Moreover, the passband frequency represents the upper limit of the passband while the stopband frequency represents the lower limit of the stopband (see figure E.2).
- ***Stopband Attenuation*** - "is the minimum attenuation[1] level with the designated stop band of the filter"[2]. Basically, it indicates the point where the stopband frequency intersects the peak stopband ripple value (see figure E.2).
- ***Passband Ripple*** - is the amount of variation in the amplitude, within the designated passband of the filter. These ripples appear as waves in the passband which are letting more energy to flow through the filter than desired and can be labeled as passband deviations from the ideal frequency response of the filter (see figure E.2).

[1] the filter attenuation is a magnitude loss measured in dB, representing the ratio at a given frequency of the signal magnitude at the output of the filter over the signal magnitude at the input of the filter.
[2] https://dsp.stackexchange.com/questions/38564/whats-the-pass-band-ripple-and-stop-band-attenuation-of-a-digital-fi

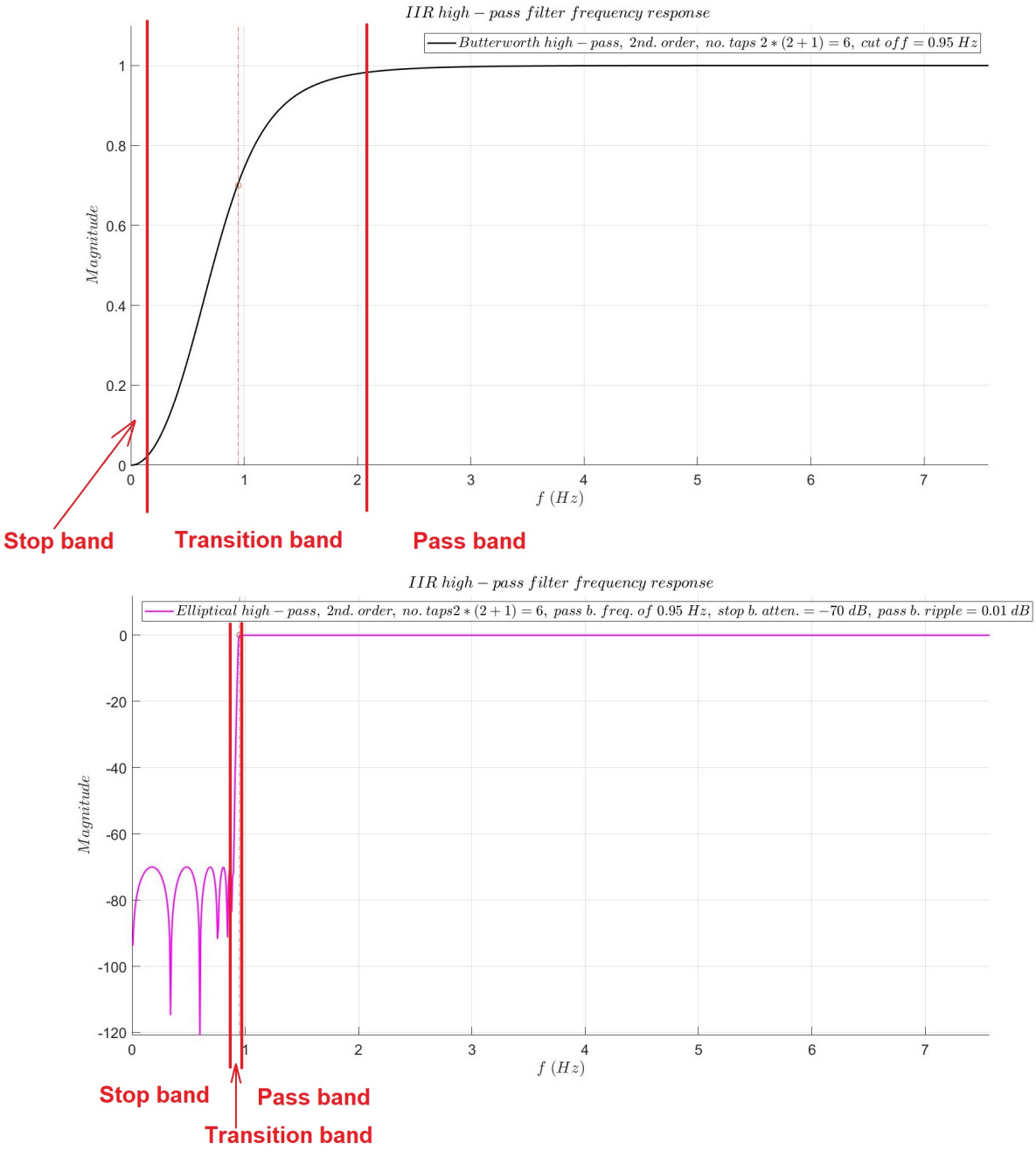

Figure E.1: Frequency response plots of a 2nd Butterworth (black) and Elliptical (magenta) IIR high-pass filter. This figure illustrates the stop-, transition and passband for each filter type

In practice there are many techniques known for designing a filter. Luckily Matlab contains many packages with functions that makes it very easy to design a filter. Some of these functions are: *butter, ellip, designfilt, highpass, lowpass* etc..
In the filter designing process it is very important to find the optimal filter that performs the closest to the desired frequency response. For this, plots of the frequency responses of different filters need to be compared with the ideal frequency response. As an example figure E.3 presents a comparison between frequency responses of an ideal 2nd order high-pass filter (blue), a 2nd order Butterworth (black) and a 2nd order Elliptical (magenta) high-pass filter, which were designed to be applied on the acquired accelerometer data of the cantilever beam experiment. From this figure one can easily understand that the 2nd order Elliptical high-pass filter would perform much closer to the desired ideal filter.
To further attest the better functioning in removing unwanted noise of a 2nd order Elliptical filter, both pre-

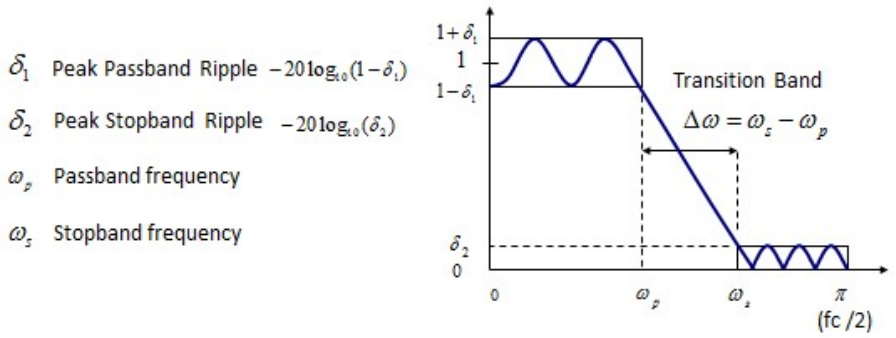

Figure E.2: Filter parameters in the filter design process. Visualization of the passband and stopband frequencies, peak passband and stopband ripples

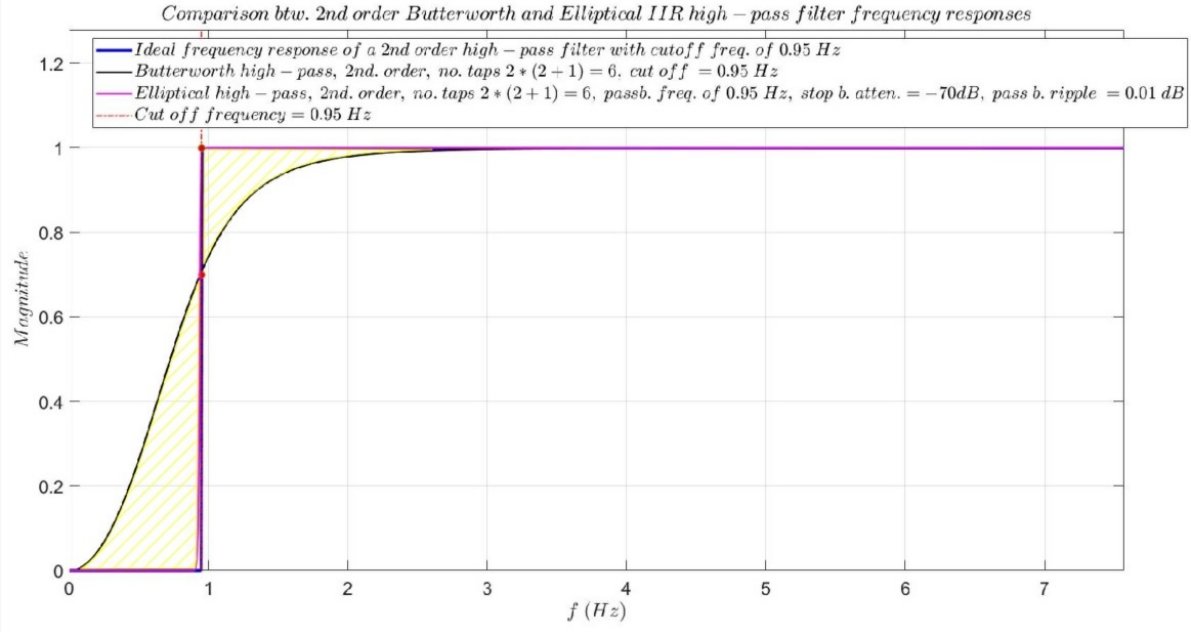

Figure E.3: Frequency responses comparison of an ideal 2nd order high-pass filter (blue), a 2nd order Butterworth (black) and a 2nd order Elliptical (magenta) high-pass filter. Unwanted frequency pass due to the broad transition band of the Butterworth filter is illustrated by the yellow hashed areas

viously defined high-pass filters were applied on an one-hour East (X) acceleration sequence ($a_{078}^{S,sc}$) from the second day (day 078) of the WID stage. The resulting high-pass filtered acceleration sequence ($\delta a_{078}^{S,sc}$) are plotted on top of each other (Butterworth – black, Elliptical - magenta) and can be visualized in figure E.4. To this also the single-side amplitude spectra of the Butterworth- and Elliptical filtered East (X) acceleration signal were plotted on top of each other. As one can see from this figure, the amplitude spectrum and the output signal that was filtered with the previously presented Butterworth filter present smaller amplitudes. This is mainly because the transition band of the Butterworth filter is removing a small part of the desired frequency components that should be within the desired pass band. At the same time the Butterworth filter is letting more unwanted frequency components from the stop band pass through. These two irregularities in Butterworth's filter functioning, produced by its broad transition band, are highlighted in hashed yellow in figure E.3. Therefore, the magenta colored patterns from both subplots of figure E.4 are describing a more trustful filtered East (X) acceleration signal that's been better cleaned from the influence of unwanted (low frequent) noise.

Hence, it can be concluded that for this application a high- and low-pass filtering scheme based on a 2nd order Elliptical filter would remove the unwanted frequency components much better than a similar scheme based on a 2nd order Butterworth filter. Therefore, a 2nd order Elliptical filter was proposed to be used in the accelerometer noise removal process of the cantilever beam experiment.

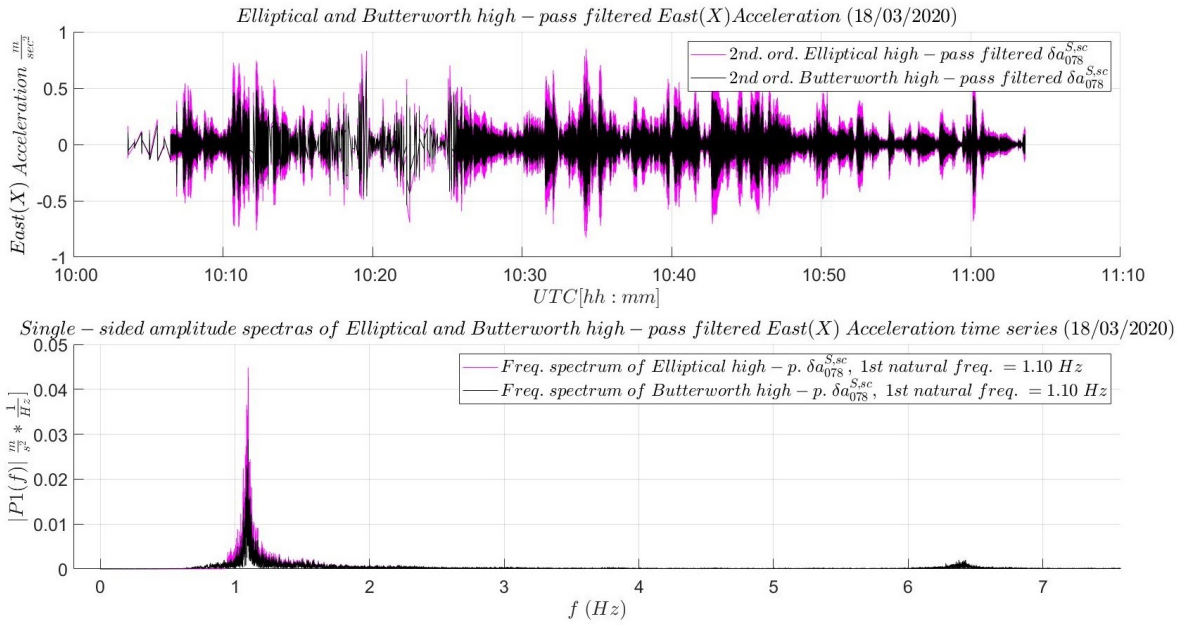

Figure E.4: Comparison of the effect of a 2nd order Butterworth (black) and Elliptical (magenta) high-pass filter on the accelerometer based East (X) displacement time series

After having an optimal filter designed for a certain application, one would be interested in the application of it to the input signal. Since most of the aforementioned filter design Matlab functions return the feed forward (a_k) and backward (b_l) coefficients[3], these can be input into some handy filter functions, such as Matlab's *filter* or *filtfilt* function, in order to apply the desired mathematical operation to the input signal.

[3] also know as transfer function coefficients

F

Appendix F: Cantilever Beam Experiment - Choice of the Optimal Digital Integrator/ Differentiator

The present appendix substantiates the choice of the cumulative trapezoidal integrator and the Parks-McClellan/Remez differentiator for performing digital integration and differentiation within the proposed reverse and forward transform algorithms, for validating GNSS based displacement values.

Generally, It is been proven by (Brandt [1]) that the performance of the trapezoidal digital integrator is satisfactory for low-frequency SHM applications, labeling its performance to be on average 3% poorer than that of an ideal integrator. This can be proven also on behalf of the collected acceleration data set from the cantilever beam experiment and can be visualized in the last subplot of figure F.1, where the relative error δ of this digital integrator, was computed based on:

$$\delta(f) = \left| \frac{(H_t - H_c)}{H_t} \right| * 100\ [\%] \tag{F.1}$$

where:

$\delta(f)$ = relative error of the digital integrator as a function of frequency
H_t = ideal frequency response of the digital integrator
H_c = current/ actual frequency response of the digital integrator

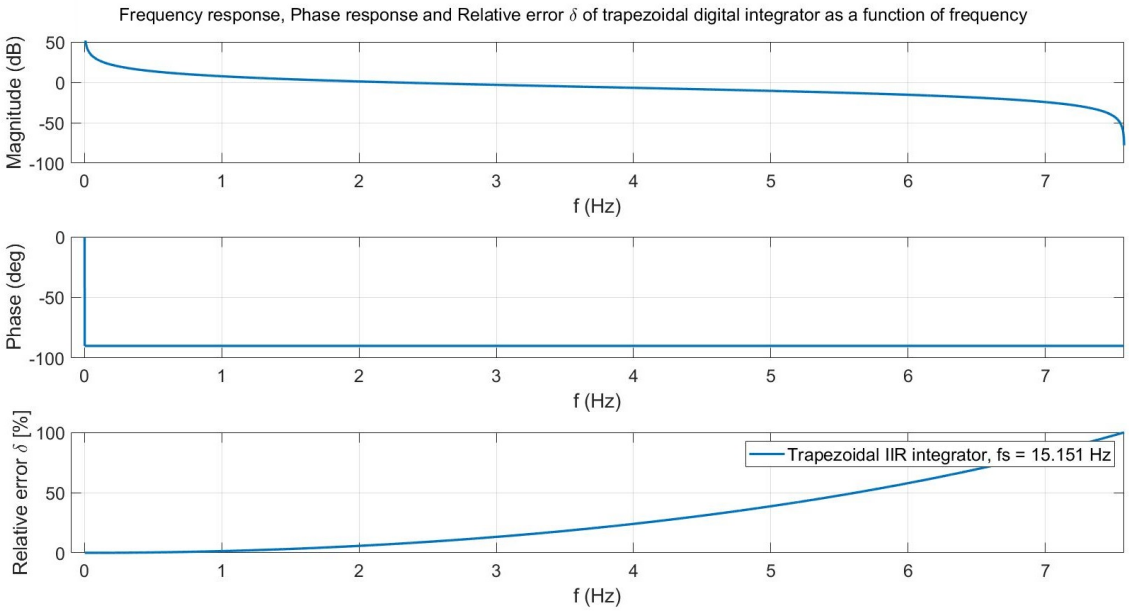

Figure F.1: Frequency response, phase response and relative error δ of trapezoidal IIR integrator

In this figure, the relative error of this digital integrator δ shows by how much the current/ actual frequency response (H_c) is deviating from the ideal frequency response (H_t) of the integrator, designed to be applied to a digital signal sampled at 15.151 Hz[1].
Hence, the third subplot proves that for digital signals sampled at 15.151 Hz, the trapezoidal integration method would falsely determine velocities and displacements by 24% for acceleration signals that are containing a large amount of their energy above 4 Hz.
Since most of the major structures have natural frequencies in the range of 1-2.5 Hz, the application of this type of digital integrator is a safe and effective option both in time as well as in frequency domain.

Moreover, in the book of (Brandt [1]) a comparison between the most frequently used differentiator, know as *diff* differentiator, and some other, more performant differentiators, such as the central difference/ gradient differentiator and a high order ($o = 80$) maximum flat FIR differentiator with linear-phase response, known as Parks-McClellan/Remez differentiator, was considered, labeling the Parks-McClellan/Remez differentiator as best for deriving acceleration values. The design and application of this type of differentiator is discussed below.
The Parks-McClellan/Remez differentiator is nothing else but a high order maximum flat FIR differentiator with linear-phase characteristics, that ideally approximates an optimal differentiator with frequency response $H(\hat{\omega}_0) = i\hat{\omega}_0$. Its design is based on feed forward coefficients that are symmetric around $\frac{(M-1)}{2}$, where

[1] equal to the sampling rate of the acquired acceleration data set of the cantilever beam experiment.

$M = o+1$ is the filter length. These coefficients are determined based on a recursive algorithm that reads:

$$c_1 = \frac{\frac{o}{2}}{\frac{o}{2}+1}, ..., \; c_n = (-1) * c_{n-1} * \left(\frac{(n-1) * (\frac{o}{2} - n + 1)}{n * (\frac{o}{2} + n)} \right) \quad n = 1, 2, ..., \frac{o}{2} \tag{F.2}$$

where:

c_n = recursion coefficients for defining the Parks-McClellan/Remez differentiator

Hence, the c_n coefficients are used for designing the FIR filter by placing them on the right side of the filter in the feed forward coefficients vector A, right after a 0-feed forward coefficient found at $\frac{(M-1)}{2}$. To the left of this 0 value, the c_n coefficients are mirrored and their sign is changed. In the end the feed forward coefficients vector A takes the final form of:

$$A = [-c_n \; ... \; -c_1 \; 0 \; c_1 \; ... \; c_n] \tag{F.3}$$

The difference between the Parks-McClellan/Remez differentiator and lower order maximum flat filter differentiators is that the Parks-McClellan/Remez differentiator "behaves better close to the Nyquist frequency" (Brandt [1]), meaning that its frequency response is closer to the frequency response of an ideal digital differentiator. In such a case, the digital differentiation process can perform a correct differentiation operation also close to the Nyquist frequency. To illustrate the performance rate of each aforementioned differentiator, a plot with the relative error δ of a diff differentiator (red), an 8^{th} order maximum flat filter differentiator (yellow) and the Parks-McClellan/Remez differentiator (blue) was created.
Figure F.2 proves that from all studied differentiators Park-McClellan differentiator performs the best. As one can see from this figure, its relative error starts to get significant close to the Nyquist frequency while the 8^{th} order maximum flat differentiator stats to diverge by 40% from the ideal differentiator for input signals that contain a lot of energy above 2 Hz. Moreover, the *diff* differentiator presents an overall poor performance and its use should be avoided for any kind of SHM applications. Therefore, Park-McClellan differentiator should be considered in the differentiation processes of this study.

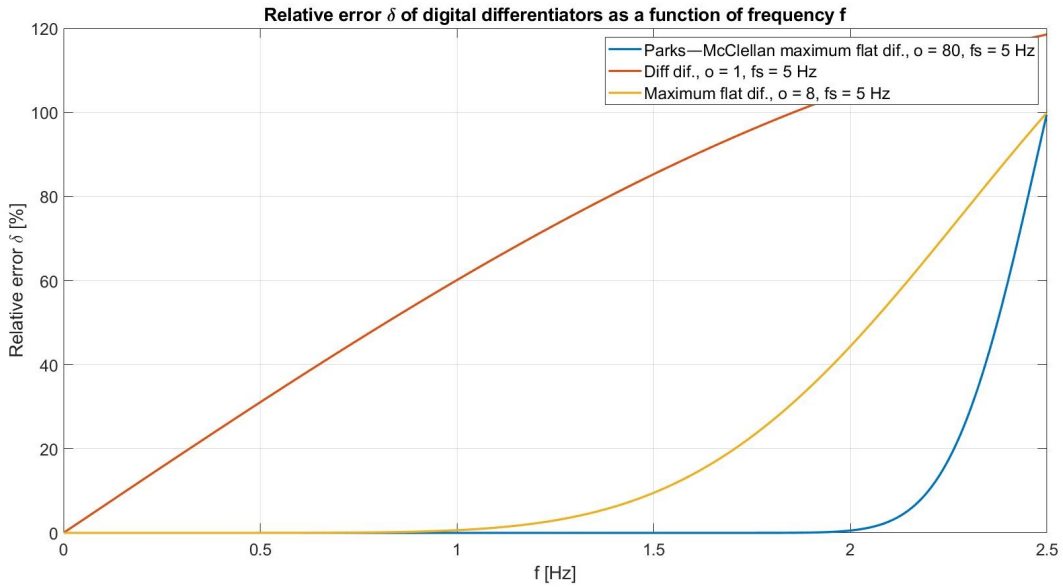

Figure F.2: Relative errors δ of diff differentiator (red), maximum flat differentiator of order 8 (yellow) and Parks-McClellan differentiator (blue). The differentiators were designed for input signals with a sampling frequency of 5 Hz.

As a side note, the relative error values δ from figure F.2 were computed based on F.1, where the actual frequency response (H_c) for each differentiator was corrected for phase delay by applying the following expression:

$$H_{c_{cor}} = H_c * e^{i2\pi \frac{o}{2} \hat{\omega}_0} \tag{F.4}$$

where:

$H_{c_{cor}}$ = Phase delay corrected frequency response
H_c = Current/ actual frequency response of the digital integrator
$\hat{\omega}_0$ = Normalized angular frequency

and the true/ ideal frequency response (H_t) was equal to $H_t = i(\hat{\omega}_0)$.

REFERENCES

[1] A. Brandt, *Noise and Vibration Analysis: Signal Analysis and Experimental Procedures* (John Wiley & Sons, 2011).

G

Appendix G: Galileo Constellation, Orbital Repeat Period Determination

In this appendix, the determination of the orbital repeat period of Galileo constellation based on satellite orbit determination principles is discussed.
Firstly, in order to make the reader better understand the architecture of the Galileo constellation, a view over its three orbital planes (A,B,C) is presented below:

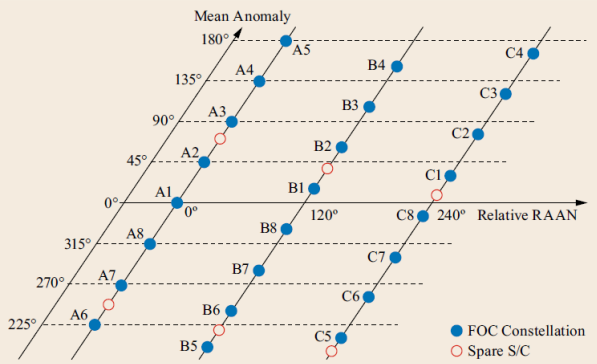

Slot - Satellite ID

A1 - GSAT0218 PRN E31	B1 - GSAT0220 PRN E13	C1 - GSAT0214 PRN E05
A2 - GSAT0210 PRN E01	B2 - GSAT0221 PRN E15	C2 - GSAT0209 PRN E09
A3 - GSAT0215 PRN E21	B3 - GSAT0204 PRN E22	C3 - GSAT0213 PRN E04
A4 - GSAT0217 PRN E27	B4 - GSAT0219 PRN E36	C4 - GSAT0103 PRN E19
A5 - GSAT0206 PRN E30	B5 - GSAT0101 PRN E11	C5 - GSAT0104 PRN E20
A6 - GSAT0211 PRN E02	B6 - GSAT0102 PRN E12	C6 - GSAT0207 PRN E07
A7 - GSAT0216 PRN E25	B7 - GSAT0222 PRN E33	C7 - GSAT0208 PRN E08
A8 - GSAT0205 PRN E24	B8 - GSAT0203 PRN E26	C8 - GSAT0212 PRN E03

Figure G.1: Galileo constellation slot (left) . List of Satellite IDs (right). Courtesy to: (Teunissen and Montenbruck [1], pg. 249)

Based on the number of the satellites present on one plane of $n = 8$ and on the fact that each plane has a near-circular[1] shape, one is able to define the angular distance between concurrent satellites within the same plane and the angular distance between consecutive planes as:

$$\begin{aligned} \frac{360°}{n} &= \frac{360°}{8} = 45° \\ \frac{360°}{P} &= \frac{360°}{3} = 120° \end{aligned} \tag{G.1}$$

where:
n = number of Galileo satellites on one plane
P = number of orbital planes

In the next step, the determination of Galileo's orbital repeat period in a non-inertial frame fixed at the centre of the Earth, is performed. For this one can consider that a Galileo satellite is influenced only by the Earth exerted gravitational force F. Therefore, by considering that the satellite is orbiting the Earth in such a way that the Earth's gravitational force equals with the satellite exerted centrifugal force (F_{cf}) (see G.4), one is able to define the revolution period of a satellite (T) as:

$$F = -G\frac{M * m}{r^2} \tag{G.2}$$

$$F_{cf} = m\omega^2 r \tag{G.3}$$

$$(G.2) + (G.3) \rightarrow \omega = \sqrt{\frac{GM}{r^3}} \tag{G.4}$$

$$\omega = \frac{2\pi}{T} \tag{G.5}$$

$$(G.4) + (G.5) \rightarrow T = \frac{2\pi}{\sqrt{\frac{GM}{r^3}}} \tag{G.6}$$

where:
G $= 6.674 * 10^{-11} [\frac{m^3}{kg * s^2}]$ - universal constant of gravity
M $= 5.973 * 10^{24}$ [kg] - approximate mass of the Earth
m = satellite's mass [kg]
r = radial distance between Earth and satellite, in this case equal with the semimajor axis a=29600318 [m] of the circular orbit
ω = angular velocity of the satellite $[\frac{rad}{sec}]$

By filling in the known values in G.7 the orbital period of the Gallileo constellation is equal with:

$$T = \frac{2\pi}{\sqrt{\frac{6.674*10^{-11}*5.973*10^{24}}{29600318^3}}} = 50682.2102\,[sec] = 14.07839172\,[h] = 14h\ 4min\ 42.21sec \tag{G.7}$$

[1] eccentricity of the orbital plane, $e \approx 0$.

REFERENCES

[1] P. Teunissen and O. Montenbruck, *Springer Handbook of Global Navigation Satellite Systems* (Springer, 2017).

H

Appendix H: GNSS Data Processing Configurations & Fixed Ambiguity Filtration

In this appendix, the preferred GNSS data processing configurations feed in RNX2RTKP and RTKNAVI AP's for performing PPK and RTK processing, are listed in the next table:

Table H.1: PPK & RTK processing configurations feed in RNX2RTKP & RTKNAVI

RTKLib PPK & RTK processing configurations		
Positioning Mode	Kinematic	
Sat. constellation, PPK processing	GPS/ Galileo	
Sat. constellation, RTK processing	GPS, Galileo, Beidou	
Frequencies/ Filter Type	L1+L2	Forward
Min Ratio to Fix Ambiguity	3	
Elevation Mask [°]	15°	
Integer Ambiguity Resolution	Continuous	
Output - Solution Format	E(X)/N(Y)/U(Z)-Baseline	
Output - Output Solution Status/ Debug Trace	Residuals	
Base Station: BRD01, Coords. ITRF14 at epoch 2020.1		
X (ECEF) [m]	3954573.96748	
Y (ECEF) [m]	326545.84086	
Z (ECEF) [m]	4976847.93959	
Misc - Time Interpolation of Base Station Data	Tick	

Despite the general advise of using ETRS89 for any geodetic application run on the European continent, just like the cantilever beam experiment, ITRF based solutions are preferred due to the handy static precise point positioning (PPP) absolute position estimation function offered by the Natural Resources Canada (NRCAN) department. Hence, the absolute ECEF positions of the reference station from the last part of table H.1 were determined by sending a collection of 1 Hz code and CP measurements, acquired by the reference station two days and a half before the beginning of the cantilever beam experiment, to the NRCAN department. NRCAN[1] was using this information to process the GNSS data via static PPP, outputting the following ITRF14(2020.1) geographic coordinates solutions:

$$\textbf{\textit{Latitude}}: 51^\circ\,37'\,19.72729'',\ \textbf{\textit{Longitude}}: 4^\circ\,43'13.60080'',\ \textbf{\textit{Ellipsoidal Height}}: 47.093m \tag{H.1}$$

These solutions were converted in ECEF-XYZ Cartesian coordinates corresponding to the GRS80 ellipsoid via *lla2ecef* Matlab's function, resulting in the following values equal with the ones listed in the previous table:

$$\boldsymbol{X}: 3954573.9674779m,\ \boldsymbol{Y}: 326545.8408620m,\ \boldsymbol{Z}: 4976847.9395898m \tag{H.2}$$

In some cases, the resulting relative position and/ or CP residuals time series were containing random data gaps. An example of a gap in relative position estimates can be found in the lower part of figure H.1. This figure indicates a sub sample from the raw code and CP observations, uninterruptedly collected by the reference and rover stations at 1 respectively 5 Hz rate, and their corresponding relative position solutions which are fragmented by a gap of 1.6 seconds. It is believed that such gaps were caused by the malfunctioning of the last chosen processing configuration "Misc - Time Interpolation of Base Station Data" (see table H.1), which should linearly interpolate the base station data to the rover epochs. This particular data processing problem of not being able to produce exactly 86400 at 1 Hz respectively 432000 daily position/ residuals solutions at 5 Hz rate can be solved by first identifying the missing time instants during each day of interest and filling the corresponding missing observations gaps with not-a-number (NaN) values. To do so, a Matlab script was implemented, which searches for gaps in the time series of each day and updates the entire RNX2RTKP .pos and/ or .pos.stat structure with NaN values corresponding to the missing time instants in order to define complete GNSS based data sets. Prior to any data analysis process, this correction process was run for each relative position and/or CP residuals time series of each day of the cantilever beam experiment.

[1] https://webapp.geod.nrcan.gc.ca/geod/tools-outils/ppp.php?locale=en

BRD01 reference station 1 Hz .obs

```
> 2020  3 18  7 58 41.0050000  0 34
E27  29955205.060                  -3589.301        30.000    29955197.753                  -2751.476        24.000
G 7  25709575.518   135104720.226  -3668.801        43.000    25709569.395  105276363.539   -2859.273        36.000
G15  22936690.659   120533104.365   1703.281        48.000    22936684.647   93921918.025    1327.292        43.000
G18  25958010.784   136410244.490  -2776.714        38.000    25958006.201                  -2163.552        32.000
...

> 2020  3 18  7 58 42.0050000  0 35
E27  29955888.126                  -3589.493        30.000    29955880.920                  -2750.686        24.000
G 7  25710273.779   135108389.250  -3669.106        44.000    25710267.532  105279222.528   -2859.479        36.000
G15  22936366.599   120531401.292   1702.849        48.000    22936360.558   93920590.953    1327.086        43.000
G18  25958539.309   136413021.588  -2777.681        37.000    25958534.675  106295910.997   -2163.644        32.000
```

BRD02 rover station 5 Hz .obs

```
> 2020  3 18  7 58 41.4070000  0 34
G 8  26846760.308                3      -1578.876        24.000    26846749.063                3      -1223.291        23.000
G13  22276727.979   117065064.759        -238.735        46.000
G21  27275936.337   143335995.354       -1823.170        42.000
G18  26436641.766   138925464.172       -3027.324        43.000    26436633.997  108253582.963   -2358.538        36.000
...

> 2020  3 18  7 58 41.6070000  0 34
G 8  26846820.867                3      -1578.538        24.000    26846809.003                3      -1239.419        24.000
G13  22276737.069   117065112.481        -238.694        46.000
G21  27276005.691   143336359.905       -1822.941        42.000
G18  26436756.951   138926069.586       -3027.179        43.000    26436749.226  108254054.735   -2358.668        36.000
```

RNX2RTKP 5 Hz .pos -> gap in solutions

```
%  (e/n/u-baseline=WGS84,Q=1:fix,2:float,3:sbas,4:dgps,5:single,6:ppp,ns=# of satellites)
%  UTC                   e-baseline(m)  n-baseline(m)  u-baseline(m)   Q  ns   sde(m)   sdn(m)   sdu(m)   sden(m)  sdnu(m)  sdue(m) age(s)  ratio
2020/03/18 07:58:41.400       -13.9041         7.0711         0.2298   1   6   0.0048   0.0064   0.0179  -0.0023  -0.0054   0.0048   -0.60   52.6
2020/03/18 07:58:43.000       -13.9084         7.0707         0.2282   1   6   0.0048   0.0065   0.0178  -0.0023  -0.0052   0.0048    0.00   52.5
```

Figure H.1: Example of collected reference and rover station code and CP observations on day 078 at 07:58:41.4 UTC and the resulting relative position estimates from RNX2RTKP AP. The collected raw observations seem to be uninterruptedly gathered. The last set of .pos observations indicate a gap in solutions caused by one of the processing configurations of the RNX2RTKP processing algorithm that was meant to interpolate the code and CP observations of the reference station at 5 Hz rate

Moreover, in order to consider only trustful baseline estimates for future analyses, a baseline estimates filtration procedure is proposed. This filtration procedure aims to eliminate the estimated relative positions that:

- have their East/ North/ Up formal standard deviation values[2] above 1.5/1.5/2.5 centimeters[3].
- had a lower number of tracked satellites than 5.
- were based on float ambiguities.

The selection of the proposed criteria within the filtration procedure is made with the scope of producing only statistically meaningful relative position solutions that can facilitate the displacement estimation for high-precision SHM applications such as the cantilever beam experiment. Basically these criteria mitigate float solutions or baseline solutions as a result of less than 5 acquired satellite signals at the same time, which correspond to unacceptable solutions degrading the positioning precision up to the meter level. Thus, the first criterion defines exactly the limiting precision margins accepted for the cantilever beam experiment, above which any related position solution should not be considered for further SHM analyses.

[2] $\sigma_{E/N/U}$ – computed based on the least-square based parameter estimation process implemented in the RTKLib package.

[3] critical values which are assumed to be equal with 3 time the derived horizontal and vertical positioning precision of the GNSS module straight out of the box(see last part of subsection 3.2.4).

I

Appendix I: Relative Position based Multipath Correction. Definition & Application

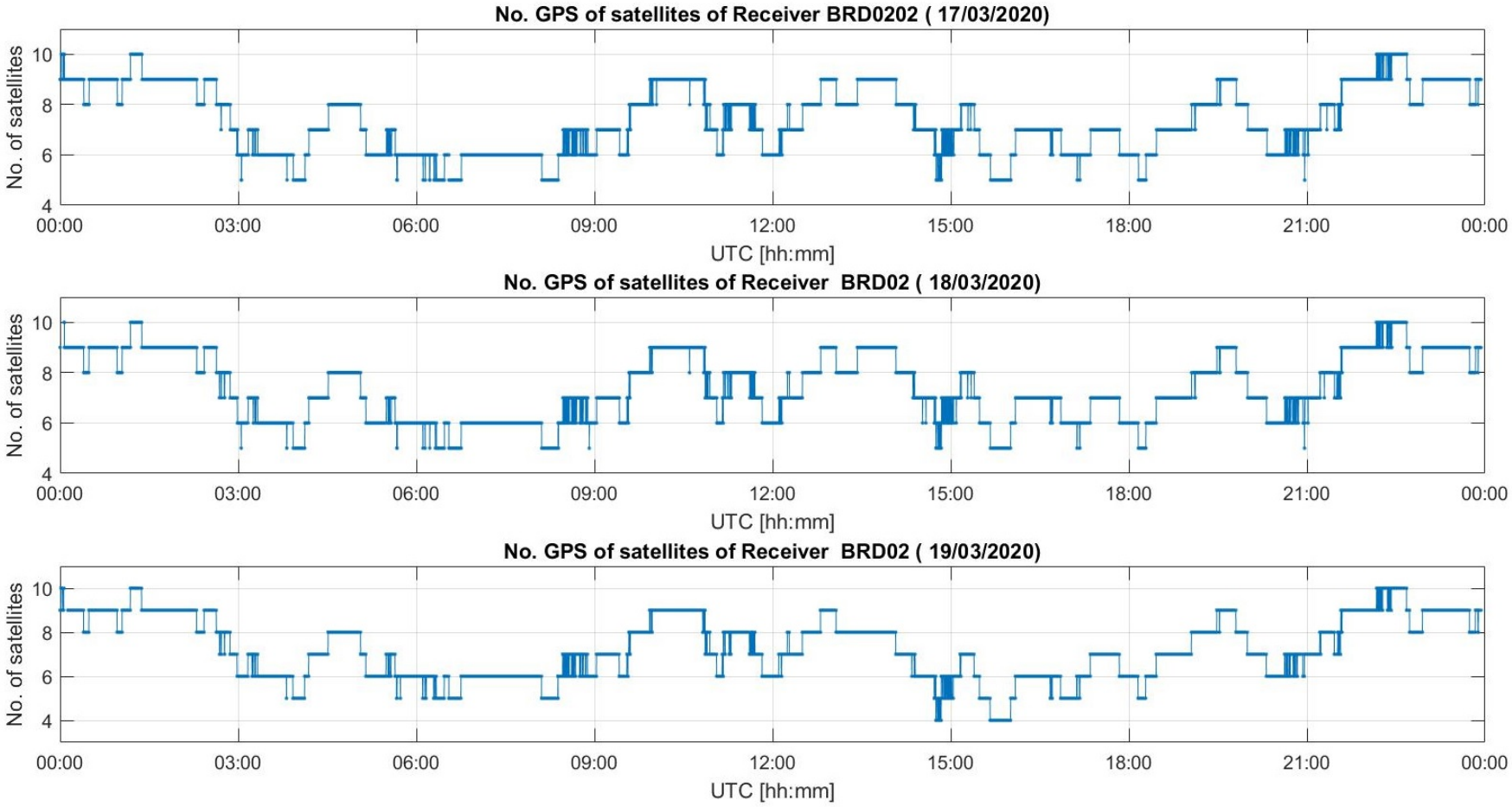

Figure I.1: Number of satellites vs UTC time over each day of interest. The UTC time scales of day 078 and 079 are aligned with respect to the time scale of day 077. This plot indicates that over the three considered days the GPS geometry configuration was kept almost identical at any time instant

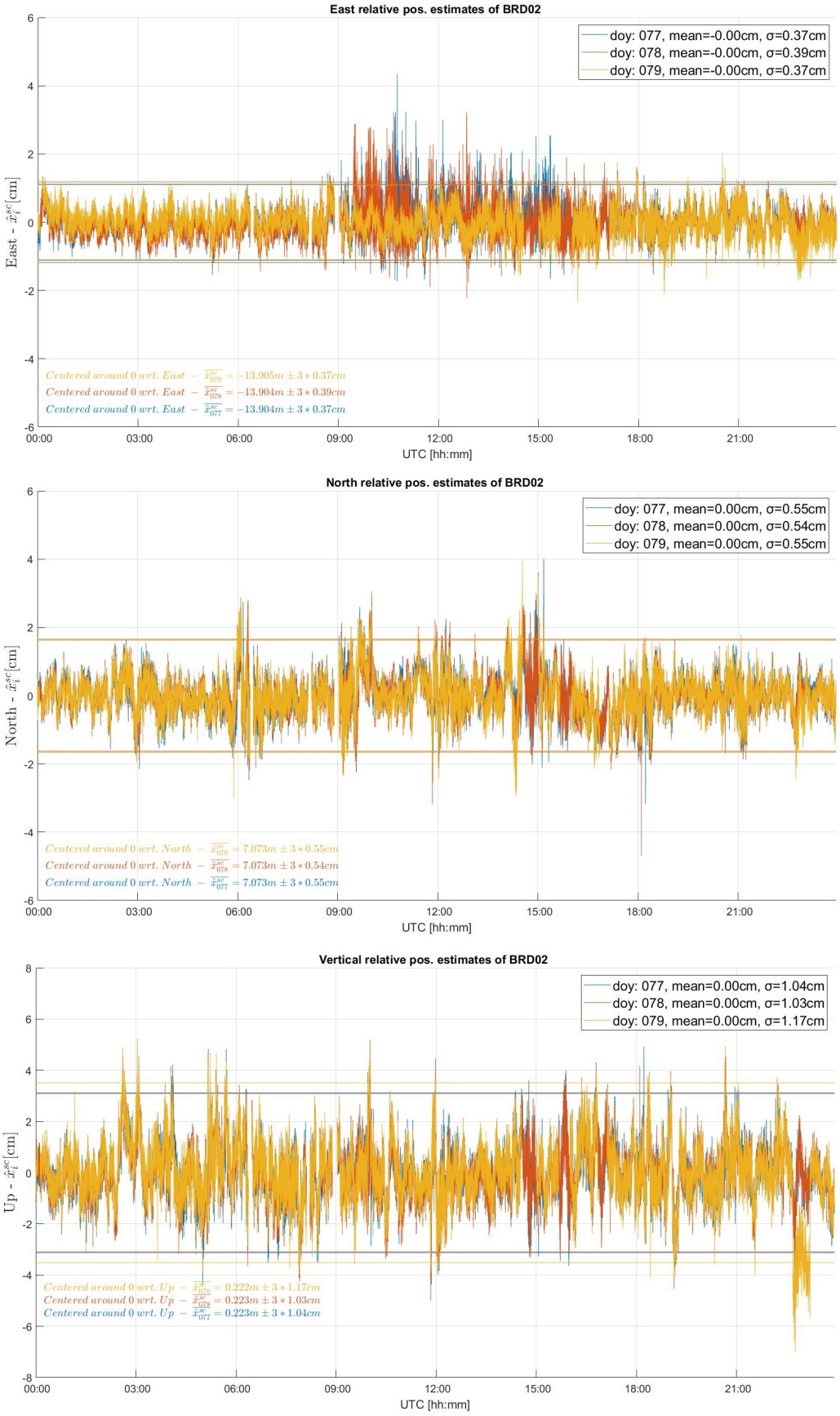

Figure I.2: Overlap of day's 077, 078 and 079 zero-centered East (X)/ North (Y)/ Up (Z) position time series ($\hat{x}_i^{sc}$) vs. UTC time

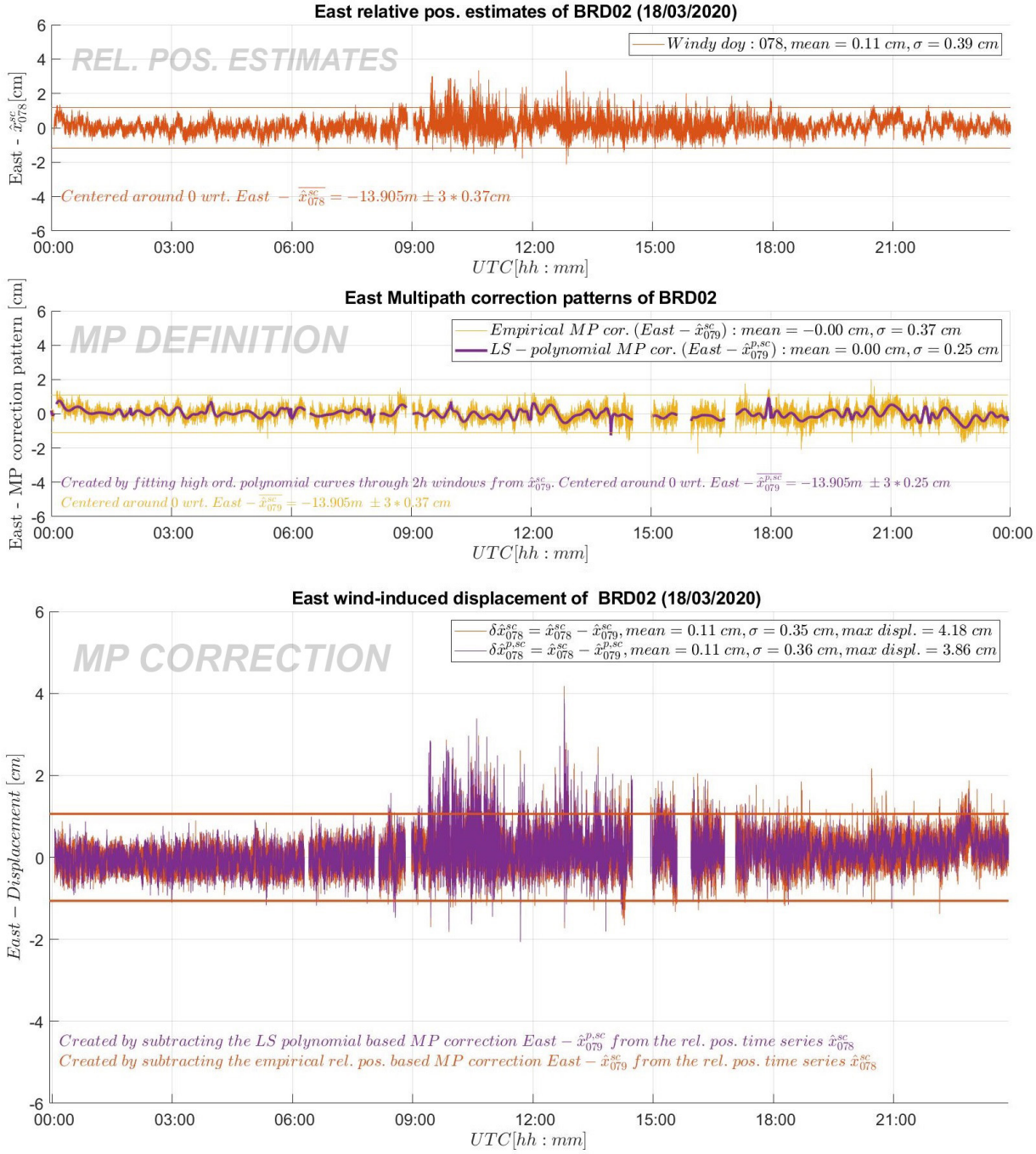

Figure I.3: Figure of the entire East (X) displacement estimation process, containing the plot of the East (X) position time series of day 078 ($\hat{x}^{sc}_{078}$), the plot of the overlapping empirical (yellow - $\hat{x}^{sc}_{079}$) and least-squares polynomial based (purple - $\hat{x}^{p,sc}_{079}$) MP corrections, and the plot of the resulting MP corrected East (X) wind-induced displacements time series of day 078 ($\delta\hat{x}^{sc}_{078}$ & $\delta\hat{x}^{p,sc}_{078}$)

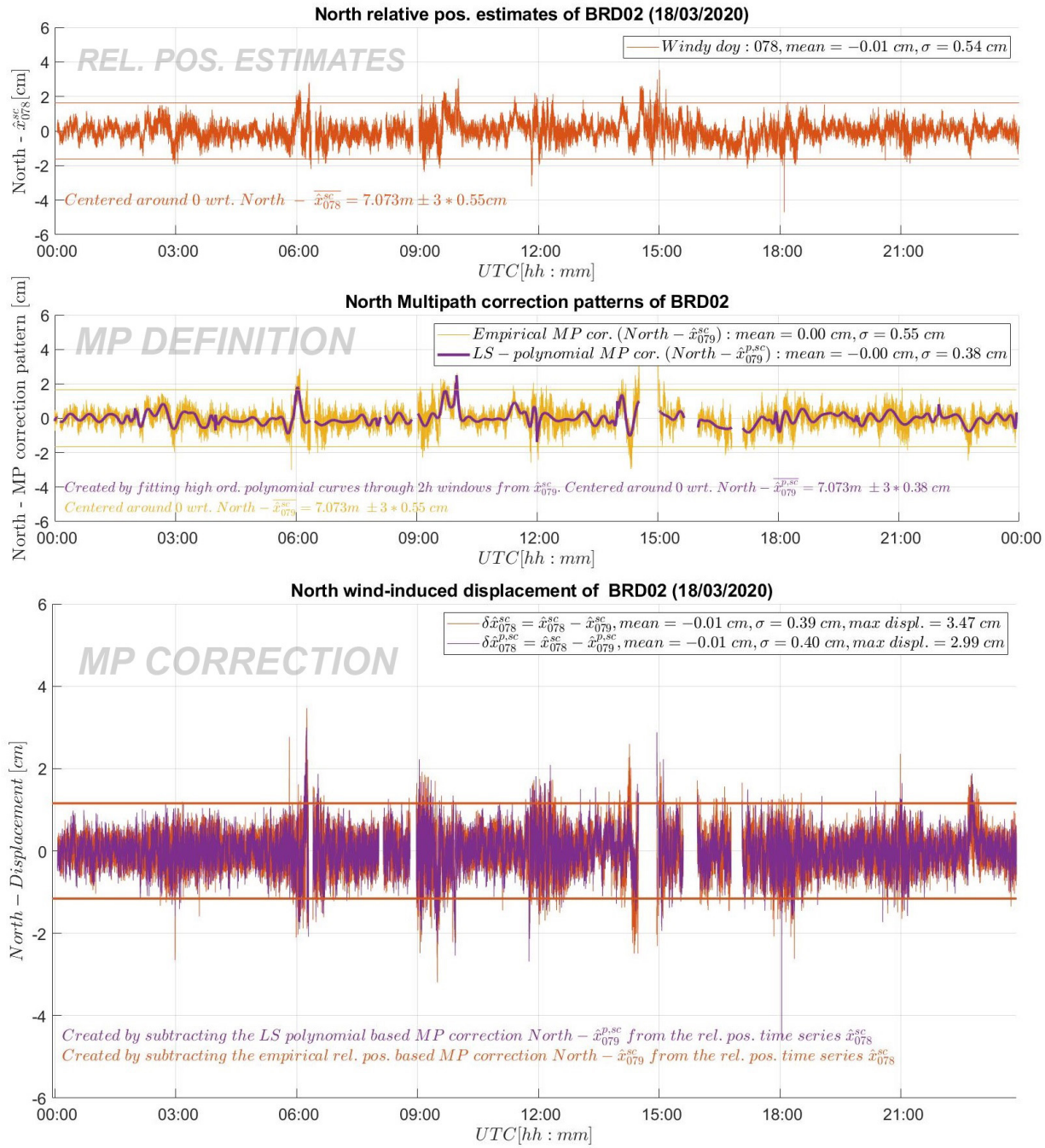

Figure I.4: Figure of the entire North (Y) displacement estimation process, containing the plot of the North (Y) position time series of day 078 ($\hat{x}^{sc}_{078}$), the plot of the overlapping empirical (yellow - $\hat{x}^{sc}_{079}$) and least-squares polynomial based (purple - $\hat{x}^{p,sc}_{079}$) MP corrections, and the plot of the resulting MP corrected North (Y) wind-induced displacements time series of day 078 ($\delta\hat{x}^{sc}_{078}$ & $\delta\hat{x}^{p,sc}_{078}$)

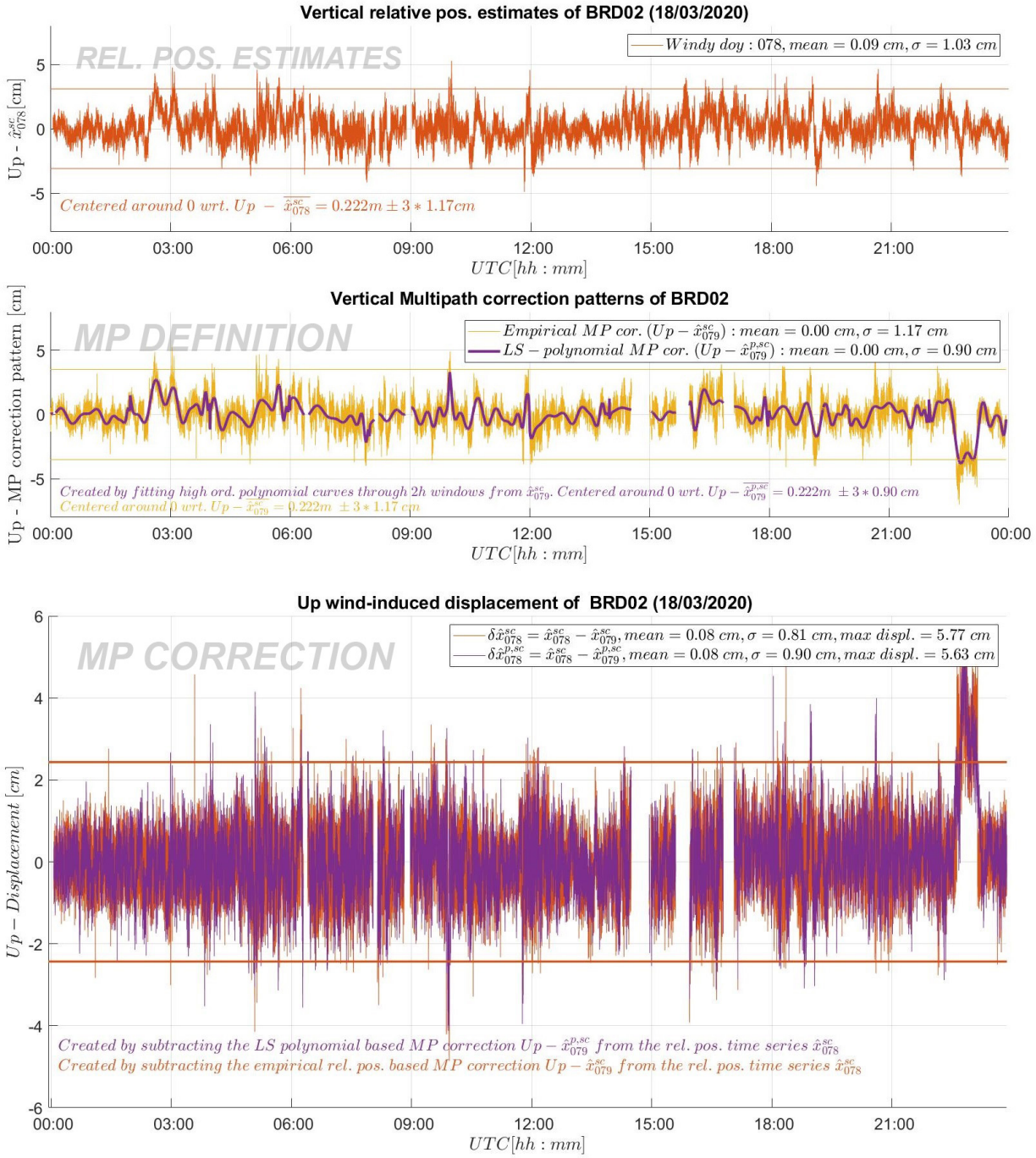

Figure I.5: Figure of the entire Up (Z) displacement estimation process, containing the plot of the Up (Z) position time series of day 078 ($\hat{x}^{sc}_{078}$), the plot of the overlapping empirical (yellow - $\hat{x}^{sc}_{079}$) and least-squares polynomial based (purple - $\hat{x}^{p,sc}_{079}$) MP corrections, and the plot of the resulting MP corrected Up (Z) wind-induced displacements time series of day 078 ($\delta\hat{x}^{sc}_{078}$ & $\delta\hat{x}^{p,sc}_{078}$)

J

Appendix J: Cantilever Beam Experiment Results, WID stage, day 078. Statistical Cross Correlation Analysis, Plots of the Daily Orthogonal Wind Components- and Displacement Time Series

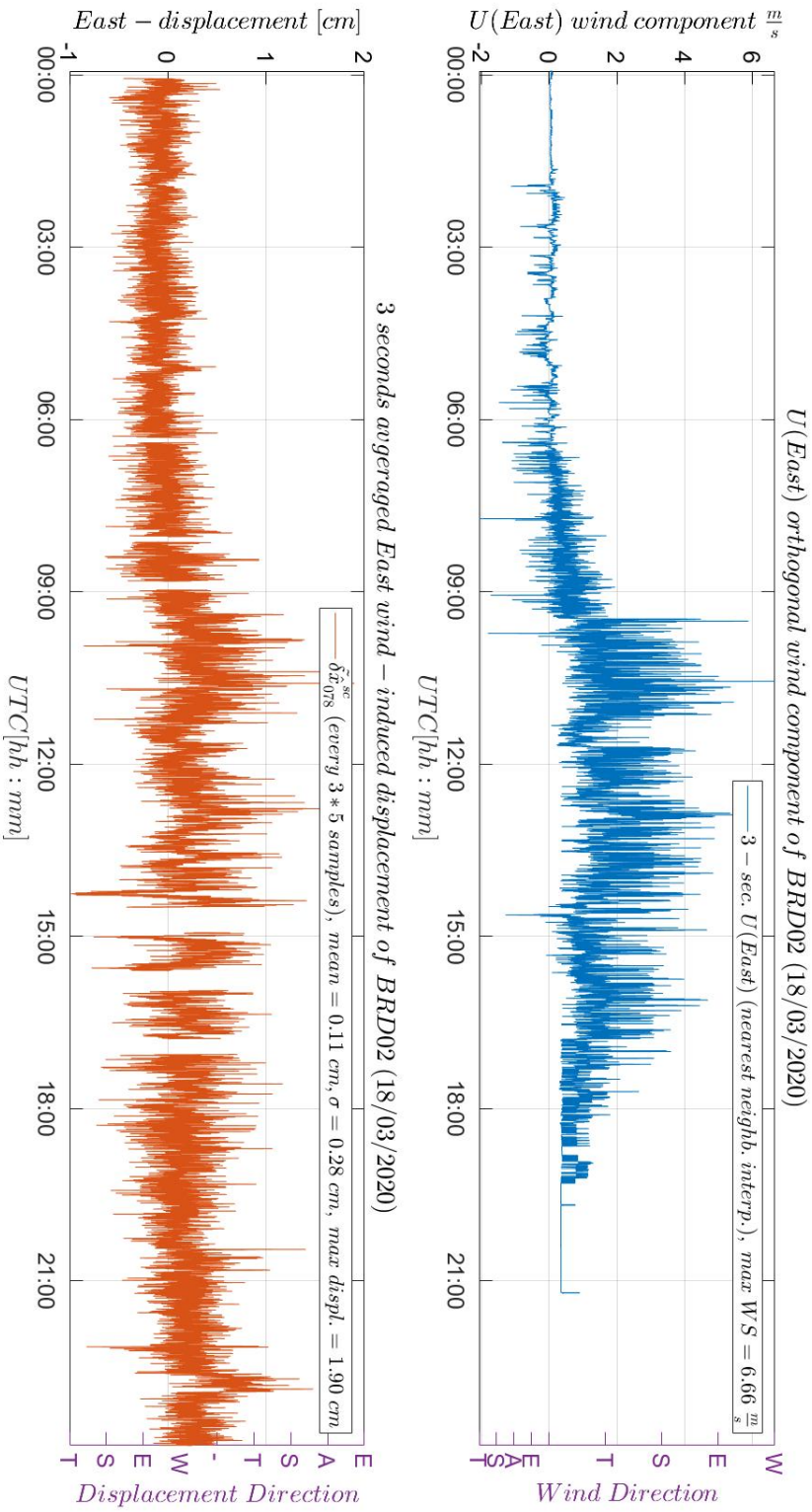

Figure J.1: Figure of the U (East) orthogonal wind components- (blue) and GNSS based East (X) displacement time series (red) of day 078, both aligned in time and corresponding to a 3 seconds sampling period.

J

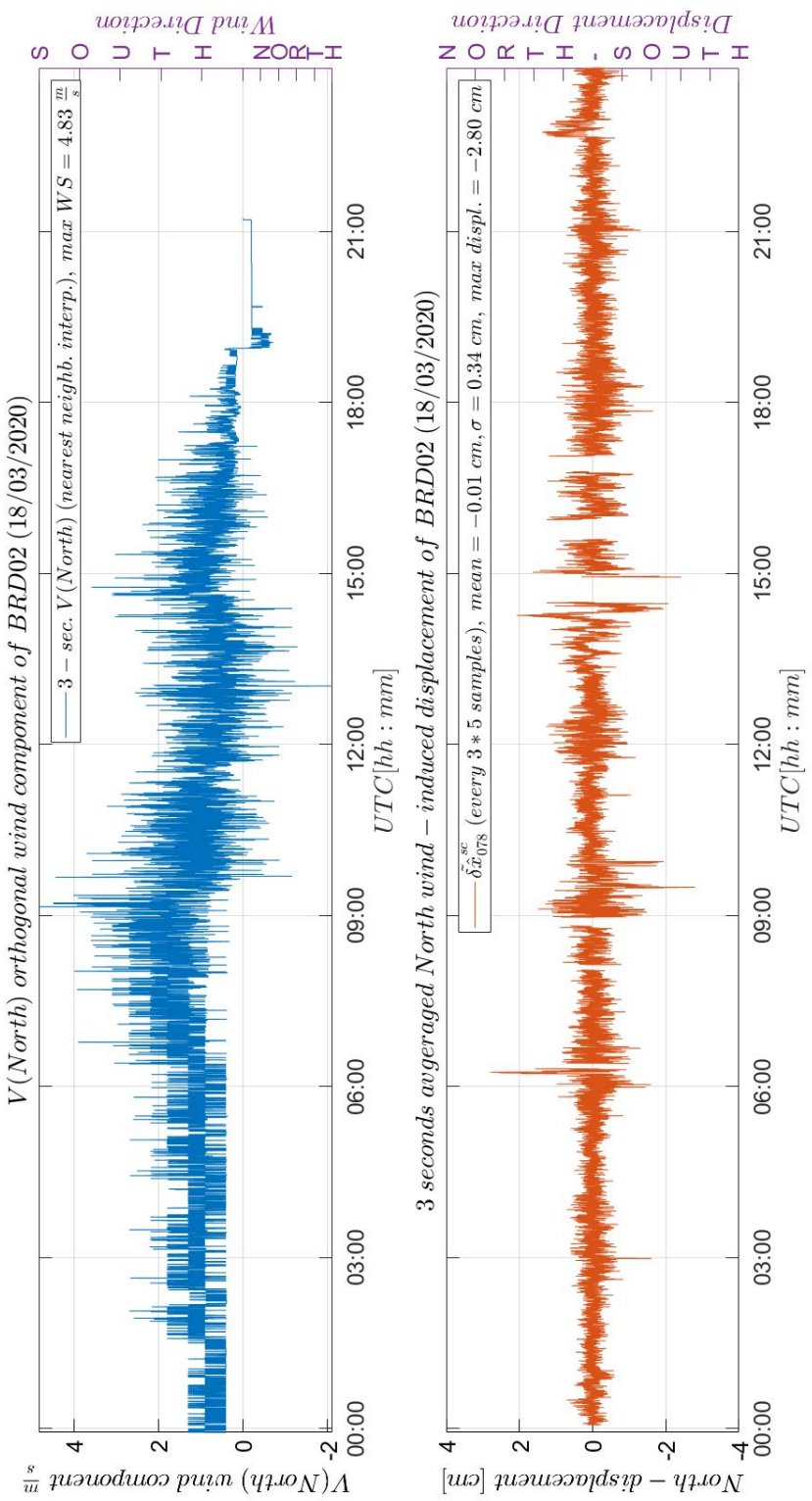

Figure J.2: Figure of the V (North) orthogonal wind components- (blue) and GNSS based North (Y) displacement time series (red) of day 078, both aligned in time and corresponding to a 3 seconds sampling period.

J

K

Appendix K: Validation of Cantilever Beam Experiment Results, WID stage, day 078. Forward Transformation Process

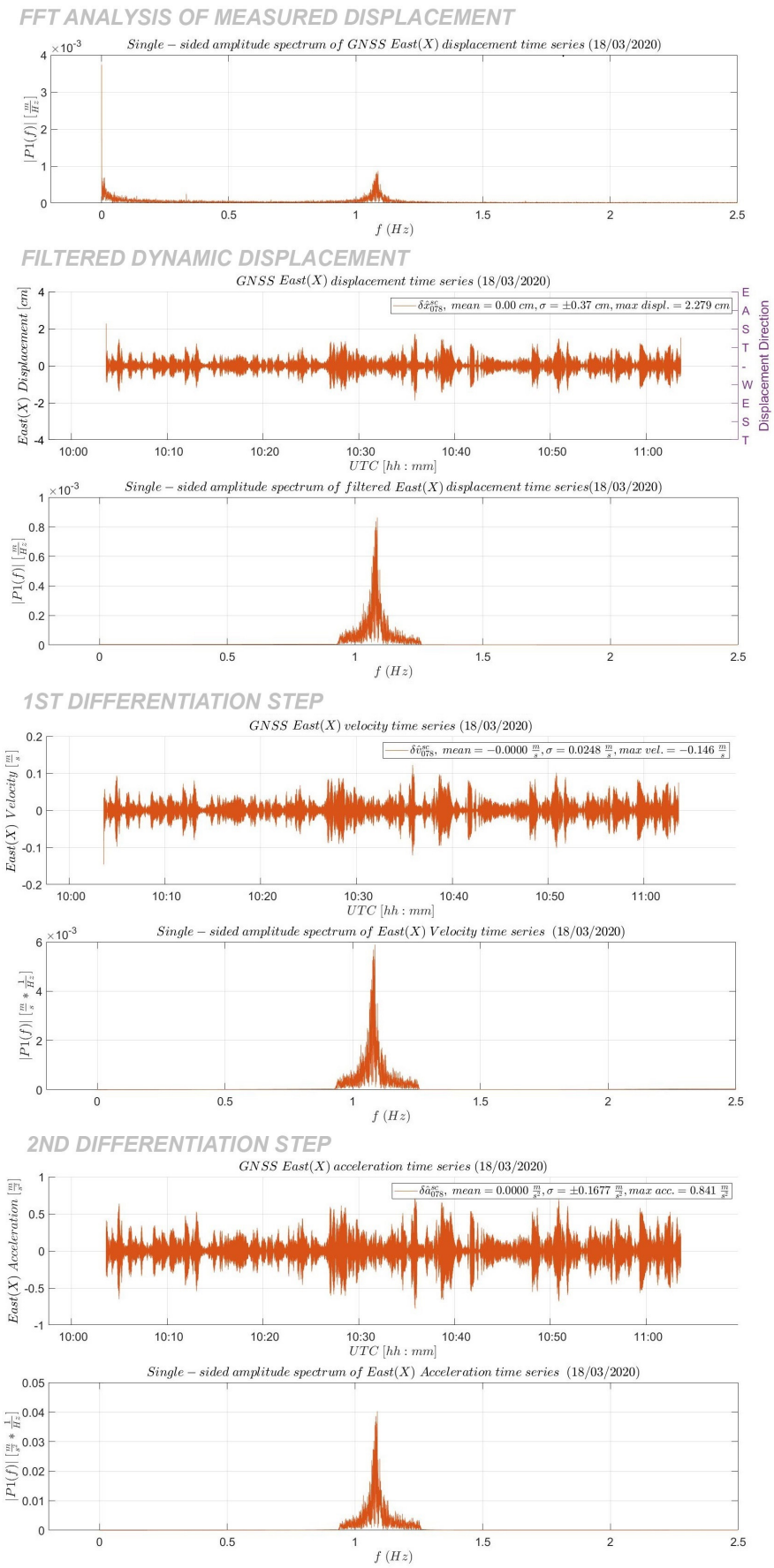

Figure K.1: Results of each stage of the forward transformation process run on the sequence of GNSS based displacements of day 078 corresponding to the period with the highest recorded wind speed.

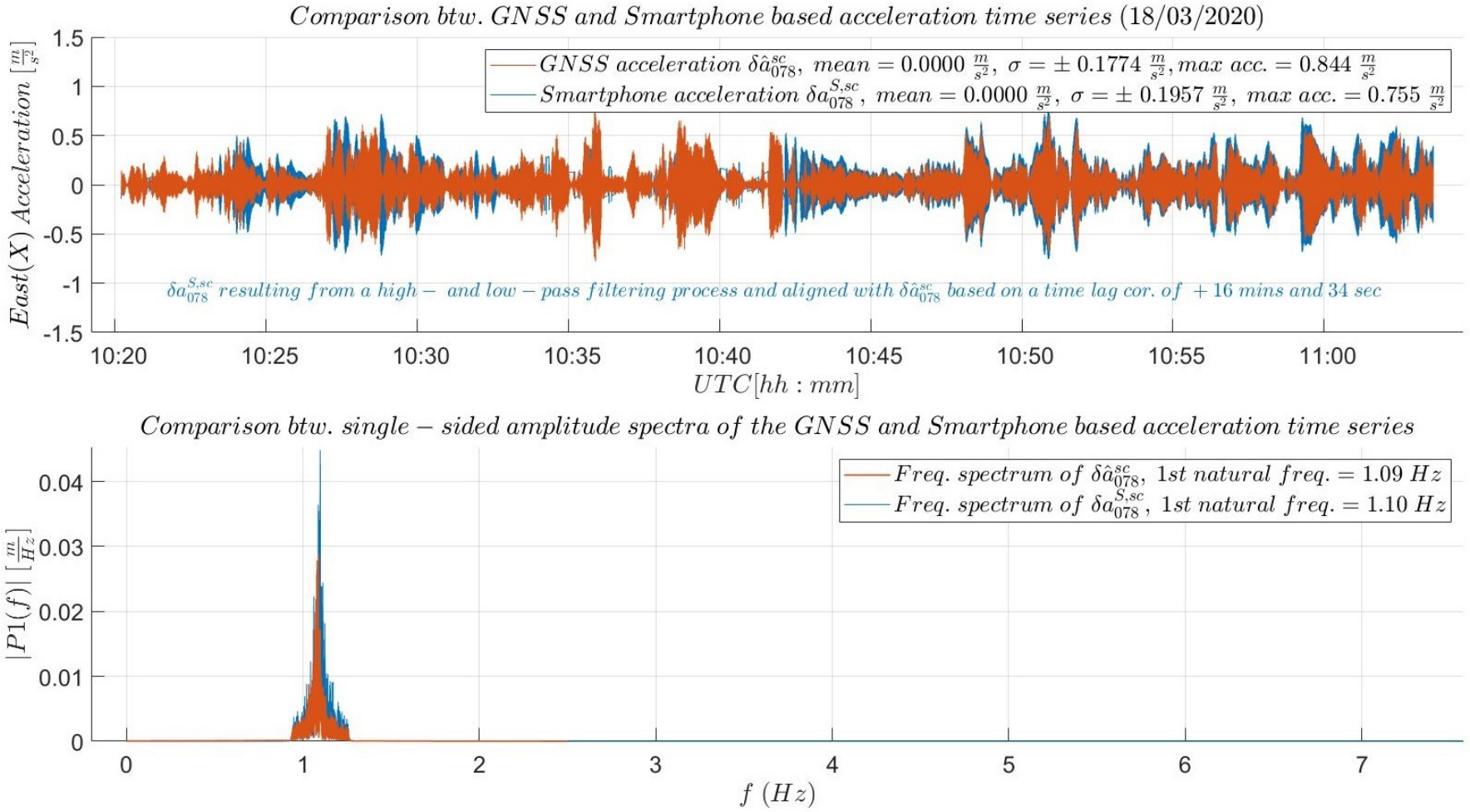

Figure K.2: Comparison between the derived GNSS based acceleration time series ($\delta\hat{a}_{078}^{sc}$, red) and the filtered smartphone accelerometer based acceleration time series ($\delta a_{078}^{S,sc}$, blue), as a result of the the forward transformation process run on the sequence of GNSS based displacements of day 078 corresponding to the highest recorded wind speed. Good visual similarity between the candidate acceleration time series can be observed after 10:47 UTC. The natural frequency of the cantilever beam is attested to be equal to 1.1 Hz

L

Appendix L: Validation of Cantilever Beam Experiment Results, WID stage, day 078. Reverse Transformation Process

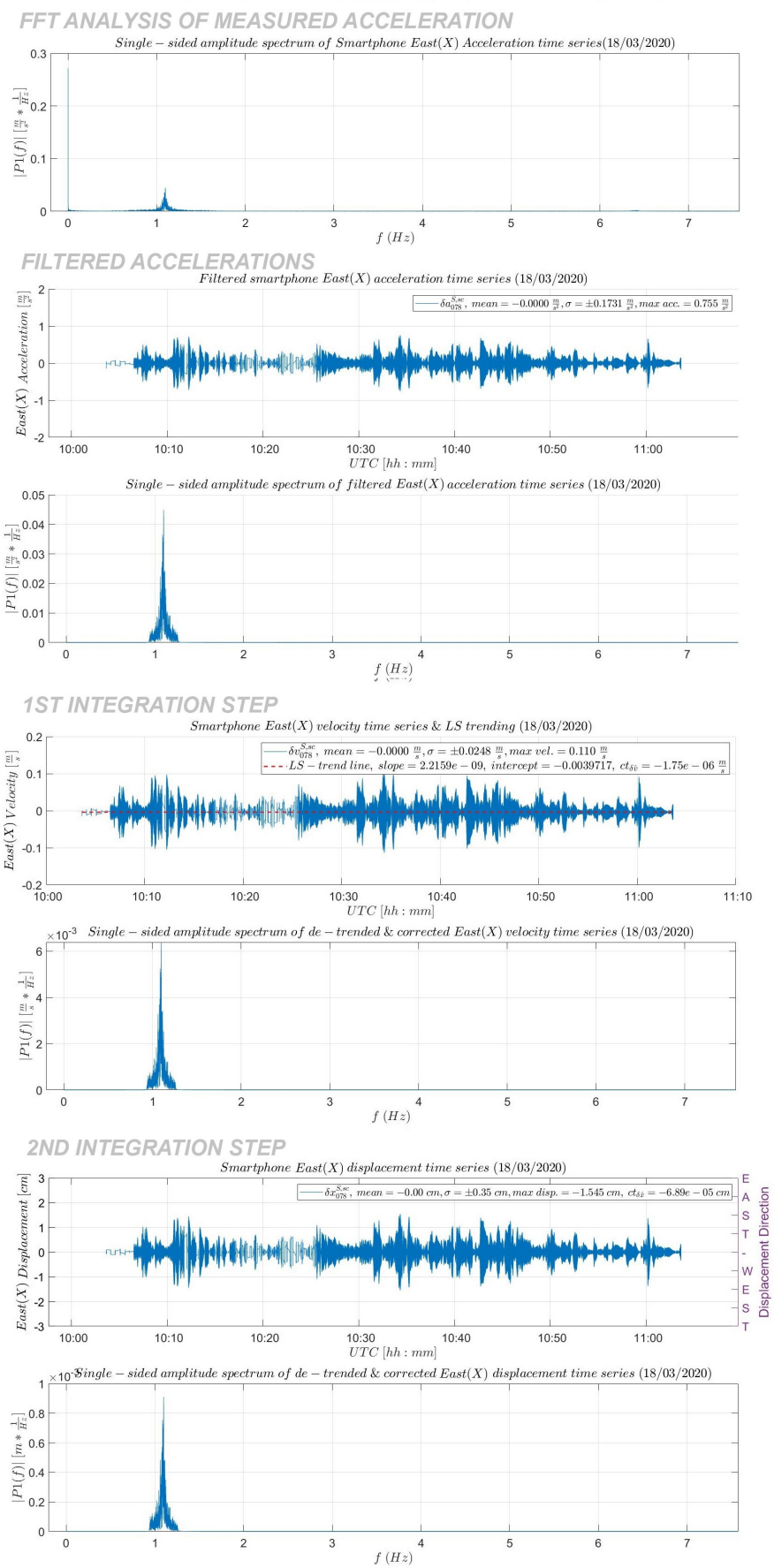

Figure L.1: Results of each stage of the reverse transformation process run on the sequence of smartphone based accelerations of day 078 corresponding to the period with the highest recorded wind speed.

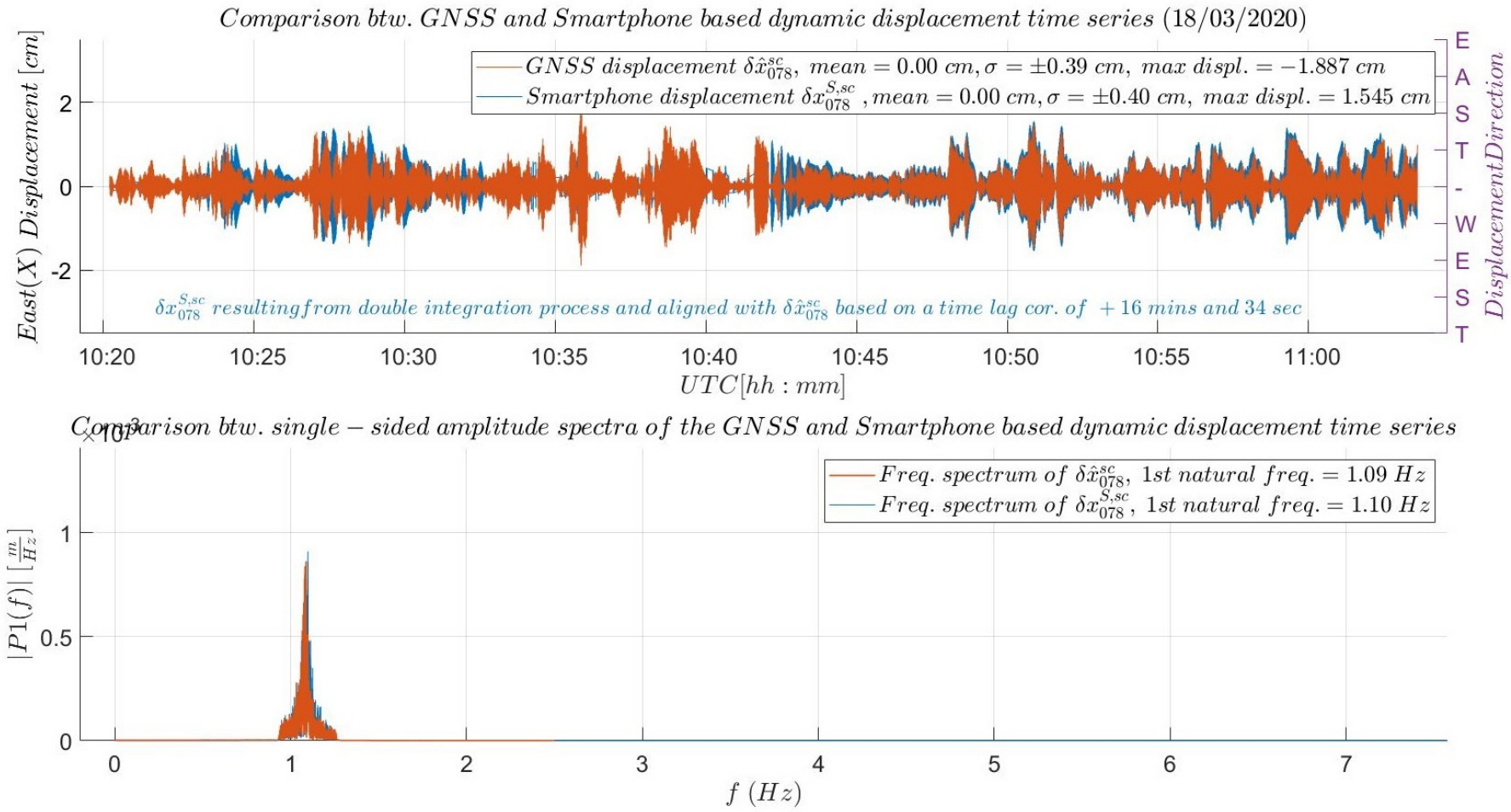

Figure L.2: Comparison between the filtered GNSS based displacement time series ($\delta\hat{x}_{078}^{sc}$, red) and the derived smartphone accelerometer based displacement time series ($\delta x_{078}^{S,sc}$, blue), as a result of the the reverse transformation process run on the sequence of smartphone based accelerations of day 078 corresponding to the highest recorded wind speed. A good visual similarity between the candidate displacement time series can be observed after 10:47 UTC. The natural frequency of the cantilever beam is attested to be equal to 1.1 Hz

M

Appendix M: Random Noise Processes. Time Correlation Analysis for the Evidence of the Whiteness of Observation Time Series

In general the whiteness of a set of observations can be questioned via a time correlation analysis, by calling for the auto-correlation sequence ($\rho(\tau)$) of the considered observations time series, which is formally defined as the ratio between the auto-covariance (Q_{yy}) of the digital signal at lag[1] τ and the auto-covariance at lag 0 equal with the variance of the studied data set:

$$\rho(\tau) = \frac{Q_{yy}(\tau)}{Q_{yy}(0)} = \frac{Q_{yy}(\tau)}{\sigma^2} \tag{M.1}$$

where:

Q_{yy} = auto-covariance of the considered digital signal
τ = time lag [s]

In general, the auto-covariance is a measure of concomitant variation of the samples of the random process $y(t)$, which is "depending only on the time difference between instant $t+\tau$ and t" (Tiberius and Amiri-Simkooei [1]) while the auto-correlation function ρ is a derived measure of the similarity between sample pairs of $y(t)$ and $y(t+\tau)$. Therefore, one could use the auto-correlation function to find out if close-by samples have a certain degree of similarity as an indication of deliberately data replication or manipulation within a time series of observations. For obtaining the desired auto-correlation sequence Matlab's *xcorr* function can be run on the considered time series of observations. Visually the resulting auto-correlation sequence can be illustrated through a correlogram[2], just as the three correlograms from figure M.1 resulting from a time correlation analysis performed on East (X)/ North (Y)/ Up (Z) random noise sequences of a 2-hour block GNSS based displacements sequence collected during day 079 of the cantilever beam experiment (see subsection 3.2.4 and 4.4). Alongside to the correlogram, the 2σ confidence interval is plotted to indicate the 95% confidence region of no correlation. Hence, the presence of the resulting auto-correlation sequence within this interval can be translated into a trace of no correlation in the considered time series of observations, where any divergence of the auto-correlation sequence from the 95% interval limits shows a (re)gain in correlation. For obtaining the desired 2σ confidence interval Matlab's *std* function can be run on the considered auto-correlation sequence. The resulting standard deviation value needs to be multiplied by 2 in order to define the 95% interval.
In case of the annexed example of the East (X)/ North (Y)/ Up (Z) auto-correlation noise sequences from figure M.1, one can observe that to a large extent these auto-correlation sequences do not cross the confidence regions after reaching 0 for the first time. This is a good sign that the observations present a specific degree of time correlation defined by the exponential decaying behaviour of their auto-correlation sequences. This specific behaviour is mathematically introduced in the last part of this appendix.

There are two particular random processes to consider when trying to identify data replication and these are: the purely random noise process and the auto-regressive noise process of order 1 (AR1). From their names one can understand that the aforementioned processes classify the behavior of random noise present in random processes due to unknown sources. Therefore, a thorough inspection of the presence of random noise in the considered data set is mandatory for attesting the whiteness of a sequence of collected observations.
The purely random noise process, also known as white noise process, "yields a sequence of uncorrelated random noise variables" (Tiberius and Amiri-Simkooei [1]), for which the auto-correlation function peaks at lag 0 and drops immediately to 0 for any other lag.

$$\rho(\tau) = \begin{cases} 1, & \tau = 0 \\ 0, & \tau \neq 0 \end{cases} \tag{M.2}$$

Hence, if the resulting auto-correlation coefficients derived from the random noise sequence of the considered data set follow a random noise process behavior, then the whiteness of the observations can be attested.

M

[1] τ is a multiple of the sampling period, which in case of the cantilever beam experiment (for the accelerometer) is equal to $\frac{1}{f_s} = \frac{1}{15.151}1 = 0.066\ seconds$.
[2] figure of the auto-correlation function as a function of lag τ. The auto-correlation sequence is normally mirrored around the auto-correlation of lag 0, corresponding to a 2*m-1 long sequence where m equals the length of the input signal.

On the other hand, *the auto-regressive noise process of order 1* yields a sequence of weakly correlating random noise variables, for which the auto-correlation function peaks at lag 0 and exponentially decays to zero driven by a correlation coefficient β within (0,1).

$$\rho(\tau) = \beta^{|\tau|} \tag{M.3}$$

where:

β = correlation coefficient

A zero-mean AR(1) random noise process is mathematically defined by:

$$y_t - \beta y_{t-1} = e_t \tag{M.4}$$

where:

y_t = noise sample at time instant t

(M.4) describes a noise process where observations are time correlated, becoming even more correlated when they are closer in time. By rearranging (M.4) one can understand how the present observation can be replicated based on previously measured samples and a purely random noise pattern:

$$y_t = e_t + \beta y_{t-1} \tag{M.5}$$

where:

$\beta = e^{-\alpha}$, $(\beta \in (0,1))$, correlation coefficient
α = reciprocal value of the correlation time[3] of the considered sequence of observations.

Such a noise process may result from applying a recursive scheme, for e.g a digital filter, on the raw, uncorrelated observations. This process is being known as observations time correlation and is been used by manufacturers to improve the sampling and acquisition performances of sensors.

REFERENCES

[1] C. Tiberius and A. Amiri-Simkooei, *Time Series Analysis - Hand-out,* Geoscience and Remote Sensing Department, TU Delft (2005).

[3] can be used for defining the correlation time ($\frac{1}{\alpha}$) of the considered sequence of observations.

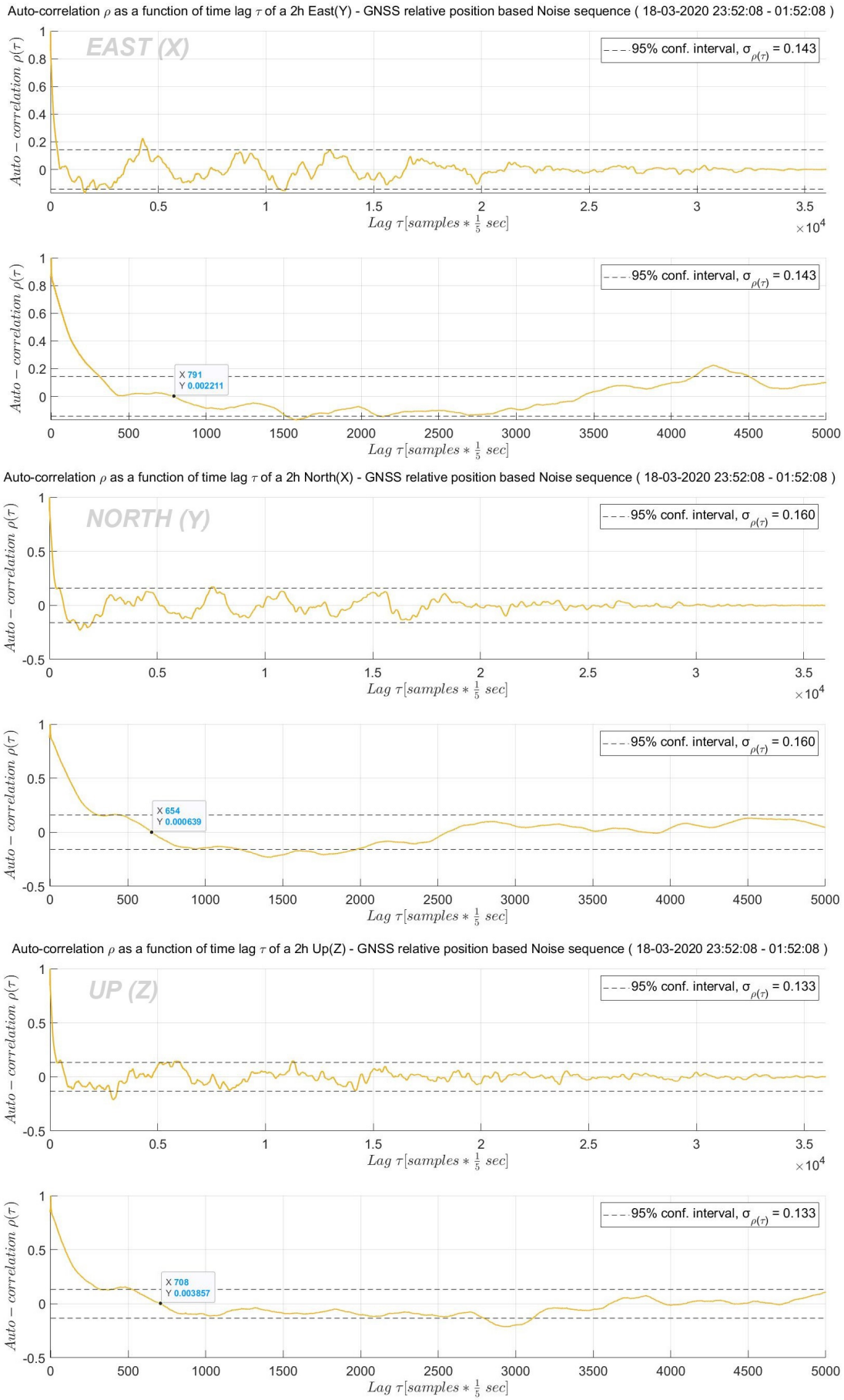

Figure M.1: Example of correlograms of the random noise sequences derived from the first (b=1) East (X), North (Y) and Up (Z) MP correction blocks. For each cardinal direction top panel contains the entire auto-correlation sequence while the panel from below contains a zoom in over the first 5000 lags of the auto-correlation sequence. For each direction the later plot indicates the point (sample no. 791, 654 and 708) where the correlation of the GNSS data drops to zero for the first time

M

N

Appendix N: Example of the Real-Time Implementation of the Relative Position Based MP Correction. The PRN Codes Check

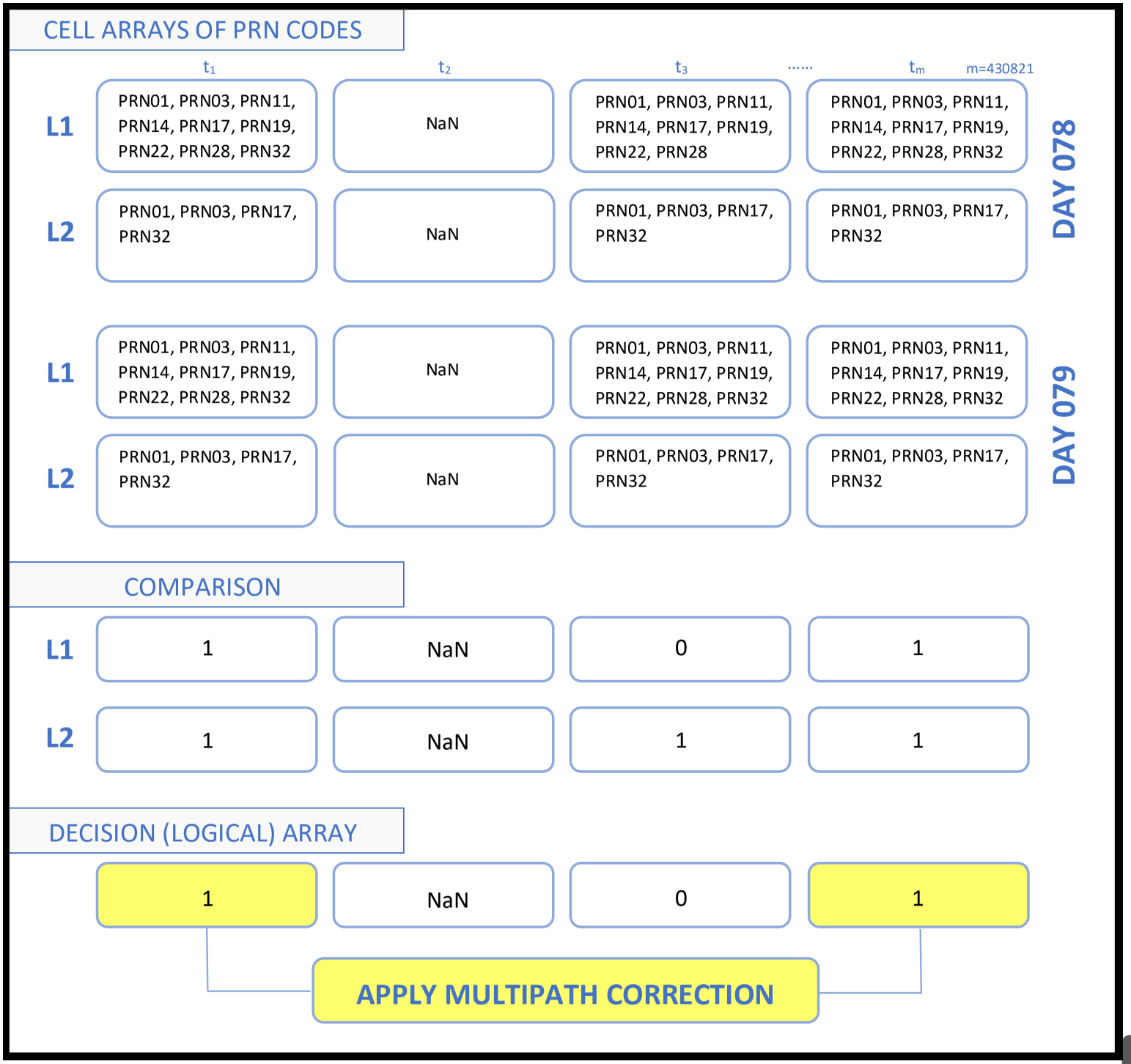

Figure N.1: Example of the complete real time implementation process of the empirical MP correction based on the repeatability of frequency dependent cell arrays of PRN code

O

Appendix O: Scheme of the 1D & 3D Outlier & Slip Test Approach. Synthetic Simulation Analysis of the Effectiveness of the 1D Outlier & Slip Test Approach. Example of a Displacement Slip Situation through a Nominal 1D & 3D Outlier Test

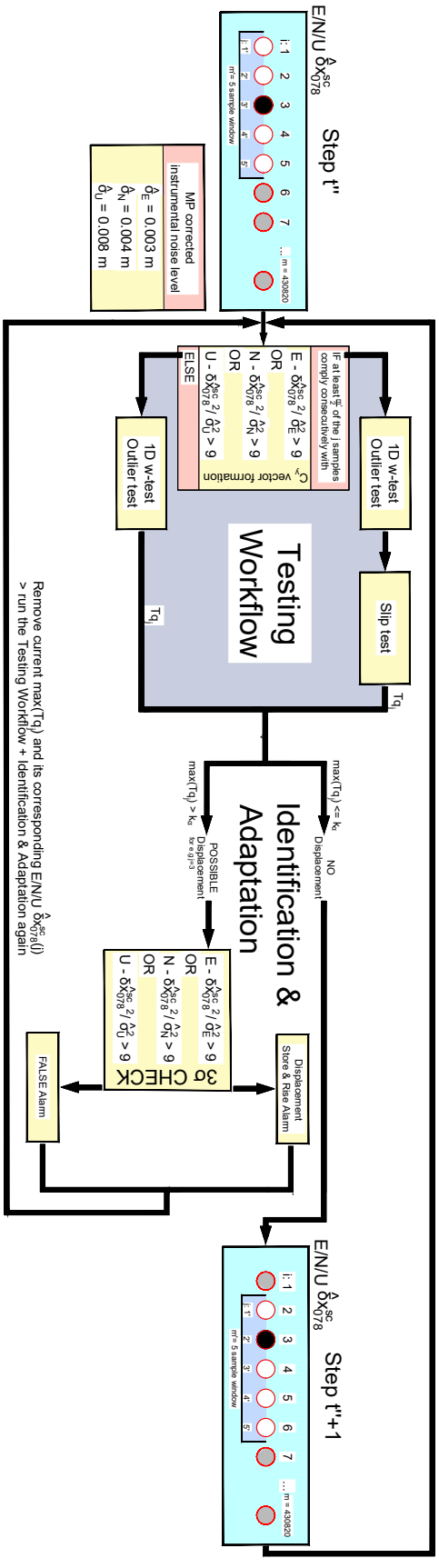

Figure O.1: Scheme of the 1D Outlier & Slip test procedure. In the figure a 1-second sliding window is illustrated. A single "real" displacement at index 3 is marked with a black dot

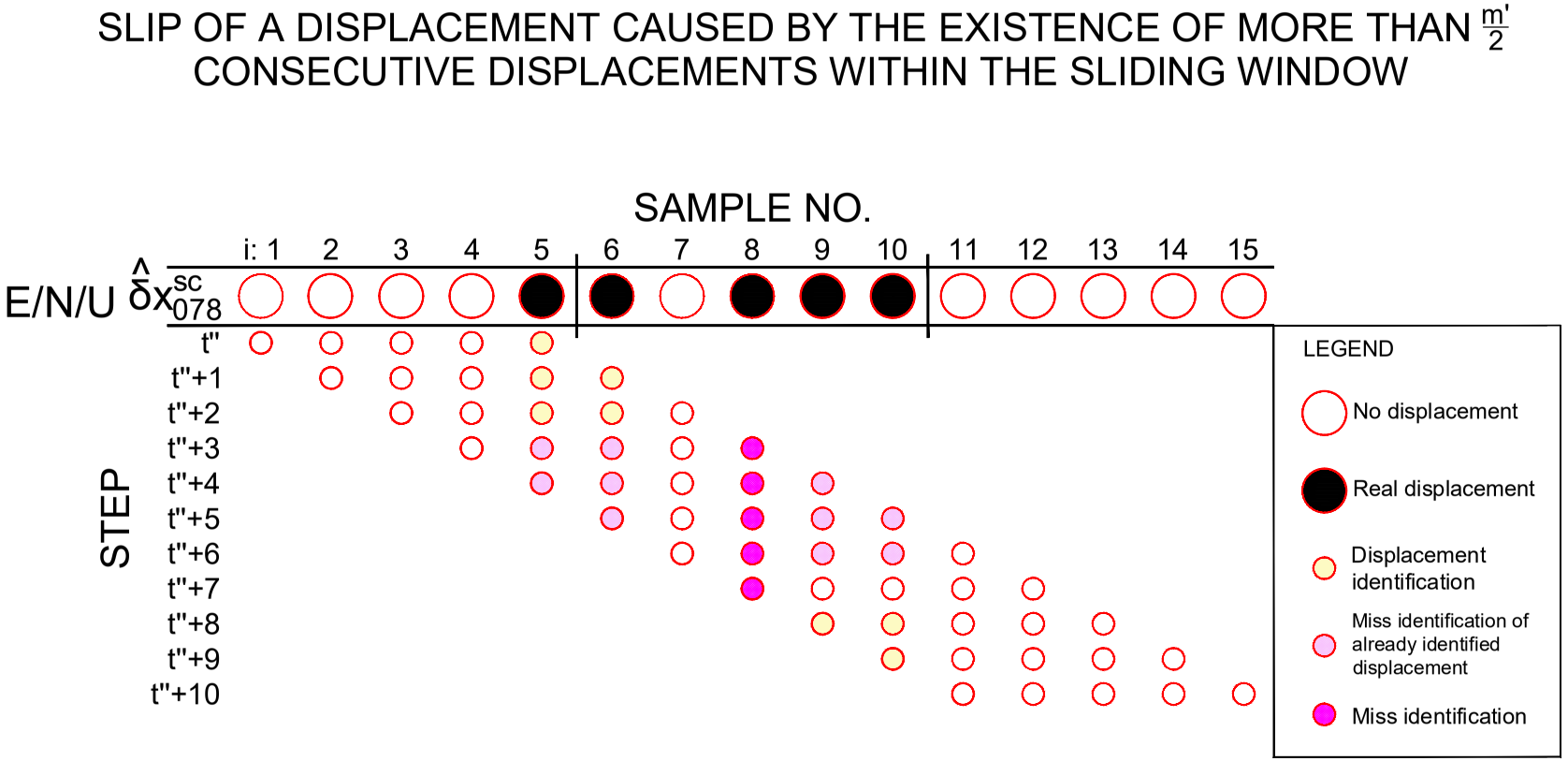

Figure O.2: Example of a slip of a displacement through a nominal 1D outlier test sliding window procedure. The slip happens at index 8 and is marked by bright magenta dots. The slip was caused by the 3 consecutive real displacement observations at index 8,9 and 10

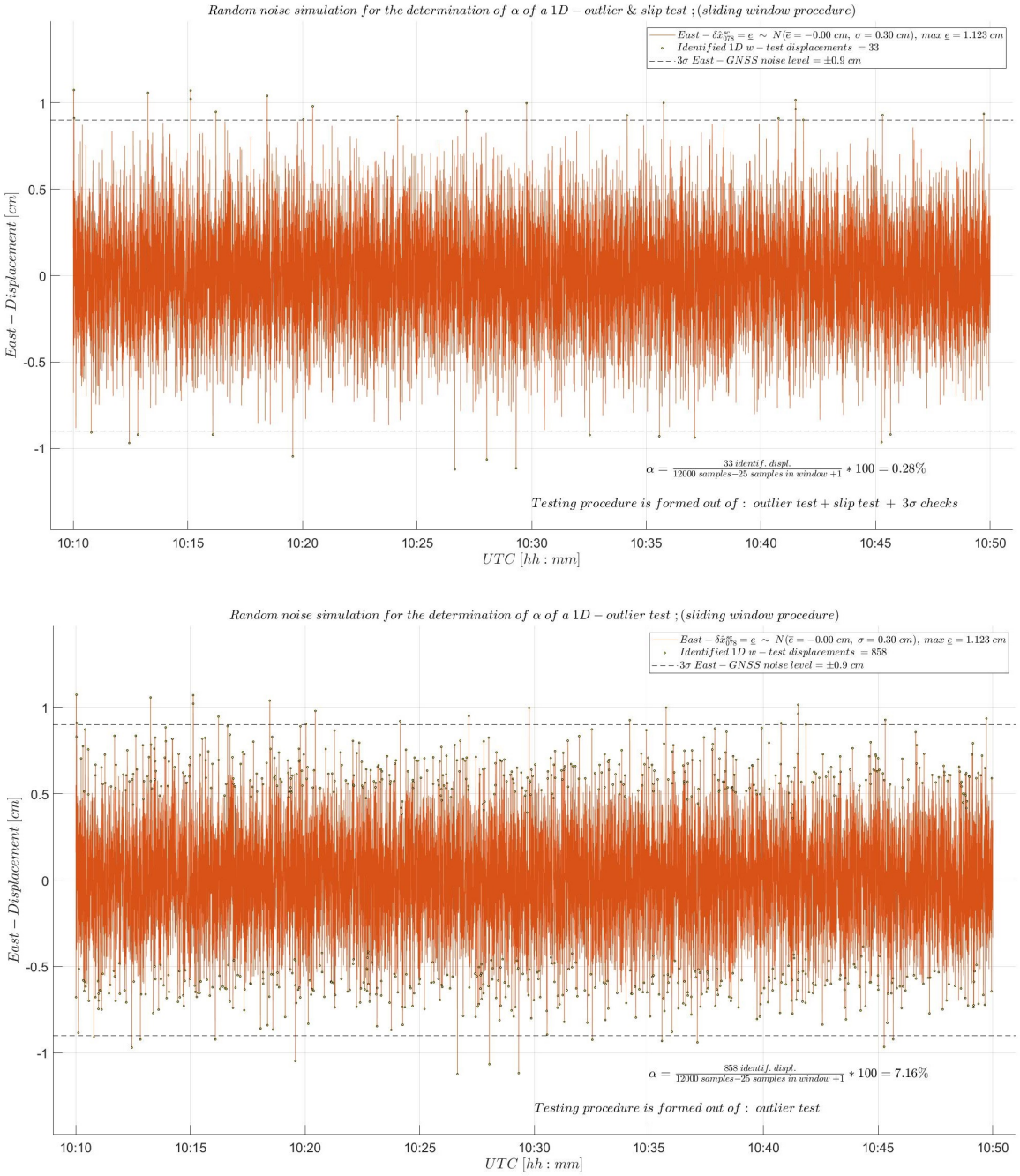

Figure O.3: Simulation analysis for determining the empirical false alarm probability of the 1D outlier & slip testing procedure. In the plot from above a random noise sequence of mean equal to 0 and standard deviation equal to 0.003 meters was fed in the 1D outlier & slip testing procedure along with the 3σ check procedure, resulting in an α value of only 0.28%. Without the 3σ check procedure (below) the 1D outlier & slip testing procedure would reach a large false alarm probability of 7.16%

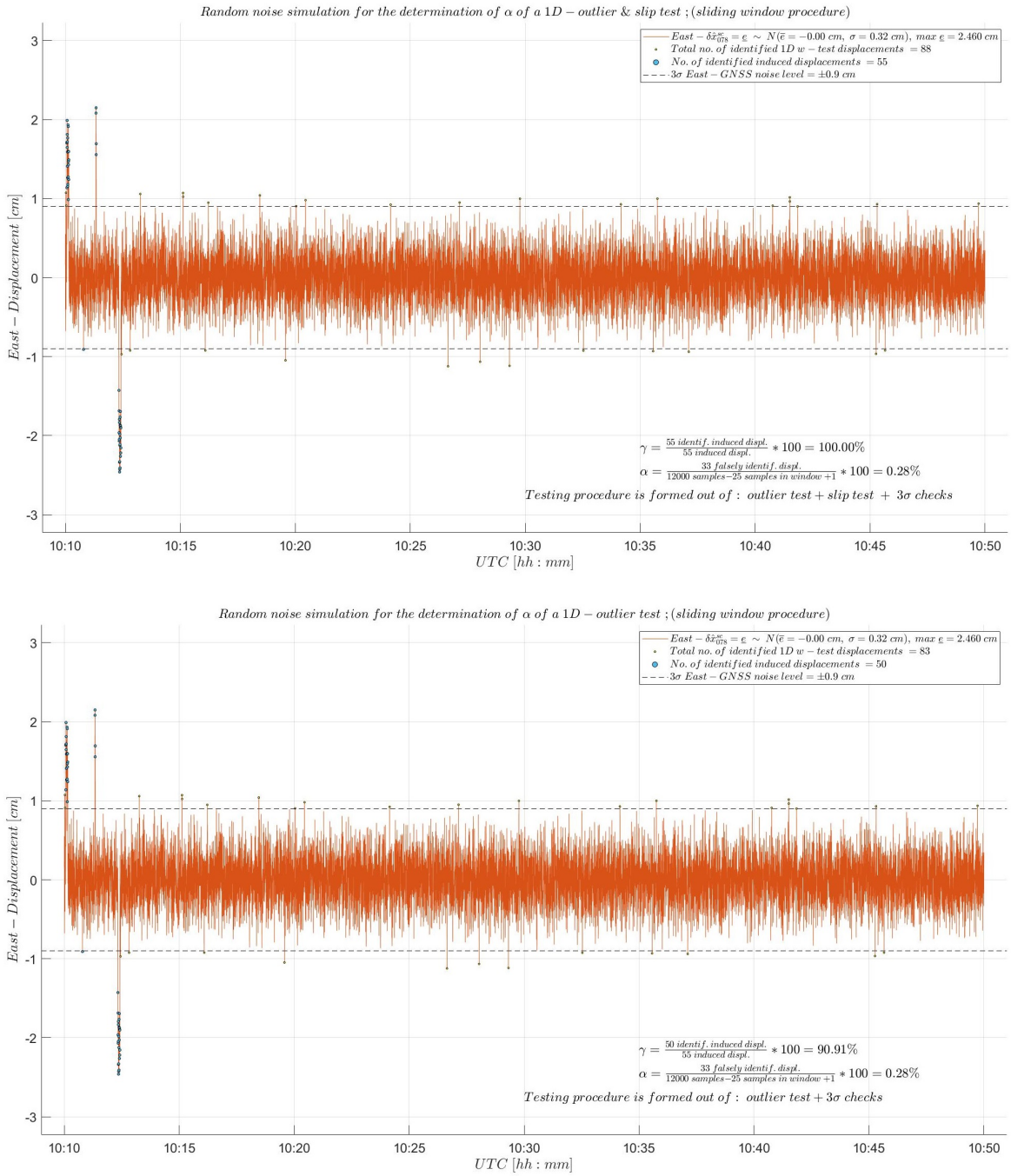

Figure O.4: Simulation analysis for determining the empirical probability of correct displacement detection (γ) of the 1D outlier & slip testing procedure (top) and of the nominal 1D outlier testing procedure (below). Within the generated random noise sequence, 3 sets of 26, 3 and another 26 consecutive displacements were induced (light blue dots). Hence, in the plot from above the 1D outlier & slip testing procedure could identify all 55 induced displacements, resulting in a maximum γ of 100%. On the other hand, in the plot from below the nominal 1D outlier testing procedure missed to detect 5 from the 55 induced displacements, resulting in a γ value of 90.91%.

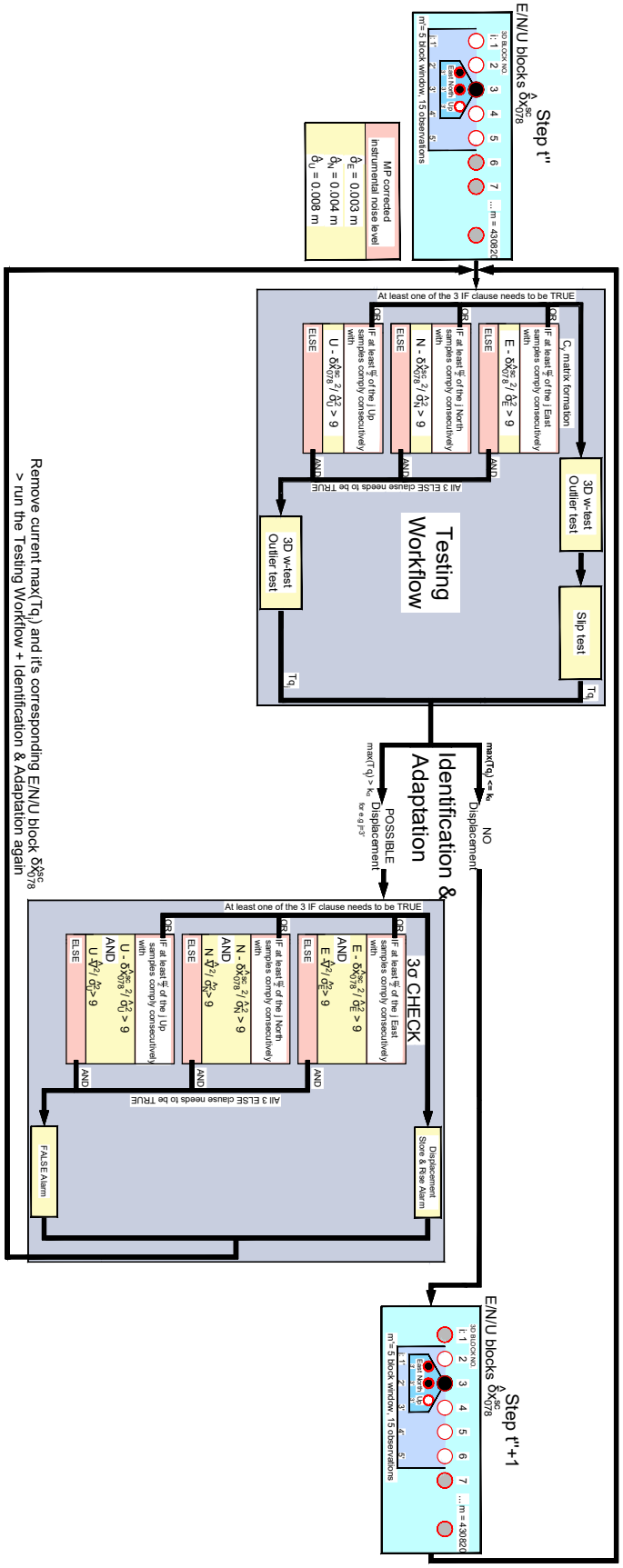

Figure O.5: Scheme of the 3D Outlier & Slip test procedure. In the figure a 1-second sliding window is illustrated consisting of 5(=m') 3D displacement observation blocks. A single "real" East (X) and North (Y) displacement at index 3' is marked with black dots

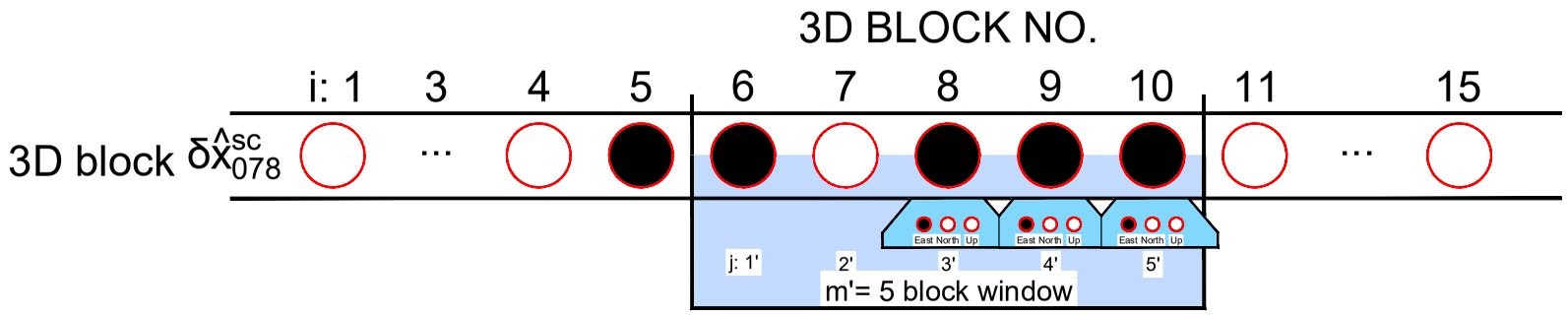

Figure O.6: Example of a slip of a displacement through a nominal 3D outlier test sliding window procedure. The figure is illustrating the format of the 3D displacement observation blocks. Each sliding window is consisting of 5(=m') 3D blocks, hence 15 observations. The slip will happen at i=8 and is caused by 3 consecutive East (X) displacement observations within the 8^{th}, 9^{th} and 10^{th} block

P

Appendix P: Theoretical Minimum Detectable Bias Analysis. Resulting Plots.

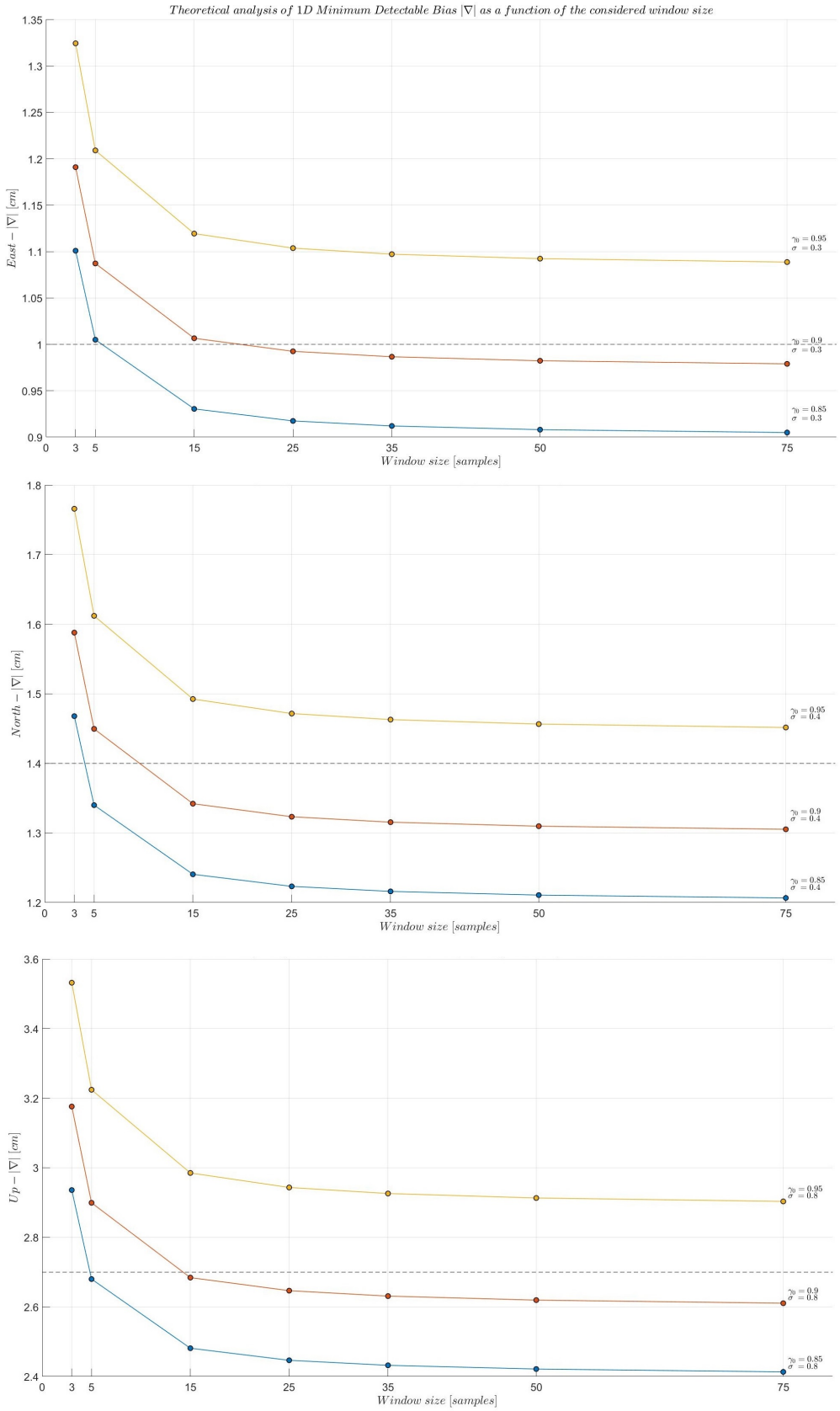

Figure P.1: 1D outlier test based MDB analysis as a function of the window size for γ_0 = 0.85 (blue), 0.9 (red) and 0.95 (yellow) and the MP corrected GNSS noise level of σ_E = 0.3, σ_N = 0.4 and σ_U = 0.8 cm. The user-defined MDB thresholds of 1 cm on East (X), 1.4 cm on North (Y) and 2.7 cm on Up (Z) direction are marked by the black dashed lines. A 1D outlier test with a power of 0.9 and a window size of 15 samples meets the user defined MDB thresholds

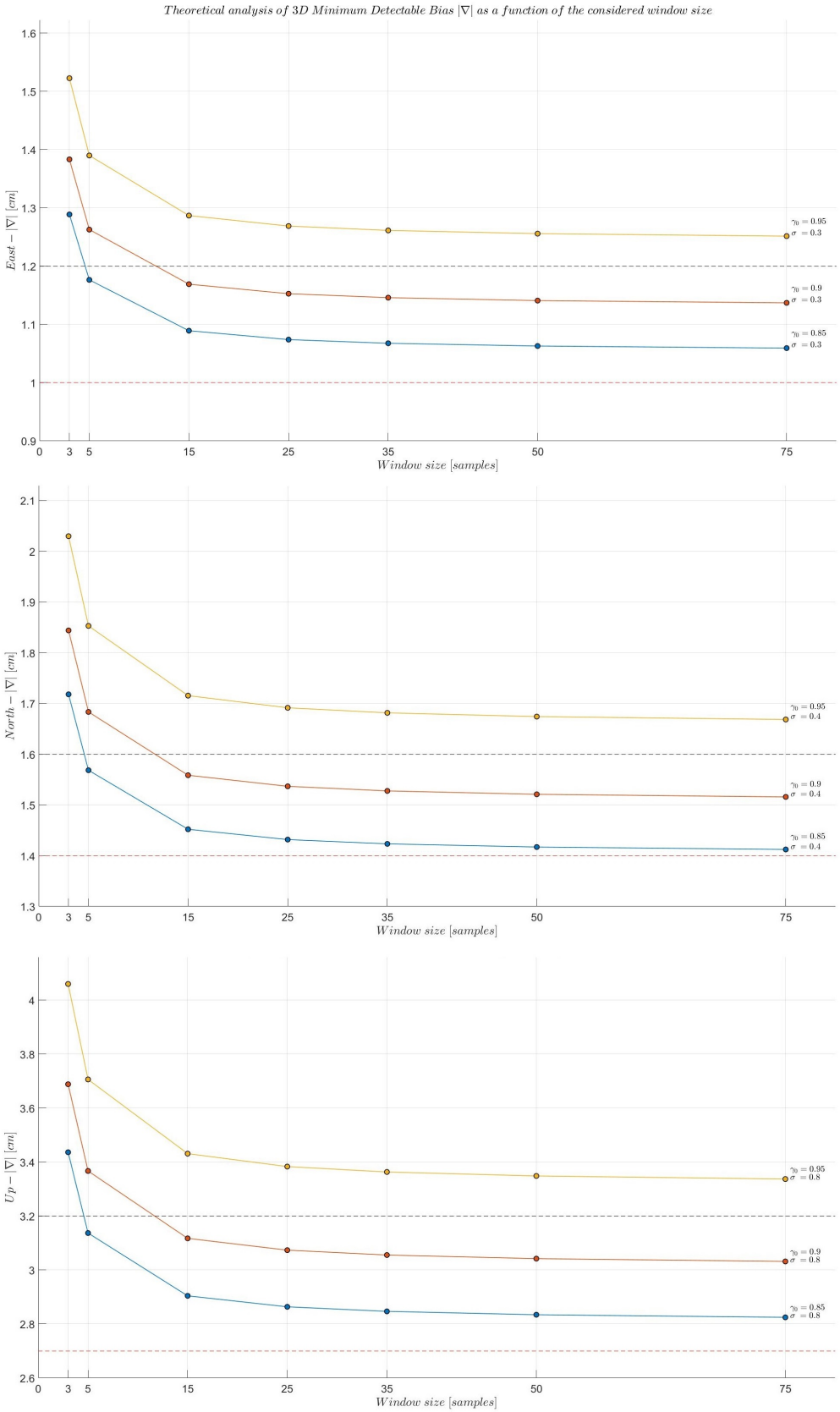

Figure P.2: 3D outlier test based MDB analysis as a function of the window size for γ_0 = 0.85 (blue), 0.9 (red) and 0.95 (yellow) and the MP corrected GNSS noise level of σ_E = 0.3, σ_N = 0.4 and σ_U = 0.8 cm. The user-defined MDB thresholds of 1.2 cm on East (X), 1.6 cm on North (Y) and 3.2 cm on Up (Z) direction are marked by the black dashed lines. The previous MDB thresholds from the 1D analysis are marked by the red dashed lines. A 3D outlier test with a power of 0.9 and a window size of 15 samples meets the user defined MDB thresholds

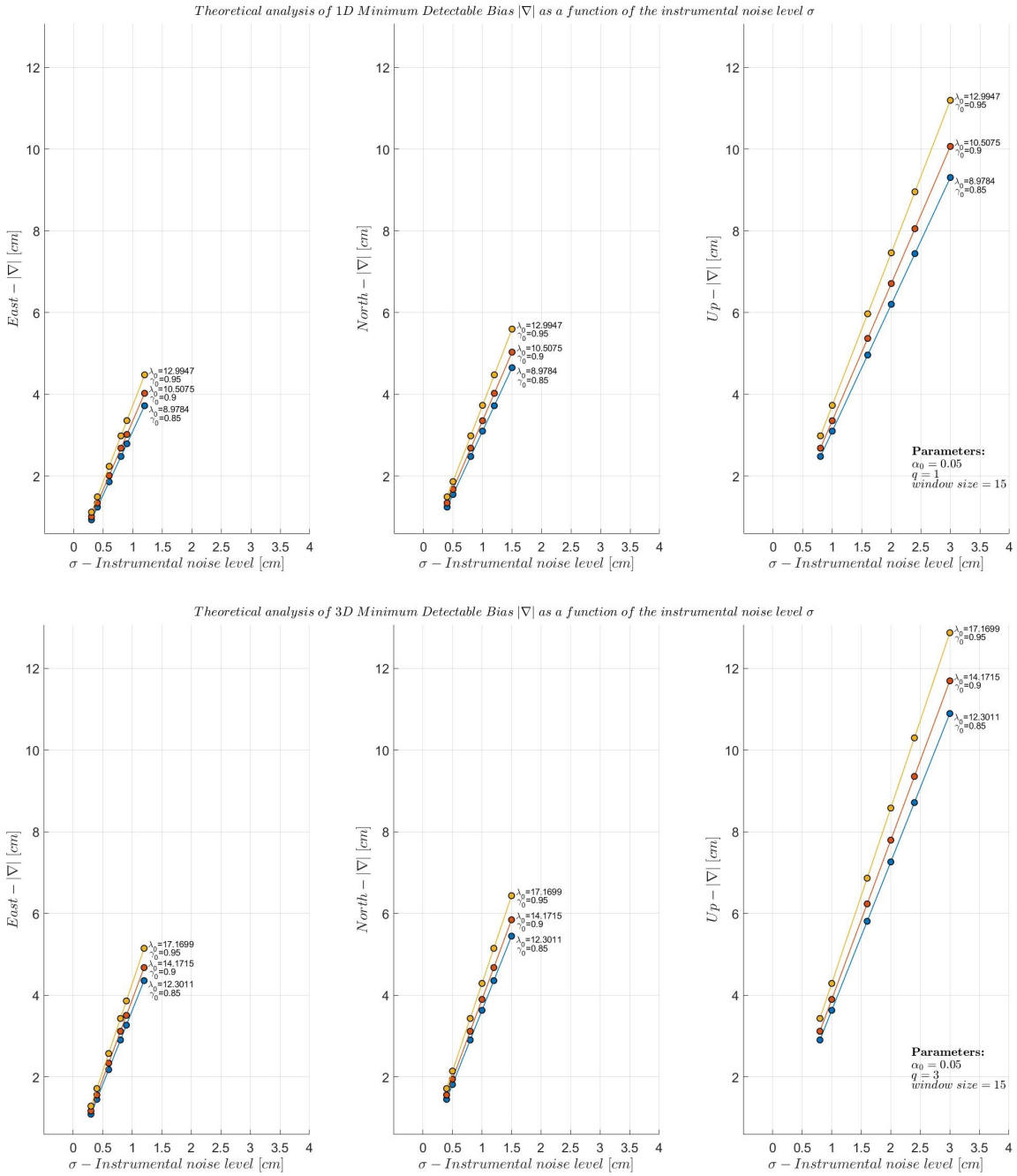

Figure P.3: Comparison between the 1D (above row) and 3D (below row) outlier test based MDB analysis as a function of the preset instrumental noise level for γ_0 = 0.85 (blue), 0.9 (red) and 0.95 (yellow) and a window size of 15 samples. For each power the MDB on each orthogonal direction is linearly increasing with the instrumental noise level

Q

Appendix Q: Intitial Thesis Project Proposal & Gantt Chart.

TU Delft

Final Graduation Project Proposal

Real-Time Structural Health Monitoring of Large-Scale Buildings using Low-Cost Dual Frequency GNSS Receivers

Project Proposal and Plan

Alexandru Mihai Lăpădat[1]

[1] MSc student Geoscience and Remote Sensing department, faculty of Civil Engineering and Geosciences, TU Delft, the Netherlands
Student number: 4796365, a.m.lapadat@student.tudelft.nl

Possible case study structure: High-rise steel-concrete tower, bridge, road sign(s)

Equipment:

- Low-cost dual frequency GNSS modules, 2 X u-blox ZED-F9P module – receiver(s) and antenna(s) – with sampling rate of up to 10 Hz
- Smartphone accelerometer (Bosch BMI160 – 16 bit digital triaxial accelerometer with resolution of 0.0023928 $\frac{m}{s^2}$ and maximum range of $\pm$78.4532 $\frac{m}{s^2}$)

GNSS Positioning accuracy: $\pm$10 mm in horizontal plane, $\pm$20 mm in vertical plane

Displacements of interest: Static, quasi-static and dynamic responses of case study structure under severe loading

Types of perturbing loads and buildings response:

- Wind load (at least 8 Beaufort wind gales of approximatively 19 $\frac{m}{s}$) > lateral and torsional displacements and horizontal accelerations
- Thermal influence > static and long-term displacement of structure

Research Goal:

- Demonstrate the effectiveness of *low-cost dual frequency GNSS equipment* for *real-time structural health monitoring* (SHM) of static, quasi-static and dynamic responses of major structures under the influence of severe loading by means of multipath (MP) corrected Real Time Kinematic (RTK) differential positioning, through experimental research and statistical approaches.

Addressed research questions:

- ***What is the accuracy capability of a low-cost dual frequency GNSS receiver and is it sufficient for monitoring wind-induced displacement of large-scale structures?***

  Unanswered question from conducted additional graduation work. Under the assumption that the used low-cost dual frequency GNSS receivers can sense centimeter order displacements another experiment on a more flexible, cantilever beam element is desirable (see *Further intended steps* section from below).

- ***What are the main steps for developing a low-cost real-time GNSS based monitoring system for sensing static, quasi-static and dynamic displacements of large-scale structures exerted by natural factors?***

  The answer of this question should lead to the development of an *implementation methodology of a real-time monitoring system* based on the theoretical aspects that will be studied. Note that this study will focus more on sensing wind-induced displacements. Ideally, this study is aiming on the implementation of such a system in real life, hence the intention of *creating a GNSS based SHM system prototype* as an end-result of the experimental research is desirable.

- ***What is the effectiveness of such system for measuring building displacements in real-time and accurately identify critical displacements?***

  The aim of this question is to make one develop a *statistical displacement detection algorithm* and test its effectiveness in deploying *trustful alarms* when critical displacement thresholds are exceeded. If time permits the design and optimization of a decision algorithm that is minimizing false alarms detection is taken into consideration.

- ***What are the benefits of integrating a secondary measuring technique such as smartphone accelerometers in the low-cost SHM system?***

  The answer to this question should be drawn from examples where high frequent responses, that were not detectable by the low-cost GNSS modules, could be retrieved from acceleration data sets improving the effectiveness of the compound low-cost SHM system. In addition, by integrating a smartphone accelerometer in the SHM system, one can extract vibration responses and monitor the integrity of construction parameter of more rigid structures.

- ***What are the steps for implementing a real-time MP mitigation procedure within the low-cost structural health monitoring system?***

  The aim of this question is to define and deploy a real-time integration plan for all previous applied corrections discussed in the additional graduation work. The definition of antenna-independent MP pattern can be based on:

  - ***Carrier phase (CP) residuals (most likely to be only discussed)***
  - ***Relative position/ Displacements estimates (most likely to be implemented)***

  spanning over full sidereal days, since the MP effect 'leaks' in the relative position estimates, receiver clock error and estimated carrier phase residuals. The main difference between these two correction patterns is the erroneous quantity on which MP corrections need to be applied. In case of the CP residual based MP correction this can be applied in real time to the raw carrier phase observations after converting its values from meter to cycle units. Moreover, this correction procedure can be defined for each satellite in reach, making it easier to identify and mitigate low elevation angle satellites that intensify the MP effect.
  On the other hand, relative position estimate-based MP correction can be applied on relative position time series of the same antenna, with the advantage of having only three correction time series, corresponding to East-West, North-South or Up direction.
  In both cases the geometry of the GPS constellation needs to be kept identical over full sidereal days.

Non-trivial error sources of GNSS modules and accelerometers. Correction procedure:

- Multipath (MP) effect – acquisition of satellite signals via multiple paths caused by reflection and diffraction. Has distinct effect on each GNSS antenna
  - Correction via position estimates- ((Kijewski-Correa and Kochly 2007)) and/ or carrier phase residuals based multipath signature (novel procedure that was never been discussed). Both procedures are fully dependent on constraining satellite geometry over each sidereal day
  - Identification of dominant frequency range of MP via Fourier analysis and design and application of a high-pass or bandpass filter scheme to separate displacement perturbing activity from low and high frequent noise ((Moschas and Stiros 2015), (Chan, Xu et al. 2006))
- GNSS antenna phase center (PC) error – the PC is an imaginary point where carrier phase signals are received by the GNSS antenna, which constantly changes depending on elevation and azimuth direction of the received CP signal coming from a transmitting

satellite. This error source is composed out of two quantities, an average phase center offset (PCO) with respect to the physical antenna reference point, and phase center variations (PCV) produced by the not homogeneous electromagnetic field of the antenna. It can influence the RTK positioning process under the premise that one is using different antennas at the reference and rover stations

  - A relative callibration process can be performed between two similar antennas emplaced on a reference- and test pier, with known distance in between. Measured distances between these two antennas will be used to define a priori positions of the PCO on the test pier with respect to the reference pier. This should be confronted with the positions coming from a different type of antenna installed on the test pier in order to define its average PCO with respect to the reference antenna. In addition, the PCV values can be determined by forming single-difference phase residuals with respect to the determined average PCO of the test antenna and by fitting a least squares polynomial to separate the PCV values from the variation due to residual clock delay differences of the two GNSS receivers. It is important to note that the the PC errors will cancel out under the assumption that one is using same type of GNSS antennas over short distances for performing RTK positioning ((Mader 1999))

- Atmospheric delay errors: Troposhpere zenith delay and Ionosphere delay – both errors influnce RTK measurements over long distances drastically (m-errors) because of the distinctive composition of the troposhere- and ionosphere layers causing different signal refraction on th GNSS signals acquired by the reference and rover station
  - The troposheric zenith delay can be estimated as an extra horuly unknwon parameters in the position estimation process or can be extracted from numerical troposheric delay models while the ionosphere delay can be elliminated by forming ionosphere-free linear combinations out of dual frequency GNSS observations and by using global ionosphere models ((Peter J.G. Teunissen 2017))
    When performing RTK positioning over short distances these errors have the same effect on GNSS measurements collected by the reference and rover receivers. Hence they will be elliminated on behalf of the double difference carrier phase estimation process implemented in the RTK positioning process

- GNSS forward transformation from displacements to accelerations for validation purposes
  - Correction by filtering MP effect via high-pass filter, double differentiate the filtered GNSS measurements, cross-correlation lag correction between GNSS estimate- and measured accelerations ((Li, Rizos et al. 2005))

- Accelerometer drift error caused by ambient temperature change and internal components sensitivity over long periods
  - Acceleration mean and trend removal ((Kong, Allen et al. 2018)), gravity compensation based on orientation measurements

- Accelerometer baseline correction in case of reverse transformation from acceleration to displacement values for incorporating acceleration and GNSS data sets to measure a broader range of frequencies and capture static, quasi-static and dynamic movements of major structures
  - Integration of acceleration data assuming that first integration (velocity) constant is equal to 0; Find velocity constant from both accelerometer and GNSS data sets via trending and average both trends. Resulting trend needs to be subtracted from velocity time serie derived from accelerometer data; Second integration step assuming that displacement constant is equal to 0. Average the resulting displacement time series with a trend fitted through the GNSS displacement time series (equal to displacement constant) ((Li, Rizos et al. 2005))

Results validation:

Since this study is aiming on demonstrating the effectiveness of using low-cost GNSS equipment for SHM purposes through experimental research (see *Further intended steps* chapter from below) an independent validation procedure by laser- and/ or gravity-based measuring equipment such as laser distometer and accelerometers is desirable.

- Robotized total station (RTS)/ laser distometer for measuring static and quasi-static responses covering low frequency ranges up to 2 Hz
- Low-cost smartphone accelerometer. Robust, low energy consumption and low-price validation solution of the GNSS based displacement results in the middle frequency range between 0.2 - 2 Hz, suitable for retrieving high-frequent dynamic behavior of buildings

A compound low-cost measuring system obtained by supplementing the low-cost GNSS receivers with a smartphone accelerometer is desirable for capturing static, quasi-static and dynamic building responses to get a detailed view over building's behavior caused by extreme loading.

Further intended steps:

- Cantilever beam experiment:

This first intended experiment has the aim to attest that the horizontal accuracy potential ($\pm$10 mm) of the low-cost dual frequency GNSS module is sufficient for measuring cm-order wind-induced displacements of structures. The obtained displacement results will be validated with an RTS/ laser distometer and/ or smartphone accelerometer measurements (via forward or reverse transformation). Furthermore, the possibilities of measuring and determining positions in real-time on site is desirable. Therefore, a new measuring set-up is proposed. Two identical u-blox ZED-F9P modules will be used for performing RTK differential positioning, where one of them will act as reference station while the other one, installed on top of the cantilever beam, will act as rover station. A minimum distance between them will be chosen. By choosing the same antenna for performing RTK differential positioning the phase center offsets (PCO) and phase center variations (PCV) will cancel out. Hence, no phase center (PC) calibration of the GNSS antennas will be addressed. **5 Hz** data sets will be collected, logged and processed in real time by a near-by processing station (laptop) through USB connection, via "u-center" software and/ or RTKLib's functionality "RTKNAVI". In addition, a weather station and anemometer will record precipitation, wind speed and direction measurements at the same time in order to later ask for statistical cross correlation between displacement- and meteorological data.
Firstly, displacement in all 3 directions (E/N/U) will be artificially induced for which validation is desirable.
Secondly, validation of wind-load model-based hypothesis (predicting deflections of up to $\pm$11 cm under 6 Beaufort breeze loads) by sensing wind-induced displacements of cantilever beam is desirable. The integration of (at least) one of the aforementioned MP correction procedures and of the cross-correlation analysis methodology is desirable (preferably in real time).

- Future identification of interesting, flexible case study building on which several advanced real-time tests should be conducted. Rijkswaterstaat road sign option.
- Integration of all previous applied correction in an algorithm that works in real-time:
  - MP signature initialization (post-processing) and application (real-time) for case study building
  - Missed observations correction. Appending of NaNs for missing measurements (post-processing)
  - Real-time ambiguity fixing success rate evaluation and screening (fully dependent on the precision of the estimated float ambiguities)

  - Standard deviation and number of satellites-based real-time filtration (in case of relative position-based MP correction)
  - 3σ criterion real-time filtering implementation. For this an adaptive moving average should be used for defining mean and standard deviation values based on past observation

- Deformation analysis via statistical tests integrations (Overall Model Test + w-test) to signal construction problems by sending real-time messages

  If time allows the implementation of a newly developed theoretical study on risk integrity of deformation monitoring can be taken into consideration for implementation. For this a limited number of displacement related alternative hypotheses should be defined and confronted with a null hypothesis

Benefits of using low-cost GNSS for structural health monitoring:

- Facilitates damage detection of high-rise structures over long time at low prices. This can be identified by the change of damage-sensitive structural features such as:
  - position of the building that exceeds a critical threshold (static and quasi-static response)
  - the natural frequency value of the structure in comparison with the finite element modeling based and/ or design calculation based natural frequency value; Frequency amplitude changes over time (dynamic response)
- Validation of building design after construction completion for a better understanding of structure behavior evolution that can be reflected in better future construction designs, improved design codes and dynamic models. By these the dynamic characteristics of the structure can be derived (modal frequencies, damping ratios, change in vibration amplitudes)
- Alarm deployment scheme, if building displacements and/ or construction parameters exceed critical threshold(s). Suitable for maintenance planification

Novelty of the research:

- Until now only a very limited amount of research was done on ***real-time*** SHM based on GNSS technology ((Behr, Hudnut et al. 1998), (Olmo, Abadia et al. 2016), (Celebi and Sanli 2002)) and no study was testing the capabilities of ***low-cost GNSS*** *equipment* for conducting such study. In addition, most of the studies only test the capabilities of outputting displacement estimates based on RTK differential positioning principle but they do not take into account on a *real-time MP mitigation procedure*. Therefore, this study is *primarily* aiming on developing a near real-time displacement-based MP correction, that will increase the degree of novelty of this research study
- In addition to the ordinary displacement detection statistical tests, the *definition and optimization of a displacement detection strategy that accurately quantifies false alarms* is desirable. From a theoretical point of view the later aspect is an asset increasing the degree of novelty

Project Planning and Gantt Chart:

The project planning is summarized in the Gantt chart from below:

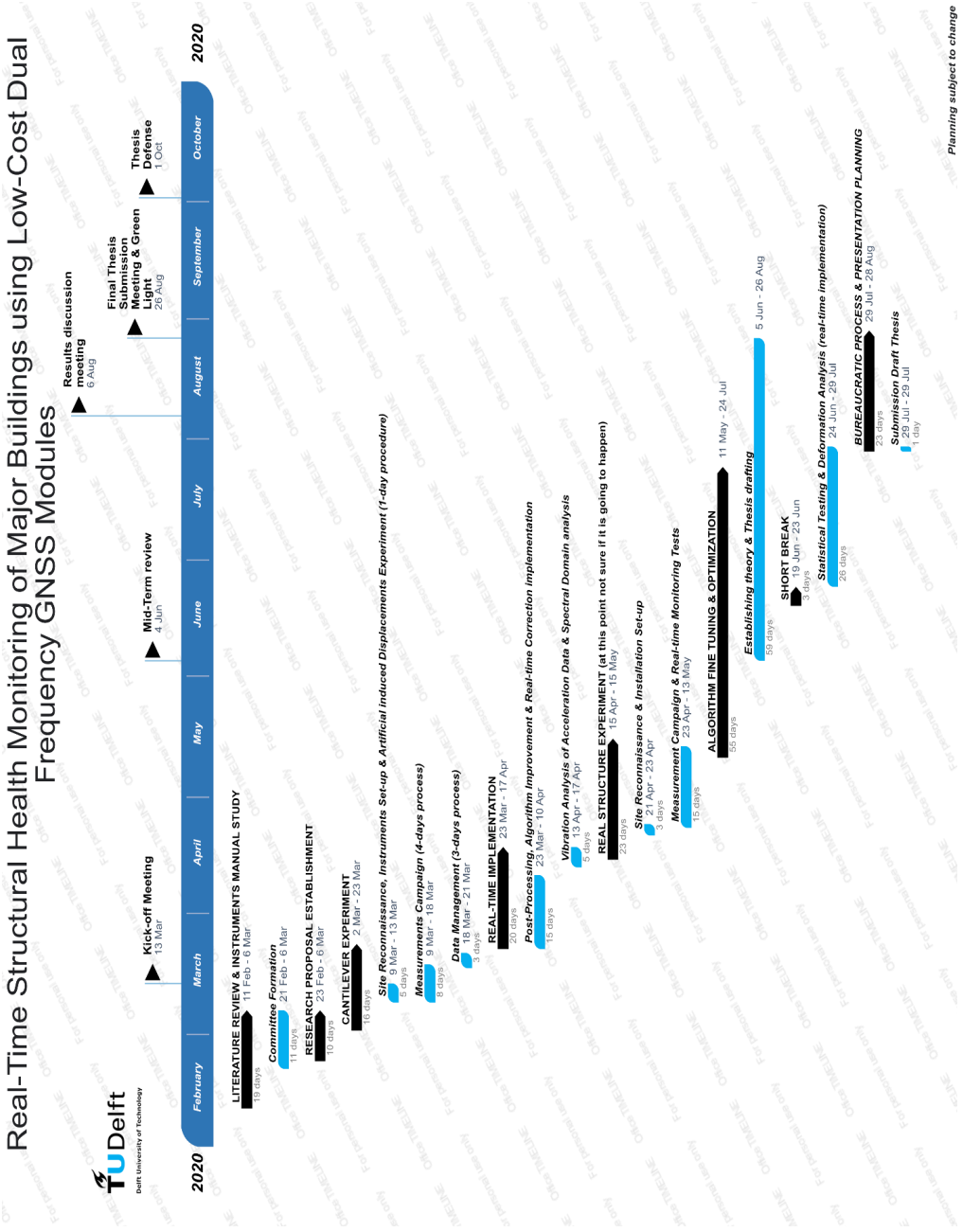

R

Appendix R: Auxiliary Practical Recommendations

– ***Choice of a better smartphone accelerometer data logging app***

Before conducting any SHM experiment, over long periods it is advisable to test as many data gathering smartphone applications as possible, in order to identify the most optimal one that can continuously collect the smartphone accelerometer data at a predefined sampling rate, without fragmenting it.
In case of the cantilever beam experiment two smartphone apps were tested over a fairly short period. However, after conducting the experiment it was found that the preferred one (Matlab Mobile) missed to collect more than half of the acceleration observations, recording 85% of the time at a rate of 15.151 Hz instead of 10 Hz, resulting in a strongly fragmented and miss-sampled acceleration time series. This was hampering the alignment of the smartphone and GNSS data sets, making the integration of the smartphone accelerometer data sets for real time displacement detection analyses impossible.

– ***Use of a weather station with a higher logging rate***

It is advisable to integrate a weather station in the SHM system that is able to collect wind speed, wind direction & precipitation data at a faster sampling period that 3 seconds. This is necessary in order to limit as much as possible or even avoid to down sample the original GNSS based displacement data set when checking for a strong statistical correlation between the GNSS based displacement and the meteorological data to attest that the identified structural displacements are induced by wind. Most probably such a meteorological equipment will be hardly identifiable and one would need to find a clever interpolation method to interpolate the 3-seconds meteorological observations to the desired sampling period.

– ***Practical consideration for the installation of the anemometer***

It is advisable to install the vane of the anemometer at, at least, 30 centimeters above the weather station in order to capture the natural wind direction flow. Additionally, the anemometer's vane needs to be calibrated to point towards true North[1].

[1] more details on the installation procedure of an anemometer can be found at: https://www.davisinstruments.com/product_documents/weather/manuals/07395-277_IM_6410.pdf

Master of Applied Earth Sciences
in Geoscience and Remote Sensing
Delft University of Technology

2020

Picture from Pixabay: https://pixabay.com/photos/skyscrapers-sky-cityscape-tall-up-1081737/